Università degli Studi di Napoli *Federico II*

DOTTORATO DI RICERCA IN

FISICA

Ciclo XXXIII

Coordinatore: prof. Salvatore Capozziello

Search for new physics contributions entering the tWb electroweak vertex at 13 TeV with the CMS experiment

Settore Scientifico Disciplinare FIS/01

Dottorando
Agostino De Iorio

Tutore
Prof. Alberto Orso Maria Iorio

Anni 2018/2021

To my family

Contents

Introduction

The Standard Model (SM) of Particles Physics is the current framework in which the electromagnetic, weak, and strong interactions successfully find an explanation. The SM is verified with high precision for most processes it describes, and all particles it predicted have been now been observed, after the discoveries of the Higgs boson at the LHC in 2012 and of the top quark at the TeVatron in 1994. Since then, intense studies have been performed to measure the features and the properties of such particles and their couplings.
The top quark in particular holds a special place in the Standard Model, as it is the most massive elementary particle ever discovered. As a consequence of its mass, it is also characterised by a very short lifetime: the decay occurs before it can hadronise, implying that most of the top quark properties can be directly inferred from the its decay products, as if it was a free particle. Another notable feature of top quark physics is that a distinct hierarchy can be identified in top quark decays: it almost exclusively decays in a W boson and a b quark. Decay modes in a W boson and a d or s quarks are allowed, but they are strongly suppressed, so much that up to now they have never been studied directly. This feature stems from the fact that there is a distinct preference of top quarks for couplings with b quarks via electroweak charged current interactions. The mixing among families is regulated in the SM by a matrix of fundamental parameters named the Cabibbo-Kobayashi-Maskawa (CKM) matrix. Through the study of top quark decays and electroweak couplings it is possible to extract the magnitude of the CKM matrix elements related to the third row, which, according to constraints from low energy measurements, should exhibit a remarkable hierarchical structure. Such hierarchical structure might also be an indication of a new more fundamental underlying physics model. In order to precisely study this sector of the SM, the best tool currently available is the Large Hadron Collider (LHC). The LHC is a circular accelerator designed to provide proton-proton collisions with a luminosity of 10^{34} $\mathrm{cm}^{-2}\mathrm{s}^{-1}$ and a centre-of-mass energy of $\sqrt{s} = 14$ TeV. The LHC is equipped with four main experiments: ALICE, ATLAS, CMS, and LHCb. The aim of LHC is to provide further proof on the validity of the SM and to give clues of new physics at the TeV scale.

The first goal of the present thesis work is the first direct measurement of the CKM matrix elements $|V_{\mathrm{tb}}|$, $|V_{\mathrm{ts}}|$ and $|V_{\mathrm{td}}|$ in events where single top quarks are produced via electroweak charged-current interactions. The main mechanisms for electroweak charged current production of single top quarks is the $t-$channel. The data analysed correspond to an integrated luminosity of 35.9 fb^{-1} of proton-proton collisions at a centre-of-mass energy of $\sqrt{s} = 13$ TeV collected with the CMS experiment at the LHC during 2016. The performed analysis explicitly probes in great detail the left-handed only interactions at the tWb vertex at energy regimes around the electroweak scale. New physics might rise in right-handed couplings, or manifest at higher energy regimes, both indirectly or directly via new resonances. There is experimental evidence, both in particle physics and in astrophysics observations, suggesting that the SM in not the ultimate fundamental theory. Many physics models have been proposed to extend it in a more general picture, so to provide an explanation to such phenomena, and several of them predict new particles that could have a mass larger than the one of the top quark. The top quark could therefore have a privileged relationship with new physics particles and play a crucial role in their discovery. The LHC is the perfect tool to perform direct searches for new particles thanks to the high-energy collisions and the large number of top quark produced. In the present work a search for a beyond the SM W$'$ boson decaying in tb quarks in leptonic final states is presented. Data from proton-proton collisions with a centre-of-mass energy of $\sqrt{s} = 13$ TeV, corresponding to 137.2 fb^{-1}, collected by the CMS experiment at the LHC from 2016 to 2018 are analysed.
An upgrade of the LHC accelerator complex in the next years will allow to significantly increase the collision rate, further improving the results obtained so far and effectively extending the physics reach of the machine. The CMS experiment foresees a series of detector upgrades to cope with the new challenging conditions. Part of this work documents the testing and validation of the Gas Electron Multiplier chambers that are part of the Muon System upgrade.

The present thesis is organised in six chapters:

- Chapter 1 briefly introduces the SM of elementary particles with a focus on the CMS matrix and the top quark physics.

- Chapter 2 reports the current limitations of the SM and presents promising models proposed to solve some of the SM issues. Particular attention is paid to models that predict a W$'$ boson, whose production modes and experimental results are presented.

- Chapter 3 presents a detailed description of the LHC accelerator machine and of the CMS detector. It also reports the activity for the upgrade of the CMS muon system with the triple-GEM detectors.

- Chapter 4 concerns definition, selection and reconstruction of the physics objects used in the analyses.
- Chapter 5 focuses on the detailed description of the analysis set up for the measurements of the CKM matrix elements $|V_{\mathrm{tb}}|$, $|V_{\mathrm{ts}}|$ and $|V_{\mathrm{td}}|$ in single-top $t-$channel events.
- Chapter 6 is devoted to the description of the analysis designed to investigate the presence of the Sequential SM W$'$ boson.

Chapter 1

The Standard Model of particle physics

1.1 Overview

The Standard Model (SM) of particle physics is an $SU(3)_C \times SU(2)_L \times U(1)_Y$[1] quantum field theory that describes three of the four known fundamental interactions in a single model. Its development began in 1961 from the effort of Sheldon Glashow [1] in unifying the electromagnetic and weak interactions, carried on in 1967 by Steven Weinberg [2] and Abdus Salam [3], who incorporated the Higgs mechanism [4–6]. Glashow, Weinberg and Salam won the Nobel Prize in Physics in 1979 "for their contributions to the theory of the unified weak and electromagnetic interaction between elementary particles, including, inter alia, the prediction of the weak neutral current". Over the years, the SM received other contributions aimed at the inclusion of the strong interaction in the Glashow, Weinberg, and Salam framework. The quantum field theory of the strong interaction is called quantum chromodynamics (QCD) and it was developed during the 60s and 70s. The main contributions to QCD come from Murray Gell-Mann and George Zweig [7], who suggested the existence of quarks with different flavours, and Moo-Young Han with Yoichiro Nambu [8] and Oscar W. Greenberg [9], who suggested the existence of a new quantum number called *colour* introducing so the $SU(3)_C$ symmetry. The SM reached its present form when, in 1973, David Politzer [10] and David Gross together with Frank Wilczek [11] suggested the theory of the asymptotic freedom of strong interaction.

The predictions of the SM were confirmed by numerous measurements over the past 60 years, which notably include the discovery of the three massive bosons

[1] The C and Y subscripts refer to the conserved quantity, or charges of the groups, colour and hypercharge respectively, and L refers to the left-handed nature of the interaction.

(W^+, W^- and Z) at CERN in 1983 by the UA1 and UA2 experiments [12–14], the discovery of the top quark at TeVatron in 1994 by the D0 and CDF experiments [15], and finally the discovery of the Higgs boson at CERN in 2012 by the ATLAS and CMS experiments [16, 17]. Thanks also to those compelling experimental evidences, the SM is widely accepted by the scientific community as the main model to describe fundamental interactions in particle physics. The SM is however not sufficient to provide a full picture of the known universe, as not only it fails to explains several phenomena, but also has some elements of weakness that suggest it is not the most fundamental theory. This Chapter will present the description of the SM and its mathematical derivation from prime principles, with a focus on the Cabibbo-Kobayashi-Maskawa matrix, the physics of the top quark, and the top quark production in proton-proton collisions at the Large Hadron Collider.

1.2 Particles in Standard Model

The SM treats both matter and force fields with the same formalism, since interactions are themselves regarded as mediated by particles. Particles in the SM are divided in fermions and bosons. Fermions have half-integer spin and obey the Fermi-Dirac statistics, while bosons have integer spin and obey the Bose-Einstein statistics. Fundamental fermions in SM are categorised as either quarks or leptons, which are divided into three families with different properties. Each family, or generation, is a doublet of particles associated to an isospin quantum number.

Leptons are composed by three massive electric charged particles and three massless neutral ones. Leptons take part to electromagnetic and weak interactions but not in strong one. The three generations of leptons and their main properties are listed in Table 1.1.

Generation	Particle	Spin	Charge	Mass [MeV]
I	e	1/2	-e	0.511
	ν_e	1/2	0	0
II	μ	1/2	-e	105.7
	ν_μ	1/2	0	0
III	τ	1/2	-e	1776.86
	ν_τ	1/2	0	0

Table 1.1: Main properties of the SM leptons [18].

Quarks are fermions that carry electromagnetic, weak and strong charges. In nature six different types, or flavours, of quarks exist and they are named as:

up, down, charm, strange, top and bottom. Quarks are grouped into the three generations as listed in Table 1.2. For all fermions, an antifermion is present with

Generation	Particle	Spin	Charge	Mass [MeV]
I	u	1/2	2/3 e	2.32 ± 0.10
	d	1/2	-1/3 e	4.71 ± 0.09
II	s	1/2	2/3 e	1280 ± 25
	c	1/2	-1/3 e	92.9 ± 0.7
III	t	1/2	2/3 e	$173.34 \pm 0.27 \pm 0.71 \times 10^3$
	b	1/2	-1/3 e	4180 ± 30

Table 1.2: Main properties of the SM quarks [18].

the same mass and opposite quantum numbers. Each interaction described by the SM is associated to a boson multiplet, whose components are referred to as mediators for the interaction, and to an absolutely conserved quantum number. The SM bosons are listed in Table 1.3.

1.3 Quantum electrodynamics

Quantum electrodynamics (QED) is the quantum field theory of the electromagnetic interaction. The Lagrangian density for the QED can be obtained by a gauge principle starting from the free Lagrangian density of the Dirac field ψ:

$$\mathscr{L}_D = i\bar{\psi}\gamma^\mu\partial_\mu\psi - m\bar{\psi}\psi, \tag{1.1}$$

where the first is the kinetic term and the last is a mass term. In particular m is the fermion mass parameter, γ^μ are the Dirac matrices and ψ and $\bar{\psi}$ are the 4-components spinor and its adjoint, respectively. ψ can be written in term of its

Interaction	Mediators	Spin	Charge	Mass [GeV]
Electromagnetic	γ	1	0	0
Weak	W^+,W^-	1	$e, -e$	80.354 ± 0.007
	Z	1	0	91.1876 ± 0.0021
Strong	8 gluons (g)	1	0	0
Yukawa	H	1	0	125.10 ± 0.14

Table 1.3: Standard model mediator bosons and fundamental interactions [18].

chiral components as:

$$\psi = \begin{pmatrix} \psi_R \\ \psi_L \end{pmatrix}$$

The free Lagrangian density of the electromagnetic field is:

$$\mathscr{L}_\gamma = -\frac{1}{4} F^{\mu\nu} F_{\mu\nu}, \tag{1.2}$$

where $F^{\mu\nu}$ is the field strength tensor and can be written in terms of the vector potential A^μ as:

$$F^{\mu\nu} = -F^{\nu\mu} = \partial^\mu A^\nu - \partial^\nu A^\mu. \tag{1.3}$$

The electromagnetic field is associated to the photon, i.e. the propagator of the electromagnetic interaction. So the free Lagrangian density for QED can be obtained by adding 1.1 and 1.2:

$$\mathscr{L}^0_{QED} = \mathcal{L}_\gamma + \mathcal{L}_D = i\bar{\psi}\gamma^\mu \partial_\mu \psi - m\bar{\psi}\psi - \frac{1}{4} F^{\mu\nu} F_{\mu\nu}. \tag{1.4}$$

This Lagrangian density describes the kinematics of a non-interacting fermion in an electromagnetic field and it is globally invariant under a $U(1)_q$ transformation:

$$\psi \to \psi' = e^{i\theta}\psi \tag{1.5}$$

but it does not extend in any way the theory. Instead by imposing the locally invariance under the transformation $U(1)_q$ one obtains:

$$\psi \to \psi' = e^{i\theta(x)}\psi, \tag{1.6}$$

where this time the parameter $\theta(x)$ depends on space-time coordinates. This causes an interaction term to arise:

$$\mathscr{L}_{int} = -q\bar{\psi}\gamma^\mu A_\mu \psi = -J^\mu A_\mu. \tag{1.7}$$

This term can be re-absorbed by redefining the derivative used in the operators. The covariant derivative is introduced as:

$$D_\mu \equiv \partial_\mu - iqA_\mu \tag{1.8}$$

and substituted to the standard derivative, allowing to re-establish the entire invariance of the Lagrangian density. Finally, the Lagrangian density for the QED is:

$$\begin{aligned} \mathscr{L}_{QED} &= i\bar{\psi}(\not{D} - m)\psi - \frac{1}{4} F^{\mu\nu} F_{\mu\nu} = \\ &= i\bar{\psi}\gamma^\mu \partial_\mu \psi - m\bar{\psi}\psi - \frac{1}{4} F^{\mu\nu} F_{\mu\nu} - q\bar{\psi}\gamma^\mu A_\mu \psi, \end{aligned} \tag{1.9}$$

where $\not{D} = \gamma^\mu D_\mu$ and the fields transform, under the gauge transformation, as:

$$A_\mu \to A_\mu - \frac{1}{q}\partial_\mu \theta(x) \qquad \psi \to e^{-i\theta(x)}\psi. \tag{1.10}$$

1.4 The Electroweak theory

The original description of the weak interaction, due to Fermi (1934) [19], was formulated as a four-fermion contact interaction, where the coupling strength is dictated by the Fermi constant $G_F = 1.16638 \times 10^{-5}$ GeV^{-2}. A dimensional coupling constant leads to divergences in the cross sections calculations, since the scattering amplitude turns out to grow with the scale of the process rather than decrease. This type of interaction, that was originally successful in explaining the electroweak interactions short-range interaction approximation, was later on interpreted as the low-energy approximation of a massive bosons mediated interaction.

1.4.1 The Glashow-Salam-Weinberg model

The model developed by Glashow, and successfully extended by Salam and Weinberg, is a non-Abelian $SU(2)_L$ quantum field theory. In the $SU(2)_L$ group of symmetry L stands for the left-handed chiral components of the fields, as in this theory, it is the only one involved in the weak interaction. Since the generators of $SU(2)_L$ are the Pauli matrices, it is useful to adopt the formalism of the angular momentum, therefore the particles eiegenstates of the weak interaction are arranged in six doublets of weak isospin. By naming t the weak isospin and t_3 its projection along one axis of choice, the six doublets for leptons are:

$$t = 1/2 \qquad \begin{matrix} t_3 = +1/2 \\ t_3 = -1/2 \end{matrix} \qquad \begin{pmatrix} \nu_e \\ e \end{pmatrix}_L \begin{pmatrix} \nu_\mu \\ \mu \end{pmatrix}_L \begin{pmatrix} \nu_\tau \\ \tau \end{pmatrix}_L ,$$

and for quarks are:

$$t = 1/2 \qquad \begin{matrix} t_3 = +1/2 \\ t_3 = -1/2 \end{matrix} \qquad \begin{pmatrix} \mathrm{u} \\ \mathrm{d}' \end{pmatrix}_L \begin{pmatrix} \mathrm{c} \\ \mathrm{s}' \end{pmatrix}_L \begin{pmatrix} \mathrm{t} \\ \mathrm{b}' \end{pmatrix}_L .$$

The weak interaction eigenstates d′, s′, and b′ are a linear combination of the strong interaction eigenstates (or mass eigenstates). Such feature does not stem from prime principles, but rather from the observation of mixing between mass eigenstates in weak interactions. The mixing of different flavours is given by:

$$\begin{pmatrix} \mathrm{d}' \\ \mathrm{s}' \\ \mathrm{b}' \end{pmatrix} = V \begin{pmatrix} \mathrm{d} \\ \mathrm{s} \\ \mathrm{b} \end{pmatrix},$$

where V is the complex unitary matrix named Cabibbo-Kobayashi-Maskawa (CKM) matrix:

$$V = \begin{pmatrix} V_{\mathrm{ud}} & V_{\mathrm{us}} & V_{\mathrm{ub}} \\ V_{\mathrm{cd}} & V_{\mathrm{cs}} & V_{\mathrm{cb}} \\ V_{\mathrm{td}} & V_{\mathrm{ts}} & V_{\mathrm{tb}} \end{pmatrix}.$$

Since the theory does not provide any prediction for the CKM matrix elements, their values must be inferred from experiments. Sec. 1.4.4 reports a detailed derivation of the CKM matrix, its parametrisation, and its most significant properties.

The GSW model is developed in a similar way with respect to the QED theory. A local $SU(2)_L$ gauge transformation acting on the weak isospin doublets is imposed:

$$\begin{pmatrix} \nu_\ell \\ \ell^- \end{pmatrix}_L' = e^{-\frac{i}{2}\vec{\alpha}(x)\cdot\vec{\tau}} \begin{pmatrix} \nu_\ell \\ \ell^- \end{pmatrix}_L , \tag{1.11}$$

where $\vec{\tau}$ are the Pauli matrices and $\vec{\alpha}(x)$ is the vector of real parameters of the transformation. Three gauge fields, named W^1, W^2, and W^3, transforming as a $t = 1$ multiplet (a triplet) under the group, are introduced. Two of these can be combined together in order to give two vector bosons $W^\pm$, that are electrically charged and can induce transitions between the members of the weak isospin doublets. The third gauge boson of the triplet should be electrically neutral. This feature can be exploited to provide an unified description of electromagnetic and weak forces by introducing a new $SU(2)_L \times U(1)_Y$ symmetry group. The new Abelian $U(1)_Y$ group is associated with a quantum number named weak hypercharge just as $SU(2)_L$ was associated with weak isospin. Glashow proposed that the Gell–Mann-Nishijima relation, which was originally introduced to relate quantum numbers and electric charge of baryons by defining $SU(2)_L$ multiplets, should also hold for these weak analogues, giving:

$$eQ = e\left(t_3 + \frac{y}{2}\right) \tag{1.12}$$

which represent the electric charge Q (in units of e) of the t_3 member of a weak isomultiplet, assigned a weak hypercharge y. Clearly, therefore, the lepton doublets, (ν_e, e^-) etc. have $y = -1$, while the quark doublets (u, d') etc. have $y = +1/3$. When the local gauge principle is applied to this group, the charged vector bosons appear as before but there are now two neutral vector bosons, whose combination will be responsible for the weak neutral current processes and for electromagnetism. In order to make the electroweak Lagrangian density invariant under the $SU(2)_L \times U(1)_Y$ group, the covariant derivative needs to be defined as:

$$D_\mu = \partial_\mu + ig\frac{\vec{\tau}}{2}W_\mu + ig'yB_\mu, \tag{1.13}$$

where g and g' are the two coupling constants for the two interactions. Neglecting the mass term for now, the electroweak Lagrangian density must include a Dirac term for fermions:

$$\mathscr{L}_{fermions} = \sum_f \bar{\psi}\gamma^\mu D_\mu \psi \tag{1.14}$$

and a term for the dynamics of the gauge boson fields

$$\mathscr{L}_{gauge} = -\frac{1}{4}W_i^{\mu\nu}W^i_{\mu\nu} - \frac{1}{4}B^{\mu\nu}B_{\mu\nu}, \tag{1.15}$$

where $W_i^{\mu\nu}$ and $B^{\mu\nu}$ are the tensor fields:

$$W_i^{\mu\nu} = \partial^\mu W_i^\nu - \partial^\nu W_i^\mu \tag{1.16}$$
$$B_i^{\mu\nu} = \partial^\mu B^\nu - \partial^\nu B^\mu \tag{1.17}$$

and W^μ is a three component vector field.
The complete Lagrangian density for the electroweak processes therefore is:

$$\begin{aligned}\mathscr{L}_{EW} =& - i\psi_L\gamma^\mu\left(\partial_\mu + ig\frac{\vec{\tau}}{2}\cdot W_\mu + ig'yB_\mu\right)\psi_L + \\ & - i\psi_R\gamma^\mu\left(\partial_\mu + ig'yB_\mu\right)\psi_R + \\ & - \frac{1}{4}W_i^{\mu\nu}W^i_{\mu\nu} - \frac{1}{4}B^{\mu\nu}B_{\mu\nu} + \\ & + \frac{1}{2}g\,\epsilon_{ijk}W_i^{\mu\nu}W_{j\mu}W_{k\nu} + \frac{1}{4}g^2\,\epsilon_{ijk}\epsilon_{imn}W_{j\mu}W_{k\nu}W_m^\mu W_n^\nu,\end{aligned} \tag{1.18}$$

where ψ_L and ψ_R are the left and right-handed chiral components of the particle fields, and the terms in the last line describe the three and four-point self interactions of the vector bosons that arise because of the non-Abelian nature of the $SU(2)_L$ group. The four gauge fields can be combined to produce the physical vector fields for the $W^\pm, Z$ bosons and the photon:

$$W_\mu^\pm = \sqrt{\tfrac{1}{2}}\left(W_\mu^1 \mp W_\mu^2\right) \tag{1.19}$$
$$A_\mu = B_\mu\cos\theta_W + W_\mu^3\sin\theta_W \tag{1.20}$$
$$Z_\mu = -B_\mu\sin\theta_W + W_\mu^3\cos\theta_W \tag{1.21}$$

where θ_W is the Weinberg angle, or weak mixing angle, defined as:

$$\cos\theta_W = \frac{g}{\sqrt{g^2+g'^2}}, \quad \text{and} \quad \sin\theta_W = \frac{g'}{\sqrt{g^2+g'^2}} \tag{1.22}$$

The electromagnetic charge therefore is:

$$q = g'\cos\theta_W = g\sin\theta_W \tag{1.23}$$

1.4.2 Spontaneous symmetry breaking and Higgs mechanism

The electroweak theory up to now does not foresee a mass term for $W^{\pm}$ and Z bosons. In order for them to acquire mass, the simplest and most elegant way is the spontaneous symmetry breaking (SSB) mechanism. The SSB succeeds in giving mass to particles and foresees the introduction of an additional particle: the Higgs boson. The Higgs boson field is a doublet of complex scalar fields that can be written as:

$$\begin{pmatrix} \phi^+ \\ \phi^0 \end{pmatrix} = \begin{pmatrix} \phi_1 + i\phi_2 \\ \phi_3 + i\phi_4 \end{pmatrix} \tag{1.24}$$

and the Lagrangian density associated to this field is:

$$\begin{aligned} \mathscr{L}_H &= (D^\mu \phi)^\dagger D_\mu \phi - V(\phi) = \\ &= (D^\mu \phi)^\dagger D_\mu \phi - \frac{1}{2}\mu^2 \phi^\dagger \phi - \frac{1}{4}\lambda (\phi^\dagger \phi)^2, \end{aligned} \tag{1.25}$$

where $V(\phi)$ is the potential responsible of the symmetry breaking. When the covariant derivative 1.13 acts on the Higgs field it produces the following Lagrangian density:

$$\mathscr{L}_H = (D^\mu \phi)^\dagger D_\mu \phi - \frac{1}{2}\mu^2 \phi^\dagger \phi - \frac{\lambda}{4}(\phi^\dagger \phi)^2 - \frac{1}{4}F^{\mu\nu}F_{\mu\nu} - \frac{1}{4}G^{\mu\nu}G_{\mu\nu}, \tag{1.26}$$

where:

$$D^\mu \phi = \left(\partial^\mu + ig\frac{\vec{\tau}}{2}W^\mu + ig' y B^\mu\right)\phi \tag{1.27}$$

$$F^{\mu\nu} = \partial^\mu W^\nu - \partial^\nu W^\mu - g W^\mu \times W^\nu \tag{1.28}$$

$$G^{\mu\nu} = \partial^\mu B^\nu - \partial^\nu B^\mu. \tag{1.29}$$

By requiring that $\mu^2 < 0$ and $\lambda > 0$ the minimum of the potential is not unique, as shown in the Figure 1.1, and the Higgs field assumes the value:

$$\phi = \begin{pmatrix} 0 \\ \frac{1}{\sqrt{2}}(v + H(x)) \end{pmatrix}, \tag{1.30}$$

where:

$$v = -\sqrt{-\frac{\mu^2}{\lambda}}. \tag{1.31}$$

By substituting 1.30 in 1.26, one finds:

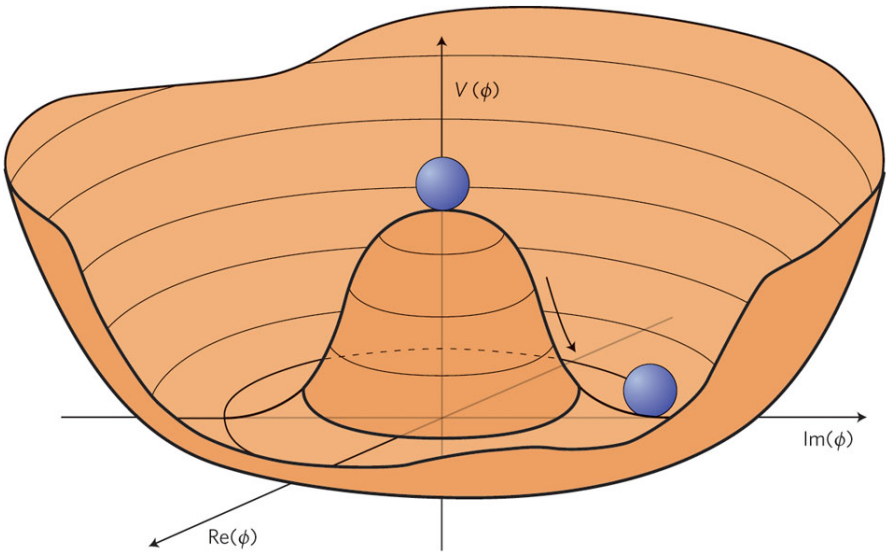

Figure 1.1: Shape of the Higgs potential for $\mu^2 < 0$.

$$\begin{aligned}\mathscr{L}_{G\Phi} = &\frac{1}{2}\partial_\mu H \partial^\mu H - \mu^2 H^2 + \\ &- \frac{1}{4}(\partial_\mu W^1_\nu - \partial_\nu W^1_\mu)(\partial^\mu W^{1\nu} - \partial^\nu W^{1\mu}) + \frac{1}{8}g^2 v^2 W^1_\nu W^{1\nu} \\ &- \frac{1}{4}(\partial_\mu W^2_\nu - \partial_\nu W^2_\mu)(\partial^\mu W^{2\nu} - \partial^\nu W^{2\mu}) + \frac{1}{8}g^2 v^2 W^2_\nu W^{2\nu} \\ &- \frac{1}{4}(\partial_\mu Z_\nu - \partial_\nu Z_\mu)(\partial^\mu Z^\nu - \partial^\nu Z^\mu) + \frac{1}{8}(g^2 + g'^2)v^2 Z_\nu Z^\nu \\ &- \frac{1}{4}F^{\mu\nu}F_{\mu\nu}.\end{aligned} \tag{1.32}$$

The first line of 1.32 shows that we have a scalar field of mass $\sqrt{2}\mu$ and foresees the introduction of an additional particle. The next two lines show that the components W^1 and W^2 of the triplet (W^1, W^2, W^3) acquire a mass:

$$M_1 = M_2 = \frac{1}{2}gv \equiv M_W. \tag{1.33}$$

The third line shows that the field Z acquires a mass:

$$M_Z \equiv \frac{1}{2}v\sqrt{g^2 + g'^2} = \frac{M_W}{\cos\theta_W}. \tag{1.34}$$

Finally, the last line shows that the field A^μ is massless, retrieving the same behavior as from the QED:

$$M_A = 0. \tag{1.35}$$

1.4.3 Masses of leptons

The fermion mass term $-m\bar{\psi}\psi$ is not invariant under the $SU(2)_L \times U(1)_Y$ group because of the different transformation of the right and left-handed chiral components of the fields. It is possible to introduce a gauge invariant mass term with a Yukawa coupling between the fermion field and the Higgs field written as:

$$\mathscr{L}_Y = g_f(\bar{\psi}_L \phi \psi_R - \bar{\psi}_R \phi^\dagger \psi_L), \tag{1.36}$$

where g_f is the Yukawa coupling constant. By substituting 1.30 in 1.36 one obtains:

$$\begin{aligned} \mathscr{L}_Y =& \frac{g_f}{\sqrt{2}}\left[(\nu_\ell,\ \ell)\begin{pmatrix}0\\ v+H\end{pmatrix}\ell_R + \ell_R(0,\ v+H)\begin{pmatrix}\nu_\ell\\ \ell\end{pmatrix}\right] = \\ =& \frac{g_f}{\sqrt{2}}(v+H)(\ell_L\ell_R + \ell_R\ell_L), \end{aligned} \tag{1.37}$$

so that the constant coefficient of $(\ell_L\ell_R + \ell_R\ell_L)$ is the mass term for leptons:

$$m_f = \frac{v}{\sqrt{2}} g_f. \tag{1.38}$$

Even if this kind of Yukawa coupling solves the problem of leptons' masses, it does not arise from a gauge principle and it is purely phenomenological.

1.4.4 Masses of quarks and CKM matrix

Analogously to the lepton case, one can write for quarks:

$$\begin{aligned} \mathscr{L}_Y =& \frac{1}{\sqrt{2}}\left[g^d_{i,j}(u_{i,L},\ d_{i,L})\begin{pmatrix}0\\ v+H\end{pmatrix} d_{j,R} + g^u_{i,j}(u_{i,L},\ d_{i,L})\begin{pmatrix}-(v+H)^*\\ 0\end{pmatrix} u_{j,R} + h.c.\right] = \\ =& \frac{1}{\sqrt{2}}(v+H)[g^u_{ij}(u_{i,L}u_{j,R} + u_{j,R}u_{i,L}) + g^d_{ij}(d_{i,L}d_{j,R} + d_{j,R}d_{i,L}) + h.c.] \end{aligned} \tag{1.39}$$

where u_i = (u, c, t) and d_i = (d, s, b), and the mass term are:

$$m^u_{ij} = -\frac{v}{\sqrt{2}} g^u_{ij} \quad m^d_{ij} = -\frac{v}{\sqrt{2}} g^d_{ij}. \tag{1.40}$$

The mass terms m^u and m^d are not diagonal in this basis but they can be made diagonal with four different transformations on the triplets $u_{i,L}$, $u_{i,R}$, $d_{i,L}$, and $d_{i,R}$ written as:

$$u_{\alpha,L} = (\mathcal{U}^u_L)_{\alpha i} u_{i,L} \quad u_{\alpha,R} = (\mathcal{U}^u_R)_{\alpha i} u_{i,R} d_{\alpha,L} = (\mathcal{U}^d_L)_{\alpha i} d_{i,L} \quad d_{\alpha,R} = (\mathcal{U}^d_R)_{\alpha i} d_{i,R} \tag{1.41}$$

where α is the index in the mass diagonal basis and i is the index in the non-diagonal weak interaction basis.

$$\mathscr{L}_Y = \frac{1}{\sqrt{2}}(v+H)\left[m^u \mathrm{u}\bar{\mathrm{u}} + m^d \mathrm{d}\bar{\mathrm{d}} + m^s \mathrm{s}\bar{\mathrm{s}} + m^c \mathrm{c}\bar{\mathrm{c}} + m^t \mathrm{t}\bar{\mathrm{t}} + m^b \mathrm{b}\bar{\mathrm{b}}\right] \tag{1.42}$$

The same transformations must be applied to the interacting term invariant under the $SU(2)_L \times U(1)_Y$ symmetry that still contains the eigenkets of the weak interaction. When this operation is worked out, the term of the coupling with the Z boson, i.e. the neutral current coupling term, is diagonal also in the mass basis if the transformations of Eq. 1.41 are unitary, instead the term of the coupling with the W boson, i.e. charged current coupling term, is:

$$\begin{aligned}
\mathscr{L}_{CC} &= -\frac{g}{\sqrt{2}}(\bar{u}_{i,L},\ \bar{d}_{i,L})\gamma^\mu \tau_+ W_\mu^+ \begin{pmatrix} u_{Li} \\ d_{Li} \end{pmatrix} + h.c. \\
&= -\frac{g}{\sqrt{2}}\bar{u}_{iL}\gamma^\mu d_{Li} W_\mu^+ + h.c. \\
&= -\frac{g}{\sqrt{2}}\bar{u}_{\alpha_L}\left[(\mathcal{U}_L^u)_{\alpha i}(\mathcal{U}_L^d)^\dagger_{\beta i}\right]\gamma^\mu d_{L\beta} W_\mu^+ + h.c.,
\end{aligned} \tag{1.43}$$

where the matrix:

$$V_{\alpha\beta} = \left[\mathcal{U}_L^u \mathcal{U}_L^{d\dagger}\right]_{\alpha\beta} \tag{1.44}$$

is unitary but not diagonal. V is the CKM matrix and it is a 3×3 unitary matrix. It can be parametrised by three mixing angles and the CP-violating KM phase as follow:

$$V_{\mathrm{CKM}} = \begin{pmatrix} 1 & 0 & 0 \\ 0 & c_{23} & s_{23} \\ 0 & -s_{23} & c_{23} \end{pmatrix} \begin{pmatrix} c_{13} & 0 & s_{13}e^{-i\delta} \\ 0 & 1 & 0 \\ -s_{13}e^{i\delta} & 0 & c_{13} \end{pmatrix} \begin{pmatrix} c_{12} & s_{12} & 0 \\ -s_{12} & c_{12} & 0 \\ 0 & 0 & 1 \end{pmatrix}, \tag{1.45}$$

where $s_{ij} = \sin\theta_{ij}$, $c_{ij} = \cos\theta_{ij}$ and δ is the phase responsible for all CP-violating phenomena in flavour-changing processes in the SM. The angles θ_{ij} can be chosen to lie in the first quadrant, so s_{ij}, $c_{ij} \geq 0$.

It is known experimentally that $s_{13} \ll s_{23} \ll s_{12} \ll 1$, and it is convenient to exhibit this hierarchy using the Wolfenstein parametrization. By defining:

$$\begin{aligned}
s_{12} = \lambda = \frac{V_{\mathrm{us}}}{\sqrt{|V_{\mathrm{us}}|^2 + |V_{\mathrm{us}}|^2}}, \qquad s_{12} = A\lambda^2 = \lambda\left|\frac{V_{\mathrm{cb}}}{V_{\mathrm{us}}}\right|, \\
s_{13}e^{i\delta} = V_{\mathrm{us}}^* = A\lambda^3(\rho + i\eta) = \frac{A\lambda^3(\bar{\rho}+i\bar{\eta})\sqrt{1-A^2\lambda^4}}{\sqrt{1-\lambda^2}[1-A^2\lambda^4(\bar{\rho}+i\bar{\eta})]}
\end{aligned} \tag{1.46}$$

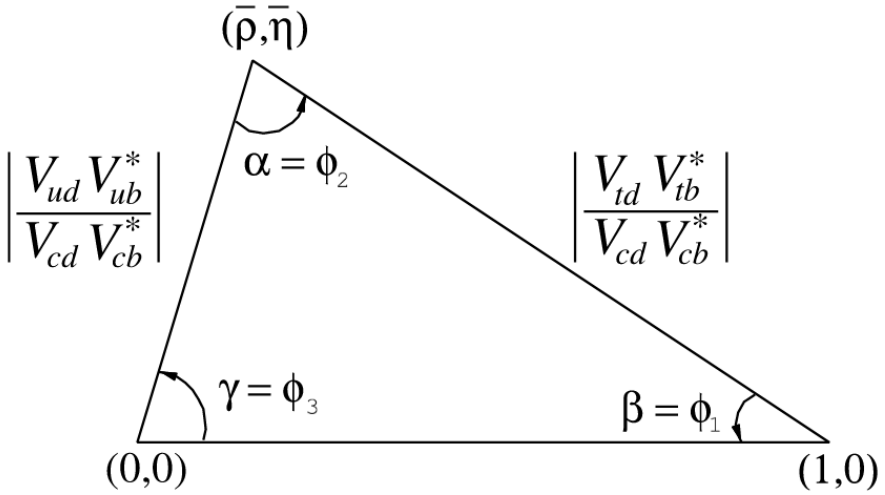

Figure 1.2: Graphical representation of the unitarity triangle obtained as reported in Eq. 1.48.

These relations ensure that $\bar{\rho} + i\bar{\eta} = -V_{\rm ud}V^*_{\rm ub}/V_{\rm cd}V^*_{\rm cb}$ is phase convention independent, and the CKM matrix written in terms of λ, A, $\bar{\rho}$, and $\bar{\eta}$ is unitary to all orders in λ:

$$V_{\rm CKM} = \begin{pmatrix} 1-\lambda^2/2 & \lambda & A\lambda^3(\rho+i\eta) \\ -\lambda & 1-\lambda^2/2 & A\lambda^2 \\ A\lambda^3(1-\rho-i\eta) & -A\lambda^2 & 1 \end{pmatrix} + \mathcal{O}(\lambda^4). \qquad (1.47)$$

The CKM matrix elements are fundamental parameters of the SM, so their precise determination is important. The unitarity of the CKM matrix imposes $\sum_i = V_{ij}V^*_{ik} = \delta_{jk}$ and $\sum_j = V_{ij}V^*_{kj} = \delta_{ik}$. The six vanishing combinations can be represented as triangles in a complex plane, of which those obtained by taking scalar products of neighbouring rows or columns are nearly degenerate. The areas of all triangles are the same, half of the Jarlskog invariant, J [20], which is a phase-convention-independent measure of CP violation, defined by $\mathrm{Im}[V_{ij}V_{kl}V^*_{il}V^*_{kj}] = J\sum_{mn}\epsilon_{ikm}\epsilon_{jln}$.

The most commonly used unitarity triangle, reported in Figure 1.2, arises from:

$$V_{\rm ud}V^*_{\rm ub} + V_{\rm cd}V^*_{\rm cb} + V_{\rm td}V^*_{\rm tb} = 0, \qquad (1.48)$$

by dividing each side by the best-known one, $V_{\rm cd}V^*_{\rm cb}$.

Its vertices are exactly (0,0), (1,0), and $(\bar{\rho}, \bar{\eta})$. An important goal of flavour physics is to overconstrain the CKM elements, and many measurements can be conveniently displayed and compared in the $\bar{\rho}, \bar{\eta}$ plane. A global fit on the SM parameters is then performed in order to extract, amongst the others, the elements

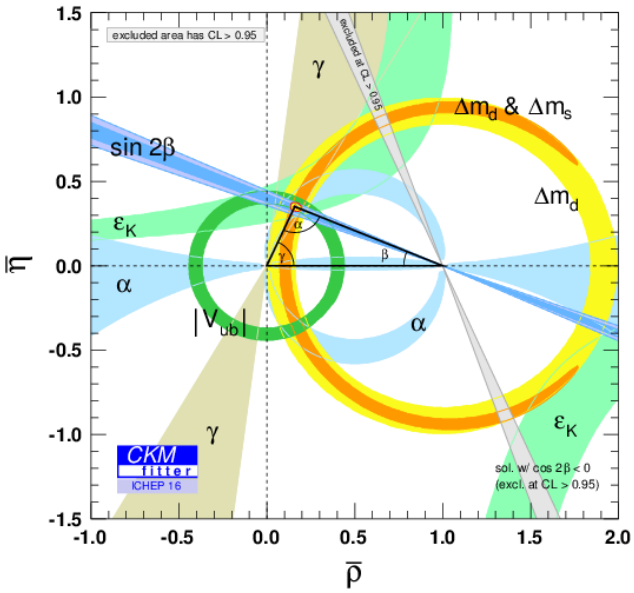

Figure 1.3: Global fit of the SM parameters in the $\rho - \eta$ plane [24].

of the CKM matrix. The most recent fit [21], reported in Figure 1.3, gives the following values:

$$V_{\text{CKM}} = \begin{pmatrix} 0.974390^{+0.000014}_{-0.000058} & 0.224834^{+0.000252}_{-0.000059} & 0.003683^{+0.000075}_{-0.000061} \\ 0.224701^{+0.000254}_{-0.000058} & 0.973539^{+0.000038}_{-0.000060} & 0.04162^{+0.00026}_{-0.00080} \\ 0.008545^{+0.000075}_{-0.000157} & 0.04090^{+0.00026}_{-0.00076} & 0.999127^{+0.000032}_{-0.000012} \end{pmatrix}. \tag{1.49}$$

The CKM matrix has a well known scale dependence above the weak scale [22, 23], below $\mu = m_{\text{W}}$ the CKM elements can be treated as constants, with all μ-dependence contained in the running of quark masses and higher-dimension operators.

1.5 Quantum chromodynamics

The quantum chromodynamics, or QCD for short, is the non-Abelian quantum gauge field theory which describes the strong interaction between quarks. The symmetry group for this theory is $SU(3)_C$, where the subscript C stands for the charge associated with this symmetry, named colour. This theory is invariant under the $SU(3)_C$ transformation:

$$\psi \to \psi' = e^{ig_s \vec{\alpha}(x)\cdot\vec{T}}\psi, \tag{1.50}$$

where $\vec{T} = T^{\alpha}$ are the eight generators of the symmetry group, which are related to the Gell-Mann matrices:

$$T^a = \frac{1}{2}\lambda^a \tag{1.51}$$

and $\vec{\alpha}(x)$ are eight functions of the space-time coordinate x. The commutation rules of λ_a are:

$$\left[\frac{\lambda_a}{2}, \frac{\lambda_b}{2}\right] = i f_{abc}\frac{\lambda_c}{2}, \tag{1.52}$$

where f_{abc} are the structure constants of the groups and the indices run from 1 to 8. Because the generators of $SU(3)_C$ are represented by 3×3 matrices, the field ψ includes three additional degrees of freedom. This new degree of freedom, colour, has three possible states labelled as red, green, and blue. The $SU(3)_C$ local phase transformation corresponds to rotating states in this colour space about an axis whose direction is different at every point in space-time. The imposition of local invariance under the $SU(3)_C$ group leads to the introduction of the covariant derivative:

$$D_\mu = \partial_\mu + i g_s \frac{\lambda_a}{2} G^a_\mu. \tag{1.53}$$

where G^a_μ are the 8 gluon fields that transform as:

$$G^a_\mu \rightarrow G'^a_\mu = G^a_\mu + i g_s f^{abc}\theta_b(x) G_{c,\mu}. \tag{1.54}$$

When this is applied to the Dirac equation for quarks, by adding the contributions of the gluons one obtains the complete Lagrangian density for the QCD:

$$\mathscr{L}_{QCD} = \bar{\psi}\gamma^\mu\partial_\mu\psi - m\bar{\psi}\psi - igs\bar{\psi}\gamma^\mu\lambda_a\psi G^a_\mu - \frac{1}{4}G^{\mu\nu}_a G^a_{\mu\nu}, \tag{1.55}$$

with $G^{\mu\nu}_a$ the tensor field defined as

$$G^{\mu\nu}_a = \partial^\mu G^\nu_a - \partial^\nu G^\mu_a - g_s f_{abc} G^{b,\mu} G^{c,\nu}. \tag{1.56}$$

Also in this case, like in the electroweak theory, self-interaction terms arise due to the non-Abelian nature of the symmetry group.

The QCD theory exhibits two relevant properties, that significantly differentiate it from the electroweak theory: colour confinement and asymptotic freedom. Both these two properties stem from experimental evidence and are successfully described in the context of the SM explanation of the strong interactions.

The former property has been formulated to cope with the experimental fact that no coloured hadron is observed in nature. Hadrons are interpreted as bound states of quarks in the QCD parton model and so they must be colour singlets. This imposes restrictions on the quark bound state configurations can exist. All

this can be summarized by saying that the quark colour degree of freedom must be confined.

The latter property can be explained with the fact that the coupling constant of the strong interaction varies with the scale of the interaction. The form of the *running* coupling constant is the following:

$$\alpha_s\left(|q^2|\right) = \frac{\alpha_s(\mu^2)}{\left[1 + \alpha_s(\mu^2)\frac{33-2N_f}{12\pi}\ln\frac{|q^2|}{\mu^2}\right]}, \tag{1.57}$$

where q^2 is the transferred 4-momentum, μ is a scale parameter for the strength of the coupling, N_f is the number of fermions capable of strong interactions at the scale considered. It can be seen that $\alpha_s(|q^2|)$ decreases as $|q^2|$ increases. For $|q| \sim 200$ MeV the value of α_s is large enough that any perturbative approach cannot be applied. In this region the calculations are carried on with the QCD-lattice approach.

For increasing values of $|q^2|$, $\alpha_s(|q^2|)$ decreases and one moves towards a regime in which perturbative approach is a good approximation.

1.6 Top quark physics

The top quark is the heaviest particle known in Nature. It is a fermion with electric charge $(2/3\,e)$ and colour charge, so it participates to all the interactions. It has a natural mass, that means that its Yukawa coupling to the vacuum expectation value is close to 1. For this reason, the top quark has a privileged relation with the Higgs boson and it could also have a role in any model that would explain the EW symmetry breaking mechanism. Due to its very short lifetime, that is of order of 2×10^{-25} seconds, the top quark in the vast majority of cases decays before it has the chance to hadronise. So its angular properties are directly accessible through its decay products. The top quark decays via weak charged current interaction, almost exclusively in a W boson and a b quark.

The top quark physics showcases many unique features that are a consequence of its large mass. The value of top quark mass significantly affects the predictions for many observables of the SM as well of BSM extensions, either directly or via radiative corrections. So it is a key input to electroweak precision fits and, together with the value of the Higgs boson mass and α_S, it has direct implications on the SM predictions for the stability of the electroweak vacuum. The value of the top quark mass has also cosmological consequences for example on Universe lifetime [25].

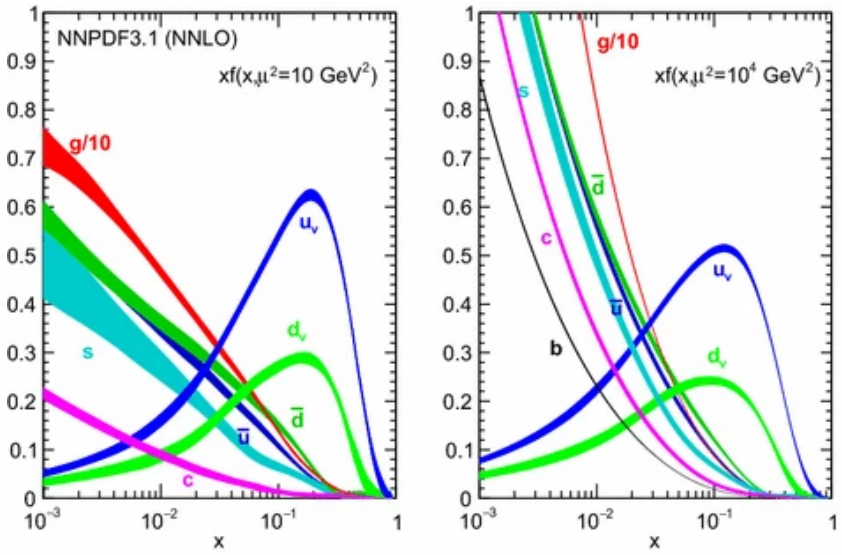

Figure 1.4: PDF sets used at the LHC experiments evaluated at $\mu^2 = 10$ GeV^2 (left) and $\mu^2 = 10^4$ GeV^2 (right) [39].

1.6.1 Top quark physics at the LHC

In general, top quarks are produced in p-p collisions through the strong interaction, predominantly via gluon fusion, creating a top quark-antiquark ($t\bar{t}$) pair. Top quarks can also be singly produced via the electroweak interaction, in which case the dominant mechanism involves an exchange of a W boson in the $t-$channel, a process which has been precisely measured at the LHC [26–35]. The total cross section can be written via a factorisation approach, as the convolution of the parton distribution functions (PDFs) of the proton and the cross section of the parton processes:

$$\sigma(pp \to X) = \sum_{i,j} \int_0^1 dx_i \int_0^1 dx_j f_i^p(x_i, \mu_f^2) f_j^p(x_j, \mu_f^2) \hat{\sigma}_{ij}(x_i, x_j, \hat{s}, \mu_f, \alpha_s(\mu_r)), \tag{1.58}$$

where i, j runs over the possible combinations of gluons or quark-antiquark or quark-quark pairs concurring at the parton process. The functions $f_i^p(x_i, \mu_f^2)$ and $f_j^p(x_j, \mu_f^2)$ are the PDFs evaluated at a fixed factorisation scale μ_f, usually posed at the scale of the process. The evolution of the PDFs between two different scales μ_F is regulated by the Dokshitzer–Gribov–Lipatov–Altarelli–Parisi (DGLAP) equations [36–38]. The PDFs are not predicted by the theory but they need to be inferred from experiments; Figure 1.4 shows the PDFs used at the LHC experiments evaluated at $\mu^2 = 10$ GeV^2 (left) and $\mu^2 = 10^4$ GeV^2 (right). The quantity $\hat{\sigma}_{ij}(x_i, x_j, \hat{s}, \mu_f, \alpha_s(\mu_r))$ of Eq. 1.58 is the cross section of the parton process and

depends on relative moments x_i and x_j carried by the partons with respect to which of the proton, the the centre-of-mass energy $\hat{s} = x_i x_j \sigma$ of the process, the scale of the process μ_f and the value of the strong coupling constant α_S evaluated at renormalisation scale r.

In proton-proton collisions the single top quark production could happen via three main channels:

- t-channel: This is the process with the largest cross section. A light-flavour quark q from one of the colliding protons interacts with a b quark by exchanging a space-like virtual W boson, producing a top quark and a recoiling light-flavour quark q′, called the spectator quark.

- tW associate production: This is the process with the second largest cross section. A gluon interacts with an initial b-quark by exchanging a virtual b-quark, producing a t-quark and a W boson.

- s-channel: This is the process with the smallest cross section. A quark-antiquark pair annihilates to produce a time-like virtual W boson, which decays to a t-quark and a b-antiquark.

Rarer production modes are also possible, e.g. the tZ or tγ associate production, recently observed by the CMS Collaboration [40, 41]. Figure 1.5 show the status of current measurements of single top quark production cross sections. The solid lines stands for the predicted cross section within the SM while the points represent the most recent or the most accurate measured values.

1.6.2 V_{tb} extraction

The single top quark production processes are particularly indicated to perform the measurement of the CKM element V_{tb}. The first historical approach to V_{tb} extraction has been to directly derive it from the cross section by neglecting $|V_{\mathrm{td}}|$ and $|V_{\mathrm{ts}}|$ since, from low-energy measurements, they are significantly smaller than $|V_{\mathrm{tb}}|$. So in the assumption that the top quark exclusively decays to a b quark and a W boson, $|V_{\mathrm{tb}}|$ can be inferred as:

$$|f_{\mathrm{LV}} \mathrm{V}_{\mathrm{tb}}| = \sqrt{\frac{\sigma_{t-\mathrm{ch.},t+\bar{t}}}{\sigma^{\mathrm{theo}}_{t-\mathrm{ch.},t+\bar{t}}}}, \tag{1.59}$$

where f_{LV} is the anomalous form factor that takes the possible presence of an anomalous tWb coupling into account. Within the SM, $f_{\mathrm{LV}} = 1$. For these approaches, the production is assumed to happen exclusively via a tWb vertex, meaning that $|V_{\mathrm{tb}}|$ is exactly equal to unity, while in the decay it is not constrained to

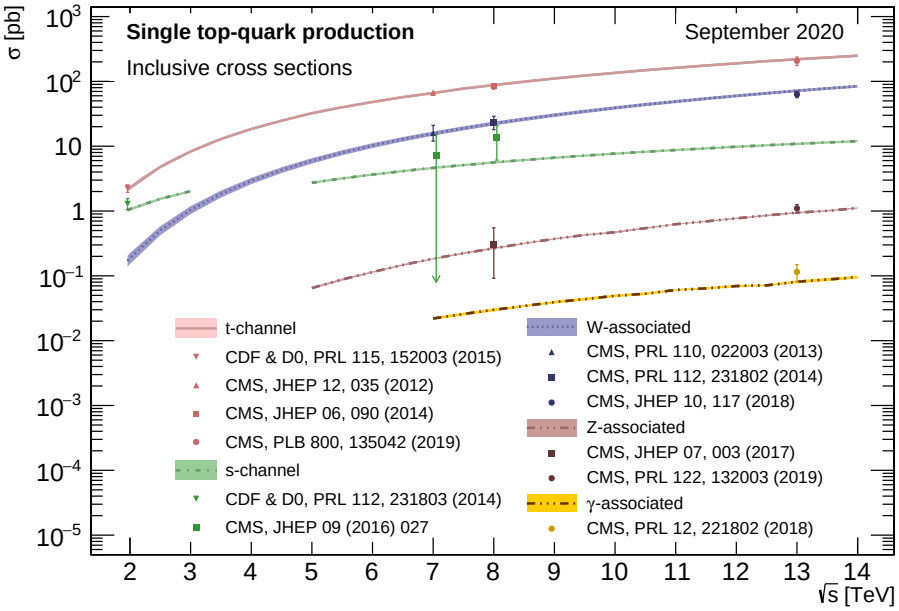

Figure 1.5: Status of current measurements of single top quark production cross sections performed by the CMS Collaboration [42].

be 1. Indeed this assumption is quite strong and could lead to a bias in the V_{tb} measurement.

The most recent measurement using this strategy performed by the CMS Collaboration [34] quotes:

$$|f_{\mathrm{LV}}\mathrm{V}_{\mathrm{tb}}| = 1.00 \pm 0.08(\mathrm{meas}) \pm 0.02(\mathrm{theo}). \tag{1.60}$$

This result is in agreement with value obtained from the combination of all the single-top-quark production cross section measurements with the full Run-I data [43]:

$$|f_{\mathrm{LV}}\mathrm{V}_{\mathrm{tb}}| = 1.02 \pm 0.04(\mathrm{meas}) \pm 0.02(\mathrm{theo}). \tag{1.61}$$

Extractions of V_{tb} are also performed in $\mathrm{t\bar{t}}$ events both by Tevatron and LHC experiments [44–47] from which the relevant lower limit of $|V_{\mathrm{tb}}| > 0.975$ at 95% confidence level is set.

1.6.3 Top quark polarisation

The top quark decay width is larger than the QCD hadronisation scale and of the spin decorrelation scale. This implies that, not only does the top quark

decay before hadronisation occurs, but also its spin information is preserved in the angular distribution of its decay products. The top quarks and antiquarks that are produced at the LHC via the strong interaction are mostly unpolarised at leading order. However, the spins of the top quarks and antiquarks are strongly correlated.

By factorising decay density matrices ρ and $\bar{\rho}$ [48], the squared matrix element can be written as:

$$|\mathcal{M}(\mathrm{q\bar{q}}/gg \to \mathrm{t\bar{t}} \to (\ell^+\nu b)(\ell^-\bar{\nu}\bar{b}))|^2 \sim Tr[\rho R \bar{\rho}] \tag{1.62}$$

The spin density matrix R can be studied by using the double differential cross section in terms of the polarisation angles of the top quark and antiquark:

$$\frac{1}{\sigma}\frac{d\sigma}{d\cos\theta_1^i d\cos\theta_2^j} = \frac{1}{4}\left(1 + B_1^i \cos\theta_1^i + B_2^j \cos\theta_2^j - C_{ij}\cos\theta_1^i \cos\theta_2^j\right) \tag{1.63}$$

The single differential cross sections can be derived in order to measure the polarisation and the spin correlation of the $\mathrm{t\bar{t}}$ system as:

$$\frac{1}{\sigma}\frac{d\sigma}{d\cos\theta_1^i} = \frac{1}{2}\left(1 + B_1^i \cos\theta_1^i\right) \quad \frac{1}{\sigma}\frac{d\sigma}{d\cos\theta_2^j} = \frac{1}{2}\left(1 + B_2^j \cos\theta_2^j\right), \tag{1.64}$$

and:

$$\frac{1}{\sigma}\frac{d\sigma}{d\cos\theta_1^i \cos\theta_2^j} = \frac{1}{2}\left(1 - C_{ij}\cos\theta_1^i \cos\theta_2^j\right)\ln\left(\frac{1}{\cos\theta_1^i \cos\theta_2^j}\right). \tag{1.65}$$

The coefficients B_1^i and B_2^i are the top quark and antiquark polarisation coefficients with respect to each reference axis i, C_{ii} are the diagonal spin correlation coefficients for each reference axis i, and C_{ij} are the cross spin correlation coefficients for each pair of axes $i \neq j$. The dilepton channel is perfect for a spin measurement because the spin analysing power of the leptons is close to one and all measurements are found to be consistent with the expectations of the SM [49].

In single top quark production processes, due to the $V - A$ structure of the weak interaction, the top quark is produced highly polarised along the spectator quark direction. A powerful observable to investigate the coupling structure in t-channel production is the differential cross section in terms of the polarisation angle defined as the angle between the direction of the lepton and of the spectator quark in the top rest frame:

$$\frac{1}{\sigma}\frac{d\sigma}{d\cos\theta_X^*} = \frac{1}{2}(1 + P_{\mathrm{t}}^{(\vec{s})}\alpha_X \cos\theta_X^*) = \left(\frac{1}{2} + A_X \cos\theta_X^*\right) \tag{1.66}$$

The analysis [35] requires a single isolated lepton, 2 or 3 quarks, up to 2 of them coming from a b quark. Figure 1.6 shows the polarisation angle distribution

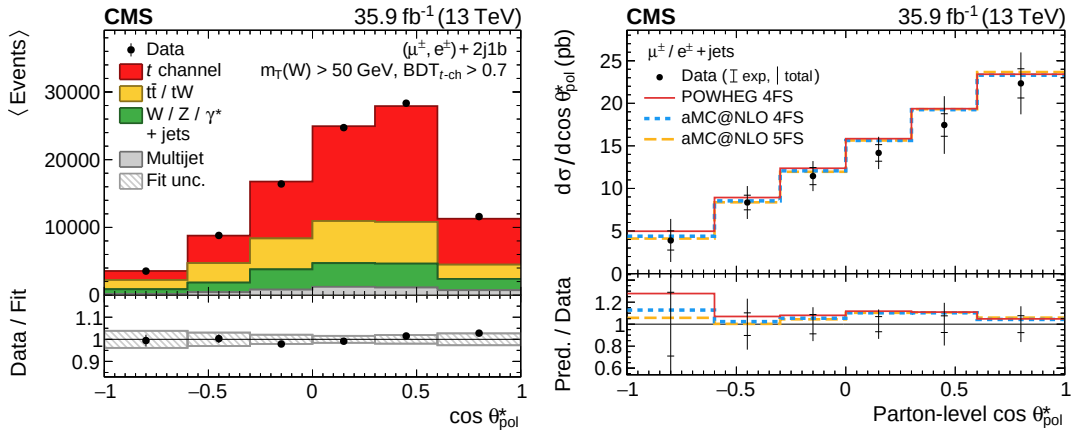

Figure 1.6: Distributions of the polarisation angle distribution at detector level, on the left, and, at parton level, after an unfolding procedure performed on the right [35].

as seen at detector level (left) and, for a direct comparison at parton level with MC prediction, after an unfolding procedure performed by a χ^2 fit is applied (right). The result obtained is:

$$A_{e/\mu} = 0.439 \pm 0.032(\text{stat}) \pm 0.053(\text{syst})$$

and it is in agreement with the SM prediction.

1.6.4 W boson helicity

The spin-angular properties of the top quark can be completely studied because it decays before the hadronisation could intervene. In particular the top quark polarisation or the helicity of W bosons from the top quark decay. Since only left-chiral particles intervene in the $V-A$ structure of the weak interaction, in the top rest frame, the W^+ boson cannot be produced with positive helicity, because its production is suppressed by a factor $m_{\mathrm{b}^2}/M_{\mathrm{W}^2}$. So the total helicity of the W^+ boson is an overlap of states with null ($\lambda = 0$) or negative ($\lambda = -1$) helicities. The ratio between the two components is given by:

$$\frac{\Gamma(\mathrm{t} \to \mathrm{b}_L \mathrm{W}_{\lambda=0})}{\Gamma(\mathrm{t} \to \mathrm{b}_L \mathrm{W}_{\lambda=-1})} \simeq \frac{m_{\mathrm{t}}^2}{2m_{\mathrm{W}}^2} \tag{1.67}$$

In the SM, at the leading order the fraction $\mathcal{F}_0$ for the W boson longitudinal polarisation, $\lambda = 0$, is given by:

$$\mathcal{F}_0 = \frac{m_{\mathrm{t}}^2/2m_{\mathrm{W}}^2}{1 + m_{\mathrm{t}}^2/2m_{\mathrm{W}}^2} \simeq 0.7. \tag{1.68}$$

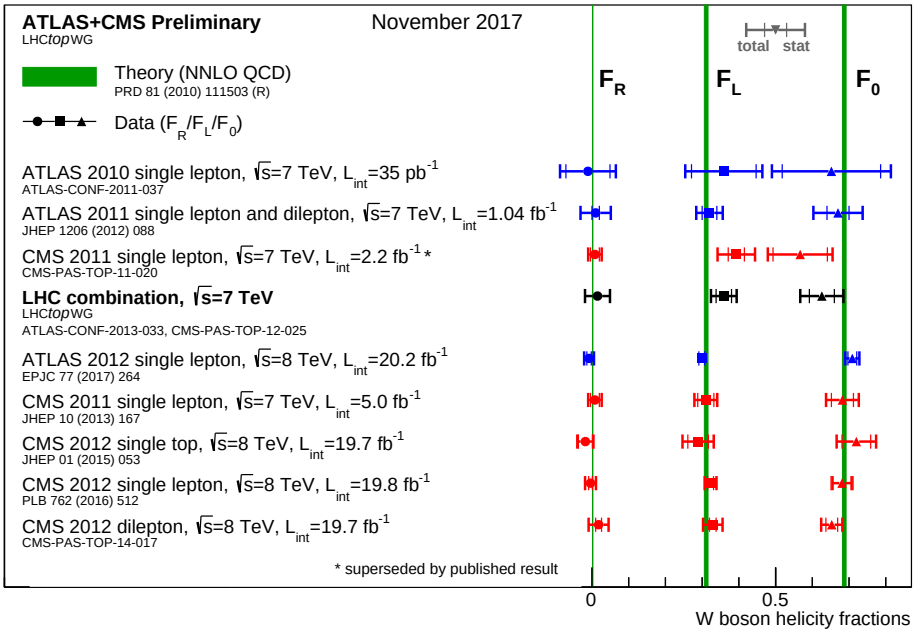

Figure 1.7: Summary of measured W helicity fractions by the ATLAS and CMS Collaborations at 7 and 8 TeV, compared to the respective theory predictions. The uncertainty on the theory predictions is shown but is very small.

The fractions $\mathcal{F}_+$ and $\mathcal{F}_-$ stand for the right-handed and left-handed polarisation respectively, and, in the SM, $\mathcal{F}_+ = 0$ and $\mathcal{F}_- = 0.3$. The measurements performed by the ATLAS and CMS Collaborations confirmed the SM predictions, as reported in Fig. 1.7.

Chapter 2

New physics beyond the Standard Model

2.1 Unsolved issues in the Standard Model

The SM succeeds in giving an exhaustive explanation of three fundamental interactions: electromagnetic, weak, and strong. The theory successfully predicts the existence and the features of the weak neutral current, the existence and masses of the W and Z bosons, the charm quark as required by the GIM mechanism, and the existence of the top quark and its measurable contributions to radiative corrections, driven by its large mass, which are a further validation of the mathematical-consistence of renormalisable field theory. Although the original formulation does not provide for massive neutrinos, they can be included by the addition of right-handed states ν_R (Dirac) or by introduction of Majorana neutrinos and the see-saw mechanism. Another great success is the prediction of the existence of the Higgs boson, which is the last major experimental validation of the SM at the electroweak scale. Despite all of these successes, the SM model fails in giving an explanation of many other phenomena. Some notable problems still unsolved are:

- Gravity: the SM does not include in any way General Relativity, and there is no obvious explanation of the large difference between the Planck and the SM interaction scales.

- Matter-antimatter asymmetry: the sole SM $\mathcal{CP}$-violation in the quark sector is not sufficient to justify the actual matter-antimatter asymmetry measured in the universe.

- Hierarchy in fermion masses: there is no explanation or prediction of fermion masses that occur in a hierarchical pattern which varies over 5 order of mag-

nitudes between the top quark and the electron, and even more mysterious are the neutrinos, which are many orders of magnitude lighter still.

- Higgs mass fine tuning: the tree-level (bare) Higgs mass receives corrections from fermion loop diagrams which are quadratically-divergent and that are not cancelled by the boson loop diagrams. With the present framework the Higgs mass should be of several orders of magnitude greater than the observed one if no new physics exists until the Plank scale $M_P = G_N^{-1/2} \sim 10^{19}$ GeV.

- Dark matter: from astrophysical observations it is found that the orbits followed by galaxies are different from which expected considering the gravitational effects of the usual matter; it could be explained with the existence of an amount of extra matter not composed of known M particles. Such matter is referred to as "dark matter", since it is does not interact via electromagnetic force.

- Dark energy: from cosmological observations, in particular from the red shift measurement, it is discovered that the Universe is accelerated. There is an unknown form of energy, called dark energy, which is hypothesised to permeate all of space, tending to accelerate the expansion of the universe. This phenomenon has no explanation in the SM framework.

- Flavour changing neutral current: the SM does not predict the observed suppression of flavour changing due to neutral currents. These processes are not present in the SM at tree level and are suppressed in loop processes by the unitarity of the CKM matrix; extensions of the SM can generate new flavor changing neutral current processes, leading to signals which, if observed, would be unambiguous evidence of new interactions.

Many models have been proposed to solve those problems or to include new phenomena in a more general picture. The great variety of the models proposed can be arranged into three main families:

– theories based on the same SM fields but that introduce new interactions, such as SuperSymmetry (SUSY), grand unification models and string theory;

– theories that introduce new fields and new interactions, amongst others Compositeness, Little Higgs, Technicolor;

– and theories that consider more than the usual three space dimensions, such as Kaluza-Klein models.

Almost all models predict new resonances with properties similar to those of the SM. In particular, the W′ and Z′ bosons are very similar to the W and Z bosons: they have spin 1 and are respectively electrically charged and neutral. They mediate charged and neutral current processes as their SM counterparts, but have usually much larger mass. Models predicting W′ and Z′ bosons with very small mass also exists but they will not discussed here. Some of the BSM models predict W′ and Z′ boson masses in the range accessible to current-day experiments like the ones at the LHC. At hadron colliders, new heavy resonances with significant couplings to quarks and leptons could be detected via Drell-Yan processes, that have a quite clean di-lepton or lepton-neutrino final state. Obviously W′ and Z′ also couple to quarks, but hadronic final states are usually more difficult to study in the environment of an hadron collider. Nevertheless, final states involving a top quark are particularly interesting due to the special properties of the top quark. Moreover the fact that top quarks have a visible decay chain can allow to further probe other features like the chirality of the interaction.

The Lagrangians describing the interactions of these new particles with the ones of the SM usually have many free parameters. New physics models often differ in the approach they follow to restrict the number of free parameters or in the assumptions they make on them. For example, the Sequential SM (SSM) fixes the coupling of W′ and Z′ bosons to have the same magnitude of SM W and Z bosons. In other phenomenological studies such as [50–53], the W′ and Z′ bosons are described by a minimal set of free parameters mimicking the behaviour of new resonances predicted in some popular models.

2.2 Theories including W′ and Z′ bosons

2.2.1 Extra dimensions

The first proposal for the existence of more than three spacial dimensions is due to T. Kaluza and O. Klein [54] in the 1920s. The idea consists of a fifth dimension beyond the four of the usual space and time, whose existence would ultimately allow to unify gravitation and electromagnetic fields. The original hypothesis presented by Kaluza [55], consists of a purely classical extension of general relativity to 5D, with a metric tensor of 15 components which are interpreted as follows: ten components are identified with the 4D space-time metric, four components with the electromagnetic vector potential, and one component with an unidentified scalar field sometimes called the radion or the dilaton. A 5D space-time field was also introduced by Einstein, who interpreted ten of its components as 4D Einstein field equations, four as the Maxwell equations for the electromagnetic field, and an equation for the scalar field. Kaluza introduced the assumption that

no component of the five-dimensional metric depends on the fifth dimension. This hypothesis, *cylinder condition*, prevents to introduce terms involving derivatives of the fields with respect to the fifth dimension. Finally, Klein gave Kaluza's classical five-dimensional theory a quantum interpretation [56, 57]. In Klein's interpretation the fifth dimension was curled up and microscopic, and it could be represented as a circle with a radius of 10^{-30} cm. Klein also made a contribution to the classical theory by providing a properly normalised 5D metric. In the 1940s the classical theory was completed, and the full field equations including the scalar field were derived. Even if their original idea failed the formalism they developed is still used nowadays.

In the 1980, the idea to enlarge the dimensions was proposed also in the context of the string theory in the attempt to include a consistent quantum gravity theory. These extra dimensions are supposed to be reduced to four at the Planck scale, and so this theory is not testable with the current level of knowledge and technology. Following a different approach, Arkani-Hamed, Dimopoulos, and Dvali (ADD) proposed a theory to explain the weakness of the gravity interaction with two or more extra dimensions in which only the gravitational interaction could propagate [58]. The size of this extra dimensions, ranging from one mm to $\sim 1/\text{TeV}$ could lead to observable consequences in present and future experiments.

Another different interpretation was given by Randall and Sundrum who postulated a five-dimensional Anti-de Sitter (AdS) space-time[1] with a compactification scale of order 1/TeV. The Randall-Sundrum theory is based on a warped geometry, whose redshift factor is able to explain the large difference between EW and Planck scales. Like in the ADD model only the gravitational interaction is allowed to propagate in the fifth dimension, even if this condition can be relaxed by letting the SM gauge fields [59, 60] and SM fermions [61, 62] propagate in whole 5D space-time.

The physics of warped extra-dimensional models can be reinterpreted thanks to the AdS/conformal field theory (CFT) correspondence. It is possible to relate these models to four-dimensional strongly-interacting theories and understand their properties by comparing them to the ones of the four-dimensional composite states [63] and this opens new possibilities to deal with unsolved question in particle physics, such as flavor problem, grand unification, and the origin of electroweak symmetry breaking or SUSY breaking.

Many models have observable implications that could be detected by the present experiments. Stringent constraints are already be set by cosmological and astronomical observations. Deviations from the SM ascribable to extra dimensions are also searched for at the colliders. Amongst others, the ATLAS and CMS Collabo-

[1] In mathematics and physics, n-dimensional anti-de Sitter space (AdS_n) is a maximally symmetric Lorentzian manifold with constant negative scalar curvature.

rations produced many results that do not find any evidence able to support these models.

2.2.2 Alternative Higgs models

The discovery of a light scalar boson compatible with the Higgs boson gave the last strong confirmation of the validity of the SM at the EW scale. Nevertheless it raises other problems, one of the most prominent of which is the naturalness problem, i.e. the mass of the Higgs boson should receive contributions of order up to the Planck scale. The way these contributions are cancelled out is not known. There are two broad classes of models addressing the naturalness problem. One is based on the SUSY theories, in which each particle has a partner that is able to exactly cancel the contribution to the Higgs boson mass. These theories hypothesise a larger group of symmetry that is able to include SM symmetry group. The lowest possible value is $SU(5)$ and it predicts the existence of many particles already accessible to the current experiments, but none of them has been found so far. Another possibility, more compatible with recent results, is that the strong interaction produces four light resonances identified with the Higgs doublet and the EWSB proceeds through vacuum misalignment. In that case, the Higgs boson itself has a finite size, i.e. not an elementary particle, and thus never feels the UV degrees of freedom that would otherwise have dragged its mass to much higher scales.

Composite Higgs model

The idea that the Higgs boson itself could be a composite bound state emerging from a new strongly-coupled sector has been reconsidered thanks to the insights gained from the AdS/CFT duality. To be consistent with the current EW data a mass gap separation between the Higgs resonance and the other resonances of the strong sector is necessary. The mass gap can be derived from the dynamics if the strong sector exhibits a global symmetry, G, broken by a subgroup, H, at the scale f, such that three Nambu-Goldstone bosons can be identified with the massive W and Z bosons and a forth one with the Higgs boson. The simplest coset G/H are $SU(3)/SU(2)$ or $SO(5)/SO(4)$. It is also possible to have non-minimal cosets with extra Goldstone bosons leading to additional Higgs bosons in the spectrum. Some composite Higgs models have also been developed in the framework of 5D warped geometry according to the AdS/CFT correspondence. Another possible way to introduce composite Higgs models is through the concept of partial compositeness [64], i.e. the idea that there are only linear mass mixing between elementary fields and composite states. In these models the SM particles have both elementary and composite components and they interact with the strong

sector and the Higgs boson only through their composite component. Such models have important consequences on the flavour properties, chiefly the suppression of large flavour changing neutral currents involving light fermions. It also plays an important role in dynamically generating a potential for the would-be Goldstone bosons. Partial compositeness also links the properties of the Higgs boson to the spectrum of the fermionic resonances, i.e. the partners of the top quark.

Little Higgs model

The Little Higgs boson models [65, 66] are based on the idea that the Higgs doublet is a (pseudo) Nambu-Goldstone boson arising from a global symmetry breaking at the TeV scale. The gauge group of these theories is a direct product of several copies of the same factor, for example $SU(2) \times SU(2)$, and each of the groups can be considered as living along an additional dimension of the space. The terms contributing to the Higgs boson mass cancel out until there is a two-loop contribution involving both groups, given the symmetry of the problem. This is enough to be consistent with the level of precision of the current measurements.

2.2.3 Left-Right symmetry

One of the most peculiar features of the SM is the complete asymmetry between left and right helicity exhibited by the weak interaction due to its V-A structure. Many physicists, starting from Lee and Yang [67], discussed about the possibility of the restoration of the left-right symmetry at an higher scale of energy. There is anyways another way to face this problem: introduce a Left-Right (LR) symmetric theory, in which the weak interaction stays left chiral and a new groups of charged and neutral bosons are introduced, mirroring the weak gauge bosons of the SM. The symmetry gauge group for the minimal models is $SU(2)_L \times SU(2)_R \times U(1)_{B-L}$[2], where $SU(2)_L$ and $SU(2)_R$ are the symmetry groups for the weak interaction and its mirror, respectively, and $U(1)_{B-L}$ for the electromagnetic interaction. This group is then spontaneously broken similarly to the SM. The symmetry between the two $SU(2)$ groups is then completed with a generalised parity $\mathcal{P}$ or a generalised charge conjugation $\mathcal{C}$. The role played by the discrete symmetries is to relate the couplings of the theory, especially the Yukawa ones. In the first case, the Yukawa matrices are Hermitian and, in the second one, they are instead symmetric, and these differences imply relevant restrictions on the pattern of the left and right quark and lepton mixing matrices [68]. The spontaneous breaking of $\mathcal{P}$ (and also $\mathcal{CP}$) requires also R-handed neutrino degrees of freedom. These additional neutrino multiplets give rise to Majorana masses and allow for scenarios such

[2] B and L stand for the baryon and lepton numbers, respectively.

that the neutrino masses are naturally light, i.e. $m_{\nu_\ell} \ll m_\ell(\ell = e, \mu, \tau)$ [69]. Another viable LR model is based on the gauge group $SU(2)_L \times SU(2)_R \times SU(4')$, where $SU(4')$ unifies the lepton and the quark sectors. In this case the unification of the left and right couplings is achieved by demanding the entire Lagrangian, except the Higgs boson mass term, to be invariant under a discrete symmetry, transforming $SU(2)_L$ into $SU(2)_R$. The non invariance of the Higgs boson mass term allows the right-handed gauge bosons to be heavier than the left-handed ones being compatible with the current observations. Other mechanism of spontaneous parity breaking can be introduced that do not require the Higgs mass terms to be non invariant from the beginning. All distinctions between left- and right-handed sectors, then, could arise purely as a result of spontaneous breakdown of the local symmetry.

2.2.4 Sequential Standard Model

The Sequential SM (SSM) is maybe one of the easiest ways to introduce a new boson, W_{SSM}. All its couplings to SM particles are fixed to the ones of the SM W boson. In other words the coupling constant g_{SSM} is equal to $g = e/\sin\theta_W$. Given its simplicity, this model is usually assumed as a good benchmark, because its results can be easily reinterpreted in different scenarios and it is also very useful to compare sensitivity of different experiments.

2.2.5 The 331 model

Even if the SM received several experimental confirmations, there are some tensions between data and predictions from the precision flavour physics. Extensions of the SM have been proposed to make these tensions compatible. One of the simplest model is the one based on the gauge group $SU(3)_C \times SU(3)_L \times U(1)_X$, briefly referred to as 331 model. The model, originally proposed in 1992 [70, 71], introduces new sources of flavour and $\mathcal{CP}$ violation through the interaction of the ordinary fermions with new vector bosons. The SM gauge groups $SU(2)_L \times U(1)_X$, and consequently, $U(1)_Q$, are obtained with a spontaneous symmetry breaking mechanism. This model foresees the presence of two Higgs sectors, one of them at a scale much larger than the EW one. One very interesting feature of the 331 model is that the number of fermion generations is equal to the number of colours. This constraint naturally follows from the requirement of anomaly cancellation, and, differently from the SM, it offers a formal justification for the existence of 3 fermion generations. Enlarging the gauge symmetry group from $SU(2)_L$ to $SU(3)_L$ implies the existence of five additional bosons, one neutral (Z') and four potentially charged ($\mathrm{V}^{\pm Q_V}$ and $\mathrm{Y}^{\pm Q_Y}$) depending on specific assumptions of the model.

These new bosons couple to SM leptons, but not with the SM quarks, which can only be coupled to them by means of SM gauge bosons [72].

2.2.6 Top flavour model

Another possibility to extend the SM is to consider a larger gauge group, like for example $SU(2)_1 \times SU(2)_2 \times U(1)_Y$ [73]. Here, differently from the LR model already discussed, the first and second generations of fermions couple to $SU(2)_1$ and the third generation couples to $SU(2)_2$. In this model the weak interaction mediated by new bosons has a privileged coupling with the third families of fermions. The extra $SU(2)$ group could also be used to break the weak interaction dynamically via the Nambu-Jona-Lasinio mechanism [74, 75]. Predicted values of the mass of the new boson range from 800 GeV to the TeV scale [76].

2.3 Interaction Lagrangian

The lowest dimension effective Lagrangian of interactions of W′ boson to fermions in most general form can be written as:

$$\begin{aligned}\mathscr{L} =& \frac{V'_{q_i q_j}}{2\sqrt{2}} g' \bar{q}_i \gamma_\mu \left[a^R_{q_i q_j} \left(1+\gamma^5 \right) + a^L_{q_i q_j} \left(1-\gamma^5 \right) \right] \mathrm{W}' q_j + \\ & \frac{g'}{2\sqrt{2}} \bar{\nu}_\ell \gamma_\mu \left[a^R_{\bar{\nu}_\ell \ell} \left(1+\gamma^5 \right) + a^L_{\bar{\nu}_\ell \ell} \left(1-\gamma^5 \right) \right] \mathrm{W}' \ell + h.c.,\end{aligned} \tag{2.1}$$

where $a^R_{q_i q_j}$ and $a^L_{q_i q_j}$ are the left and right couplings of W′ to quarks, $a^R_{\bar{\nu}_\ell \ell}$ and $a^L_{\bar{\nu}_\ell \ell}$ are the left and right couplings of W′ to leptons, g' is the coupling constant of the interaction and $V'_{q_i q_j}$ is the element of a quark mixing matrix, defined in an analogous way as the SM CKM matrix. All these parameters are free and different models have different assumptions and corresponding implications. If the model includes also a Z′ boson, the W′-to-Z′ ratio will be an ulterior free parameter. The existence of such bosons implies the presence of a tree-level mass mixing between the gauge bosons. The diagonalisation of such matrix leads to a W-Z mass ratio and couplings of the observed W boson different from the SM values; this implies that the W-W^0 mixing angle, θ_+, must be smaller than about 10^{-2} and, similarly, a Z-Z^0 mixing must be. The W′ coupling to WZ is fixed by Lorentz and gauge invariances, and to leading order in θ_+ is given by:

$$\frac{g\theta_+ i}{\cos\theta_W} \left[W'^+_\mu (W^-_\nu Z^{\nu\mu} - Z_\nu W^{-\mu\nu}) + Z^\nu W^{-\mu} W'^+_{\nu\mu} \right] + h.c., \tag{2.2}$$

where $W^{\mu\nu} = \partial^\mu W^\nu - \partial^\nu W^\mu$ and so on.

The W′ coupling to the SM Higgs boson, h^0 is:

$$-\xi_h g' M_W W'^{+}_{\mu} W^{-\mu} h^0 + h.c., \tag{2.3}$$

where q' is the gauge coupling of the W′ boson, and the coefficient ξ_h satisfies $\xi_h \leq 1$ in simple Higgs sectors.

In this work, more precisely in Chapter 6, the assumption considered is the one of the SSM, i.e. g' is identified with the SM weak interaction coupling $g_w = e/\sin\theta_W$, and the interaction of the W′ boson with quarks has been investigated, with the quark mixing matrix $V'_{q_i q_j}$ identified with the SM CKM matrix. By referring to Eq. 2.1, the following cases are considered: $a^R_{q_i q_j} = 1$ and $a^L_{q_i q_j} = 0$ for the pure right handed (RH) scenario, $a^R_{q_i q_j} = 0$ and $a^L_{q_i q_j} = 1$ for the pure left handed (LH) scenario, and $a^R_{q_i q_j} = 1/\sqrt{2}$ and $a^L_{q_i q_j} = 1/\sqrt{2}$ for the mixed couplings scenario. The pure RH and LH cases are usually the ones considered to set limits on the mass hypotheses in direct searches. The main difference between RH and LH cases is that in the latter case the interference with the SM has to be considered. The processes that could contribute to the W′ boson production in the $s-$channel are the SM single top quark production modes. For large values of the W′ boson mass, the only process that has a significant contribution is the SM single top quark $s-$channel, while the $t-$channel and the tW associate production can be neglected [77]. For the leading $s-$channel subprocess $\mathrm{u\bar{d}} \to \mathrm{t\bar{b}}$, the cross section can be written as:

$$\begin{aligned}\hat{\sigma}(\hat{s}) =& \frac{\pi\alpha^2_{\mathrm{W}}}{6} V^2_{\mathrm{tb}} V^2_{\mathrm{ud}} \frac{(\hat{s}-M_t^2)^2(2\hat{s}+M_t^2)}{\hat{s}^2} \left[\frac{1}{(\hat{s}-m^2_{W})^2 + \gamma^2_{\mathrm{W}} m^2_{\mathrm{W}}} + \right. \\ &+ 2a^L_{\mathrm{ud}} a^L_{\mathrm{tb}} \frac{(\hat{s}-m^2_{\mathrm{W}})(\hat{s}-M^2_{\mathrm{W}'}) + \gamma^2_{W}\Gamma^2_{\mathrm{W}'}}{((\hat{s}-m^2_{\mathrm{W}})^2 + \gamma^2_{\mathrm{W}} m^2_{W})((\hat{s}-M^2_{\mathrm{W}'})^2 + \Gamma^2_{\mathrm{W}'} M^2_{\mathrm{W}'})} + \\ &+ \left. \frac{(a^L_{\mathrm{ud}} a^L_{\mathrm{tb}})^2 + (a^R_{\mathrm{ud}} a^R_{\mathrm{tb}})^2 + (a^L_{\mathrm{ud}} a^R_{\mathrm{tb}})^2 + (a^R_{\mathrm{ud}} a^L_{\mathrm{tb}})^2}{(\hat{s}-M^2_{\mathrm{W}'})^2 + \Gamma^2_{\mathrm{W}'} M^2_{\mathrm{W}'}} \right],\end{aligned} \tag{2.4}$$

where $\hat{s} = x_{\mathrm{u}} x_{\bar{\mathrm{d}}} s$, with s being the scale of the process. The first term of Eq. 2.4 is the pure SM single top quark production in the $s-$channel, the second one is the interference term and the last one is the pure BSM production.

An important part of this thesis work consisted in the study of the W′ model in the MadGraph5_MC@NLO framework [78]. The model used is an extension of the SM, including additional interaction of fermions to a W′ boson following the lowest-order effective Lagrangian, as in Eq. 2.1. This model accounts for the fully differential production and decay of a W′ boson, with arbitrary vector and axial-vector couplings, to any final state at next-to-leading order in QCD. It allows a complete factorisation of couplings at next-to-leading order in both the partial

width of the W′ boson, and in the full two-to-two cross section. The model is fully detailed in Refs. [79, 80]. The process investigated is pp→W′ →tb, where the top quark is decayed in MadSpin [81] according to the decay chain t→Wb. Different scenarios are taken into account:

- pure LH without SM interference;
- pure RH;
- LH plus SM interference;
- LH-RH mixed couplings plus SM interference.

Since the ratio $\Gamma_{W'}/M_{W'}$ is a free parameter of the model, different values are investigated. The narrow width case has been chosen to have $\Gamma_{W'}/M_{W'} = 1\%$ and the masses range from 2 TeV up to 6 TeV by steps of 200 GeV. The lower bound is chosen accordingly to the currently available limits [82]. Table 2.1 reports the values of the cross sections times the branching fractions calculated with the MadGraph5_MC@NLO generator for the process pp→ W′ →tb→Wbb for the narrow width case.

For the wide width case three different hypotheses are made: 10%, 20% and 30%. Also in this cases the masses range from 2 to 6 TeV but by a step of 400 GeV. Table 2.2 reports the values of the cross sections times the branching fractions calculated with the MadGraph5_MC@NLO generator for the process pp→ W′ →tb→Wbb for the wide width cases.

2.4 W′ boson searches

Given the large number of models predicting new bosons, many searches of such particles, both direct and indirect, have been conducted in a wide variety of final states, both at electron-positron and hadron colliders.

The first searches for W′ production were performed at LEP-II, where the W′ boson could have been produced in pairs in processes mediated by photons or Z bosons. Through precise cross section measurements it was possible to rule out values of W′ mass up to 105 GeV for most of the decay modes.

At hadron colliders, a W′ boson can be produced as a resonance from a quark-antiquark pair or from EW bosons processes. For values of the total decay width much smaller than its mass ($M_{W'}/\Gamma_{W'} \sim 7\%$), the $s-$channel process $p\bar{p} \to f\bar{f}X$, where X is any final state, can be written as the branching fraction $\mathcal{B}(W' \to f\bar{f})$ times the production cross section:

$$\sigma(p\bar{p} \to W'X) = \frac{\pi}{6s} \sum_{i,j} \left[(C^L_{q_{ij}})^2 + (C^R_{q_{ij}})^2 \right] \omega_{ij} \left(\frac{M^2_{W'}}{s}, M_{W'} \right). \qquad (2.5)$$

Mass [GeV]	Width [GeV]	Cross Section × BR (pb)			
		LH no SM	RH	LH with SM	LH+RH
2000	20	1,342	1,397	1,375	1,462
2200	22	0,8111	0,8439	0,9087	0,9701
2400	24	0,5005	0,5203	0,6308	0,6756
2600	26	0,3115	0,3236	0,465	0,5016
2800	28	0,1974	0,2049	0,365	0,3945
3000	30	0,1271	0,1318	0,3031	0,3277
3200	32	0,08254	0,08553	0,266	0,2863
3400	34	0,0544	0,05633	0,2434	0,2612
3600	36	0,03624	0,0375	0,2298	0,2454
3800	38	0,02449	0,02533	0,2214	0,2355
4000	40	0,01679	0,01736	0,2168	0,2293
4200	42	0,01161	0,01208	0,2141	0,2255
4400	44	0,008501	0,00879	0,2131	0,223
4600	46	0,006172	0,006384	0,2125	0,2217
4800	48	0,004538	0,004696	0,2125	0,221
5000	50	0,003381	0,003501	0,2128	0,2204
5200	52	0,00254	0,002633	0,2131	0,2202
5400	54	0,001929	0,002008	0,2139	0,2201
5600	56	0,001476	0,001533	0,2142	0,22
5800	58	0,001138	0,001182	0,2148	0,2201
6000	60	0,0008807	0,0009153	0,2154	0,2203

Table 2.1: Cross section obtained with the MadGraph5_MC@NLO generator for narrow widths (1%) W′ boson for different mass hypotheses.

The functions ω_{ij} include the information about proton structure, and are given to leading order in α_S by:

$$\omega_{ij}(z,\mu) = \int_1^z \frac{dx}{x}\left[u_i(x,\mu)\bar{d}_j\left(\frac{z}{x},\mu\right) + \bar{u}_i(x,\mu)d_j\left(\frac{z}{x},\mu\right)\right], \tag{2.6}$$

where $u_i(x,\mu)$ and $d_j(\frac{z}{x},\mu)$ are the parton distribution functions inside the proton at the factorisation scale μ and parton momentum fraction x and z/x for the up- and down-type quarks of the i-th generation, respectively. QCD corrections to W′ production are sizeable (they also include quark-gluon initial states), but preserve the above factorisation of couplings at next-to-leading order [79].

The easiest searches to perform in an hadron environment are the ones that require an high-p_{T} lepton and a large amount of missing transverse momentum, ascribable to the escaping neutrino, standing for the decay chain $\mathrm{W}' \to \ell\nu$. The invariant mass of the lepton-neutrino system is reconstructed in the transverse plane, obtaining a Jacobian peak, which ends at $M_{\mathrm{W}'}$ as reported in Fig. 2.1.

Since the branching fractions in $\mu\nu$ and $e\nu$ are not guaranteed to be equal, the results are given separately for these two decay modes. The current results

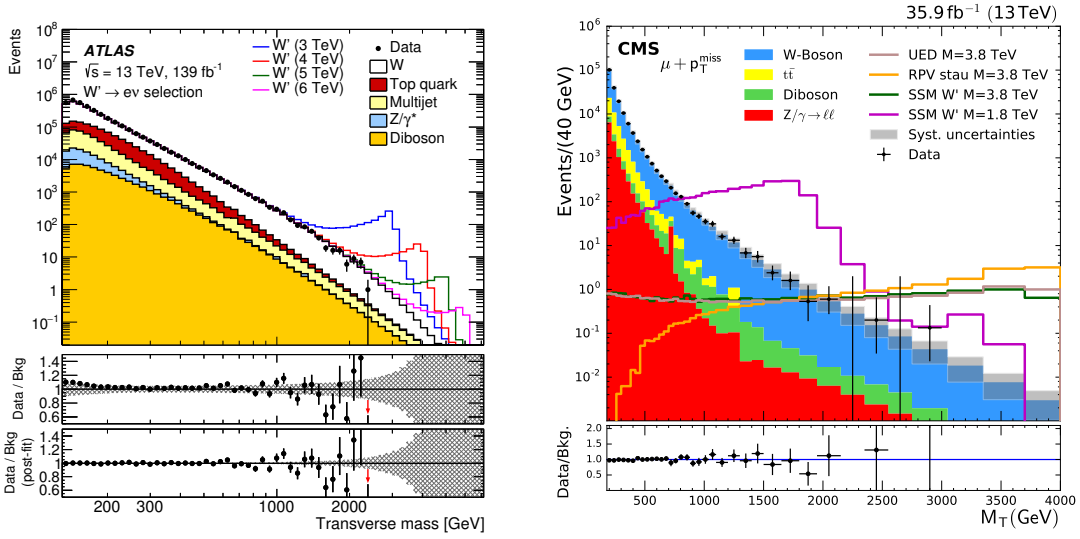

Figure 2.1: Distributions of the transverse mass for data and predicted background events in the electron (left) and muon (right) channels. Expected signal distributions for several SSM W′ boson masses are shown stacked on top of the total expected background for the ATLAS Collaboration [83]. Signal examples for W′ masses of 1.8 and 3.8 TeV, for RPV SUSY and split-UED are shown for the CMS Collaboration [84].

Mass [GeV]	Width [GeV]	Cross Section × BR (pb)			
		LH no SM	RH	LH with SM	LH+RH
2000	200	0,148	0,154	0,2508	0,3059
	400	0,07863	0,08177	0,1953	0,2436
	600	0,05403	0,05617	0,1825	0,2254
2400	240	0,05875	0,06106		
	480	0,03287	0,03416		
	720	0,02314	0,02404		
2800	280	0,02556	0,02655	0,1969	0,2222
	560	0,01496	0,01554	0,1897	0,2132
	840	0,01115	0,01158	0,1898	0,2115
3200	320	0,01197	0,01242		
	640	0,007494	0,007778		
	960	0,005784	0,006004		
3600	360	0,005971	0,006191	0,2004	0,215
	720	0,004044	0,004195	0,1998	0,2139
	1080	0,003249	0,003372	0,2009	0,214
4000	400	0,003271	0,00339		
	800	0,002355	0,002443		
	1200	0,00195	0,002024		
4400	440	0,001899	0,001967	0,2069	0,2165
	880	0,001437	0,001491	0,2072	0,2165
	1320	0,001232	0,001278	0,2081	0,2168
4800	480	0,001173	0,001217		
	960	0,00094	0,0009753		
	1440	0,0008208	0,0008519		
5200	520	0,0007642	0,0007929	0,2116	0,2185
	1040	0,0006335	0,0006573	0,212	0,2185
	1560	0,0005667	0,0005882	0,2129	0,2187
5600	560	0,000518	0,0005376		
	1120	0,000449	0,000466		
	1680	0,0004055	0,0004209		
6000	600	0,0003715	0,0003858	0,2148	0,2198
	1200	0,0003255	0,000338	0,2153	0,2198
	1800	0,0002973	0,0003086	0,2155	0,2198

Table 2.2: Cross section obtained with the MadGraph5_MC@NLO generator for wide widths (10%, 20%, and 30%) W′ boson for different mass hypotheses.

assume a negligible interference between the LH W′ and EW W boson, while for the RH coupling a RH neutrino is assumed to be much lighter than the W′ boson. Usually the SSM is used as a benchmark model and the lepton universality is

also assumed to be preserved. Both ATLAS and CMS collaborations set limits on the W′ production cross section times branching fraction in $\mu\nu$, $e\nu$, and in the combined $\ell\nu$ final states [83, 84]. The ATLAS Collaboration performed a search for a heavy charged-boson resonance decaying into a charged lepton (electron or muon) and a neutrino with data sample of 139 fb^{-1} [83] of proton-proton collisions at $\sqrt{s} = 13$ TeV. The observed transverse mass distribution computed from the lepton and missing transverse momenta is consistent with the distribution expected from the SM, and upper limits on the cross section for $pp \to \mathrm{W}' \to \ell\nu$ are extracted ($\ell = e$ or μ). These vary between 1.3 pb and 0.05 fb depending on the resonance mass in the range between 0.15 and 7.0 TeV at 95% confidence level for the electron and muon channels combined. Gauge bosons with a mass below 6.0 TeV and 5.1 TeV are excluded in the electron and muon channels, respectively, in a model with a resonance that has couplings to fermions identical to those of the SM W boson. Figure 2.2 reports the exclusion plot for the electron, muon and combined channels and the cross-section limits for resonances with several fixed Γ/m values in the range between 1% and 15%. Similarly, the CMS Collaboration performed a search for new high-mass resonances in proton-proton collisions having final states with an electron or muon and missing transverse momentum. The analysis uses proton-proton collision data collected in 2016 with the CMS detector at the LHC at a centre-of-mass energy of 13 TeV, corresponding to an integrated luminosity of 35.9 fb^{-1}. The transverse mass distribution of the charged lepton-neutrino system is used as the discriminating variable. No significant deviation from the SM prediction is found. The best limit, from the combination of electron and muon channels, is 5.2 TeV at 95% confidence level for the mass of a W′ boson with the same couplings as those of the standard model W boson. Exclusion limits of 2.9 TeV are set on the inverse radius of the extra dimension in the framework of split universal extra dimensions. In addition, model-independent limits are set on the production cross section and coupling strength of W′ bosons decaying into this final state. An interpretation is also made in the context of an R parity violating supersymmetric model with a slepton as a mediator and flavor violating decay [84].

The $\tau\nu$ channel is treated separately due to the different decay channels of the τ leptons that could have both leptonic and hadronic final states and also because some models predict privileged coupling of the W′ boson with the third families of quarks and leptons. The ATLAS Collaboration searched for excesses above the SM expectation in the $\mathrm{W}' \to \tau\nu$ channel in p-p collision data corresponding to 36.1 fb^{-1} at a centre-of-mass energy of $\sqrt{s} = 13$ TeV. Only τ-lepton decays with hadrons in the final state are considered. Heavy W′ bosons with masses less than 3.7 TeV in the SSM and masses less than 2.2–3.8 TeV depending on the coupling in the non-universal $G(221)$ model are excluded at the 95% confidence level [85]. Similarly the CMS Collaboration excluded $0.4 < m_{\mathrm{W}'} < 4.0$ TeV at 95% CL in

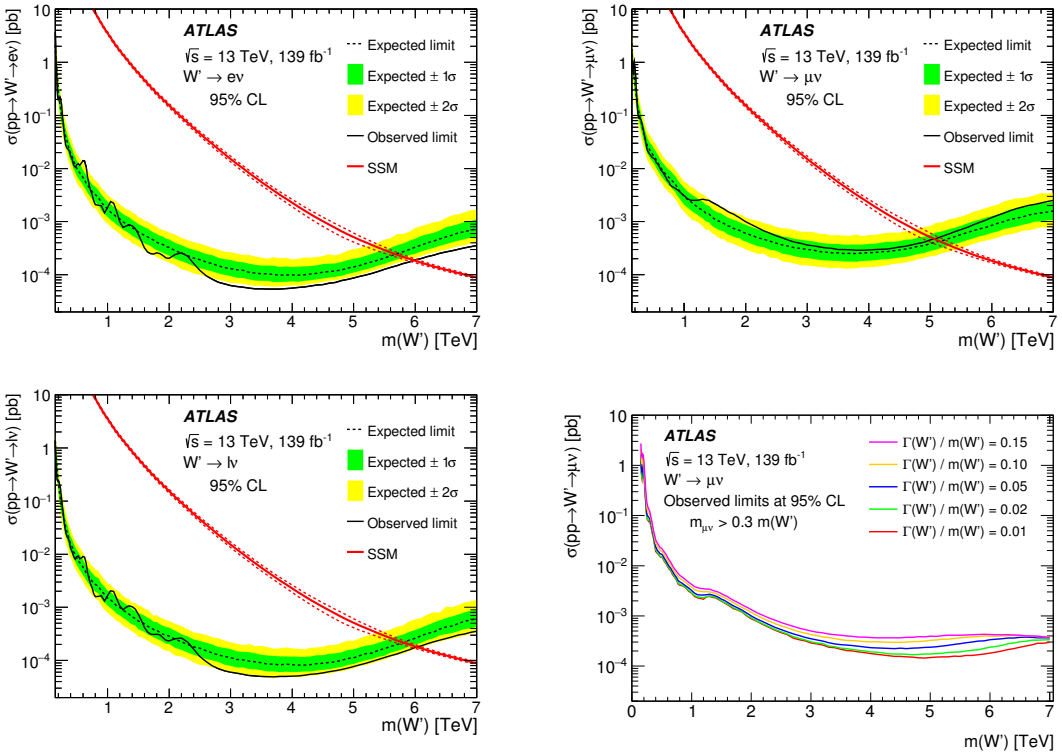

Figure 2.2: Observed and expected upper limits at the 95% CL on the $pp \to \mathrm{W}' \to \ell\nu$ cross section in the electron (top), muon (middle), and combined (bottom) channels as a function of W′ mass in the Sequential Standard Model and cross-section limits for resonances with several fixed Γ/m values in the range between 1% and 15% for the combined channel.

the hypothesis of the SSM [86].

Even if more challenging at hadron colliders, both ATLAS and CMS Collaboration performed searches of the W′ boson in the hadronic final states [87–89]. The CMS Collaboration performed a search for narrow and broad resonances with masses greater than 1.8 TeV decaying to a pair of jets. The search uses proton-proton collision data at $\sqrt{s} = 13$ TeV collected at the LHC, corresponding to an integrated luminosity of 137 fb^{-1}. The background contribution, arising from SM processes, to the dijet invariant mass spectrum is extracted from data, and no significant evidence for the production of new particles is observed. Model independent upper limits are reported on the production cross sections of narrow resonances, and broad resonances with widths up to 55% of the resonance mass. Limits are presented on the masses of narrow resonances from various models: string resonances, scalar diquarks, axigluons, colorons, excited quarks, color-octet scalars, W′ and Z′ bosons, Randall-Sundrum gravitons, and dark matter mediators. The analysis rules out W′ masses up to 3.6 TeV at 95% confidence level [89]. A search in dijet final state is also performed by the ATLAS Collaboration using p-p collisions corresponding to 37 fb^{-1} at $\sqrt{s} = 13$ TeV. In this case, masses of the W′ boson are excluded up to 3.6 TeV at 95% confidence level [88].

More complex final states are also investigated for models in which the W′ boson is supposed to decay in a Z′ and a W bosons. In this case, the ATLAS Collaboration searched for dijet resonances in events with at least one isolated charged lepton in 139 fb^{-1} of $\sqrt{s} = 13$ TeV proton–proton collision data. The dijet invariant-mass (m_{jj}) distribution constructed from events with at least one isolated electron or muon is searched in the region $0.22 < m_{jj} < 6.3$ TeV for excesses above a smoothly falling background from SM processes. The W′ → Z′W model is excluded for Z′ masses up to 2 TeV, assuming the maximal cross-section, which occurs when the mass difference between the W′ and Z′ is 250 GeV, resulting in an indirect limit on the W′ too [87].

The large amount of data collected at the LHC also allowed to test rarer decay channel, e.g. W′ →Wh, by both ATLAS [90, 91] and CMS Collaborations [92, 93]. Cross-section limits are set for W′ masses in the range between 0.5 and 5.0 TeV. The ATLAS and CMS 13 TeV analyses both set the most stringent lower limit on the mass: $M_{\mathrm{W}'} > 2.7$ TeV for the Heavy Vector Triple weakly-coupled scenario A [94].

2.4.1 W′ →tb searches

A special mention is instead to the W′ →tb decay mode. The channel is particularly important because a W′ boson that couples only to right-handed fermions cannot decay to leptons when the right-handed neutrinos are heavier than $m_{\mathrm{W}'}$. Additional motivations are provided by a W′ boson with enhanced couplings to the

third generation, e.g. Top Flavour described in Sec. 2.2.6, and by a leptophobic W′ boson. On the experimental side, such channels have a more striking signature, if compared to other hadronic decays due to the presence of two b quarks in the final state, one coming from the W′ decay and the other from the top quark decay, together with the additional decay products of the W boson. The ATLAS Collaboration performed a search with proton–proton collisions at a centre-of-mass energy of $\sqrt{s} = 13$ TeV and correspond to an integrated luminosity of 36.1 fb^{-1} [95]. This analysis focuses on final states with an electron or muon plus jets. The search covers resonance masses between 0.5 and 5.0 TeV and considers right-handed W′ bosons. For right-handed W′ bosons with coupling to the SM particles equal to the SM weak coupling constant, masses below 3.15 TeV are excluded at the 95% confidence level. This search performs also the combination with the fully hadronic final state [96] excluding RH W′ bosons masses below 3.25 TeV at the 95% confidence level, as reported in Fig. 2.3. The CMS Collaboration also presented a search in this channel with proton–proton collisions at a centre-of-mass energy of $\sqrt{s} = 13$ TeV and corresponding to an integrated luminosity of 35.9 fb^{-1}. Both RH and LH W′ hypotheses are tested. For the LH case the interference with the SM single top quark $s-$channel is taken into account. Both cases for $M_{\nu_R} \ll M_{\mathrm{W}'}$ and $M_{\nu_R} > M_{\mathrm{W}'}$ are considered for the expected cross sections and the exclusion plot obtained is reported in Fig. 2.3. The CMS Collaboration used the cross

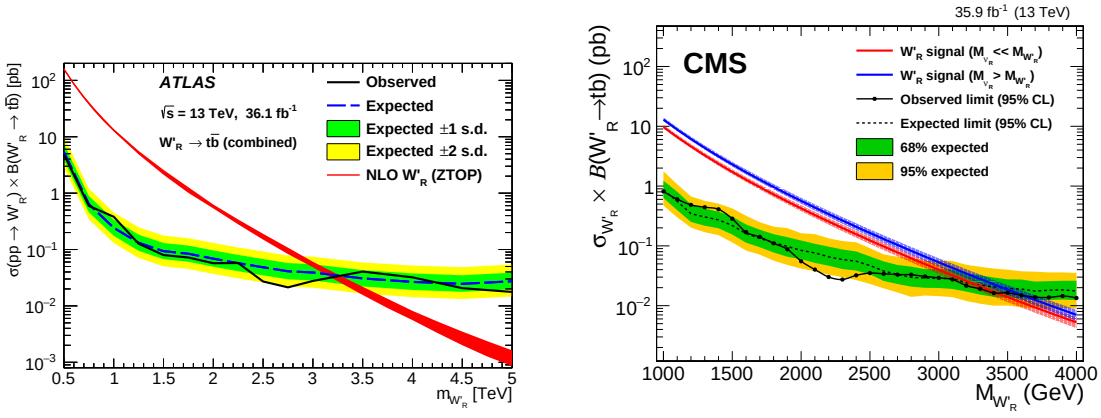

Figure 2.3: Upper limit at 95% CL on the RH W′ boson production cross section for the combined electron and muon channels. Signal masses for which the theoretical cross section (in red and blue for $M_{\nu_R} \ll M_{\mathrm{W}'}$ and $M_{\nu_R} > M_{\mathrm{W}'}$, respectively) exceeds the observed upper limit (in solid black) are excluded at 95% CL. The green and yellow bands represent the ±1 and 2 standard deviations uncertainties in the expected limit, respectively. [82].

section measurement to also extract limits on the values of left-handed (a_L) and

right-handed (a_R) couplings according to the formula:

$$\sigma = (1 - a_L^2)\sigma_{SM} + \frac{1}{a_L^2 + a_R^2}\big[a_L^2(a_L^2 - a_R^2)\sigma_L + a_R^2(a_R^2 - a_L^2)\sigma_R + \\ + 4a_L^2 a_R^2 \sigma_{LR} - 2a_L^2 a_R^2 \sigma_{BSM}\big]. \tag{2.7}$$

The results obtained are shown in Fig. 2.4 as function of the left-handed (a_L) and right-handed (a_R) couplings for different W′ mass hypotheses. The measurement

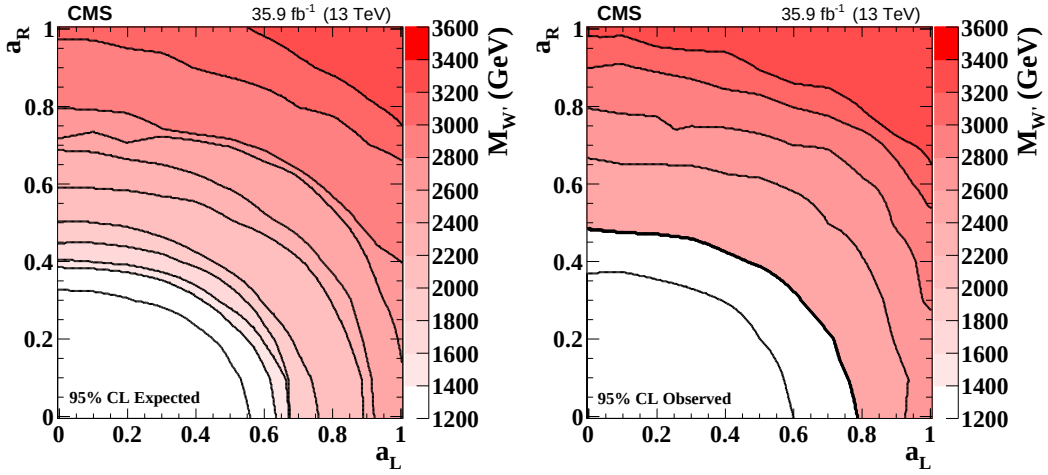

Figure 2.4: Expected (left) and observed (right) limits on the W′ boson mass as function of the left-handed (a_L) and right-handed (a_R) couplings. Black lines represent contours of equal W′ boson mass [82].

with proton-proton collision data collected in 2016-2018 with the CMS detector at the LHC at a centre-of-mass energy of 13 TeV, corresponding to an integrated luminosity of 137 fb^{-1} is the topic of this work and is described in details in Sec. 6.

The channel W′ →tb can be also investigated in full hadronic final state. The ATLAS Collaboration set upper limit at 95% CL at 3.0 (2.9) TeV [96] for RH(LH) W′ by using proton-proton collisions at $\sqrt{s} = 13$ TeV corresponding to 36.1 fb^{-1}. The CMS Collaboration, instead, searched for LH W′ production excluding masses up to 3.4 TeV [97] by using proton-proton collisions at $\sqrt{s} = 13$ TeV corresponding 137 fb^{-1}.

2.4.2 Low-energy constraints

Constraints on W′ boson properties are also set from experiments involving energies much below the predicted W′ mass. The existence of such boson will imply deviations from SM expectations on low-energy effects that are measured

with very high precision. Since these are indirect measurements, the predictions are model-dependent and exclusion limits rely to the particular choice of the free parameters of the model considered. One example is represented by the W-W$'$ mixing that alter the properties of the SM W boson. Limits can be set from the measurements of the ZWW couplings that provide a leading constraint for fermiophobic W$'$ bosons [98]. In models where the W$'$ couplings to quarks are not suppressed, W-W$'$ bosons box diagrams contribute to neutral meson mixing. In the case of W$'$ couplings to RH quarks as in the LR symmetric model, the limit from $K_L - K_S$ mixing is severe: $M_{\mathrm{W}'} > 2.9$ TeV for $C_q^R = gV_{\mathrm{CKM}}$ [99]. However, if no correlation between the W$'$ and W couplings is assumed, then the limit on $M_{\mathrm{W}'}$ may be significantly relaxed [100]. The W$'$ boson could also affect at tree level various low-energy processes. First of all, it would have a detectable impact on the measurement of the Fermi constant in muon decay, which in turn would affect many predictions involving EW interactions. A recent measurement of parity violation in polarised muon decay ruled out W$'$ masses below 600 GeV, assuming W$'$ couplings to RH leptons as in LR symmetric models and a light RH neutrino [101]. Other examples of processes receiving W$'$ boson contribution are the neutron electric dipole moment and the β decays. If RH neutrinos have Majorana masses, then there are tree-level contributions to neutrinoless double-beta decay, and a limit on $M_{\mathrm{W}'}$ versus the ν_R mass may be derived [102]. For ν_R masses below a few GeV, the W$'$ boson contributes to leptonic and semileptonic B meson decays, so that limits may be placed on various combinations of W$'$ parameters [100]. For ν_R masses below ~ 30 MeV, the most stringent constraints on $M_{\mathrm{W}'}$ are due to the limits on ν_R emission from supernovae.

Chapter 3

The CMS experiment at LHC

The prime motivation of the Large Hadron Collider (LHC) [103] is to provide an explanation of the nature of electroweak symmetry breaking for which the Higgs mechanism is responsible. The experimental study of the Higgs mechanism can also shed light on the mathematical consistency of the SM at energy scales above about 1 TeV. Various alternatives to the SM invoke new symmetries, new forces or constituents. As discussed in Chapter 2, there are many compelling reasons to investigate the TeV energy scale and beyond.

The LHC also provides high-energy heavy-ion beams at energies over 30 times higher than at the previous accelerators, allowing to further extend the study of QCD matter under extreme conditions of temperature, density, and parton momentum fraction (low-x). Hadron colliders are well suited to the task of exploring new energy domains, and the region of 1 TeV constituent centre-of-mass energy can be probed if the proton energy and the luminosity are high enough. The access at the TeV and multi-TeV scale could reveal hints of new physics beyond the SM and provide answers to the current open questions in the fundamental particle physics.

To exploit the physics potential of at LHC, four great experiments have been designed. In this chapter an overview of the LHC machine and operation, and a detailed description of the Compact Muon Solenoid (CMS) experiment are given.

3.1 The Large Hadron Collider

The LHC at CERN (Conseil européen pour la recherche nucléaire) near Geneva is the largest circular accelerator to date and one of the most powerful tools for fundamental particle physics research. It is designed to collide proton beams with a centre-of-mass energy of 14 TeV and a luminosity of 10^{34} cm^{-2}s^{-1}. It can also collide heavy (Pb) ions with an energy of 2.8 TeV per nucleon and a peak lumi-

nosity of 10^{27} cm^{-2}s^{-1}. The aim of the LHC is to reveal the physics beyond the SM with centre of mass collision energies of up to 14 TeV.

The number of events per second generated in the LHC collisions is given by:

$$N_{event} = L\sigma_{event} \tag{3.1}$$

where σ_{event} is the cross section for the event under study and L is the machine luminosity. The machine luminosity depends only on the beam parameters and can be written, for circular proton-proton accelerators and assuming a Gaussian beam distribution, as:

$$L = \frac{N_b^2 \gamma_r f_{rev} n_b}{4\pi\epsilon_n \beta^*} F, \tag{3.2}$$

where N_b is the number of particles per bunch, n_b the number of bunches per beam, f_{rev} the revolution frequency, γ_r the relativistic gamma factor, ϵ_n the normalised transverse beam emittance, β^* the beta function at the collision point, and F the geometric luminosity reduction factor due to the crossing angle at the interaction point.

The LHC is located in an underground 26.7 km long tunnel which was originally built to host the CERN Large Electron Positron (LEP) accelerator. The tunnel is located between 45 and 170 meters below the surface, crossing the border between France and Switzerland, and it is connected to the CERN accelerating complex by two tunnels.

The CERN accelerating complex is shown in Figure 3.1 and produces proton beams of energy of 450 GeV: the first step of accelerating process is performed by LINAC 2 (LINear particle ACcelerator), which produces proton beams of energy of 50 MeV; the second step is performed by PSB (Proton Synchrotron Booster) which accelerates the beams up to 1.4 GeV; then the beams are injected in PS (Proton Synchrotron) which produces proton beams of energy of 26 GeV; finally, the last step is SPS (Super Proton Synchrotron) and the beams reach the energy of 450 GeV and can be injected in the LHC, where they reach their maximum energy of 7 TeV.

In order to achieve this goal, the LHC is composed of a superconducting cavity system of radiofrequencies (RF) which accelerate the beams, 1232 dipole magnets, necessary to keep the beams in the circular ring, 392 quadrupole magnets, which focus the beams, and other magnets for spool piece correction magnets (sextupole and octupole/decapole). The LHC magnet system makes use of the well-proven technology based on NbTi Rutherford cables and cools the magnets to a temperature below 2 K, using super-fluid helium, and operates at fields above 8.33 T.

The requirements on the beam lifetime and on beam-induced background for the experiments drive the conditions on the vacuum pressure in the magnets pipe. The LHC has three vacuum systems: the insulation vacuum for cryomagnets, the

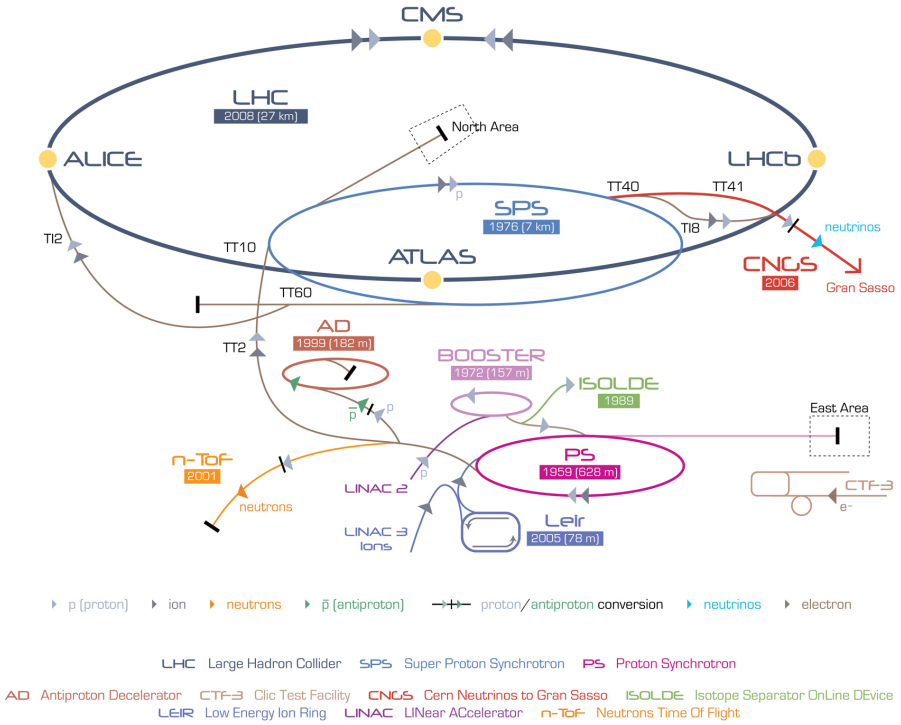

Figure 3.1: The CERN accelerating complex.

insulation vacuum for helium distribution, and the beam vacuum. The insulation vacua before cool-down do not have to be better than 10^{-1} mbar, but at cryogenic temperatures, in the absence of any significant leak, the pressure will stabilise around 10^{-6} mbar. In the interaction regions around the experiments, the requirements for the beam vacuum are much more stringent to minimise the background to the experiments. In the room temperature parts of the beam vacuum system, the pressure should be in the range 10^{-10} to 10^{-11} mbar.

3.1.1 Experiments and data taking activity

The LHC has four main experiments:

- ALICE: *A Large Ion Collider Experiment* [104] is a dedicated ion experiment; it works with $\sqrt{s} = 2.67$ TeV lead-lead ion collisions aiming at a peak luminosity of $L = 10^{27}$ cm^{-2}s^{-1}.

- ATLAS: *A Toroidal LHC ApparatuS* [105] is a general-purpose detector whose targets are precision measurements of SM, the search and the study of Higgs boson, and mechanisms due to new physics. It is 46 m long and has a 25 m diameter and it is the biggest experiment at LHC.

- CMS: *Compact Muon Solenoid* [106] is described in section 3.2.
- LHCb: *LHC-beaty* [107] is an experiment designed and optimised for the study of the b quark properties and its production mechanism.

The LHC activity started in 2019 with a pivot run at $\sqrt{s} = 0.9$ and $\sqrt{s} = 2.56$ TeV. In 2010, p-p collisions with a centre-of-mass energy at $\sqrt{s} = 7$ TeV were produced until 2011; in 2012/2013 the p-p collisions were at $\sqrt{s} = 8$ TeV. The 2010-2013 activity is called LHC Run I. In 2013 LHC stopped for the upgrade of the detectors in view of the $\sqrt{s} = 13$ TeV p-p collisions. In 2015 the LHC activity started again with $\sqrt{s} = 13$ TeV p-p collisions until 2018. This last period is called LHC Run II. The data collected during the years are reported in Table 3.1 and the CMS data collected and validated are reported too.

Period	Year	$\sqrt{s}$ [TeV]	LHC delivered [fb^{-1}]	CMS Recorded [fb^{-1}]	CMS Validated [fb^{-1}]
Run I	2010	7	40.22×10^{-2}	40.76×10^{-2}	34.68×10^{-2}
	2011	7	6.13	5.55	5.09
	2012	8	23.30	21.79	19.79
Run II	2015	13	4.22	3.81	2.39
	2016	13	40.82	37.76	35.92
	2017	13	49.79	44.98	41.53
	2018	13	67.86	63.67	59.7

Table 3.1: The cumulative luminosity delivered by LHC, recorded by CMS and certified as Good for physics analysis, during each period of activity.

3.2 The CMS experiment

The CMS experiment is one of the four great experiments at the LHC. It is a general-purpose-detector, meaning its research program includes most of the physics at the LHC, from the SM measurements, with particular focus on the Higgs boson, to new physics searches.

CMS is equipped with a huge superconducting magnet, as shown in Figure 3.2 which produces a solenoidal magnetic field of 3.8 T, from which the experiment takes its name.

It has a complex system of sub-detectors shown in Figure 3.3 that allows to identify different particles from few hundreds of MeV to several TeV with a high momentum resolution in a wide angular coverage down to few degrees from the

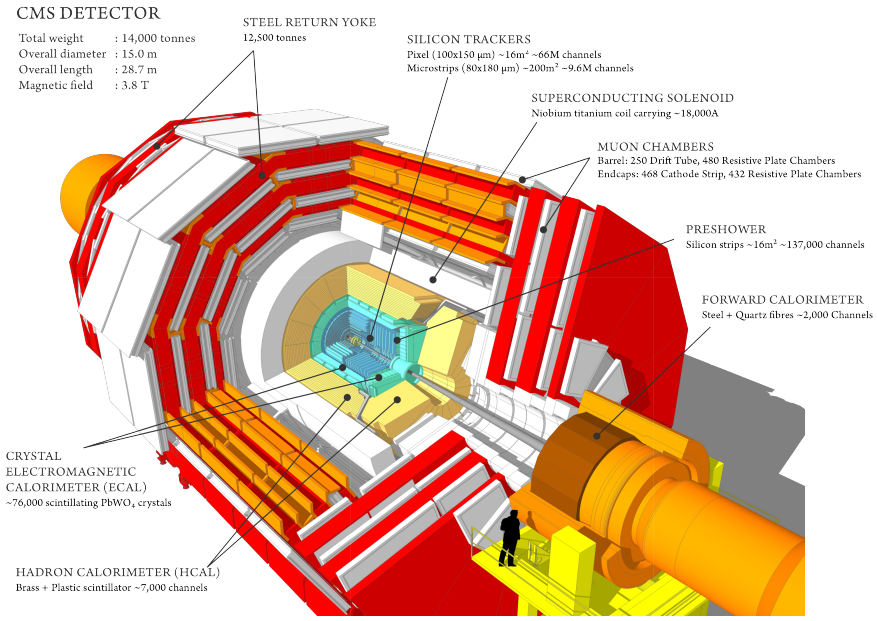

Figure 3.2: The CMS experiment.

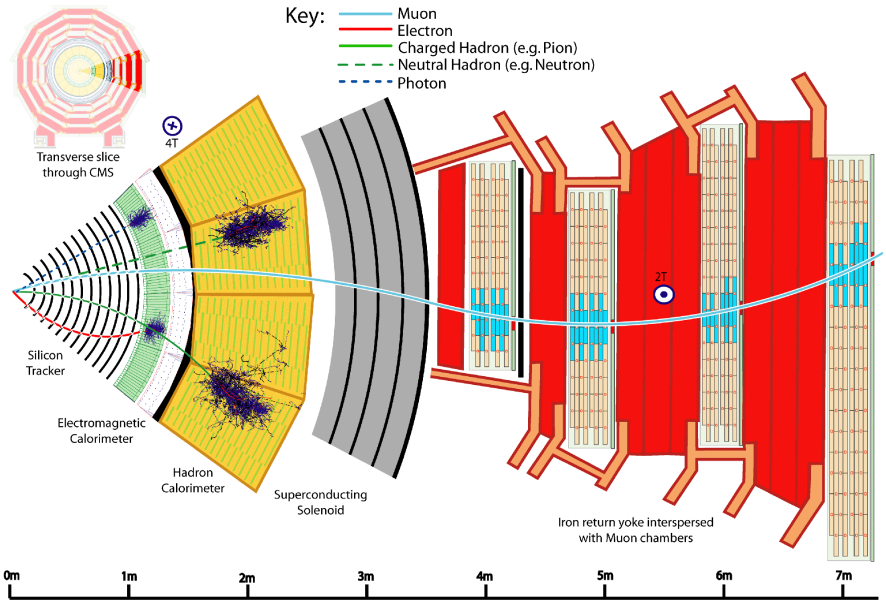

Figure 3.3: The CMS subdetectors system.

beam axis. CMS has a component where the sensitive surfaces of the detectors run coaxial to the beam, named Barrel, and two components that close the barrel, named Endcaps, where the sensitive surfaces are orthogonal to the beam axis instead. CMS has a cylindrical symmetry and it is 21.6 m long with a diameter of 14.6 m and a total weight of about 14000 tons.

The CMS coordinate system used to describe the detector is a right-handed Cartesian frame, centred in the interaction point and with the z axis along the beam line (this direction is referred to as longitudinal). The x axis is chosen to be horizontal and pointing towards the centre of the LHC ring, and the y axis is vertical and pointing upwards. The $x-y$ plane is called transverse plane. Given the cylindrical symmetry of the CMS design, usually a (ϕ, θ) cylindrical coordinate system is used in the reconstruction of the tracks of particles. ϕ is the azimuthal angle, laying in the $x-y$ plane, measured from the x axis in mathematical positive direction (i.e. the y axis is at $\phi = 90°$) and the radial coordinate in this plane is referred to as r. The polar angle θ is measured from the z axis towards the $x-y$ plane. The angle θ can be translated into the pseudorapidity η by:

$$\eta = -\ln\left(\tan\frac{\theta}{2}\right) \tag{3.3}$$

A longitudinal view of the CMS detector displaying the segmentation in η of the sub-detectors is shown in Figure 3.4. Using these parameters, a distance between

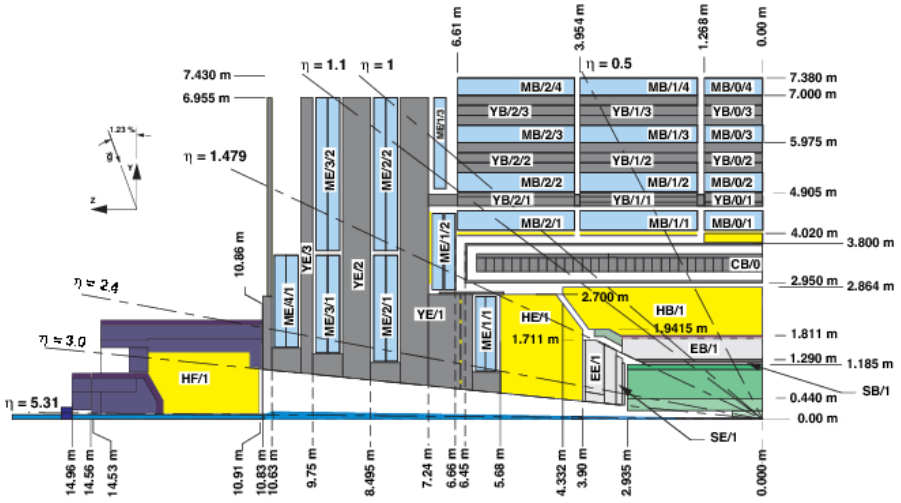

Figure 3.4: Longitudinal view of the CMS detectors.

two particle directions can be defined as:

$$\Delta R = \sqrt{(\Delta\phi)^2 + (\Delta\eta)^2} \tag{3.4}$$

Referring to the Cartesian system, the momentum of a particle can be divided in two components: the longitudinal momentum p_z and the transverse momentum p_{T}, defined as:

$$\vec{p}_{\mathrm{T}} = \sqrt{\vec{p}_x^2 + \vec{p}_y^2} \tag{3.5}$$

The magnet bends charged tracks on the ϕ plane, so that the curvature of the tracks allows for measurements of the particles p_{T}. For a particle of energy E, the variable rapidity (y) is also introduced, defined as:

$$y = \frac{1}{2} \ln \left(\frac{E + p_z c}{E - p_z c} \right) \tag{3.6}$$

For ultra relativistic particles rapidity can be approximated by pseudorapidity. Both rapidity and p_{T} are used because the centre-of-mass of parton-parton collisions can be boosted along the z direction; both these quantities have invariance properties under this kind of boost.

The CMS sub-detector system, starting from the interaction point and going outwards, consists of: the inner tracking system, the electromagnetic calorimeter, the hadron calorimeter, the magnet, and, finally, the iron return yoke interspersed with muon chambers.

3.2.1 The tracking system

The inner tracking system of CMS is designed to provide a precise and efficient measurement of the trajectories of charged particles emerging from the LHC collisions, as well as a precise reconstruction of secondary vertices. It surrounds the interaction point and has a length of 5.8 m and a diameter of 2.5 m. The CMS solenoid provides a homogeneous magnetic field of 3.8 T over the full volume of the tracker. The CMS tracker is composed of a pixel detector with three barrel layers at radii between 4.4 cm and 10.2 cm and a silicon strip tracker with 10 barrel detection layers extending outwards to a radius of 1.1 m. Each system is completed by endcaps which consist of 2 disks in the pixel detector and 3 plus 9 disks in the strip tracker on each side of the barrel, extending the acceptance of the tracker up to a pseudorapidity of $|\eta| < 2.5$. With about 200 m^2 of active silicon area the CMS tracker is the largest silicon tracker ever built [108, 109]. In 2017, the inner tracker has been changed, and the new system starts from 2.3 cm from the collision point, since an additional pixel layer was installed, as reported in Fig. 3.5. As it is extremely close to the collision centre, it is designed to operate at high radiation environment and also to have fast time response.

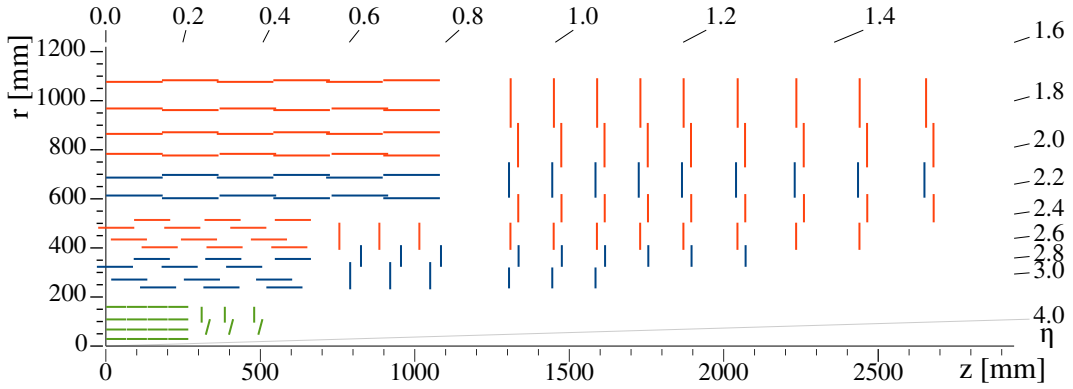

Figure 3.5: Sketch of one quarter of the Phase-1 CMS tracking system in $r - z$ view. The pixel detector is shown in green, while single-sided and double-sided strip modules are depicted as red and blue segments, respectively.

3.2.2 The electromagnetic calorimeter

The electromagnetic calorimeter of CMS (ECAL) is a hermetic homogeneous calorimeter made of 61 200 lead tungstate ($PbWO_4$) crystals mounted in the central barrel part, closed by 7324 crystals in each of the two endcaps [110]. The characteristics of the $PbWO_4$ crystals make them an appropriate choice for operation at LHC. The high density (8.28 g/cm^3), short radiation length (0.89 cm) and small Molière radius (2.2 cm) result in a fine granularity and a compact calorimeter. The scintillation decay time of these production crystals is of the same order of magnitude as the LHC bunch crossing time: about 80% of the light is emitted in 25 ns. The barrel part of the ECAL (EB) covers the pseudorapidity range $|\eta| < 1.479$, occupies a volume of 8.14 m^3 and its weight is 67.4 tons. The endcaps (EE) cover the rapidity range $1.479 < |\eta| < 3.0$, occupy a volume of 2.90 m^3 and the weight is 24.0 tons. The energy resolution of the ECAL of CMS is:

$$\left(\frac{\sigma}{E}\right)^2 = \left(\frac{2.8\%}{\sqrt{E}}\right)^2 + \left(\frac{0.12}{E}\right)^2 + (0.30\%)^2\,, \tag{3.7}$$

where E is expressed in GeV.

3.2.3 The hadron calorimeter

The CMS detector is designed to study a wide range of high-energy processes involving diverse signatures of final states. The hadron calorimeters are particularly important for the measurement of hadron jets momenta and neutrinos or exotic particles resulting in apparent missing transverse energy. The hadron calorimeter barrel and endcaps sit behind the tracker and the electromagnetic calorimeter as

seen from the interaction point [111]. The hadron calorimeter barrel is radially restricted between the outer extent of the electromagnetic calorimeter ($r = 1.77$ m) and the inner extent of the magnet coil ($r = 2.95$ m). This constrains the total amount of material which can be put in to absorb the hadronic shower. Therefore, an outer hadron calorimeter or tail catcher is placed outside the solenoid complementing the barrel calorimeter. Beyond $|\eta| = 3$, the forward hadron calorimeters placed at 11.2 m from the interaction point extend the pseudorapidity coverage down to $|\eta| = 5.2$ using a Cherenkov-based, radiation-hard technology. Since the calorimeter is inserted into the ends of a 3.8 T solenoidal magnet, the absorber must be made from a non-magnetic material. It must also have a maximum number of interaction lengths to contain hadronic showers, good mechanical properties and reasonable cost, leading to the choice of C26000 cartridge brass. The properties of this material are reported in Table 3.2.

Properties of C26000	
Chemical composition	70% Cu, 30% Zn
density	8.53 g/cm^3
radiation length	1.49 cm
interaction length	16.42 cm

Table 3.2: Physical properties of the HCAL brass absorber, known as C26000/cartridge brass.

3.2.4 The superconducting magnet

The superconducting magnet for CMS [112] has been designed to reach a 3.8 T field in a free bore of 6 m diameter and 12.5 m length with a stored energy of 2.6 GJ at full current. The flux is returned through a 10000 tons yoke comprising 5 wheels and 2 endcaps, composed of three disks each. The iron return yoke allows for a constant 1.8 T field also in the region outside the magnet.

3.2.5 The muon system

Muon detection is a powerful tool for recognising signatures of interesting processes over the very high background rate expected at the LHC with full luminosity. Therefore, as is implied by the experiment's middle name, the detection of muons is of central importance to CMS: precise and robust muon measurement was a central theme from its earliest design stages. The muon system has 3 functions: muon identification, momentum measurement and triggering. Good muon momentum resolution and trigger capability are enabled by the high-field solenoidal

magnet and its flux-return yoke. The latter also serves as a hadron absorber for the identification of muons.

The CMS muon system is designed to have the capability of reconstructing the momentum and charge of muons over the entire kinematic range of the LHC. CMS uses 3 types of gaseous particle detectors for muon identification. Due to the shape of the solenoid magnet, the muon system was naturally driven to have a cylindrical, barrel section and 2 planar endcap regions. Because the muon system consists of about 25 000 m^2 of detection planes, the muon chambers had to be inexpensive, reliable, and robust.

In the barrel region, where the neutron-induced background is small, the muon rate is low, and the 3.8 T magnetic field is to good approximation uniform and mostly contained in the steel yoke, drift chambers with standard rectangular drift cells are used. The barrel drift tube (DT) chambers cover the pseudorapidity region $|\eta| < 1.2$ and are organised into 4 stations interspersed among the layers of the flux return plates. The first 3 stations each contain 8 chambers, in 2 groups of 4, which measure the muon coordinate in the $r - \phi$ bending plane, and 4 chambers which provide a measurement in the z direction, along the beam line. The fourth station does not contain the z-measuring planes. The 2 sets of 4 chambers in each station are separated as much as possible to achieve the best angular resolution. The drift cells of each chamber are offset by a half-cell width with respect to their neighbour to eliminate dead spots in the efficiency. This arrangement also provides a convenient way to measure the muon time with excellent time resolution, using simple mean timer circuits, for efficient, standalone bunch crossing identification. The number of chambers in each station and their orientation were chosen to provide good efficiency for linking together muon hits from different stations into a single muon track and for rejecting background hits.

In the 2 endcap regions of CMS, where the muon rates and background levels are high and the magnetic field is large and non-uniform, the muon system uses cathode strip chambers (CSC). With their fast response time, fine segmentation, and radiation resistance, the CSCs identify muons between $|\eta|$ values of 0.9 and 2.4. There are 4 stations of CSCs in each endcap, with chambers positioned perpendicular to the beam line and interspersed between the flux return plates. The cathode strips of each chamber run radially outward and provide a precision measurement in the $r - \phi$ bending plane. The anode wires run approximately perpendicular to the strips and are also read out in order to provide measurements of η and the beam-crossing time of a muon. Each 6-layer CSC provides robust pattern recognition for rejection of non-muon backgrounds and efficient matching of hits to those in other stations and to the CMS inner tracker. Because the muon detector elements cover the full pseudorapidity interval $|\eta| < 2.4$ with no acceptance gaps, muon identification is ensured over the range corresponding to

$10^\circ < \theta < 170^\circ$.

Offline reconstruction efficiency of simulated single-muon samples is typically $95-99\%$ except in the regions around $|\eta| = 0.25$ and 0.8 (the regions between 2 DT wheels) and $|\eta| = 1.2$ (the transition region between the DT and CSC systems), where the efficiency drops. Negligible punchthrough reaches the system due to the amount of material in front of the muon system, which exceeds 16 interaction lengths.

Due to multiple-scattering in the detector material before the first muon station, the offline muon momentum resolution of the standalone muon system is about 9% for small values of η and p for transverse momenta up to 200 GeV. At 1 TeV the standalone momentum resolution varies between 15% and 40%, depending on $|\eta|$. A global momentum fit using also the inner tracker improves the momentum resolution by an order of magnitude at low momenta. At high momenta (1 TeV) both detector parts together yield a momentum resolution of about 5%. Note that the muon system and the inner tracker provide independent muon momentum measurements; this redundancy enhances fault finding and permits cross-checking between the systems. A crucial characteristic of the DT and CSC subsystems is that they can each trigger on the p_{T} of muons with good efficiency and high background rejection, independent of the rest of the detector. The Level-1 trigger p_{T} resolution is about 15% in the barrel and 25% in the endcap.

Because of the uncertainty in the eventual background rates and in the ability of the muon system to measure the correct beam-crossing time when the LHC reaches full luminosity, a complementary, dedicated trigger system consisting of resistive plate chambers (RPC) was added in both the barrel and endcap regions. The RPCs provide a fast, independent, and highly-segmented trigger with a sharp p_{T} threshold over a large portion of the rapidity range ($|\eta| < 1.6$) of the muon system. The RPCs are double-gap chambers, operated in avalanche mode to ensure good operation at high rates. They produce a fast response, with good time resolution but coarser position resolution than the DTs or CSCs. They also help to resolve ambiguities in attempting to make tracks from multiple hits in a chamber.

A total of 6 layers of RPCs are embedded in the barrel muon system, 2 in each of the first 2 stations, and 1 in each of the last 2 stations. The redundancy in the first 2 stations allows the trigger algorithm to work even for low-p_{T} tracks that may stop before reaching the outer 2 stations. In the endcap region, there is a plane of RPCs in each of the four stations in order for the trigger to use the coincidences between stations to reduce background, to improve the time resolution for bunch crossing identification, and to achieve a good p_{T} resolution. Finally, a sophisticated alignment system measures the positions of the muon detectors with respect to each other and to the inner tracker, in order to optimise the muon momentum resolution.

3.2.6 The trigger system

The LHC provides proton-proton and heavy-ion collisions at high interaction rates. For protons the beam crossing interval is 25 ns, corresponding to a crossing frequency of 40 MHz. Depending on luminosity, several collisions occur at each crossing of the proton bunches (approximately 20 simultaneous pp collisions at the nominal design luminosity of 10^{34} $\mathrm{cm}^{-2}\mathrm{s}^{-1}$). Since it is impossible to store and process the large amount of data associated with the resulting high number of events, a drastic rate reduction has to be achieved.

This task is performed by the trigger system, which is the start of the physics event selection process. The rate is reduced in two steps called Level-1 (L1) Trigger [113] and High-Level Trigger (HLT) [114], respectively. The Level-1 Trigger consists of custom-designed, largely programmable electronics, whereas the HLT is a software system implemented in a filter farm of about one thousand commercial processors. The rate reduction capability is designed to be at least a factor of 10^6 for the combined L1 Trigger and HLT. The design output rate limit of the L1 Trigger is 100 kHz, which translates in practice to a calculated maximal output rate of 30 kHz, assuming an approximate safety factor of three.

The L1 Trigger uses coarsely segmented data from the calorimeters and the muon system, while holding the high-resolution data in pipelined memories in the front-end electronics.

The HLT has access to the complete read-out data and can therefore perform complex calculations similar to those made in the the analysis off-line software if required for specially interesting events.

For reasons of flexibility the L1 Trigger hardware is implemented in FPGA technology where possible, but ASICs and programmable memory lookup tables are also widely used where speed, density and radiation resistance requirements are important. A software system, the Trigger Supervisor, controls the configuration and operation of the trigger components. The L1 Trigger has local, regional and global components. At the bottom end, the Local Triggers, also called Trigger Primitive Generators (TPG), are based on energy deposits in calorimeter trigger towers and track segments or hit patterns in muon chambers, respectively. Regional Triggers combine their information and use pattern logic to determine ranked and sorted trigger objects such as electron or muon candidates in limited spatial regions. The rank is determined as a function of energy or momentum and quality, which reflects the level of confidence attributed to the L1 parameter measurements, based on detailed knowledge of the detectors and trigger electronics and on the amount of information available. The Global Calorimeter and Global Muon Triggers determine the highest-rank calorimeter and muon objects across the entire experiment and transfer them to the Global Trigger, the top entity of the Level-1 hierarchy. The latter takes the decision to reject an event or to accept

it for further evaluation by the HLT. The decision is based on algorithm calculations and on the readiness of the sub-detectors and the DAQ, which is determined by the Trigger Control System (TCS). The Level-1 Accept (L1A) decision is communicated to the sub-detectors through the Timing, Trigger and Control (TTC) system. The architecture of the L1 Trigger is depicted in Figure 3.6. The L1 Trig-

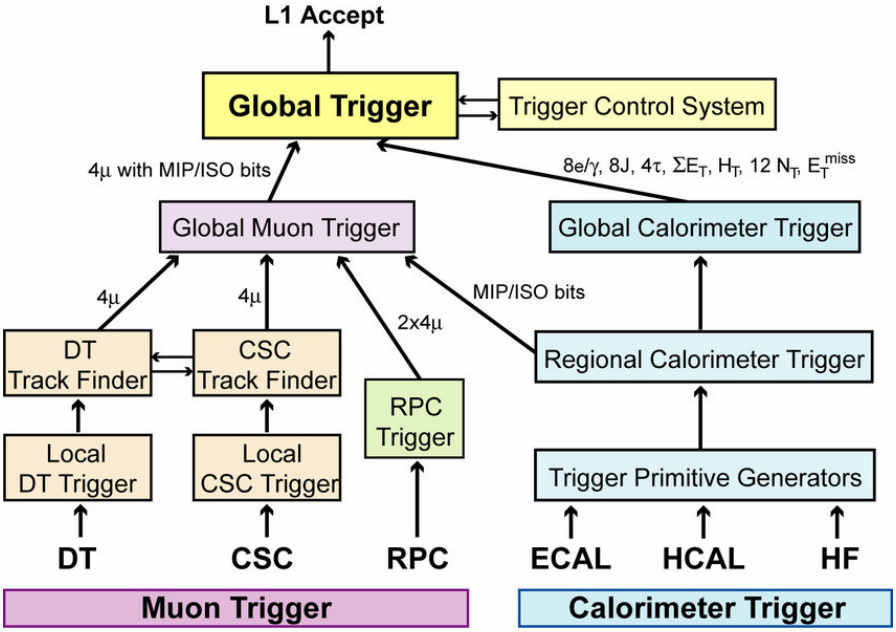

Figure 3.6: Architecture of the Level-1 Trigger.

ger has to analyse every bunch crossing. The allowed L1 Trigger latency, between a given bunch crossing and the distribution of the trigger decision to the detector front-end electronics, is 3.2 μs. The processing must therefore be pipelined in order to enable a quasi-deadtime-free operation. The L1 Trigger electronics is housed partly on the detectors, partly in the underground control room located at a distance of approximately 90 m from the experimental cavern.

3.3 Muon system upgrade with Triple-GEM detectors

The operating conditions of the LHC Run 3, in which the instantaneous luminosity will probably exceed, the project value of 2×10^{-34} cm^{-2}s^{-1}, and, later, of LHC Phase 2, in which an instantaneous luminosity of 5×10^{-34} cm^{-2}s^{-1} is expected, constitute a very hard challenge for the detectors especially in the endcap regions. The original design of the muon system was already conceived to offer

fast response and a good level of redundancy, but this will not be enough for the coming years. In order to succeed in the vast physics programme, and to achieve sensitivity to electroweak scale physics and consistent sensitivity at the multi-TeV scale searches various upgrades are necessary. One of the most important upgrades of the CMS detector during the long shutdown 2 (LS2) interested the muon system, and it was designed to improve the muon trigger and tracking performance in the prospected high luminosity environment. The technology chosen for the upgrade is that of the micro pattern gaseous detectors (MPGDs), and specifically the Gaseous Electron Multiplier, or more briefly GEM [115]. The main task of the GEM detectors is to add redundancy to the muon system in the $1.6 < |\eta| < 2.2$ pseudorapidity region, where the amount of detection layers is lowest while the background rates are highest and the bending of the muon trajectories is small due to weaker CMS magnetic field. The GEM detectors are the most suitable thanks to the their fast response and the reduced avalanche size.

The first station installed in the CMS detector is the so-called GE1/1, shown in the quadrant cross-section of CMS in Figure 3.7. Since forward RPCs were envisioned in the original conception of the CMS muon system, there is space available within CMS for installation of a sufficiently compact (thin) detector to respect the tight geometrical limitations. The proposed GE1/1 detector utilising GEM technology is an excellent choice for this region, due to its thin profile and the ability of operating well at particle fluxes far above those expected in the forward region under HL-LHC conditions. The denomination GE1/1 refers to the CMS terminology, used for the muon stations: the letter G indicates the GEM technology, the letter E indicates this is an endcap muon station, the first "1" indicates that it is part of the first muon station encountered by particles from the interaction point, and the second "1" indicates that it is the first ring of muon chambers going outward in radius from the beam line.

The GE1/1 muon station offers an improvement of the L1 muon trigger rate. This is justified considering that the bending of muons within the CMS solenoid is largest at the position of the first muon station and the longer path length traversed by muons within the first muon stations (GE1/1 and CSC station ME1/1) drastically reduces the large contribution to the overall L1 muon trigger rate coming from the higher rate at increasing $|\eta|$. Figure 3.8 shows the impact of the GE1/1 muon station on the reduction of the L1 trigger rate with respect to the current muon system.

In particular, the L1 muon trigger thresholds can be maintained at low p_{T} values, so that the efficiency for capturing interesting physics processes featuring soft leptons, ranging from Higgs precision measurements to new physics searches, can be kept high.

During the Long Shutdown 3 (LS3), after the Run 3 operations, a new silicon

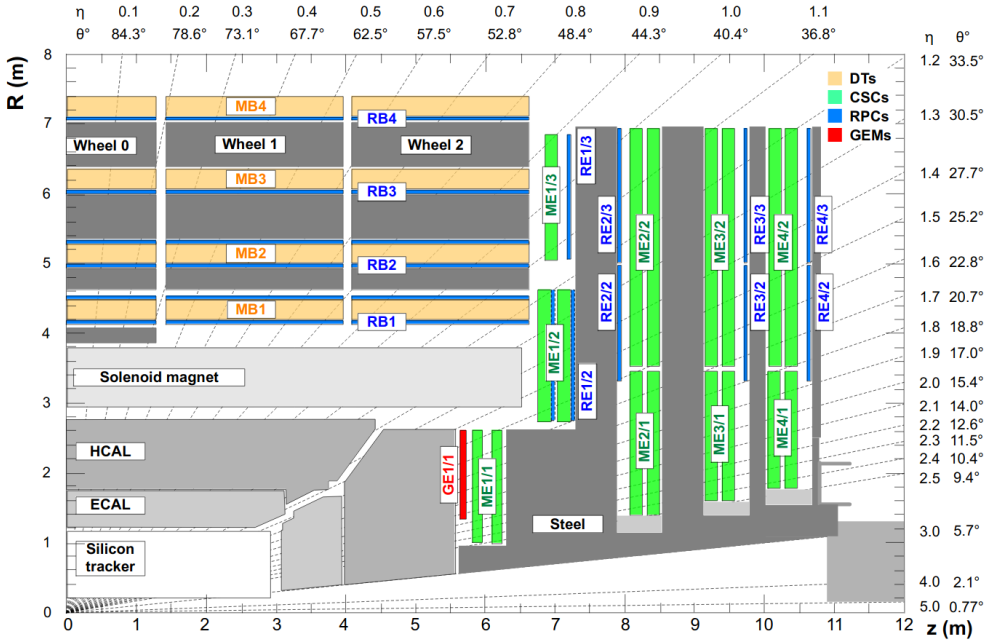

Figure 3.7: A quadrant of the $R - z$ cross-section of the CMS detector, with the addition of the proposed GE1/1 detector (highlighted in red) within the CMS muon system [115].

tracker will be installed in CMS, and together with the muon system it will allow to improve the L1 muon trigger throughout the "combined muon trigger", providing a better momentum resolution thanks to the higher resolution on the muon tracks position. The combined muon trigger will be used together with the standalone muon trigger contributing to maintain highest overall muon trigger efficiency. Alongside the new silicon tracker, during LS3, it is foreseen the installation of a second station of GEM detectors (GE2/1), and third (RE3/1) and fourth (RE4/1) stations of improved RPC (iRPC) detectors. The additional forward muon detectors will increase the average number of muon hits along a forward track up to about the same level that is already present in the barrel muon region of CMS. This is a minimal requirement for handling HL-LHC conditions, given that in the forward region the background particle rates are higher and magnetic bending power is much reduced. The new forward muon stations will provide additional redundancy, necessary to keep good performances on muons quality detection but will also contribute to keep high the efficiency of the L1 and HLT trigger rate also if the performance of the aging ME1/1 system degrades.

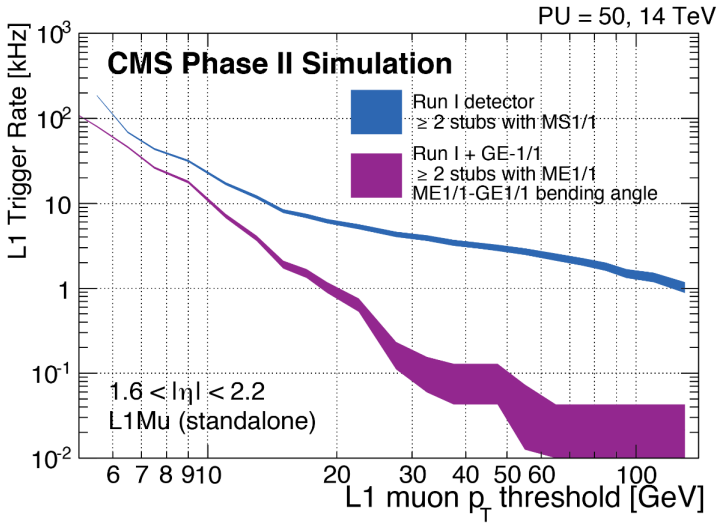

Figure 3.8: Level 1 muon trigger rates before and after the GE1/1 upgrade at a luminosity of 2×10^{34} cm^{-2}s^{-1}, for constant efficiency of 94%. ME1/1 denotes the first endcap muon station Level 1 trigger in both cases, i.e. with CSC-only or with the combination CSC and GEM trigger information. With the addition of GE1/1, the bending angle between the two stations can be used and the trigger rate is greatly reduced [115].

3.3.1 GEM technology

The GEM detector was originally proposed in 1997 [116] and since then a great work of research and development (R&D) has been done to improve the performances and the design. A large contribution to this effort also came from the CMS Collaboration especially in the last 10 years. After the conceptual optimisation of the detector the challenge for the CMS Collaboration was to produce, assembly, test and install the GE1/1 system in the CMS experiment. The detectors chosen to be installed in the GE1/1 station are ten-degree chambers segmented in both ϕ and η.

The physics phenomenon exploited in the GEM chambers is the electron amplification that occurs within a gas medium via ionisation. To achieve this goal, the GEM detectors are designed so to have a non uniform electromagnetic field, where the amplification is concentrated is small spatial regions, i.e. microscopic gaps: a GEM foil consists in a 50 μm thin polyimide foil perforated with high density microscopic holes. The holes, obtained by chemical perforation, are truncated double cones with the larger (outer) diameters around 70 μm and the smaller (inner) diameter around 50 μm; they are spaced with a pitch of 140 μm in a hexagonal pattern. A Scanning Electron Microscope (SEM) view of a GEM foil is reported in

Fig. 3.9 (left). Each side of the foil has a 5 μm thin conductive layer of copper to which a voltage of a few hundred volts is applied. This allows to creates a strong electric field ($60-100$ kV/cm) inside the holes that causes electron-ion avalanches in the gas. In order to keep the voltage applied low and, at the same time, have a good amplification factor, a configuration with a cascade of three GEM foil is adopted, commonly referred to as "Triple-GEM detector". This setup allows to avoid electrical breakdown problems, providing a total charge amplification factor up to 10^5, as the gain at each previous stage is multiplied by the gain at the following stage. The electrons, produced by a charged particle passing through the chamber due to ionisation of the counting gas, drift towards the holes and once they start to experience the very intense electric field in the holes, they acquire enough kinetic energy to produce secondary ionisation in the gas. This produces an electron avalanche process, which induces an electrical signal on the electrodes that are finely segmented in the muon bending direction (ϕ) to make the detector position-sensitive. The schematic view of the charges flows in a hole is represented in Fig. 3.9 (right).

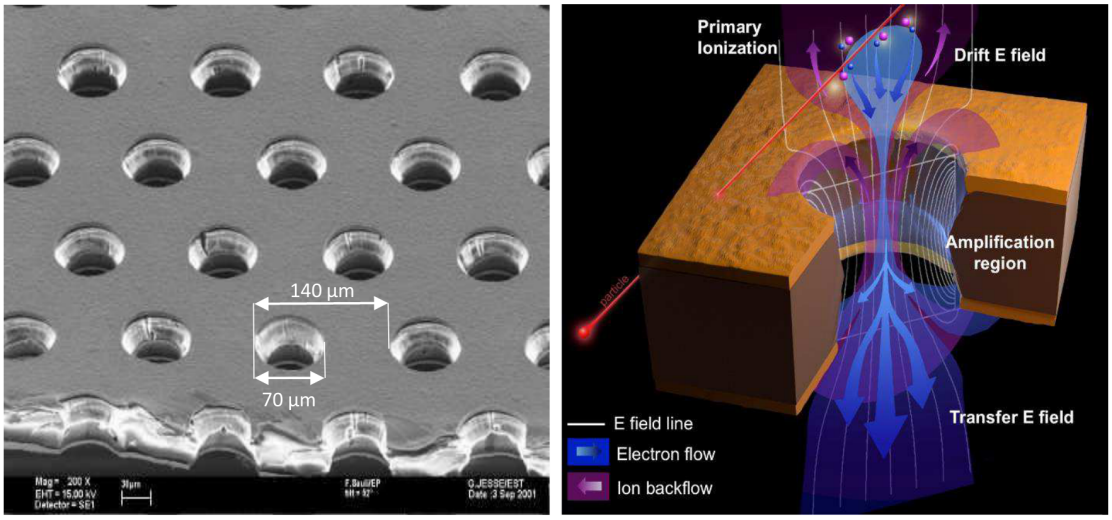

Figure 3.9: A GEM foil view at the Scanning Electron Microscope (SEM), with a focus on the geometrical structure of the hole (outer diameter of 70 μm and inner diameter of 50 μm) and on the hexagonal pattern with a pitch of 140 μm (left) and schematic view of the electric field lines (white), electron flow (blue), and ion flow (purple) through a biconical GEM hole (right) [115].

Each ten-degree chamber has 384 read-out strips in ϕ, each one covering 450 μrad, and are read by three 128-channel front-end chips. The chambers have also 8 segments in η direction, for a total of 24 independent segments. A total of 24 128-channel front-end chips, called Very Forward ATLAS TOTEM chips or simply

VFAT3, are hence needed for the read-out of a single GEM chamber. The VFAT3 architecture, reported in Fig. 3.10. is composed of 128 channels, each comprising a charge sensitive preamplifier and shaper. This is followed by a constant fraction discriminator per channel. Following the discriminator is a synchronisation unit which synchronises the comparator result with the 40 MHz clock of LHC. The data then splits into two paths, one with a fixed latency for trigger signals, and the second for tracking data which is non-synchronous. All communication with VFAT3 occurs through the E-port. This includes synchronisation to the LHC clock, slow control commands as well as fast trigger commands, data packets, calibration and monitoring. The chip is highly programmable to offer maximum flexibility.

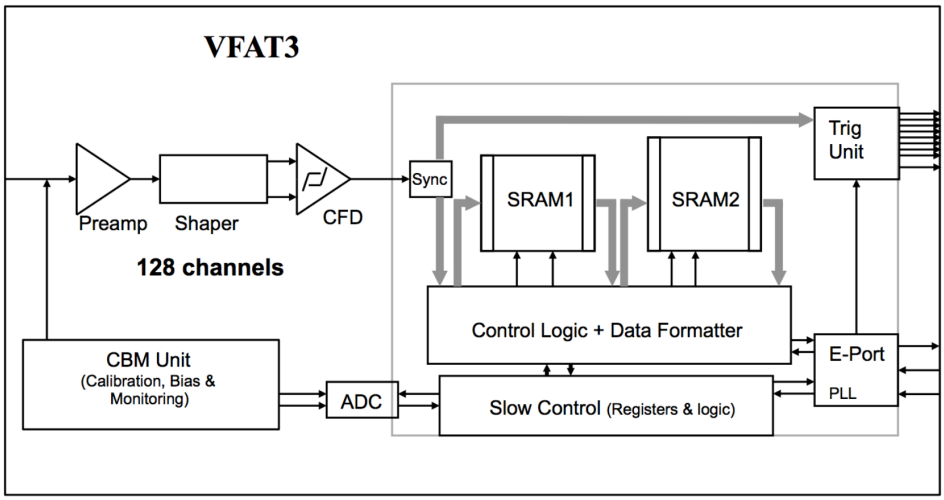

Figure 3.10: VFAT3 architecture and components [115].

The data from the VFAT3 chips are sent to the GEM Electronics Board (GEB) which delivers power and communication signals to and from the VFAT3 as well as providing the connection to the GEM strips. From the GEB, data are transmitted to one FPGA board, called the GEM OptoHybrid (OH), located on the wide end of the GEM chamber. One of the main components of the OH is a Xilinx Virtex 6 FPGA, which has been shown to be radiation-hard to levels at least two orders of magnitude higher than the expected radiation dosage. The system is designed such that one optical fibre can read out the tracking data from one GEM column, while all trigger data are carried out by a dedicated additional fibre. A single GEM chamber has three optical fibres to take the tracking and trigger data to and from the CMSGEM DAQ system. For the off-detector electronics, the μTCA standard and the CMS MP7 and AMC13μTCA boards are used. Data are transmitted between the on- and off-detector electronics through optical fibers using the CERN GigaBit Transceiver (GBT) protocol.

Each chamber so assembled is coupled with another one to form a so-called superchamber, which is finally mounted in CMS. The GEM detectors are operated in a Ar:CO_2 gas mixture in proportion 70:30. Table 3.3 recaps the main features of these detectors.

Specification/Parameter	GE1/1
Detector technology	Gaseous detector; micro-pattern gas detector (MPGD)
Charge amplification element	GEM foil (triple, cascaded, tensioned at ~ 5 N/cm)
Number of chambers in overall system	144 (72 in each endcap)
Chamber shape (active readout area)	Trapezoidal; opening angle 10.15°
Active area overlap in adjacent chambers	2.6 mrad (corresponds to 5.7 readout strip pitches)
Short chamber dimensions (active vol.)	L: 106.1 cm (centre line), W: (23.1 - 42.0) cm, D: 0.7 cm
Long chamber dimensions (active vol.)	L: 120.9 cm (centre line), W: (23.1 - 44.6) cm, D: 0.7 cm
Total chamber thickness	D: 3.5 cm
Active readout area	0.345 m^2(short ch.); 0.409 m^2(long ch.)
Active chamber volume	2.6 litres (short ch.); 3 litres (long ch.)
Radial distance from beam line	130.2 cm (at inner edge of active readout area)
Geometric acceptance in η	1.61 - 2.18 (short ch.); 1.55 - 2.18 (long ch.)
Signal readout structure	Truly radial readout strips
Readout strip dimensions	230 μrad angular strip width; 463 μrad angular pitch
Number of η-segments in readout	8
Number of readout strips per η-segment	384
Number of readout strips per chamber	3,072
Counting gas mixtures	Ar/CO_2 70:30
Nominal operational gas flow	1 chamber volume per hour
Number of gas inlets	1
Number of gas outlets	1
Nominal HV applied to drift electrode	3200 V
Nominal operational gas gain	$1 - 2 \times 10^4$
Demonstrated rate capability	100 MHz/cm^2

Table 3.3: Main features of the GE1/1 muon station installed at CMS.

3.3.2 Physics performances

The main features the GE1/1 system must have are:

- high efficiency;
- good time resolution;
- high rate capability;
- low discharge probability.

During the R&D of the final detector, two gas mixtures were considered: Ar/CO_2/CF_4 45:15:40 and Ar/CO_2 70:30. Different tests have been performed to choose the best

between the two gas mixtures and the latter has been chosen as the candidate for the final setup.

The efficiency is one of the main properties of any detector. Is it usually defined as the ratio between the number of events detected by the device under test and the total number of events happened in a certain time interval. In this case the efficiency is estimated by recording the total number of triggers N generated by the coincidence of the three scintillators and the number of hits N_1 in the test region of the chamber. It is possible that some hits, say N_2, happen in the neighbourhood regions due to a misalignment. So the efficiency is then evaluated as $\epsilon = N_1/(N - N_2)$ for both the gas mixtures as a function of the drift voltage and the results obtained are reported in Fig. 3.11. The GEM chamber with the Ar/CO_2 gas mixture is fully efficient (efficiency at the plateau greater than 98%) for lower drift voltages for the same value of the gain equal to 10^4. The lower efficiency of the other gas mixture is due to the greater quenching power of the CF_4.

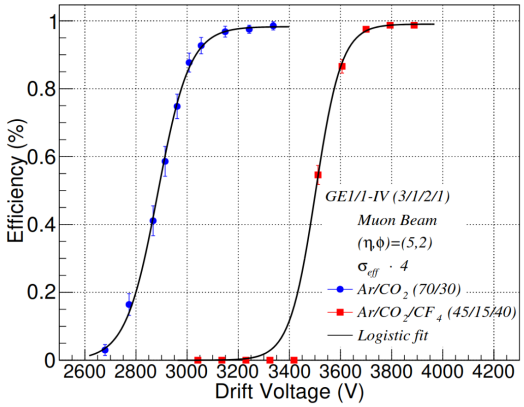

Figure 3.11: Efficiency of a GE1/1 detector for the gas compositions Ar/CO_2 70:30 and $Ar/CO_2/CF_4$ 45:15:40. Points represent the data and solid lines represent parametric fits. The error bars on data represent Gaussian one sigma uncertainty. Since the uncertainty is small, for display, the errors are multiplied by a factor of 4 ($\sigma_{eff} \cdot 4$) [117].

Another crucial property of this detector is the time resolution. The key role that the GE1/1 has to play in the L1 trigger decision imposes the response of this system to be very fast. This parameter is dependent on many factors but, mainly, by the drift velocity of the charges in the gaps between the GEM foils. The charge diffusion can be reduced by adding to the gas mixture a quencher that reduce the charge density in excess, such as the CF_4. The time resolution is measured as the standard deviation of the distribution of the time intervals that occur between the trigger and the detector signal, measured by a time to digital converter (TDC).

Since the time resolution primarily depends on the drift voltage, Fig. 3.12 (left) reports the results as a function of this parameter. Nevertheless, in order to be able to directly compare the performances of the two gas mixtures the measured time resolutions are displayed as a function of the gain and are reported in Fig. 3.12 (right). As expected, the mixture with the addition of the CF_4 component has

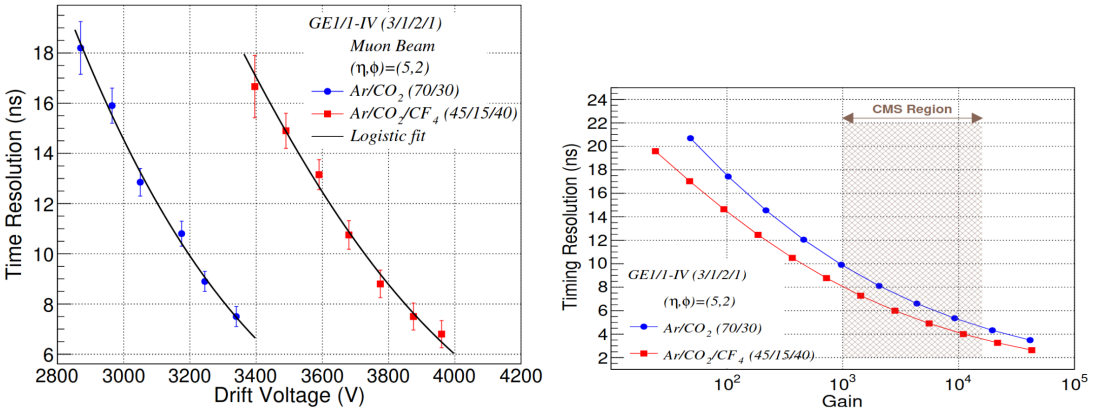

Figure 3.12: On the left, time resolution of a GE1/1 detector for the gas compositions Ar/CO_2 70:30 and $Ar/CO_2/CF_4$ 45:15:40. Points represent the data and solid lines represent parametric fits. The error bars on data represent Gaussian one sigma uncertainty. On the right, time resolution for Ar/CO_2 70:30 and $Ar/CO_2/CF_4$ 45:15:40 gases as a function of gain. The fit equations from are left plot are used to obtain data points by interpolation; the solid lines connect the points [117].

better performances and the improvement is around 24%. The CMS Region band in Fig. 3.12 shows the time resolution for the operating conditions expected in CMS.

The rate capability gives a measure of the maximum flux of incoming particles that can be detected by the chamber before it is completely saturated by the secondary ionisation charges and, as a consequence, blind to further particles passing into it. This concept is strictly related to the velocity of the extinction of the avalanche due to the passage of a particle. The operating conditions of the GE1/1 system in the CMS endcap are expected not to exceed 10 kHz/cm^2. The nominal operating gain of the GE1/1 detectors is expected to be $\sim 7 \times 10^3$ [115]. The measurement is performed by using an intense source of X-ray photons, measuring the gain as a function of the incoming rate. The current produced by the detector is measured with a pico-ammeter connected to anode of the chamber. The incident flux is varied by interposing between the X-ray photons source and the detector some copper attenuators. Figure 3.13 shows the effective gain of a full-size GE1/1 detector with the gas mixture $Ar/CO_2/CF_4$ 45:15:40 and that for a 10×10 cm^2

GE1/1 detector with the gas mixture Ar/CO_2 70:30. In both cases, the effective gain remains stable up to several hundreds of kHZ/cm^2, far beyond the operating conditions expected for HL-LHC.

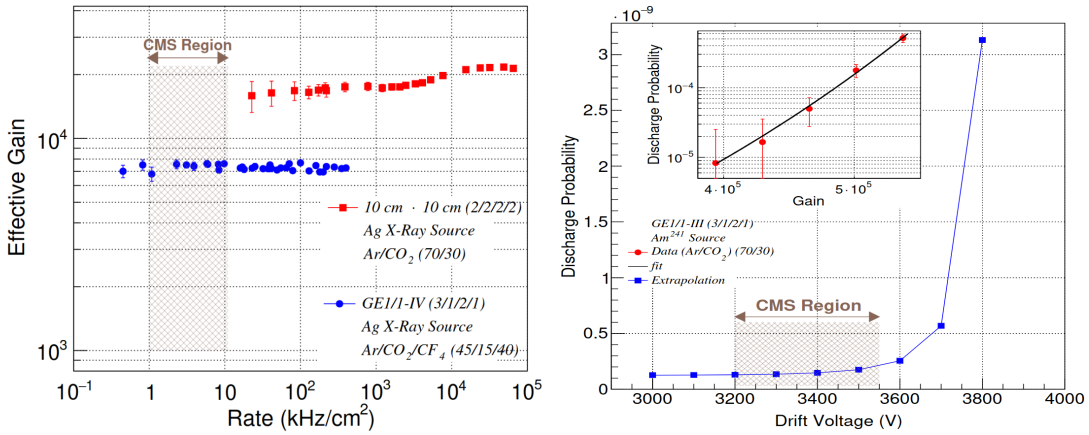

Figure 3.13: On the left, rate capabilities of a GE1/1 chamber with the gas mixture $Ar/CO_2/CF_4$ 45:15:40 and, for comparison, a 10×10 cm^2 test detector with the gas mixture Ar/CO_2 70:30. On the right, discharge probability for the gas composition Ar/CO_2. The shaded "CMS Region" spans the range of particle flux expected in CMS for HL-LHC [117].

Given the operating conditions of high gain, intense particle fluxes, and densely ionising particles the GE1/1 will be operated, the probability to produce a discharge that could damage the detector must be kept as low as possible. A discharge happens when the charges produced in the chamber exceed the Raether limit [118], for which the local electric field is amplified till the avalanche transforms into a streamer, that propagates inside the chamber and could damage the GEM electrodes and electronic equipment or provoke a electrical breakdown of the gas [119]. Several expedients have been adopted in the detector design in order to reduce the discharge probability: asymmetric distribution of charge-amplifying electric fields over the three GEM foils, division of the GEM foils in sectors, and use of protection resistors to limit the available energy in case of a discharge. First of all, the gain is not the same in the three GEM foils, but it slightly decreases from the first to the third: the gain of the first foil is 3% higher than the second, and the second is 5% higher than the third. The distribution of the total amplification on three stages and the independent read-out plane significantly reduce the discharge probability because they both lower the probability of streamer and the probability to induce a signal large enough to damage the detector and electronics. The design of a GEM chamber is also optimised to reduce discharges: the electrodes facing the drift plane are divided in sectors of 100 cm^2 and each of

them has a 10 MΩ protection resistor. In case of a discharge, the current passing through the resistor will induce a voltage drop across it, limiting the energy of a discharge and reducing its propagation. The GEM chambers are tested for the discharge rate probability by irradiating them with densely ionising α-particles from a ^{241}Am source while the gain was set to higher values (4 to 6×10^5) with respect to normal operation. Figure 3.13 (right) shows the measured discharge probability versus gain, and the measured discharge probability versus drift potential, with the CMS region indicating the operating condition expected at HL-LHC. Because an α-particle from ^{241}Am produces nearly a hundred times more primaries than a MIP, the discharge probability for a MIP must be divided by this factor. In the CMS Region this probability is less than $\sim 10^{-12}$, well within the requirements for the GE1/1 system.

3.3.3 GEM Slice test

Before the definitive version of the GEM detectors was installed, ten real size and fully equipped triple-GEM chambers were installed in the negative endcap of CMS during the Year-End Technical Stop (YETS) 2016–2017. These 10 triple-GEM chambers were arranged in 5 superchambers, called "Gemini". The convention for the location is established as follows, starting from the 3 o'clock position, position 01, the number of the superchamber are incremented by 1, each 10° moving counter-clockwise until the 36^{th} superchamber is reached. Figure 3.14 shows a schematic representation of the CMS Detector with the Gemini superchambers disposed in the position 01 and $27 - 30$ highlighted. The two triple-GEM detectors of each Gemini are identified as layer1 (L1) and layer2 (L2), layer1 being the closest one to the interaction point. The electronics of the Gemini was not the final version, in particular the VFAT version was the v2 and not the v3. There is a difference between the powering system of the Gemini $27 - 30$ and the Gemini 01. Each layer of the Gemini $27 - 30$ was powered by a single HV channel and then distributed to the detector electrodes through a ceramic divider. The Gemini 01 was powered with a multi-channel supply providing 14 HV channels (7 channels per layer) to power independently the seven electrodes of each Gemini layer. The latter is also chosen to be the final configuration for the GE1/1.

Two milestones were reached by the slice test on 9^{th} November 2017, when the Gemini took part for the first time in a cosmic run, and on 20^{th} November 2017, when they participated at a data taking run. Figure 3.15 shows an acquisition from the CMS information system in which the GEM system is active during a p-p collision run. The Gemini continued to participate at the p-p collision runs and the data collected by them were used for the reconstruction of the physics objects. Figure 3.16 shows two muons associated with hits in one of the five GE1/1 slice test super-chambers at station 1 of the endcap muon system. The muon pair had

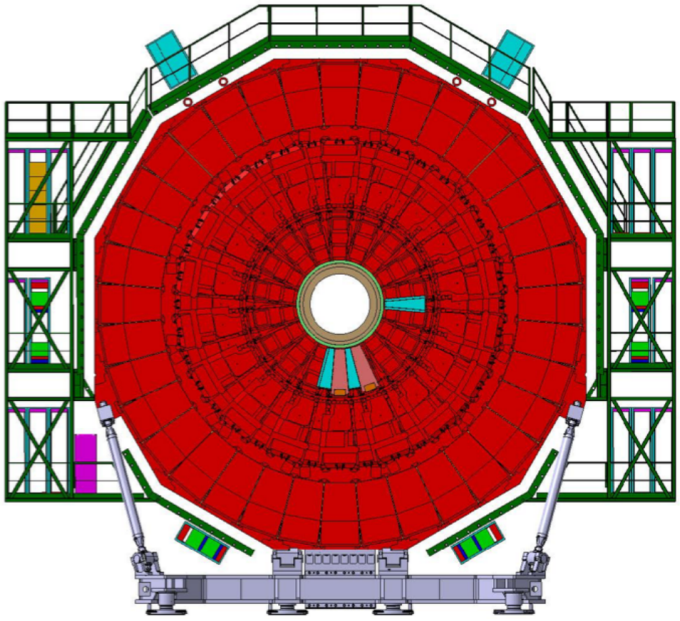

Figure 3.14: Schematic representation of the CMS Detector with the position of the Gemini superchambers highlighted. In particular azure chambers are short Gemini, while the red ones are long [120].

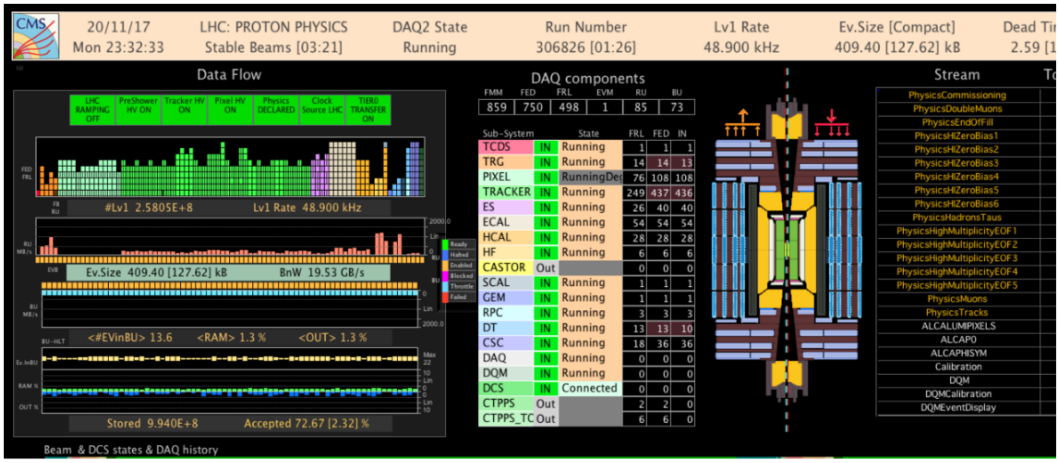

Figure 3.15: Acquisition of the CMS information system that shows the GEM system active during a p-p collision run.

$p_{\mathrm{T}} = 30.11$ GeV, $\eta = -1.956$ and $p_{\mathrm{T}} = 53.60$ GeV, $\eta = -1.993$; their combined invariant mass was of 3.01 GeV, so they came from a J/Ψ decay.

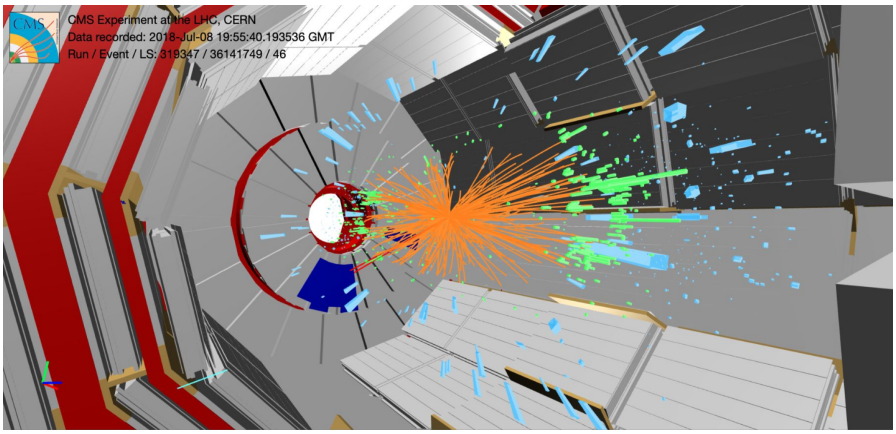

Figure 3.16: An LHC p-p collision event display in a perspective view showing two muons (the red lines), associated with hits on one of the five GE1/1 slice test superchambers (blue trapezoidal boxes) at station 1 of the endcap muon system. The antimuon ($p_{\mathrm{T}} = 30.11\,\mathrm{GeV}, \eta = -1.956$) and muon ($p_{\mathrm{T}} = 53.60\,\mathrm{GeV}, \eta = -1.993$) has a combined invariant mass of 3.01 GeV.

The data collected by the Gemini were analysed in order to test the performances of these detectors by the GEM Detector Performances Group (DPG). In the following the results of the work in the context of the GEM DPG aiming to study general behaviour of the Gemini in relation with the information coming from the first station of the CSC system will be discussed in detail. The runs 319347 and 319348 were analysed from the p-p collisions collected during the 2018 data taking by firing the "or" of all trigger paths with a single muon (the so-called SingleMuon). The investigation was focused on the behaviour of the four Gemini 27, 28, 29, and 30. The raw data collected by the Gemini are digitised and reconstructed into their physical position on the chamber, through the use of the geometrical information of the whole CMS detector. The digitised data are called Digis and the reconstructed hits are called RecHits. A clear and fast indication on the status and performances of the detectors can be inferred by the so-called occupancy plot. In the occupancy plot, the RecHits are shown in the global (x, y) coordinates of the laboratory frame. A lack of RecHits in this plane could indicate a bad functioning or a damage of the detector. In Fig. 3.17 the occupancy plot for the runs 319347 and 319348 are reported for the layer1, on the left, and for the layer2, on the right. The RecHit x coordinate in the global CMS reference frame has the value of the strip hit by the avalanche, while the y coordinate has the value of the centre of the $i\eta$ since no information is measured on that coordi-

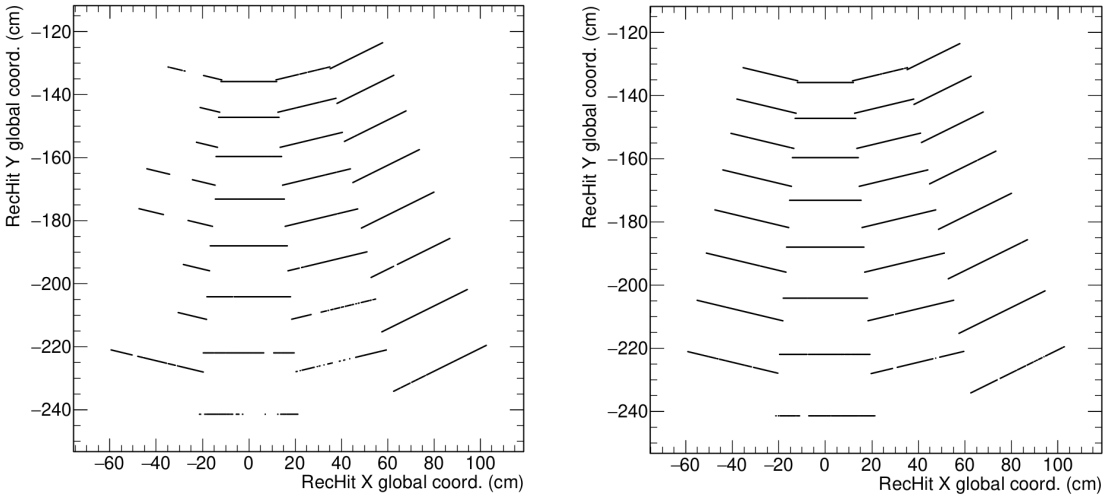

Figure 3.17: Total occupancy for the layer1, on the left, and for the layer2, on the right, for the runs 319347 and 319348 in global CMS coordinate. The layer1 of the Gemini 27, the first on the left, shows a bad functioning since there are no RecHits.

nate, therefore the value of the centre of the $i\eta$ is chosen. The occupancy plots, reported in Fig. 3.17, show that for the layer1 of the Gemini 27, the first on the left, is not working correctly since large portions of the detector did not collect any RecHits. This was due to the damage of the VFAT2 that were not properly protected by the discharge with a security resistor. This problem is now solved by the new version of the VFAT and similar problem is not expected to happen on the GE1/1 detectors. Instead the layer2 shows a good behaviour, the distribution of the RecHits is homogeneous except for some holes in Gemini 28 and 29.

An analogous study can be done by examining the RecHits in the reference frame ($i\eta$, chamber). In this case one looses the information on the single VFAT but can obtain information about the noisiness of a particular $i\eta$ of a chamber. Figure 3.17 shows the total occupancy of the layer1 and layer2 of the Gemini in the ($i\eta$, chamber) reference frame. In this case one can notice that the Gemini 29 is noisy especially in $i\eta$ 1 and 2. The noisiness can depend on multiple factors: from low thresholds on the VFAT Analogical-to-Digital Converter (ADC) to broken or damaged strips on the read-out board. The layer2 instead has a normal behaviour and from it the different flux of particles the $i\eta$ are receiving can be appreciated. The $i\eta$ 8 is the nearest to the beam axis and so it is exposed to the highest rate of particles with respect to all other $i\eta$, and this reflects on the higher number of RecHits reconstructed on that $i\eta$.

For a better characterisation of the condition of the chambers, the behaviour

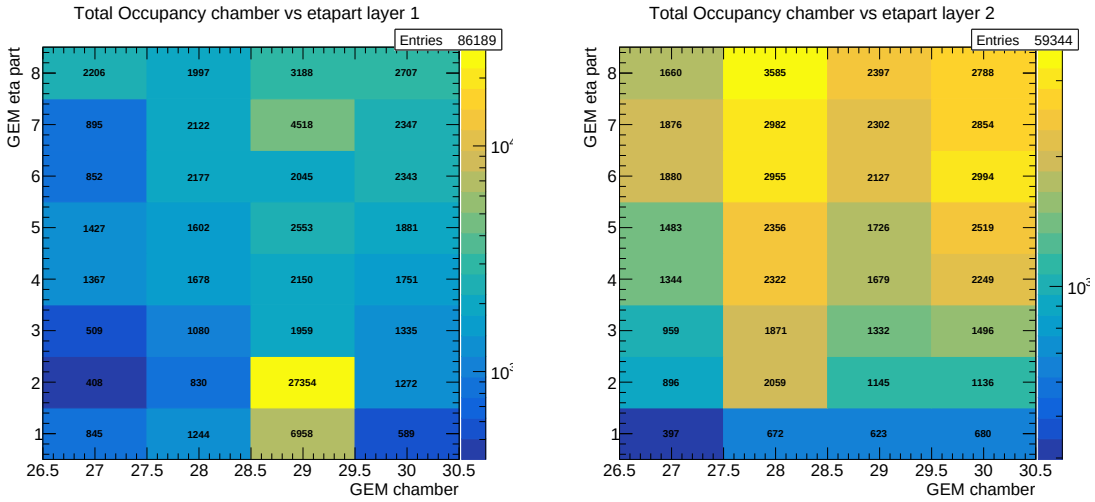

Figure 3.18: Total occupancy of the layer1 and layer2 of the Gemini in the $i\eta$, chamber reference frame for the runs 319347 and 319348. The layer1 of the Gemini 29 shows that this chamber is noisy especially the $i\eta$ 1 and 2.

of the single strips of the read out board is investigated. Each chamber has 384 strips, 128 for each VFAT, with a radial disposal and a fixed spacing of 463 μrad. Figure 3.19 shows four different behaviours inside a $i\eta$. In a perfectly working $i\eta$, a uniform number of hit on each strip is observed, as shown in Fig. 3.19a. In case in the $i\eta$ there are noisy strips, the aspect of the same distribution is more like the one reported in Fig. 3.19b. It could also happen that a strip is silent even if the VFAT is perfectly working, as shown in Fig. 3.19c. In both the last cases, the problem is caused by a damage of the single strip or a group of contiguous strips. A different behaviour that could occur is when a problem affects the entire VFAT, that could be mechanical, VFAT unplugged from its connection, or electrical, damage from discharge, and it is reported in Fig. 3.19d.

An important feature to be investigated is also the size of the avalanche on the read out board which is related to the number strips hit by a single incoming particle. This information is reconstructed as the cluster size of the RecHit. In Fig. 3.20 two typical behaviours are reported. In case the read out board of the $i\eta$ of the Gemini is correctly working, the average cluster size is around 2, but this depends also on the position of the partition $i\eta$ since for high values of the $i\eta$, so closer to the beam axis, the strips are closer to each other and the cluster size tends to be higher with respect to the ones of $i\eta$ farther away from the beam axis.

But if the read out of the $i\eta$ is damaged, the cluster size distribution will be shifted toward lower values. In particular, Fig. 3.20 (right) shows an example of an $i\eta$ with a damage. In this case, one sees that for the layer1, which presents the

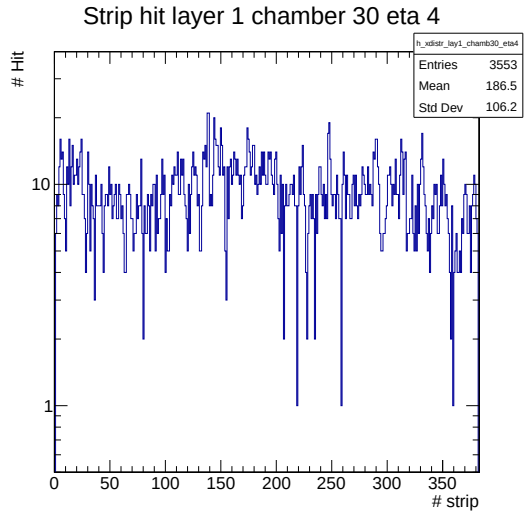

(a) Example of normal functioning $i\eta$.

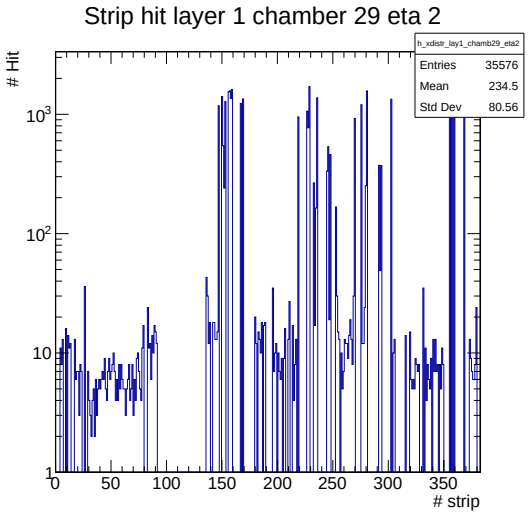

(b) Example of noisy strips $i\eta$.

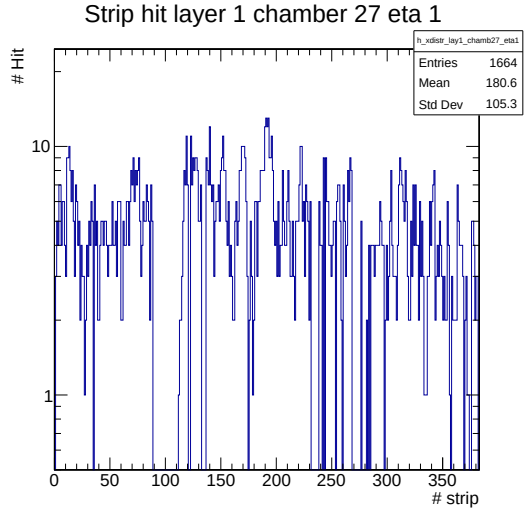

(c) Example of silent strips in a VFAT.

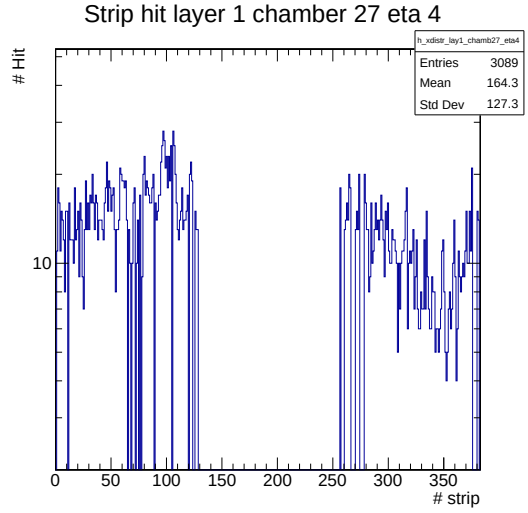

(d) Example of silent VFAT.

Figure 3.19: Examples of the four different behaviours that could happen inside a $i\eta$.

damaged strip, the cluster size is 1 in the 92% of the cases in contrast to the 50% that can be seen, for example, in layer2, that is correctly working. There can also be cases where more than one strip is damaged or noisy.

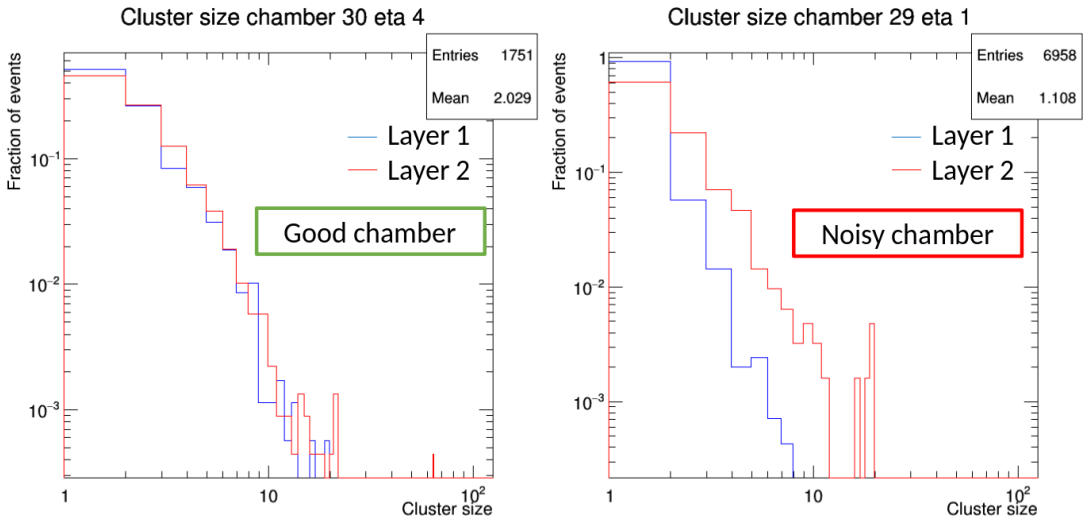

Figure 3.20: Typical behaviours for the cluster size of the Gemini: on the left, the cluster size for a correctly working $i\eta$ on both layers is reported, while on the right, the cluster size for a $i\eta$ with a broken strip on the layer1 (blue line) is reported.

Another study performed was the propagation of a CSC segment from the CSC1/1 system to the GE1/1. A CSC segment describes a reconstructed track segment in the 6 layers of a CSC chamber. It is characterised by a starting point (x_0, y_0)[1] and a direction (dx, dy, dz). The CSC segment can be propagated on each layer of the Gemini by using the following equations:

$$\begin{aligned} x &= x_0 + \frac{dx}{dz}D \\ y &= y_0 + \frac{dy}{dz}D \\ z &= D, \end{aligned} \tag{3.8}$$

where D is the z-coordinate of the layer of the Gemini chamber in the CSC local reference frame. The propagation is supposed to be linear since the distance between CSC and Gemini is short and the magnetic field is not much intense. The propagation is performed 4 four steps:

[1]The z coordinate is fixed and is given by the position of the chamber in the CMS global reference frame.

1. each Gemini is paired with the CSC segment coming from the nearby CSC that it is facing (e.g. from CSC 28 to GEM 28, lay 1-2);

2. the CSC segment is projected on the plane ($z = D$) of each GEM layer by using Eq. 3.8;

3. the propagation of the CSC segment is performed on each $i\eta$ and then is checked if the propagated RecHit is inside $i\eta$ area;

4. once the $i\eta$ has been found, a propagated RecHit (x, y, D) is defined.

The RecHit found with the propagation procedure is matched with the physical GEM RecHit having the minimum x distance from it. In ideal detector and conditions, this distance, also referred to as residual, is expected to be zero. In real cases, the detectors could be inefficient, and the expected RecHit is not found, or one can incorrectly match the propagation with spurious signals due to intrinsic noise of the detector, not associated with a physical incoming particle. The distribution of residuals (or residuals, in short) gives a measure of the spatial resolution that can be reached by the GEM detectors. In order to make a rough comparison, one should consider that each strip has 230 μrad width and the spacing from the contiguous (pitch) is 463 μrad. This distance is different for each $i\eta$ when translated in linear coordinate. Table 3.4 reports the value of the strip widths for each $i\eta$. Figure 3.21 shows the residuals for an $i\eta$ 1, on the left, and an $i\eta$ 7, on the right.

$i\eta$	1	2	3	4	5	6	7	8
Strip width (cm)	0.0933	0.0769	0.0703	0.0634	0.0567	0.0527	0.0470	0.0426

Table 3.4: Width of the strip expressed in cm.

The distribution of the residual has been fitted with a Gaussian function between -5 and 5 cm. The parameter σ of the fitted function gives an indication of the spatial resolution of the chamber. The parameters for the distributions reported in Fig. 3.21 are 0.55 cm and 0.37 cm respectively, and need to be compared with the corresponding pitches of 0.0933 cm and 0.0470 cm. It has to be kept in mind that the mean value of the cluster size is 2 and so the spatial resolution of the two analysed $i\eta$ are ~ 3 and ~ 5 strips, corresponding to $\sim 2,7$ mm. Taking into account that no selection of goodness and no p_{T} requirement have been performed on the CSC segment, these preliminary results are very promising.

The study was then carried on by the GEM Group on the full dataset collected in the 2018 p-p collision data, corresponding to 205.4 pb^{-1} for the Gemini. Well identified muons, reconstructed by non-GEM detectors, but with at least a RecHit in the GEM detectors, and with $p_{\mathrm{T}} > 20$ GeV are used for these studies. So selected

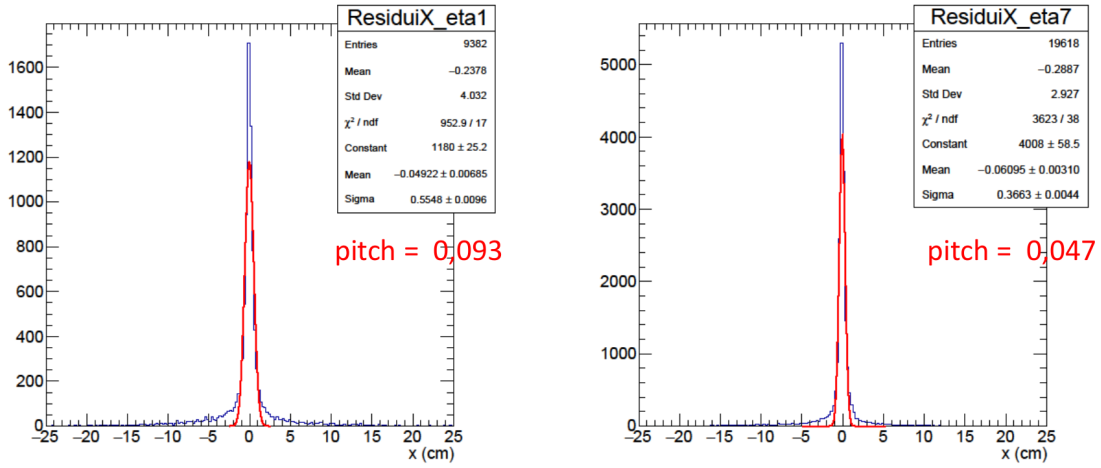

Figure 3.21: Residuals obtained as the difference between the propagated and reconstructed RecHits for an an $i\eta$ 1, on the left, and an $i\eta$ 7, on the right.

muons are propagated to the Gemini from the ME1/1 system. The propagated hit is accepted if it is far at least 20 strips from the edge of the $i\eta$ to avoid inefficiency due to the curvature of the track. The RecHit of the Gemini is considered to belong to the muon track if it is within 5 cm from the propagated hit. Under this conditions, the mean cluster size for each $i\eta$ has been studied. Figure 3.22 shows the mean cluster size for the $i\eta$ of the Gemini 28, the one that showed the best stable behaviour over the full data taking period. The mean cluster size increases at increasing values of $i\eta$, as expected. Figure 3.23 shows both the efficiency of the chamber per $i\eta$ (black marker) and the fraction of inactive strips (white marker) per $i\eta$. The measurement shows that the lowest efficiency (73%) is seen the $i\eta$ 1 and the highest efficiency (98%) in the $i\eta$ 8. In correspondence of the lowest efficiencies, there is a greater fraction, 19.0% for $i\eta$ 1 and 9.4% for $i\eta$ 2, of dead channels and this the source of the inefficiency. Despite this problem, the slice test can be considered a success because it shows, for the first time, the inclusion of the GE1/1 system in the CMS operation and the results, even if the detectors were not in their final configuration, show encouraging performances.

3.3.4 Construction and installation of GE1/1

In parallel with the slice test, the CMS Collaboration was also focused on the preparation of the full GE1/1 system. The production and quality control (QC) processes of the 144 GEM chambers, needed for the GE1/1, were fundamental steps of the upgrade. The GEM foils are entirely produced at CERN. The first two QCs, as reported in Fig. 3.24, for the inspection of the materials (QC1) and

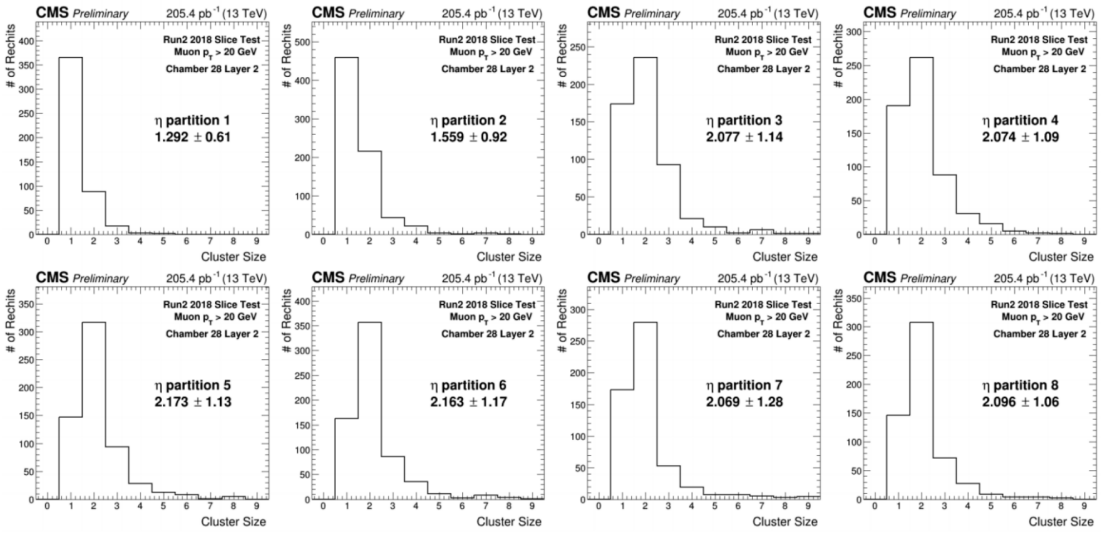

Figure 3.22: Mean cluster sizes for each $i\eta$ of the Gemini 28 layer2.

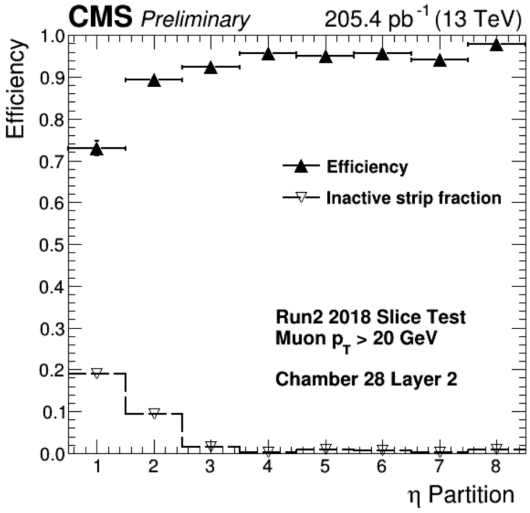

Figure 3.23: Measured efficiencies for each $i\eta$ of the Gemini 28 layer2.

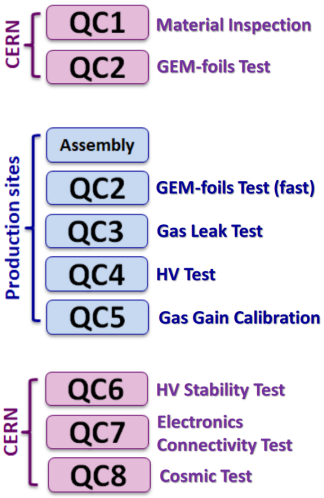

Figure 3.24: Block diagram showing the steps in the quality control for a GEM superchamber.

the test of the single GEM foils (QC2) are performed to assure to the required construction quality. After a GEM foil is validated, it is shipped to the production sites, situated in Italy (INFN Laboratori Nazionali di Frascati and INFN section of Bari), India, Belgium, Germany, Pakistan, USA and CERN. In the production sites, the GEM foils are assembled into Triple-GEM chambers in a two phases process. First of all, the components are prepared and cleaned in a clean room, as well as the HV circuits and the mounting pull out, and the O-rings are carefully chosen and checked. After that, the GEM foils are tested again, mounted on the stack and finally the chamber is closed. The entire process takes an entire workday and more details can be found in Ref. [121]. The fully assembled Triple-GEM undergoes a series of QCs to verify its integrity and performances and the typical results of these tests are reported in Figure 3.25. After a chamber is assembled, the first test it undergoes is a new HV test in order to assure the integrity of the foils. After that, the tightness of the chamber is verified, by checking the gas leak of detector by monitoring the drop of the internal over-pressure as a function of time. The test consists in filling the detector with CO_2 with an internal over-pressure of ~ 25 mbar. The acceptance limit is calculated by using:

$$P(t) = P_0 \exp(-t/\tau), \tag{3.9}$$

where P_0 is the initial internal over-pressure and parameter τ qualifies how fast the over-pressure inside the detector decreases as a function of time. The QC3 acceptance limit in terms of the gas leak time constant is $\tau \geq 3.04$ hour, which corresponds to a maximum acceptable gas leak rate of about 7 mbar/hr. Figure 3.25a shows the result of a successful QC3 test on a GEM chamber.

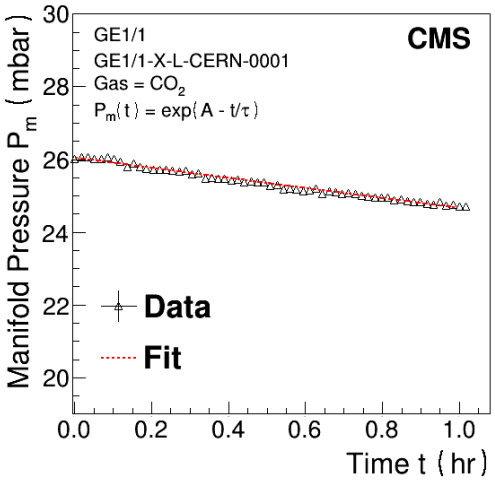

(a) Typical pressure vs time curve obtained during the GE1/1 quality control.

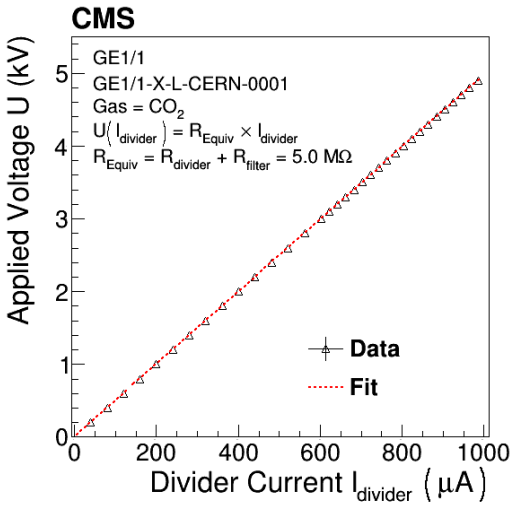

(b) Typical I(V) curve obtained during the GE1/1 quality control.

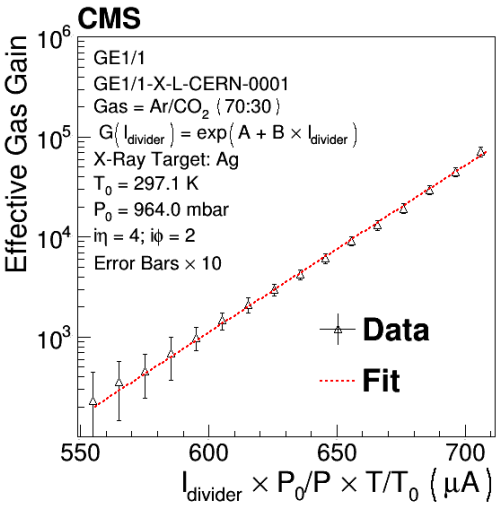

(c) Typical effective gain curve obtained during the GE1/1 quality control.

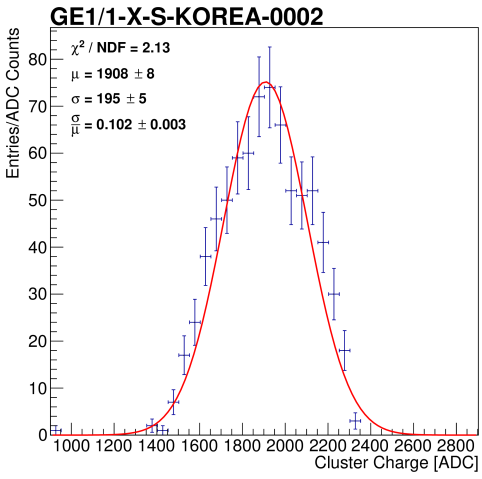

(d) Typical gas gain uniformity curve obtain during the GE1/1 quality control.

Figure 3.25: Results from quality control tests performed in the production sites to validate the assembled chambers [122].

The QC4 test is performed by applying the high voltage at the chamber filled with CO_2. The target is to study the Voltage-Current (VI) characteristic of a GE1/1 detector and to identify possible malfunctions, defects in the HV circuit and intrinsic noise rate. Initially, the detector is flushed with a continuous flow rate of CO_2 at 5 L/hr for 5 hours. The total resistance of the HV circuit is measured using a multimeter and it is used to calculate the current in the divider for every HV points. The detector is ramped up to 3000 V in the step of 200 V, and up to 4900 V in step of 100 V. For each step, the current and the intrinsic noise rate of the detector are measured. In order to be considered passed, the VI curve should be well fitted by a straight line to determine a resistance (fitted resistance), as in the case reported in Fig. 3.25b.

The QC5 effective gas gain measurement is divided into two stages: the measurement of the effective gas gain as a function of the voltage applied on the resistive high voltage divider and the measurement of the response uniformity of the detector through a dedicated readout electronics. Both tests are done in a specific radiation box containing a mini X-ray source with a silver target emitting ~ 22 keV X-ray photons. The effective gas gain G is expressed as:

$$G = \frac{I_{divider}}{R n_{e^-} e}, \tag{3.10}$$

where R is the X-ray photons interaction rate, n_{e^-} the number of primary electrons per X-ray photon, and e is the elementary electric charge. Figure 3.25c shows a typical effective gain curve obtained during the GE1/1 quality control. $I_{divider}$ is the current flowing through the HV resistive divider that provide potential to the detector electrodes. P_0 and T_0 corrections parameter are determined by averaging the temperature and pressure conditions in the P5 cavern. For the second measurement, the detector is divided in slices of 4 strips each. The detector is exposed to the X-ray photon source and, for each slice, the maximum cluster charge is stored into a charge histogram. The copper fluorescence photopeak is obtained from the charge distribution, and its mean position value of each slice is used to produce a distribution for the entire detector active area. A Gaussian function is then used to fit this distribution in order to extract the mean μ and the standard deviation σ. The Response Uniformity (R.U.) of a GE1/1 detector is defined as:

$$R.U. = \frac{\sigma}{\mu} \tag{3.11}$$

where the μ and σ parameters are the mean and standard deviation taken from a Gaussian fit of the data set of all fixed copper fluorescence peak positions from an entire GE1/1 detector. The test is considered passed if e^G, where G is the gain, as a function of $I_{divider}$ is well described by a linear function, while the second measurement is considered passed if the R.U. is $\sim 10\%$.

After a Triple-GEM is ready and validated, it is shipped to CERN, where it is equipped with the final electronics and tested again to verify that the it is fully operative and efficient. These last tests are named QC6, QC7, and QC8.

The QC6 test simply consists in verifying the stability of the foils by applying the HV to them.

In the QC7 test a GEM chamber is equipped with the electronics, GEB, Opto-Hybrid and VFAT3, and all the links, optic fibres, gas pipes, and low-voltage cables are routed in their final configuration. With the chamber in this configuration an s-curve scan is performed. The s-curve plot is one of the most representative outputs of the QC7 test. It is obtained fixing the thresholds for each of the VFATs and scanning the response of the 128 channels while increasing the amount of charge pulsed by means of an internal test pulses generator. Figure 3.26 shows the results of a s-curve scan and the x axis represents the VFAT channel number, the y axis the value of the pulsed charge in fC and the colour-scale is the number of signals over threshold. It reveals any broken, dead, or disconnected channels that might be present since the production, giving at the same time an insight on the correctness of the frontend parameters applied. The noise level of the VFATs in the QC7 working conditions can be extracted from the width of the curve and the mean represents the per-channel threshold. The s-bit threshold scan

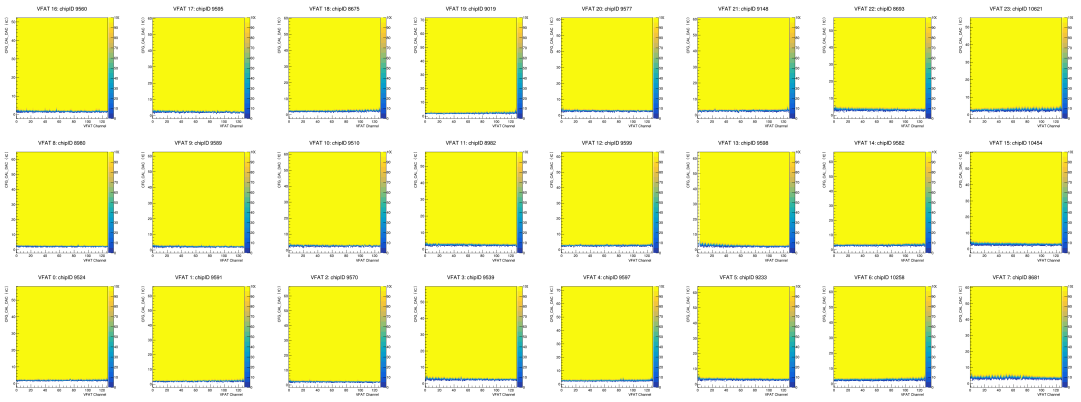

Figure 3.26: Result of a s-curve scan performed during the QC7 test [122].

plot is another representative output of the QC7 test. It is obtained by scanning the thresholds for each of the VFATs and recording the number of trigger signals given by the OR of all the 128 channels. Figure 3.27 show an example of an s-bit threshold, where the value of the VFAT register controlling the threshold is represented on the x axis, while the corresponding noise rate is in the y axis. It reveals any broken trigger lines in the VFATs or the GEB that might be present since the production, giving at the same time the noise rate for any given threshold value. The noise level accepted per VFAT determines then the value of the threshold to

be set. The test is considered passed if the all the channels are good and have

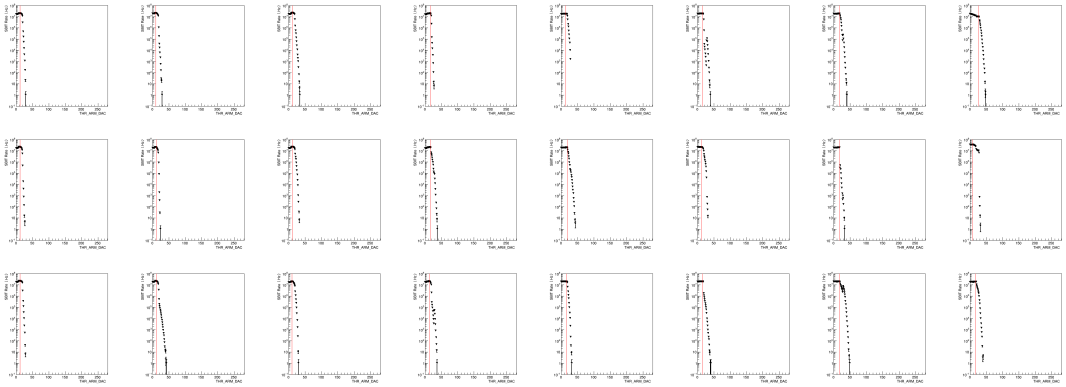

Figure 3.27: Result of a s-bit threshold scan performed during the QC7 test [122].

a low noise rate. If so, the chamber is equipped also with the cooling plate, and the s-curve scan is repeated to be sure that the electronics were not damaged by this last operation. After a chamber passes the QC7 test, it is assembled with the chimney and coupled with another one to form the definitive GEM superchamber, that is ready to undergo the QC8 test.

In the QC8, the GEM superchamber is placed in the cosmic ray stand and an s-curve scan and an s-bit threshold scans are performed as a comparison to the ones obtained in the previous test. Then a HV test is performed to ensure the integrity of the GEM foils. The last step of the QC8 is the measurement of the efficiency of the superchambers, and if passed, they are finally validated to be installed in the CMS detector. I was involved in the team who perform the QC8 test aiming at the measurement of the efficiency with the cosmic muons. The cosmic stand allows to simultaneously test 15 GEM superchambers, disposed in 3 columns with 5 superchambers each. Figure 3.28 shows a sketched view of the cosmic stand, and a picture of the same stand, respectively on the left and on the right, together with the reference frame of the cosmic stand. My main task as a member of the QC8 team was to develop the algorithm for the alignment of the superchambers in the cosmic stand. This is necessary because, even if the GEM superchambers are inserted into the stand on a sliding support, they could be misaligned with respect to other superchambers of the column. The first thing that could happen is that a chamber is shifted with respect to the column in the z plane. The only direction in which a shift implies inefficiency is the y direction. A misalignment of 1 mm in the y direction implies could lower the efficiency of $\sim 1\%$. The largest impact will be in the smallest $i\eta$, that has an area of $\sim 8 \cdot 12$ cm^2. In case of 1 mm shift, the total non covered area will be of $\sim 0.1 \cdot 12$ cm^2, in the smallest $i\eta$, for an inefficiency of $0.1/8 \sim 1\%$. A similar but smaller effect will exist also for all the other $i\eta$. The

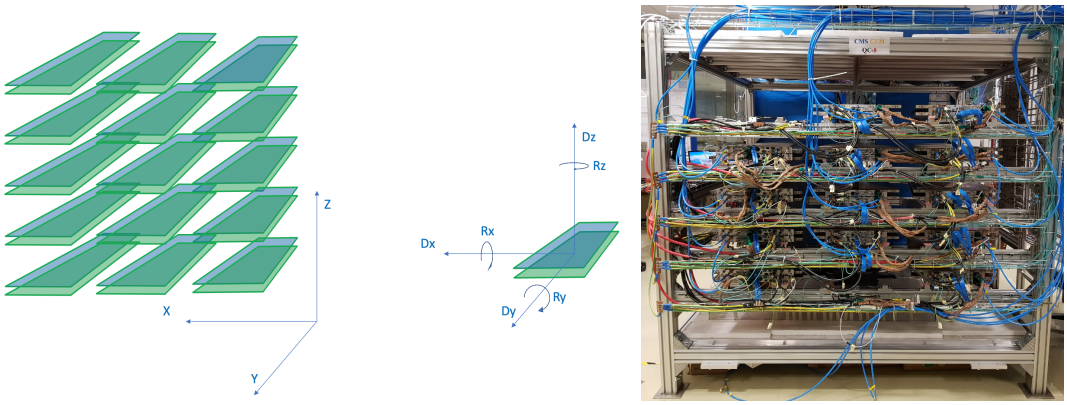

Figure 3.28: Idealised view of the cosmic ray stand with its reference frame, on the left, and a real picture of it, on the right.

shift along the other two axes are negligible, because a shift along the z direction does not have any impact on the efficiency, while a shift along the x direction would only affect the $i\eta$ 1 and 8 and the impact on efficiency is less important than the one in the y direction. Another factor that could reduce the efficiency is the rotation along the z axis. In fact, this type of rotation implies a not covered area as well as a translation in the y direction. This is also the only possible physical rotation can happen in the stand. Since the stand does not have a control system for a precise measurement of the position of the chambers to physically align the superchambers, the misalignment has to be monitored and corrected via a dedicated software, by using the tracks of the muon passing throughout the detectors. The passage of a muon in each column is triggered by two scintillators located on the top and at the bottom of each column. When a coincidence of the two scintillators happens, the event is identified as good and the data from the GEMs are collected. A seed of a track is reconstructed starting from two RecHits laying on two different chambers with a cluster size between 1 and 10. The seed is propagated to the others detectors and a reconstructed RecHit is searched for to be included in the track (iterative fit). The construction of the track goes on to all the chambers with a Kalman Filter (KF) procedure [123]. Then the best track is chosen as the one with the minimum chi squared. The residuals between the propagated and the reconstructed RecHits are stored for each $i\eta$ and for each chamber. A Gaussian fit is performed to the residuals distribution to obtain the centroids, r_i, that are used in the so-called residual correlation plot. In this plot, reported in Fig. 3.29, the centroids of the residuals are reported for each $i\eta$ and fitted with a straight line $y = mx+q$, whose parameters are the translation $Dx = q$, and the rotation $Rz = m$. The geometrical position of the superchamber is then modified, in the code, to accounts for the shift Dx and the rotation Rz. The

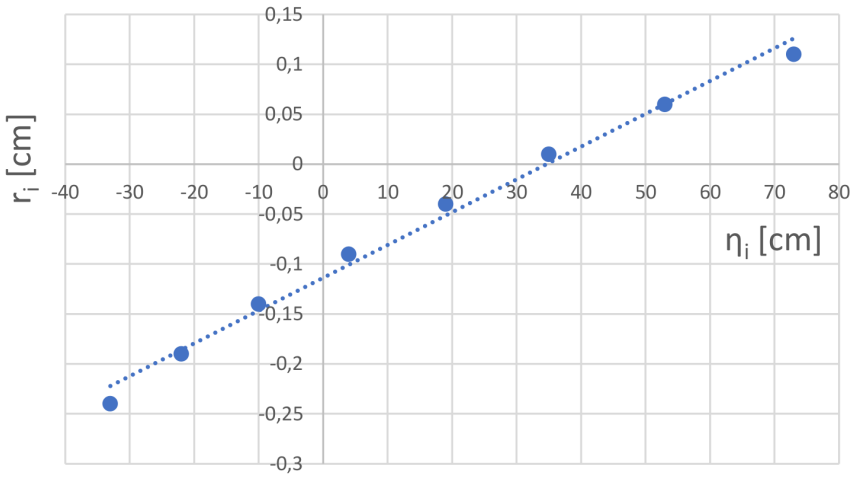

Figure 3.29: Example of the residual correlation plot: on the x-axis the position of the centre of the $i\eta$ partitions are reported while on the y-axis the centroids of the residuals are reported.

reconstruction is then repeated until $Dx < 0.03$ cm and $Rz < 0.03°$. Figure 3.30 reports a typical workflow for the alignment algorithm. Once the chambers are aligned, the efficiency can be measured. Fig. 3.31 shows the measured efficiencies for an entire row of chambers in the stand and the efficiencies for each VFAT of a full superchamber. The test is considered passed if the efficiency of each VFAT is 97%.

Up to now, all the 144 chambers needed for the GE1/1 system upgrade are ready, validated and installed in the CMS detector. Work is still ongoing for the full commissioning of the GE1/1, the development and integration of the Detector Control System (DCS) and Data Acquisition System (DAQ), which are directly connected with the hardware of the detector, and the Data Quality Monitoring (DQM), which accurately monitor the quality of data collected and the performance of the detector.

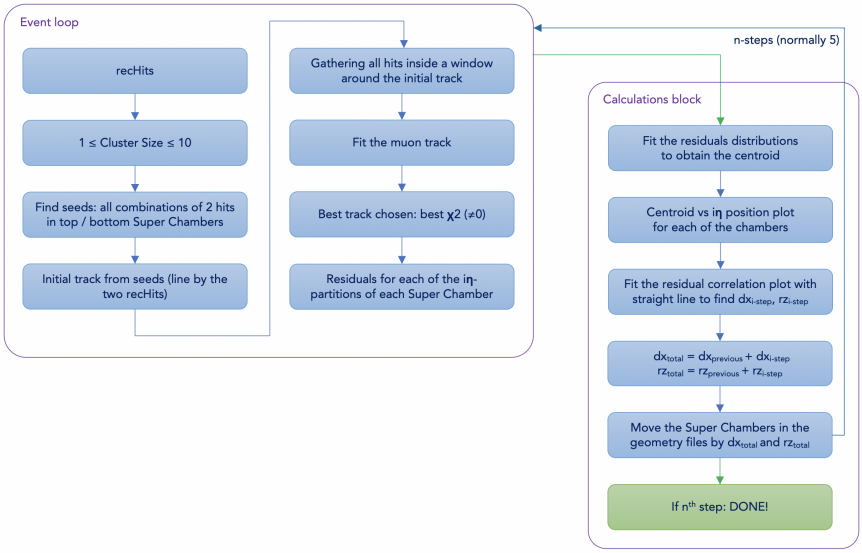

Figure 3.30: Workflow of the alignment code for the superchambers in the cosmic ray stand.

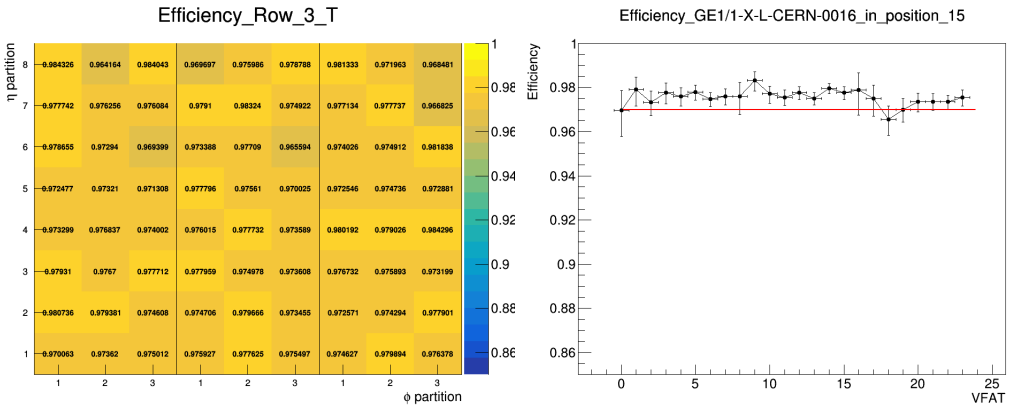

Figure 3.31: Examples of the QC8 efficiency measurements for each VFAT: for a row of chambers, on the left, and for a superchamber, on the right [122].

Chapter 4

Physics object reconstruction and classification

As described in Chapter 3, the CMS detector has a cylindrical symmetry along the beam axis, and a particle emerging from the nominal interaction point crosses different subsystems that are sensitive to its passage and can provide information on its nature and properties. The subsystems make use of different technologies, each one with specific tasks and characteristics. The reconstruction strategy leverages on the strengths of each sub-detector to get a complete and precise reconstruction of all particles: the tracker system allows to reconstruct charged-particle trajectories, interaction vertexes and, thanks to the magnetic field that bends the trajectories, the charged-particle momenta. The calorimeters instead are devoted to measuring the energy carried by the particles, the ECAL mainly absorbing electrons and photons, while the HCAL absorbing jets coming from the hadronisation of quarks, gluons, baryons and mesons. Lastly, the muon system is devoted to the measurements of the muon trajectories and momenta, since they pass through the previous systems without losing a consistent amount of energy. Neutrinos instead do not interact at all with any of the subsystems and escape undetected. A significantly improved event description can be achieved by correlating the basic elements from all detector layers (tracks and clusters) to identify each final-state particle, and by combining the corresponding measurements to reconstruct the particle properties on the basis of this identification. This holistic approach is called particle-flow (PF) reconstruction [124]. The combination of the measurements coming from the tracker, the calorimeters and the muon system allows to perform global fit to the physics objects, that can be determined with superior efficiencies and resolutions. The key ingredient so that a PF technique can be applied is a fine spacial granularity of the detector. The CMS detector is, in this sense, a good candidate since its subdetectors are sufficiently segmented to provide good separation between individual particles.

4.1 Primary vertex

The tracks are reconstructed in the inner side of the detector with a fitting procedure based on a Kalman Filter, described in Ref. [125]. The vertexes are reconstructed from those tracks with an iterative procedure as described in details in Ref. [125]. If more than one primary vertex is identified, the one with largest sum of the squared transverse momenta of associated tracks is taken as the hard-scatter vertex. Additionally the main primary vertex is required to satisfy goodness criteria: to be classified as good it must have at least 4 degrees of freedom, its distance from the nominal interaction point must be less of 2 cm in the transverse plane ($x - y$ plane) and 24 cm in the z direction.

4.2 Muons

The muons reconstruction is not PF specific since the muon spectrometer allows to identify and reconstruct muon tracks with very high efficiency over all the detector acceptance. This is mainly due to the fact that the calorimeters absorb almost all the particles except for muons and neutrinos. Three different types of muon candidates can be defined depending on how they are reconstructed:

- standalone muon: seeded by hits from DT and CSC, tracks are reconstructed only by using the muon spectrometer, gathering all the hits from all the muon subsystems through a KF procedure;
- tracker muon: tracks with $p_{\mathrm{T}} > 0.5$ GeV and a total momentum larger than 2.5 GeV are propagated to the muon system. If a match with the hits of the muon system is found, the track qualifies as a tracker muon;
- global muon: a standalone muon is matched with information of the tracker and a global fit to the resulting track is performed.

The global muons turn out to have the highest reconstruction efficiency if their momentum is above 10 GeV, i.e. when they have hits in at least two muon stations. Below this threshold, there is higher probability for muons to suffer from multiple scattering in the iron of the return yoke, so the tracker muon turns out to be the one with higher efficiency. Muons reconstructed only as stand alone ones have a contamination from cosmic muons that reach the cavern. Charged hadrons as well may be reconstructed as muons if their shower is not completely blocked in the calorimeters (punch-through). In the PF algorithm, muons are reconstructed by also exploiting information from muon energy deposit in ECAL and HCAL, further improving the identification performances. Additional quality criteria are

applied to reconstructed muon tracks in order to be used for analyses. Three main working points are defined:

- Tight;
- Medium;
- Loose.

Since in the following Tight and Loose IDs will be used, more details are given about these WPs. For the Tight WP, the muon is required to be reconstructed with the PF algorithm as a global muon and its track must be fitted with a $\chi^2/ndof < 10$. It must also have at least one muon-chamber hit included in the global-muon track fit and must cross at least two muon stations. The tracker muon associated with the global muon must have a transverse impact parameter $d_{xy} < 2$ mm and a longitudinal on $d_z < 5$ mm with respect to the primary vertex of the event to suppress cosmic muons, muons from decays in flight and tracks from PU. The track is also required to have at least one hit in the pixel detector and at least 5 hits in the total tracker system. The Loose WP, instead, only requires the muon to be reconstructed with the PF algorithm as a global muon. The requirements for the Tight and Loose WP are summarised in Table 4.1.

Table 4.1: Muon identification requirements for the Tight and Loose WP. A dash "-" indicates the requirement is not applied.

Variable	Tight muon requirement	Loose muon requirement
isGlobalMuon & isTrackerMuon	true	true
isPFMuon	true	true
$\chi^2/ndof$	< 10	-
Number of valid muon hits	> 0	-
Number of valid pixel hits	> 0	-
Number of matched stations	> 1	-
Number of tracker layers	> 5	-
$\lvert d_{xy}\rvert$	< 0.2 cm	-
$\lvert d_z\rvert$	< 0.5 cm	-

In order to select prompt leptons, both electrons and muons, produced in the decays of massive particles such as W and Z bosons, and to reject the large number of leptons produced in jets through the decay of heavy-flavour hadrons or the decay in flight of charged pions and kaons, one needs to defined the lepton isolation. The isolation is quantified by estimating the total p_{T} of the particles emitted around the direction of the lepton. The particle-based isolation relative to the lepton p_{T}

is defined as:

$$I_{PF} = \frac{1}{p_{\mathrm{T}}} \left(\sum_{h^{\pm}} p_{\mathrm{T}}^{h^{\pm}} + \sum_{\gamma} p_{\mathrm{T}}^{\gamma} + \sum_{h^0} p_{\mathrm{T}}^{h^0} \right), \tag{4.1}$$

where the sums run over the charged hadrons ($h^{\pm}$), photons (γ), and neutral hadrons (h^0) with a distance ΔR to the lepton smaller than either 0.3 or 0.4 in the (η, ϕ) plane.

To mitigate the deterioration of the isolation efficiency due to pileup, the isolation as defined in Eq. 4.1 is complemented in two ways. First, only charged hadrons associated with the hard-scatter vertex are considered. Second, the expected contributions from pileup are subtracted from the p_{T} sums of neutral hadrons and photons. the relative isolation is then defined as:

$$I_{\mathrm{rel}} = \frac{I^{\mathrm{ch.\,h}} + \max((I^{\gamma} + I^{\mathrm{n.\,h}} - I^{\mathrm{PU}}), 0)}{p_{\mathrm{T}}} , \tag{4.2}$$

where $I^{\mathrm{ch.\,h}}$, I^{γ}, and $I^{\mathrm{n.\,h}}$ are the sum of the transverse energies deposited by stable particles like charged hadrons, photons and neutral hadrons respectively, in a cone of size $\Delta R = \sqrt{(\Delta\eta)^2 + (\Delta\phi)^2} = 0.4$ around the lepton direction. In this case, the contribution from pileup in the isolation cone is removed with the so-called Delta beta correction is applied. $I^{\mathrm{PU}} \equiv \Delta\beta \sum p_T^{PU} \equiv 0.5 \sum p_T^{PU}$ is the sum of transverse momenta of tracks associated to non-leading, i.e. pileup, vertices, used to estimate the contribution of neutral particles from pileup events by applying a multiplicative factor of 0.5 that takes into account the neutral-to-charged particles ratio expected from isospin invariance. Therefore, the $\Delta\beta$ factor maps the expected neutral contribution in the isolation cone from the observed PU charged contribution.

4.3 Electrons

Electrons in the CMS detector are reconstructed by the PF algorithm by exploiting the measurements of both tracker and ECAL. The electron passing throughout the tracker is likely to emit bremsstrahlung photons, that in turn convert into electron-positron pairs. For this reason, the basic properties and the technical issues to be solved for the tracking and the energy deposition patterns of electrons and photons are similar. If the fraction of energy radiated by the electron is small, its track can be reconstructed by the tracker with a good χ^2 and propagated to the inner surface of the ECAL, where it can be matched to the closest cluster accurately. If the radiated energy is large, the same task is much more challenging and the reconstructed track could have very few hits and a large value of the χ^2 from the track fitting. A preselection based on the number of hits and the fit χ^2 is therefore applied and the selected tracks are fitted again with

a Gaussian-sum filter (GSF) [126]. The GSF fitting is more suitable to electrons than the KF used in the iterative tracking, as it allows for sudden and substantial energy losses along the trajectory. An electron track candidate is seeded by a GSF track and it is matched with a cluster in the ECAL. After the reconstruction of electrons all the tracks and clusters used are masked for the reconstruction of other objects.

Electron candidates must satisfy additional quality criteria in order to be used in physics analyses. These criteria can be established by studying some crucial variables and applying a series of requirements on them, or by using them in a boosted-decision-tree (BDT). The first approach, referred to as cut based approach, consists in applying sequential cuts on the amount of energy radiated off the GSF track, the distance between the GSF track extrapolation to the ECAL entrance and the position of the ECAL seeding cluster, the ratio between the energies gathered in HCAL and ECAL by the track-cluster association process, and the KF and GSF track χ^2 and numbers of hits. These requirements are tuned to provide four standard working points (WPs) that act as benchmarks that can be suitable for different analysis conditions:

- Veto (average efficiency $\sim 95\%$)
- Loose (average efficiency $\sim 90\%$)
- Medium (average efficiency $\sim 80\%$)
- Tight (average efficiency $\sim 70\%$),

where the veto WP is generally used in analyses requiring three or more leptons, or analyses rejecting background events with high electrons multiplicity, the loose one is used if the background rate is low, the medium WP for generic measurements involving W or Z bosons, and the tight WP for precision measurements or when the background rate is particularly high.

The relative isolation for electrons is defined as in Eq. 4.2. The contribution from pileup in the isolation cone is subtracted by assuming $I^{\mathrm{PU}} = \rho A_{eff}$, where ρ is the event-specific average pile-up energy density per unit area in the $\phi - \eta$ plane and the A_{eff} is the effective area specific to the given type of isolation.

For the second approach, instead, up to fourteen variables, including the ones of the cut based definition, are combined in BDTs trained separately in the ECAL barrel and endcaps acceptance, and for isolated and non isolated electrons. The electron BDT is trained on Drell-Yan (DY) plus jets MC samples, with prompt electrons as signal and unmatched plus non-prompt electrons as background. Reconstructed electrons from tau decays are ignored. There are 2 different multivariate analysis (MVA) electron ID versions: one with the 3 PF isolation components

as input variables (Iso), the other without (NoIso). Both MVA IDs have three categories: inner barrel ($|\eta| < 0.8$), outer barrel ($0.8 < |\eta| < 1.44$) and endcap ($1.57 < |\eta| < 2.5$)). For each region there are low-pt ($5 < p_{\mathrm{T}} < 10$ GeV) and high-pt ($p_{\mathrm{T}} > 10$ GeV) categories, for a total of 6 categories. There are three working points:

- WPLoose with a high overall efficiency (98%) for vetoing or multilepton analyses requiring high efficiency,
- WP90 with average efficiency $\sim 90\%$ in each category,
- WP80 with average efficiency $\sim 80\%$ in each category.

4.4 Photon and hadron reconstruction in PF

Once electrons, isolated photons, and muons have been reconstructed, the corresponding tracks and calorimetric clusters are removed from the PF objects collection. The remaining objects are instead used to reconstruct hadrons coming from the fragmentation of quark and gluons, and non isolated photons. Non isolated photons are reconstructed with ECAL clusters not associated to hits in the tracker, if in the tracker acceptance, or not associated to HCAL clusters for higher values of pseudorapidity. Instead HCAL deposits not associated to tracks in the tracker or ECAL clusters in the Endcaps are reconstructed as neutral hadrons. All the remaining HCAL clusters that are linked with one or more tracks in the tracker are reconstructed as charged hadrons. The energy of the hadrons is not simply the energy of the HCAL cluster but it needs to be calibrated. The calibrated energy is obtained as:

$$E_{calib} = a + b(E)f(\eta)E_{ECAL} + c(E)g(\eta)E_{HCAL}, \tag{4.3}$$

where E_{ECAL} and E_{HCAL} are the measuread energies in the calorimeters and where E and η are the true energy and pseudorapidity of the hadron. The coefficient a (in GeV) accounts for the energy losses due to the energy thresholds of the clustering algorithm and is treated as independent from E. A large sample of simulated single neutral hadrons (specifically, K^0_L) is used to determine the calibration coefficients a, b, and c, as well as the functions f and g. The barrel and endcap regions are treated separately to account for different thresholds and cell sizes. In each region, the determination of b and c is performed separately for hadrons leaving energy solely in the HCAL (in which case only c is determined) and those depositing energy in both ECAL and HCAL. The calibration is also repeated with real data from dedicated runs.

Some hadrons, by interacting with the material of the tracker, decay originating a number of charged and neutral particles from a secondary interaction vertex. This is a typical situation happening in top quark decay where the b hadrons decay in flight producing secondary vertexes that help in the reconstruction of such hadrons. In these cases, the direction of the primary particles is obtained from the vectorial sum of the momenta of the secondary charged particles, its energy is given by the sum of their energies (denoted E_{sec}), and its mass is set to the charged-pion mass. If in addition, the track associated to the primary particle allows a good measure of the four-momentum, p_{prim}, the energy of the undetected secondary particles can be estimated. The energy of the primary charged hadron is then estimated as:

$$E = E_{sec} + f(\eta, p_{prim})p_{prim}. \tag{4.4}$$

The small fraction of undetected energy $f(\eta, p_{prim})$ is obtained from the simulation of single charged-hadron events.

4.5 Jet clustering and calibration

The tracks and the calorimetric deposits are clustered in objects called jets. There are many algorithms performing the reconstruction of jets [127], but in order to avoid differences between data and MC simulation, the algorithm should be infrared and collinear safe. In the CMS detector, the jets are reconstructed starting from the PF particles with the anti-k_{T} algorithm [128] as implemented in the FastJet package [129].

Two distances are defined: d_{ij} being the distance between physics objects (particles, jet candidates) i and j and d_{iB} between object i and the beam (B). The jet clustering algorithm proceeds by looking for the smallest of the distances between d_{ij} and d_{iB}:

- if it is d_{ij} then the physics objects i and j are combined together,
- if it is d_{iB} then the object i is called jet.

The physics objects used are removed and the distances are recalculated, and the procedure repeated until no physics objects are left. The definition of the distance measures is:

$$\begin{aligned} d_{ij} &= \min(k_{ti}^{2p}, k_{tj}^{2p})\frac{\Delta_{ij}^2}{R^2}, \\ d_{iB} &= k_{ti}^{2p}, \end{aligned} \tag{4.5}$$

where $\Delta_{ij}^2 = (\eta_i - \eta_j)^2 + (\phi_i - \phi_j)^2$ and k_{ti}, η_i and ϕ_i are respectively the transverse momentum, rapidity and azimuth of particle i. For the anti-k_{T} algorithm $p = -1$.

The radius of the parameter R can vary, and in CMS the values of 0.4 and 0.8 are chosen for jet reconstruction, referring to as AK4 or narrow jets and AK8 or fat jets respectively. The pile up interactions originate other tracks and clusters that are reconstructed by the PF. After the primary vertex has been chosen, all the charged hadrons whose tracks are associated to a pile up vertex are removed from the list of particles to be used in jet reconstruction for that event. This procedure is called pileup charged-hadron subtraction and denoted as CHS [130]. Other techniques of pile up mitigation are also used as, for example, the Pile Up Per Particle Identification (PUPPI) described in Ref. [131]. Further requirements are applied to jets in order to be used in physics analyses. In particular for the AK4 CHS jets, a tight ID can be defined with an efficiency of $98 - 99\%$ in all eta regions. The details of the requirements for the tight ID are reported in Table 4.2

Requirements for jet $\lvert\eta\rvert \leq 2.7$			
Variable	Requirement in 2016	Requirement in 2017	Requirement in 2018
Neutral hadron fraction	< 0.90	< 0.90	< 0.90
Neutral EM fraction	< 0.90	< 0.90	< 0.90
Number of constituent	> 1	> 1	> 1
In addition for jet $\lvert\eta\rvert \leq 2.4$			
Charged hadron fraction	> 0	> 0	> 0 (up to $\lvert\eta\rvert = 2.6$)
Charged multiplicity	> 0	> 0	> 0 (up to $\lvert\eta\rvert = 2.6$)
Charged EM fraction	< 0.99	-	-
Requirements for jet $2.6 < \lvert\eta\rvert \leq 2.7$			
Neutral hadron fraction	-	-	< 0.90
Neutral EM fraction	-	-	< 0.99
Charged multiplicity	-	-	> 0
Requirements for jet $2.7 < \lvert\eta\rvert \leq 3.0$			
Neutral EM fraction	> 0.01	$[0.02, 0.99]$	$[0.02, 0.99]$
Neutral hadron fraction	< 0.98	-	-
Neutral multiplicity	> 2	> 2	> 2
Requirements for jet $\lvert\eta\rvert > 3.0$			
Neutral EM fraction	< 0.90	< 0.90	< 0.90
Neutral hadron fraction	-	> 0.02	> 0.02
Neutral multiplicity	> 10	> 10	> 10

Table 4.2: Requirements needed in the different years of the Run II data taking for the tight jet ID definition.

The measured energy of the jets needs a calibration in order to be related with the true energy of the particles originating the jet. A true so-called particle level jet results from the clustering (with the same clustering algorithm applied to detector jets) of all stable particles originating from the fragmenting parton, as well as of the particles from the underlying event (UE) activity. The correction is

applied as a multiplicative factor to each particle composing the jet as:

$$p_{\mathrm{T}}^{corr} = \mathcal{C} p_{\mathrm{T}}^{raw}, \tag{4.6}$$

where:

$$\mathcal{C} = \mathcal{C}_{offset}(p_{\mathrm{T}}^{raw})\mathcal{C}_{MC}(p'_{\mathrm{T}}, \eta)\mathcal{C}_{rel}(\eta)\mathcal{C}_{abs}(p''_{\mathrm{T}}). \tag{4.7}$$

The offset correction $\mathcal{C}_{offset}$ removes the extra energy due to noise and pile-up, and the MC correction $\mathcal{C}_{MC}$ removes the bulk of the non-uniformity in η and the non-linearity in p_{T}. Finally, the residual corrections $\mathcal{C}_{rel}$ and $\mathcal{C}_{abs}$ provide corrections for the relative and absolute energy scales, accounting for the small differences between data and simulation. The correction are applied in sequence and p'_{T} is the transverse momentum of the jet after applying the offset correction and p''_{T} is the p_{T} of the jet after all previous corrections. These corrections generally go under the name of Jet Energy Corrections [132] and Jet Energy Resolutions [132] or, briefly, JECs and JERs, respectively.

4.6 Missing transverse momentum

The particles that do not interact with the detector, i.e. neutrinos, are reconstructed from the momentum imbalance in the transverse plane. The PF-based $\vec{p}_{\mathrm{T}}^{\,miss}$ is the opposite of the vectorial sum of the transverse momenta of the identified PF particles

$$\vec{p}_{\mathrm{T}}^{\,miss}(raw) = -\sum_{i}^{\text{all PF}} \vec{p}_i. \tag{4.8}$$

In order to be validated to be good for physics analyses, each event is required to pass the noise filters:

- Beam halo filter: machine induced particles flying with the beam, at large radius (up to 5m) produced through beam-gas/beam-pipe interactions are occasionally detected; high energy halo muons have a non negligible probability to interact in the calorimeters producing cluster of up to several hundreds of GeV.
- HBHE and HBHEIso noise filter: the HCAL in both Barrel and Endcaps (HBHE) is known to record sporadic anomalous signals (noise) at a fixed rate independent of beam conditions, that are targeted by this filter.
- ECAL TP filter: it removes events where an ECAL dead cell trigger primitive is hit.

- Bad PF muon filter: this filter removes events where the muon is reconstructed as a PF muon but its reconstruction quality is low and it has large p_{T}, leading to artificial large missing transverse momentum.

The $\vec{p}_{\mathrm{T}}^{\,miss}$ receives corrections by propagating the vectorial difference between uncalibrated and calibrated jets to it. The correction can be expressed as

$$\vec{p}_{\mathrm{T}}^{\,miss}(corr.) = -\sum_{i}^{\text{all PF}} \vec{p}_i - \sum_{j}^{\text{all jets}} (\vec{p}_j^{\,corr} - \vec{p}_j), \tag{4.9}$$

which yields an improved $\vec{p}_{\mathrm{T}}^{\,miss}$ energy scale and resolution [133].

4.7 b jets and b tagging

A large fraction of the LHC physics program relies on the identification of jets containing the decay of a b hadron (b jets). The b jets can be discriminated from jets produced by the hadronization of light quarks and gluons based on the following characteristic properties of b hadrons:

- long lifetime: $\tau \approx 1.5$ ps, $c\tau \approx 450$ μm, $\gamma\beta c\tau \approx 1.8$ mm at 20 GeV
- large mass: ~ 5 GeV
- high track multiplicity: $\sim 4-5$
- large semileptonic branching fraction: for electrons and muons, $\sim 20\%$ each
- hard fragmentation function: a large fraction of the original b quark momentum carried by the b hadron

The CMS detector, with its excellent tracking system, robust lepton identification, and finely segmented calorimeters, is well suited to the task of identification of b jets. b tagging is a reconstruction technique that takes advantage of the above b hadron properties and assigns to each jet a likelihood that it contains a b hadron. The b tagging can be based on

- track information
- secondary vertex information
- soft lepton information
- a combination of the above

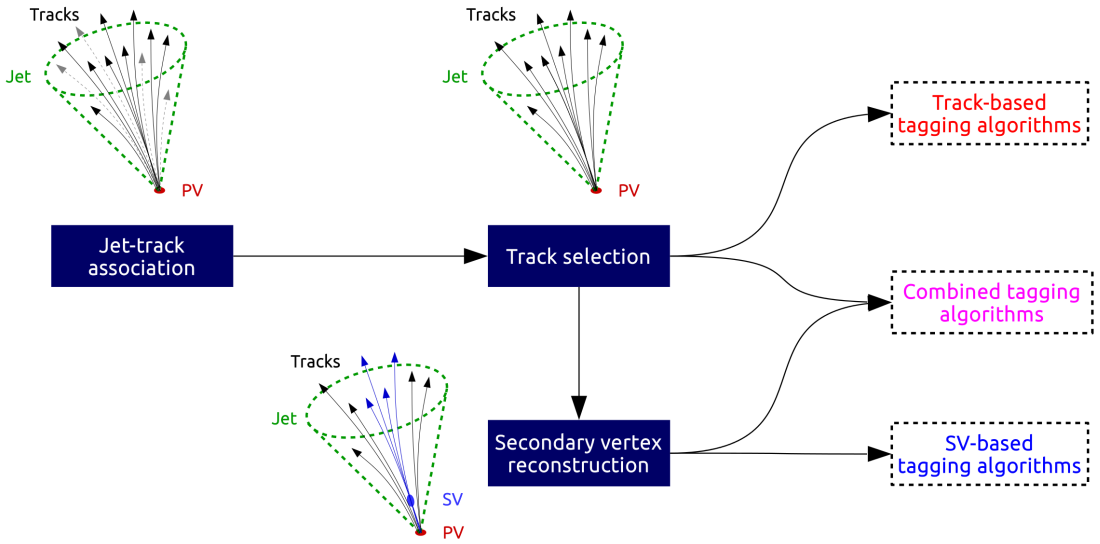

Figure 4.1: Schematic view of the workflow of b tagging algorithms in CMS.

4.7.1 b tagging in CMS

Several b-tagging algorithms of varying levels of complexity and based on different input information have been developed by CMS [134, 135]. One common feature of all these algorithms is that they produce as output a numerical discriminator and the higher the discriminator value, the more likely it is that the jet is actually a real b jet. A necessary prerequisite for b tagging is of course to reconstruct jets. The first step in the b-tagging workflow, reported in Fig. 4.1 is the jet-track association (JTA). The tracks can be associated to jets using a cone-based association, where tracks inside a certain ΔR cone from the jet axis are associated to the jet, or the so-called explicit jet-track association, where tracks linked to the charged PF jet constituents are associated to the jet. The next step is to apply some track quality criteria to the associated tracks and pass them to the track-based tagging algorithms. Such selected tracks can also be passed to a vertex reconstructor that attempts to reconstruct secondary vertices (SVs). The secondary vertices, if reconstructed, can be passed to the SV-based tagging algorithms or used together with the selected tracks in combined tagging algorithms. In addition to reconstructing secondary vertices from the tracks associated to the jet (AVR vertices), secondary vertices can also be reconstructed directly from all the tracks and then associated to jets (or used stand-alone). This second approach to the secondary vertex reconstruction uses the Inclusive Vertex Finder (IVF). The IVF vertices can be associated to jets using a cone-based or the so-called ghost association.

The following b-tagging algorithms currently exist in CMS

- Track Counting (TC) algorithms
- Jet Probability (JP) algorithms
- Simple Secondary Vertex (SSV) algorithms
- Soft Lepton (SL) algorithms
- Combined Multi Variate Algorithm (CMVA)
- Combined Secondary Vertex (CSV) algorithms
- DeepCSV algorithm
- DeepFlavour algorithm

The TC approach identifies a jet as a b jet if it contains at least N tracks each with a significance of the impact parameter exceeding some value S. The discriminator is thus the value of S for the N^{th} track, the tracks being ordered in decreasing significance. The SSV algorithm is based on the reconstruction of at least one secondary vertex. The algorithm's discriminator is a monotonic function of the three-dimensional flight distance significance. The JP algorithms combine information from all selected tracks in the jet. Lepton-based tagging algorithms identify b hadrons via their semileptonic decays. They use reconstructed electrons or muons associated with jets. Discrimination between b- and light-flavor jets can be achieved based on the p_{T} of the lepton with respect to the jet direction, the impact parameter of the lepton, or both. The CMVA tagger, instead, combines the discriminator values of various taggers to improve the identification of b jets. A more complex approach involves the use of secondary vertices, together with other lifetime information, like the IP significance or decay lengths. By using these additional variables, the CSV algorithm provides discrimination even when no secondary vertices are found, so the maximum possible b-tagging efficiency is not limited by the secondary vertex reconstruction efficiency. In many cases, tracks with an IP significance greater than 2 can be combined in a so-called pseudo vertex, allowing for the computation of a subset of secondary vertex based quantities even without an actual vertex fit. When even this is not possible, a no vertex category reverts simply to track based variables similarly to the JP algorithm. The list of variables used is:

- the vertex category (real, pseudo, or no vertex);
- 2D flight distance significance;

- vertex mass;
- number of tracks at the vertex;
- ratio of the energy carried by tracks at the vertex with respect to all tracks in the jet;
- the pseudo-rapidity of the tracks at the vertex with respect to the jet axis;
- 2D IP significance of the first track that raises the invariant mass above the charm threshold of 1.5 GeV when subsequently summing up tracks ordered by decreasing IP significance;
- 3D signed IP significances for all tracks in the jet.

These variables are used as input to a Likelihood Ratio, used twice to discriminate between b and c jets and between b and light-flavor jets, and then combined additively with a factor of 0.75 and 0.25, respectively. A "version 2" of the CSV algorithm (CSVv2) was introduced which in addition uses

- number of tracks in the jet,
- ΔR between the secondary vertex flight direction and the jet axis,
- number of secondary vertices,

and feeds them as input to an Artificial Neural Network.

The DeepCSV approach starts from the same jet features as CSVv2, but extends the range of the maximum considered tracks per jets and exploits a more modern deep neural network architecture.

The DeepFlavour algorithm [136] extends the concept of DeepCSV further increasing the number of tracks considered in each jet (up to 25), and includes, for the first time, neutral candidates as well. The algorithm does not apply any track selection and uses directly the PF jet constituents as clustered by the jet algorithm, sorted with decreasing IP significance, distance from secondary vertex, and transverse momentum. The algorithm uses a deep neural network architecture with a set of convolutional layers to learn a compressed representation for the input charged and neutral particles and secondary vertices, separately, followed by three recurrent layers that summarise the input from each set of candidates. Such compressed information is passed to a series of fully connected layers that finally provide the a-posteriori probability for the jet to contain one B-hadron, multiple B-hadrons, at least one C-hadron, being originated from a light quark or a gluon.

4.7.2 Operating points

The jet is tagged if the discriminator value is above some threshold value, often referred to as the cut value, and the efficiency for a given flavour is defined as the number of jets of that flavour which have a discriminator value that is above that cut divided by the total number of jets of the same flavor. Various algorithms for b tagging developed by the CMS experiment can identify b jets with a typical efficiency between 40% and 85% while keeping the rate of mis-identified light-flavor jets between 0.1% and 10%.

Some standard official operating points are defined for the b-tagging algorithms. These points define cuts in the discriminators and are based on the level of mis-tagging light-flavor (udsg) jets in $t\bar{t}$ events:

Tagger name	WP	WP Discr cut	Mistagging rate	b tagging efficiency
cMVAv2	loose	-0.5884	$\sim 10\%$	84
	medium	0.4432	$\sim 1\%$	66
	tight	0.9432	$\sim 0.1\%$	46
DeepCSV	loose	0.1241	$\sim 10\%$	84
	medium	0.4184	$\sim 1\%$	68
	tight	0.7527	$\sim 0.1\%$	50
DeepJet (DeepFlavour)	loose	0.0494	$\sim 10\%$	94
	medium	0.2770	$\sim 1\%$	83
	tight	0.7264	$\sim 0.1\%$	67

Table 4.3: The table reports the three working points with their relative discriminator values and mis-tagging rates for the CMVAv2, DeepCSV and DeepFlavour algorithms.

A comparison of the b tagging efficiency and the misidentification as light jet between different algorithm used in CMS is reported in Fig. 4.2.

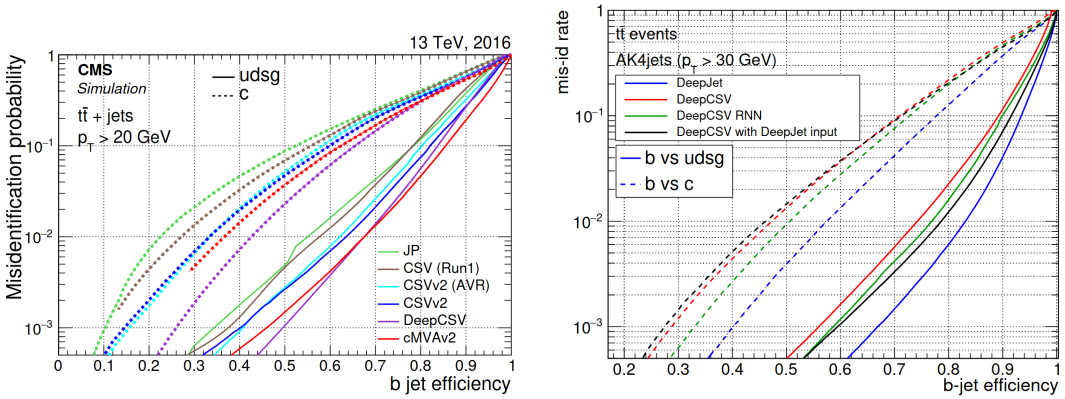

Figure 4.2: Misidentification probability for c and light-flavour jets versus b jet identification efficiency for various b tagging algorithms, on the left, and for DeepJet compared to DeepCSV, on the right, applied to jets in $t\bar{t}$ events [135, 136].

Chapter 5

Precision measurement of the tWq vertex

A distinctive feature of the electroweak sector of top quark physics is the relative magnitude of the CKM [137] matrix element V_{tb} with respect to V_{td} and V_{ts}, which leads to a strong suppression of processes involving mixing between the third and the first two quark families. A precise determination of the magnitude of these parameters allows to search for hints of potential contributions from new phenomena beyond the SM. This feature can be probed at the CERN LHC by studying the couplings of top quarks to d, s, and b quarks in electroweak charged-current interactions, where such couplings play a role at either the production or decay vertices of the top quark.

5.1 The t-channel processes

The dominant electroweak production mechanism for single top quarks is the t-channel, as described in detail in Sec. 1.6.1. In the most general case, $t-$channel production features a tWq vertex, where q stands for b, s, or d quarks both in production and in the decay of the top quark. For this reason its cross section and branching fractions are sensitive to the strength of the electroweak coupling, making it a suitable channel for direct measurements of the magnitude of CKM matrix elements $|V_{\mathrm{tb}}|$, $|V_{\mathrm{ts}}|$, and $|V_{\mathrm{td}}|$. All previous measurements quoted in Sec. 1.6.2 do only study in detail the case where q is a b quark. Figure 5.1 shows typical Feynman diagrams at leading order (LO) for the different production and decay modes involving V_{td}, V_{ts}, or V_{tb}, either in the production or the decay vertex of the top quark. Processes where no tWb vertex is present are possible, but their cross section is very small and their signature is experimentally much more challenging due to the absence of a b jet.

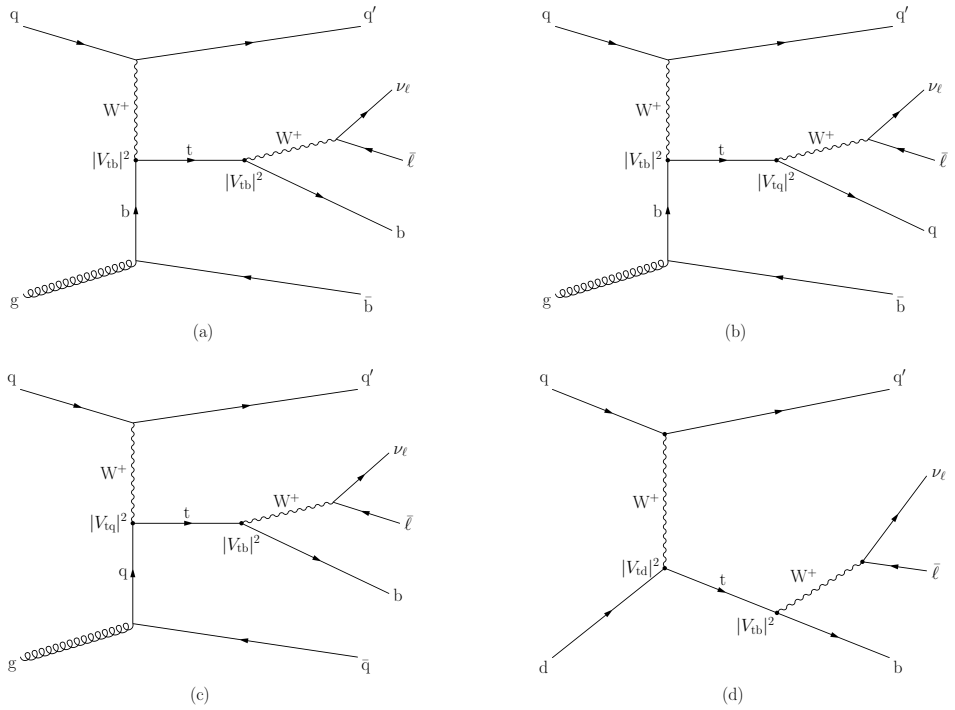

Figure 5.1: Leading-order Feynman diagrams for single top quark production via the $t-$channel featuring: (a) a tWb vertex in production and decay, (b) a tWb vertex in production and a tWq in decay, with q being an s or d quark, (c) a tWq vertex in production and a tWb in decay, and (d) a process initiated by a d quark and enhanced due to contributions from these valence quarks. The ℓ refers to e or μ leptons.

The signatures for $t-$channel processes involving V_{tb}, V_{td}, and V_{ts} either in production or decay differ in three aspects: the number of reconstructed b-tagged jets, the features of the jet involved in the reconstruction of the correct top quark candidate, and the kinematic features of the events as a result of different PDF contributions to production modes involving a b, s, or d quark. Henceforth, the $t-$channel process involving V_{tb} in both production and decay will be referred to as $ST_{\mathrm{b,b}}$, while $t-$channel processes involving V_{tb} in only production or decay will be referred to as $ST_{\mathrm{b,q}}$ and $ST_{\mathrm{q,b}}$, respectively.

There are three contributions to the inclusive single top quark $t-$channel cross section:

$$\begin{aligned}\sigma_{t-\mathrm{channel}} &= \sigma_{t-\mathrm{ch.,b}} + \sigma_{t-\mathrm{ch.,d}} + \sigma_{t-\mathrm{ch.,s}} = \\ &= \alpha|V_{\mathrm{tb}}|^2 + \beta|V_{\mathrm{td}}|^2 + \gamma|V_{\mathrm{ts}}|^2, \end{aligned} \tag{5.1}$$

where the term $|V_{\mathrm{tq}}|^2$, with q in this case standing for b, s, or d, is factored out

from the cross section. The values of the quantities in Eq. 5.1 are reported in Table 5.1.

Vertex	tWb	tWd	tWs
$\lvert V_{\mathrm{tq}}\rvert$	$0.999119^{+0.000024}_{-0.000012}$	$0.008575^{+0.000076}_{-0.000098}$	$0.04108^{+0.00030}_{-0.00057}$
$\lvert V_{\mathrm{tq}}\rvert^2$	$0.998239^{+0.000048}_{-0.000024}$	$0.000074^{+0.000013}_{-0.000017}$	$0.0016876^{+0.0000025}_{-0.0000047}$
$\sigma_{t-\mathrm{ch.,q}}$	217.0 ± 5.8 pb	1046 ± 10 pb	498 ± 10 pb

Table 5.1: Values of matrix elements inferred from low energy regime measurements [18], with the respective values of top quark decay branching fractions in the first two rows. Cross sections for inclusive $t-$channel production in the third row, obtained with POWHEG 2.0 when the respective $|V_{\mathrm{tq}}|$ is put equals to unity.

When the top quark decay modes are considered, the cross section is multiplied by the branching fraction BR(t $\to$ Wq) that can be evaluated[1] as:

$$\mathrm{BR}(\mathrm{t} \to \mathrm{Wq}) = \frac{|V_{\mathrm{tq}}|^2}{|V_{\mathrm{td}}|^2 + |V_{\mathrm{ts}}|^2 + |V_{\mathrm{tb}}|^2}. \tag{5.2}$$

All the previous approaches, as described in Sec. 1.6, consider $|V_{\mathrm{tb}}| \gg |\mathrm{V_{td,s}}|$ and neglect the latter terms. This assumption stems from the indirect determinations of V_{td} and V_{ts} from independent lower energy measurements. However, this assumption ignores any BSM modifications to the magnitude of V_{td} and V_{ts} happening in production, and does introduce biases in measurements of $|V_{\mathrm{tb}}|$. A measurement of the CKM elements V_{tb}, V_{td}, and V_{ts} can be performed considering all contributions in the $t-$channel production and decay.

The scenario with unitarity preserved

Within the SM scenario, the branching ratio can be written as in equation 5.2. If one considers also any other model in which other decays of the top quark can occur, then the same quantity could be written as:

$$\mathrm{BR}(\mathrm{t} \to \mathrm{Wq}) = \frac{|V_{\mathrm{tq}}|^2}{|V_{\mathrm{td}}|^2 + |V_{\mathrm{ts}}|^2 + |V_{\mathrm{tb}}|^2 + |V_{\mathrm{tX}}|^2}, \tag{5.3}$$

with X being any other final state. If the top quark decays only to quarks, with enhanced couplings by BSM scenarios, or if for any other reason the denominator

[1] This is an approximation neglecting all non-W decays of top quarks and the difference in mass between b, s, and d quarks.

is still equals to 1, one can use the same formulas as in the SM case. With such assumptions one obtains:

$$\begin{aligned}\sigma_{t-\text{channel}} \times \text{BR}(\text{t} \to \text{Wq}) \cong \alpha|V_{\text{tb}}|^2|V_{\text{tb}}|^2 + \\ + \alpha|V_{\text{tb}}|^2\left(|V_{\text{td}}|^2 + |V_{\text{ts}}|^2\right) + \\ + \beta|V_{\text{td}}|^2|V_{\text{tb}}|^2 \\ + \gamma|V_{\text{ts}}|^2|V_{\text{tb}}|^2,\end{aligned} \tag{5.4}$$

where the $|V_{\text{tq}}|^2\ |V_{\text{tq}}|^2$, with q=d, s, contributions were neglected in this approximation. By summing together non standard production and decay, one obtains:

$$\begin{aligned}\sigma_{t-\text{ch.}} \times \text{BR}(\text{t} \to \text{Wq}) \cong \alpha|V_{\text{tb}}|^2|V_{\text{tb}}|^2 + \\ + \alpha|V_{\text{tb}}|^2\left(|V_{\text{td}}|^2 + \frac{\beta}{\alpha}|V_{\text{td}}|^2 + |V_{\text{ts}}|^2 + \frac{\gamma}{\alpha}|V_{\text{ts}}|^2\right)\end{aligned} \tag{5.5}$$

By fixing the ratios $\frac{\beta}{\alpha}$ and $\frac{\gamma}{\alpha}$ to the SM prediction:

$$\begin{aligned}\sigma_{t-\text{ch.}} \times \text{BR}(\text{t} \to \text{Wq}) &\cong \alpha|V_{\text{tb}}|^2|V_{\text{tb}}|^2 + \alpha|V_{\text{tb}}|^2\left(7.64 \cdot |V_{\text{td}}|^2 + 3.3 \cdot |V_{\text{ts}}|^2\right) = \\ &= \alpha|V_{\text{tb}}|^2|V_{\text{tb}}|^2 + 3.3 \cdot \alpha|V_{\text{tb}}|^2\left(2.29 \cdot |V_{\text{td}}|^2 + |V_{\text{ts}}|^2\right)\end{aligned} \tag{5.6}$$

and this leads to:

$$\begin{aligned}\sigma_{t-\text{ch.}} \times \text{BR}(\text{t} \to \text{Wq}) &\cong \alpha|V_{\text{tb}}|^2|V_{\text{tb}}|^2 + \alpha|V_{\text{tb}}|^2\left(7.64 \cdot |V_{\text{td}}|^2 + 3.3 \cdot |V_{\text{ts}}|^2\right) = \\ &= \alpha|V_{\text{tb}}|^2|V_{\text{tb}}|^2 + 3.3 \cdot \alpha|V_{\text{tb}}|^2\left(|V_{\text{td}}|^2 + |V_{\text{ts}}|^2\right).\end{aligned} \tag{5.7}$$

This approximation allows to account for simultaneous variations of V_{ts} and V_{td} due to new physics and it is valid under the assumption:

$$\begin{aligned}3.3 \cdot \alpha|V_{\text{tb}}|^2\left(2.29|V_{\text{td}}|^2 + |V_{\text{ts}}|^2\right) = 3.3 \cdot \alpha|V_{\text{tb}}|^2\left(|V_{\text{td}}|^2 + |V_{\text{ts}}|^2\right) + \\ + \mathcal{O}(3.3 \cdot \alpha|V_{\text{tb}}|^2 \cdot 1.29|V_{\text{td}}|^2),\end{aligned} \tag{5.8}$$

since the ratio $\frac{|V_{\text{td}}|^2}{|V_{\text{ts}}|^2}$ is well known from low energy measurements and it is around 4×10^{-2}. This approximation is still valid as long as the ratio $\frac{|V_{\text{td}}|^2}{|V_{\text{ts}}|^2}$ is left unaltered by any new physics contribution.

Non-unitarity scenarios

In case other decays of the top quark could occur, the unitarity relation $|V_{\text{tb}}|^2 + |V_{\text{td}}|^2 + |V_{\text{ts}}|^2 = 1$ would be broken. In this case, by following the same steps of the previous lines, the computation leads to:

$$\begin{aligned}\sigma_{t-\text{ch.}} \times \text{BR}(\text{t} \to \text{Wq}) \approxeq \alpha|V_{\text{tb}}|^2 \frac{|V_{\text{tb}}|^2}{|V_{\text{tb}}|^2 + |V_{\text{td}}|^2 + |V_{\text{ts}}|^2} + \\ + \alpha \frac{|V_{\text{tb}}|^2}{|V_{\text{tb}}|^2 + |V_{\text{td}}|^2 + |V_{\text{ts}}|^2} \left(7.64 \cdot |V_{\text{td}}|^2 + 3.3 \cdot |V_{\text{ts}}|^2\right) = \\ = \alpha|V_{\text{tb}}|^2 \frac{|V_{\text{tb}}|^2}{|V_{\text{tb}}|^2 + |V_{\text{td}}|^2 + |V_{\text{ts}}|^2} + \\ + 3.3 \cdot \alpha \frac{|V_{\text{tb}}|^2}{|V_{\text{tb}}|^2 + |V_{\text{td}}|^2 + |V_{\text{ts}}|^2} \left(|V_{\text{td}}|^2 + |V_{\text{ts}}|^2\right).\end{aligned} \tag{5.9}$$

5.2 Analysis of CMS data

The analysis uses proton-proton collision data from the LHC, collected during 2016 by the CMS experiment, at a centre-of-mass energy of 13 TeV, corresponding to an integrated luminosity of 35.9 fb^{-1}, and collected with triggers requiring either one muon or electron in the final state. The data samples used for this analysis are reported in Table 5.2.

Dataset	Run	Integrated luminosity (fb^{-1})
SingleMuon(SingleElectron)	2016 B	5.8
SingleMuon(SingleElectron)	2016 C	2.6
SingleMuon(SingleElectron)	2016 D	4.2
SingleMuon(SingleElectron)	2016 E	4.0
SingleMuon(SingleElectron)	2016 F	3.1
SingleMuon(SingleElectron)	2016 G	7.5
SingleMuon(SingleElectron)	2016 H	8.6

Table 5.2: Proton-proton collision data at $\sqrt{s} = 13$ TeV collected by the CMS experiment during 2016.

5.3 Physics objects and triggers

The processes in study, whose Feynman diagrams are reported in Fig. 5.1, foresee the presence of 2 or 3 jets, 1 or 2 of them being identified as b jets, 1 electron or 1 muon, and missing transverse energy in the final state. Events are selected is if a primary vertex is reconstructed and the noise filters are passed as reported in Sec. 4.6.

5.3.1 Trigger

For the muon channel, events are selected if they pass the `HLT_IsoMu24` or the `HLT_IsoTkMu24` paths where the presence of an isolated online muon candidate with $p_{\mathrm{T}} > 24$ GeV is required. For the electron channel, events need to pass the trigger path `HLT_Ele32_eta2p1_WPTight_Gsf_vX`, where the electron is restricted to have $p_{\mathrm{T}} > 32$ GeV and $|\eta| < 2.1$. In both cases, corrections are applied to the MC samples to take into account differences in trigger response between MC simulations and Data.

5.3.2 Electrons

Events containing exactly one tight electron candidate with $E_{\mathrm{T}} > 35$ GeV, $|\eta| < 2.1$ while excluding the ECAL barrel-endcap transition region of $1.44 < |\eta| < 1.57$ are selected for the analysis. Additional quality criteria are applied based on nine variables through an optimised cut-based approach. To avoid contamination from electrons coming from jets, the selected electron is required to have a relative isolation $I^{\mathrm{e}}_{\mathrm{rel}} < 0.0588$ in the barrel and $I^{\mathrm{e}}_{\mathrm{rel}} < 0.0571$ in the endcaps. The difference in the relative isolation between barrel and endcaps is due to the greater jets rate in the latter. Corrections are applied to the MC to account for differences in reconstruction, isolation and WP definition between MC and data.

5.3.3 Muons

Events with exactly one tight muon within a pseudorapidity range of $|\eta| < 2.4$ and with a transverse momentum $p_{\mathrm{T}} > 26$ GeV are selected. Additionally, in order to select only prompt muons not coming from flight decay of particles in jets, they are required to be isolated. The relative isolation of the muon, I^{μ}_{rel}, is defined as in Eq. 4.1, and $I^{\mu}_{\mathrm{rel}} < 0.06$ is required. Corrections are applied to muons to take into account differences between MC and data due to the reconstruction and isolation algorithm and WP efficiency.

5.3.4 Veto on additional leptons

Events containing additional muons or electrons besides either one tight muon or electron candidate are vetoed. This reduces the contamination by $\mathrm{Z} + \mathrm{jets}$ and dileptonic $\mathrm{t\bar{t}}$ background events. The selection requirements for these additional leptons are loosened with respect to the tight criteria.

Veto muons are required to fall within $|\eta| < 2.4$ while having $p_{\mathrm{T}} > 10$ GeV and being reconstructed as loose muons together with a relative isolation of $I^{\mu}_{\mathrm{rel}} < 0.2$. Veto electron candidates have to pass a cut-based quality selection similar to the

tight electron selection whereas the kinematic requirements are $E_{\mathrm{T}} > 15\,\mathrm{GeV}$, $|\eta| < 2.5$. The selection chain for electron identification used for such electrons is tuned to have a higher efficiency, thus resulting in a tighter cut on the veto. The present analysis then makes use of the cut-based "electron veto" working point yielding an efficiency of $\sim 98\%$ at a plateau which is reached around $E_{\mathrm{T}} > 45$ GeV.

5.3.5 Jets

Jets are clustered from PF candidate using the anti-k_t clustering algorithm [128] with a cone size of $R = 0.4$. The influence of pileup is mitigated using the charged hadron subtraction technique (CHS) [130] in which PF candidates not associated to the primary vertex are ignored in the clustering. A potential overlap of jets with a selected tight muon or electron is omitted by ignoring jets which are closer than $\Delta R = 0.4$ with respect to tight muon or electron candidate.

The resulting jets have the standard multi-level JECs applied determined from simulation on both data and simulation. For data residual corrections derived from data themselves are further applied. Additionally the JER is corrected in simulation to match the one observed in data by smearing the jet energy using dedicated scale factors. The analysis considers jets within $|\eta| < 4.7$ whose calibrated transverse energy is greater than 40 GeV.

5.3.6 b-jets

For this study, the CMVAv2 algorithm is used at the tight working point corresponding to a threshold set to 0.9432 and a 0.1% gdus mistag efficiency, estimated based on simulated jets with $p_{\mathrm{T}} > 60\,\mathrm{GeV}$.

In order to correct the whole b-tagging CMVAv2 discriminant distribution in MC to match that in data a reweighting method is applied. The goal of this method is to predict correct b-tagging discriminant distributions as well as event yields in data by only changing the weight of selected MC events, i.e., MC events that did not pass the selection do not need to be added back. It is important to point out that with this method there is no migration of events from one b-tag multiplicity bin to an other, as each event gets a weight based on jet scale factors. In general, the jet scale factors depend on p_{T}, η and the b-tagging discriminant D. The b-tag event weight ω is obtained by

$$\omega = \prod_{i}^{N_{\mathrm{jets}}} SF(D_i, p_{Ti}, \eta_i), \tag{5.10}$$

which takes into account all selected jets.

Object	Requirements	Counts μ	Counts e
Tight muon	$p_{\mathrm{T}} > 26$ GeV $\quad \lvert\eta\rvert < 2.4 \quad I^{\mu}_{\mathrm{rel}} < 0.06$	1	0
Loose muon	$p_{\mathrm{T}} > 10$ GeV $\quad \lvert\eta\rvert < 2.4 \quad I^{\mu}_{\mathrm{rel}} < 0.2$	0	0
Tight electron	$E_{\mathrm{T}} > 35$ GeV $\quad \lvert\eta\rvert < 2.1 \quad I^{\mathrm{e}}_{\mathrm{rel}} < 0.0588$ (B) $\quad I^{\mathrm{e}}_{\mathrm{rel}} < 0.0571$ (E)	0	1
Loose electron	$E_{\mathrm{T}} > 15$ GeV $\quad \lvert\eta\rvert < 2.5 \quad I^{\mathrm{e}}_{\mathrm{rel}} < 0.2$	0	0
Jet	$E_{\mathrm{T}} > 40$ GeV $\quad \lvert\eta\rvert < 4.7$	2(3)	
b-Jet	$E_{\mathrm{T}} > 40$ GeV $\quad \lvert\eta\rvert < 2.4 \quad$ CMVAv2 ≥ 0.9432	1(2)	

Table 5.3: Summary of all the physics objects defined, their corresponding selection requirements, and the number of candidate required for the muon and electron channels.

For the b-tag efficiency correction, the b-tagging discriminant re-shape using event weights is applied, as reported in Ref. [135]. Continuous scale factors are calculated as a function of the b-tagging discriminant D in different jet p_{T} and η bins in independent regions:

- Heavy flavor (HF): $t\bar{t}$ enriched region, dilepton, exactly two jets
- Light flavor (LF): Z+jets enriched region, dilepton, exactly two jets

In the HF (LF) region, one jet is required to be (anti-) tagged. Per lepton channel (ee, $e\mu$, $\mu\mu$), the expected yield in MC is normalized to data in order to only correct the shape. Then, per (p_{T}, η) bin, MC is normalized again to data and histograms of the probe jet b-tagging discriminant D are created. Contaminations from udsb (b) and c jets, as determined in MC, are subtracted from data, which is then divided by the MC distribution of b (udsg) probe jets,

$$\mathrm{HF} : SF(D, p_T, \eta) = \frac{\mathrm{DATA} - \mathrm{MC}_{udsg+c}}{\mathrm{MC}_b}$$

$$\mathrm{LF} : SF(D, p_T, \eta) = \frac{\mathrm{DATA} - \mathrm{MC}_{b+c}}{\mathrm{MC}_{udsg}}$$

All the physics objects and their selection requirements are summarised in Table 5.3.

5.4 Background description

The most important backgrounds mimicking the $t-$channel final states are:

- $t\bar{t}$: processes where a $t\bar{t}$ quark pair is produced are the dominant background. In particular events where one t quark decays leptonically, namely through the chain $t \to Wb \to b\ell\nu$, and the other top quark decays hadronically, namely through the chain $t \to Wb \to bq\bar{q}$, have several features in common with signal events due to the presence of a real leptonic top decay. Such events are also called semi-leptonic $t\bar{t}$ events in jargon. Also events with two leptonic top decay could be a background in one of the two leptons do not pass the selection required. The $t\bar{t}$ jet multiplicity is in general higher than for the $t-$channel, and this reduces the contamination from this background.

- W + jets: processes where a W boson is produced in association to jets are an important source of background. In particular, processes where the W boson decays through $W \to \ell\nu$ and are produced in association to a c quark or $b\bar{b}$ or $c\bar{c}$ quark pair could be misidentified as signal events. Also events where W boson is associated to light partons (u, d, s quarks and gluons), can mimic signal events, in case one of the jets stemming from a light parton mimics the behaviour of a b jet.

- Multi-jet QCD: events where a well-isolated muon or electron is present and the jet-environment reproduces the signal topology in hard QCD scatterings are very rare, nevertheless, due to the much higher cross section of such multi-jet QCD processes, the contribution of such events to the background is not negligible. In this case the variable $m_{\mathrm{T}}^{\mathrm{W}}$ is very powerful in discriminating this type of contamination.

- s- and tW channels: the other single top quark processes, in particular the tW-channel, produce a non-negligible contamination in the signal region. Such backgrounds, like the $t\bar{t}$ background, share with the $t-$channel the decay chain of the top quark.

- VV, Z+jets: diboson processes like WW, WZ, and ZZ, or Z+jets processes are also minor sources of backgrounds which can reproduce in some cases the $t-$channel topology. However either the low cross section for VV processes (with V = W or Z), or the extremely narrow phase space for Z+jets processes passing the cuts, consistently limit the contamination from such processes.

- Other possible SM backgrounds (multi-boson production, multi-top production, SM Higgs) have a much smaller cross section than the $t-$channel, and in general their contribution is limited to very rare topologies. They are therefore considered negligible.

5.5 Simulated samples

Monte Carlo (MC) event generators are used to simulate signal and background samples. Single-top quark $t-$channel events are generated at next-to-leading-order (NLO) in quantum chromodynamics (QCD) with POWHEG 2.0[138–140]. The four-flavour scheme [141] is used for events with the V_{tb} vertex in production, while the five-flavour scheme [142] is used for events with one V_{td} or V_{ts} vertex in production. Top quark decays are simulated with MadSpin [81]. The $t\bar{t}$ background process [143], as well as double vector boson production [144, 145] (VV, where V stands for either a W or a Z boson), are generated with POWHEG 2.0. Associated top quark and W boson production are simulated with POWHEG in the five-flavour scheme [146]. Single top quark s-channel events (t, s-ch) are simulated with MadGraph5_MC@NLO 2.2.2 [78] at NLO. The value of the top quark mass used in the simulated samples is 172.5 GeV. For all samples PYTHIA 8.180 [147] with the tune CUETP8M1 [148] is used to simulate the parton shower, quark hadronisation, and underlying event, except for $t\bar{t}$, where the tune CUETPM2T4 is used [149]. Simulated event samples with W and Z bosons in association with jets (W + jets, Z+jets) are generated using MadGraph5_MC@NLO 2.2.2. For these processes, events with up to two additional partons emitted in the hard scattering are simulated, and the FxFx merging scheme [150] is used to avoid double counting with parton emissions generated in the parton showering. Simulated QCD multijet events, generated at LO with PYTHIA 8.180, are used to validate the estimation of this background with a technique based on control samples in data.
The default parametrisation of the PDFs used in all simulations is NNPDF3.0 [151] at LO or NLO QCD, with the order matching that of the matrix element calculation. All generated events undergo a full simulation of the detector response according to the model of the CMS detector within GEANT4 [152]. Additional p-p interactions within the same or nearby bunch crossings (pileup) are included in the simulation with the same distribution as observed in data. Except for the QCD multijet process, which is determined from a fit to data, all simulated samples are normalised to the expected cross sections. Table 5.4 summarises the details of the simulations for the samples used in the analysis.

5.5.1 Data-MC corrections

In order to take into account several experimental effects in the reconstruction of physics objects and global event properties, simulation needs to be corrected to better describe the data. Many of these corrections are derived centrally by the CMS collaboration, and the procedure is not described here in detail. At this category belongs scale factors for muon and electron ID and isolation, pile-

Process	Matrix Element	Jet Matching Method	Parton Shower	Tune	Cross Section × BR (pb)
pp→t$\bar{\text{b}}$	POWHEG-MadSpin	-	PYTHIA	CUETP8M1	136.02 (NLO)
pp→ $\bar{\text{t}}$b	POWHEG-MadSpin	-	PYTHIA	CUETP8M1	80.95 (NLO)
pp→tW	POWHEG	-	PYTHIA	CUETP8M1	35.6 (NLO)
pp→ $\bar{\text{t}}$W	POWHEG	-	PYTHIA	CUETP8M1	35.6 (NLO)
pp→tb→ $\ell\nu$bb (s-ch.)	MC@NLO	-	PYTHIA	CUETP8M1	10.32 (NLO)
pp→t$\bar{\text{t}}$	POWHEG	-	PYTHIA	CUETP8M2T4	831.8 (NLO)
pp→W	MC@NLO	FxFx	PYTHIA	CUETP8M1	49670.0 (NLO)
pp→Wq	MC@NLO	FxFx	PYTHIA	CUETP8M1	8264.0 (NLO)
pp→Wqq	MC@NLO	FxFx	PYTHIA	CUETP8M1	2628.0 (NLO)
pp→ $\ell\ell$	MC@NLO	FxFx	PYTHIA	CUETP8M1	5765.4 (NLO)
pp→WW→ $\ell\nu$qq	MC@NLO-MadSpin	FxFx	PYTHIA	CUETP8M1	45.85 (NLO)
pp→WW→ $\ell\nu\ell\nu$	MC@NLO-MadSpin	FxFx	PYTHIA	CUETP8M1	12.178 (NLO)
pp→WZ→ $\ell\nu$qq	MC@NLO-MadSpin	FxFx	PYTHIA	CUETP8M1	10.71 (NLO)
pp→WZ→ $\ell\nu\ell\nu$	MC@NLO-MadSpin	FxFx	PYTHIA	CUETP8M1	5.595 (NLO)
pp→ZZ→ $\ell\nu\ell\nu$	MC@NLO-MadSpin	FxFx	PYTHIA	CUETP8M1	3.22 (NLO)
pp→t$\bar{\text{b}}$	POWHEG-MadSpin	-	PYTHIA	CUETP8M1	0.231 (s) − 0.136 (d)
pp→ $\bar{\text{t}}$b	POWHEG-MadSpin	-	PYTHIA	CUETP8M1	0.025 (s) − 0.008 (d)
pp→t$\bar{\text{s}}$/$\bar{\text{d}}$	POWHEG-MadSpin	-	PYTHIA	CUETP8M1	0.2720
pp→ $\bar{\text{t}}$s/d	POWHEG-MadSpin	-	PYTHIA	CUETP8M1	0.1619

Table 5.4: Nominal simulation data sets with prompt leptons for the analysis of 2016 data. If not stated otherwise, the cross section obtained from the generator is used.

up reweighting, b-tagged or mis-tagged corrections, and JECs and JERs. Others corrections are specifically derived for this analysis and they are described in the following.

Trigger efficiency measurement

Muon

Muon efficiencies are calculated using the official Tag and Probe tool which utilises the known resonances, e.g. J/ψ, Z, to measure object efficiencies. In the tag-probe method, "tagged" muon is required to pass a very tight selection where as the "probe" muon is required to pass a loose selection as compared to the tagged muon. The "tag-and-probe" pair is selected such that the invariant mass of tag-and-probe falls within the selected mass resonance window. The efficiency ($\epsilon = N_{passing}/N_{passing+failing}$) in-turn for the data and MC is extracted by fitting the resonance peak. The data to MC simulation scale factors (SF) are than derived as SFs $=\epsilon^{Data}/\epsilon^{MC}$. The Muon efficiencies are extracted using the full 2016 dataset and for the MC simulation Drell-Yan process, generated with MadGraph5_MC@NLO.

Muon isolation efficiencies for the tight (loose) working points 0.06 (0.15) are extracted for the Run-BCDEF, GH and are shown in Fig. 5.2.

The efficiency of `HLT_IsoMu24 or HLT_IsoTkMu24` is measured, such that the tagged muon is required to pass the tight identification on top of isolation criterion and matched with HLT muon objects. The probe muons are required to match

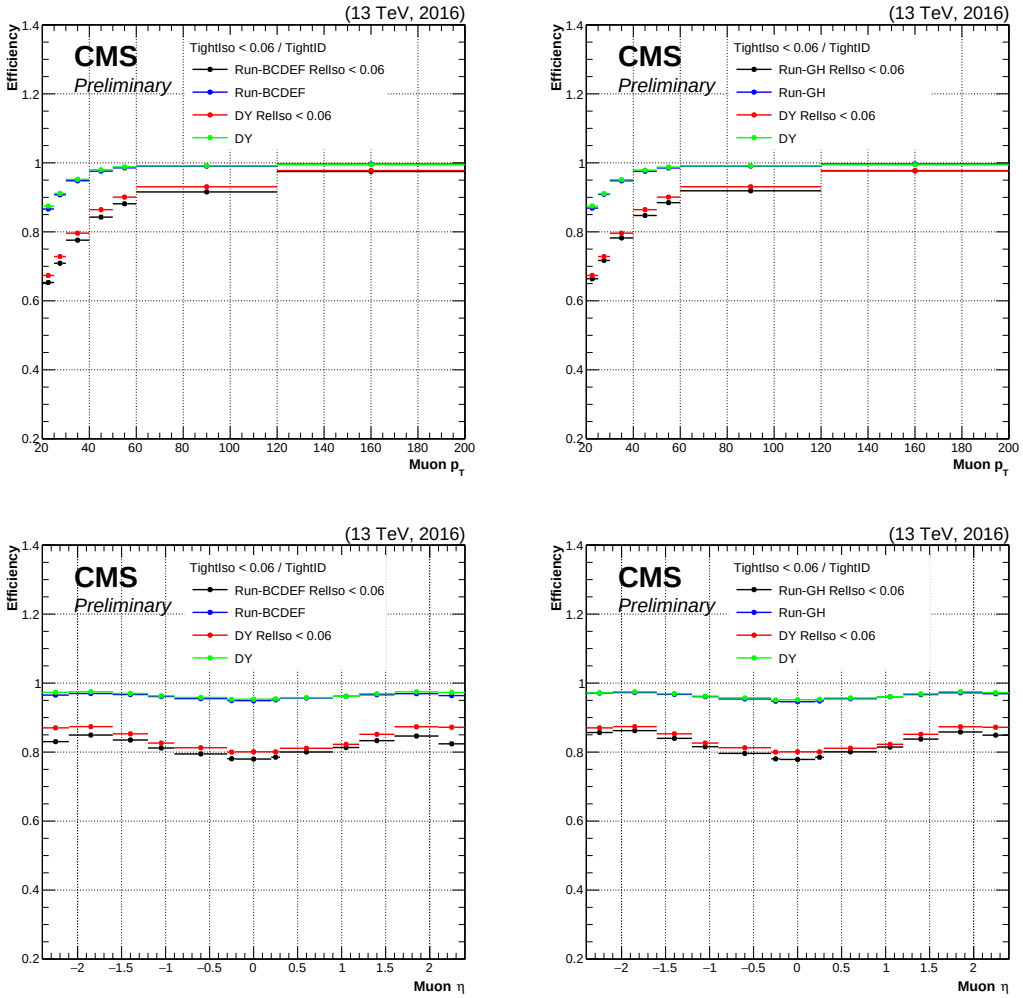

Figure 5.2: Muon tight isolation efficiency in bins of p_{T} and η for Run-BCDEF and Run-GH for $I^{\mathrm{rel}} < 0.06$ super imposed with Tight ID efficiency with $I^{\mathrm{rel}} < 0.15$ from Muon POG.

with trigger bits. Figure 5.3 shows the muon trigger efficiency in the bins of p_{T} and η for the data and MC simulations, the muon trigger efficiency with loose working point (0.15) are super imposed for a comparison.

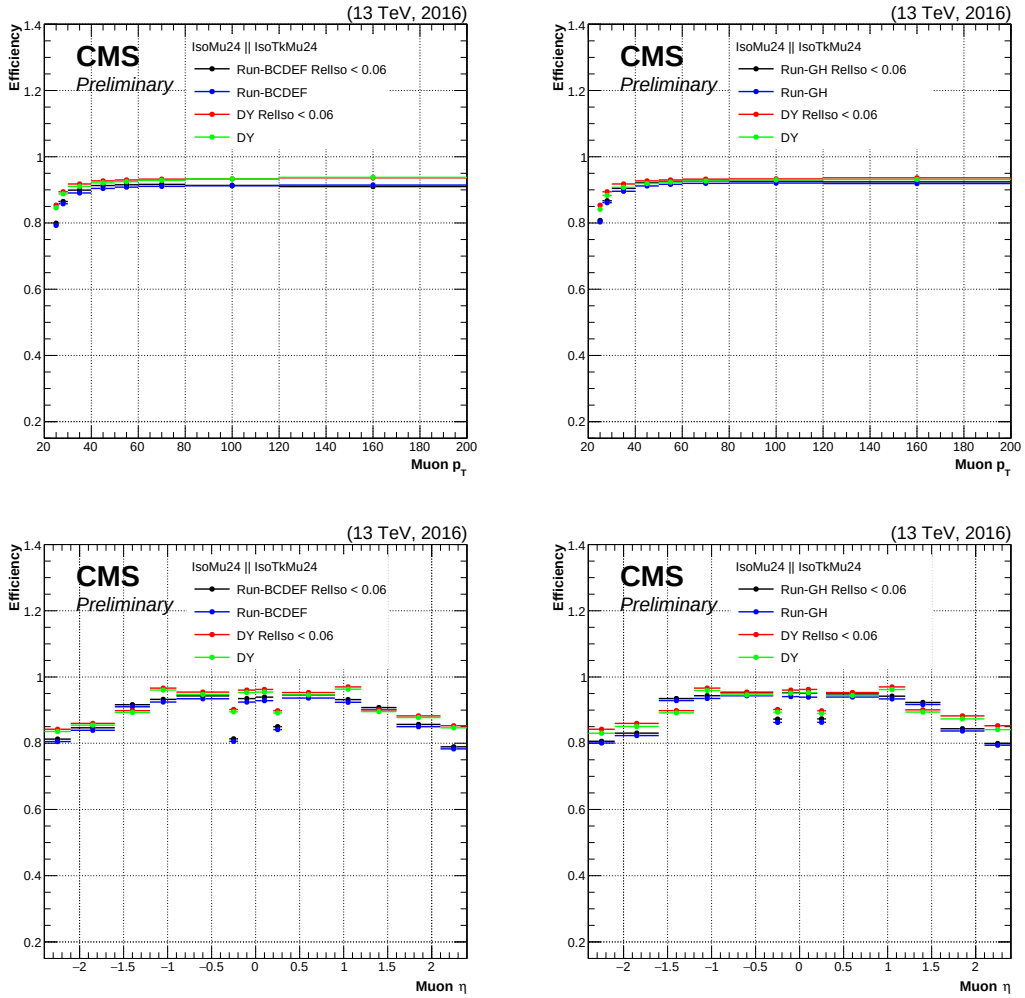

Figure 5.3: Muon trigger efficiency in bins of p_{T} and η for Run-BCDEF and Run-GH for $I^{\mathrm{rel}} < 0.06$ superposed with trigger efficiency with $I^{\mathrm{rel}} < 0.15$ from Muon POG.

Electron

Electron trigger efficiencies and scale factors for the HLT `HLT_Ele32_eta2p1_WPTight_Gsf` were calculated using the official Tag and Probe

tool. The efficiency to select events with electrons having an HLT match was estimated using a well known resonance decaying in the dileptonic channel, i.e. the decay of a Z boson to two oppositely charged electrons. The invariant mass of the dilepton-pair is restricted to be between $60 < m_{e^+e^-} < 120$ GeV. Splitting the probes into collections, where one contains electrons with an HLT match, i.e. the "passing probes", and one containing electrons without an HLT match, i.e. the "failing probes", allows to estimate the efficiency by dividing the amount of passing probes to the total number of probes:

$$\varepsilon = \frac{N_{\text{passing}}}{N_{\text{passing}} + N_{\text{failing}}}. \tag{5.11}$$

The SFs were hence calculated by dividing the efficiency estimated in data to the efficiency estimated in simulation:

$$SF = \frac{\varepsilon_{\text{Data}}}{\varepsilon_{\text{MC}}}. \tag{5.12}$$

Because of the tight cut-based ID applied for both tags and probes, the contamination with background is negligible, hence simply allowing the SFs to be measured using a cut-and-count approach.

At the end of data taking in 2016 most of the Level-1-Trigger (L1T) seeds were prescaled. This evolution of L1T prescales leads to a bias in the efficiency measurement. The lowest-p_{T} unprescaled L1T that was enabled during the whole year is `L1_SingleIsoEG34er`. To perform an unbiased calculation, in addition to the HLT match, a `L1_SingleIsoEG34er` match for the tag was demanded. The L1T match was applied by looping over all L1T objects with $E_{\text{T}} > 34$ GeV, $|\eta| < 2.131$ and l1t::EGamma::hwIso() ≥ 1 around the tag in a cone of size $\Delta R = 0.3$. If multiple L1T objects were found, the one with the highest E_{T} was chosen and if no object was found, the tag and probe pair was rejected. In order to be on the plateau of this trigger, the transverse momentum of the tag was set to be greater than 40 GeV.

Figure 5.4 shows both efficiencies for data and MC and the corresponding distribution of the SF in dependence of the transverse momentum of the probe restricted to values between $25 < p_{\text{T}} < 200$ GeV and using the full probe-eta range. A large turn-on behaviour of the HLT under study is observed, reaching the plateau of the trigger at high p_{T} values. Since only electrons with $p_{\text{T}} > 35$ GeV are being considered in the analysis, the corresponding SFs are very close to one.

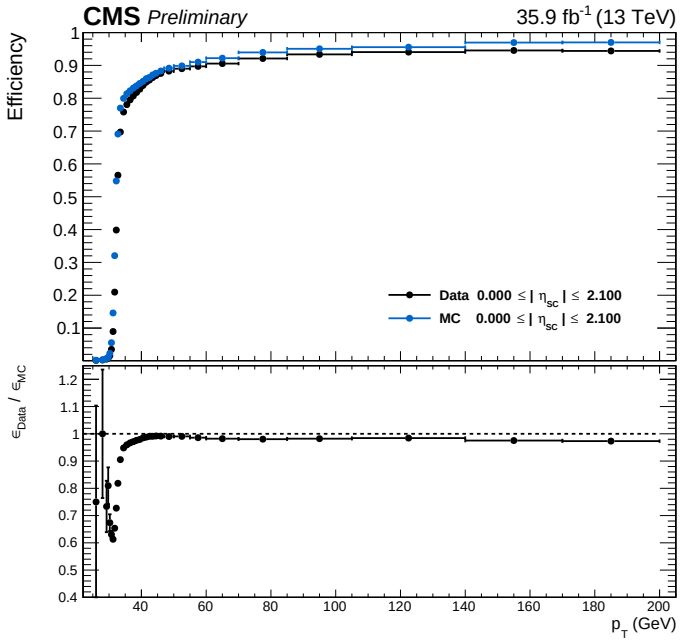

Figure 5.4: Distribution of the efficiencies in data and MC and the corresponding SF in dependence of the transverse momentum of the probe using the full probe-eta range.

5.6 Top quark reconstruction

In order to analyse the kinematics of singly produced top quarks, the four-vector of the top quarks have to be reconstructed from the decay products. All top quark decay products are reconstructed in the detector, except for the neutrino which escapes unobserved. While the transverse momentum of the neutrino can be inferred from the missing transverse energy, its longitudinal momentum has to be derived based on extra assumptions. Once the leptonically decaying W boson is reconstructed the selected jets have to be assigned to the final state quarks in the top quark decay chain.

5.6.1 W boson reconstruction

The first step in the reconstruction of the top quark from its decay products is the reconstruction of the W boson. We assume that the x and y components of the missing transverse energy are entirely due to the escaping neutrino, and apply the W boson mass constraint in order to extract the unknown z component $p_{z,\nu}$:

$$m_{\mathrm{W}}^2 = \left(E_\ell + \sqrt{p_{\mathrm{T}}^{miss\,2} + p_{z,\nu}^2}\right)^2 - \left(\vec{p}_{\mathrm{T},\ell}^{\,2} + p_{\mathrm{T}}^{miss\,2}\right)^2 - \left(p_{z,\ell}^2 + p_{z,\nu}^2\right)^2. \tag{5.13}$$

Here, p_{T}^{miss} is defined as the magnitude of $\vec{p}_{\mathrm{T}}^{\,miss}$, which is the negative of the vectorial $\vec{p_{\mathrm{T}}}$ sum of all the PF particles. The m_{W}^2 is the W boson mass, E_ℓ, $p_{\mathrm{T},\ell}$, and $p_{z,\ell}$ are the energy, the transverse and longitudinal lepton momentum components, respectively, while the same quantities with the subscript ν refers to the neutrino components. When the lepton mass is neglected, this equation has the following two solutions:

$$p_{z,\nu} = \frac{\Lambda \cdot p_{z,\ell}}{p_{\mathrm{T},\ell}^2} \pm \sqrt{\frac{\Lambda^2 \cdot p_{z,\ell}^2}{p_{\mathrm{T},\ell}^4} - \frac{E_\ell^2 \cdot p_{\mathrm{T}}^{miss\,2} - \Lambda^2}{p_{\mathrm{T},\ell}^2}}, \tag{5.14}$$

where:

$$\Lambda = \frac{m_{\mathrm{W}}^2}{2} + \vec{p}_{\mathrm{T},\ell} \cdot \vec{p}_{\mathrm{T}}^{\,miss}. \tag{5.15}$$

In most of the cases, this leads to two real solutions for $p_{z,\nu}$ and the solution with the smallest absolute value is chosen. For some events the discriminant in Eq. 5.14 becomes negative leading to complex solutions for $p_{z,\nu}$. In this case, the imaginary component is eliminated by modification of $p_{x,\nu}$ and $p_{y,\nu}$ so that $m_{\mathrm{T}}^{\mathrm{W}} = m_{\mathrm{W}}$, while still respecting the m_{W} constraint. Here $m_{\mathrm{T}}^{\mathrm{W}}$ stands for the mass of the W boson in the transverse plane. This is achieved by imposing that the determinant, and thus the square-root term in Eq. 5.14, are null. This condition gives a quadratic relation between $p_{x,\nu}$ and $p_{y,\nu}$ with two possible solutions, and one remaining degree

of freedom. The solution is chosen by finding the neutrino transverse momentum $\vec{p}_{\mathrm{T},\nu}$ that has the minimum vectorial distance from the in the $p_x^{miss} - p_y^{miss}$ plane. Top quark candidates are reconstructed by selecting one of the jets to accompany the W boson decay. Multiple top quark candidates can be reconstructed, in the different regions, depending on the hypothesis on the origin of the jet in the event.

5.6.2 Transverse W boson mass

To further suppress contributions from processes where the muon does not come from a leptonically decaying W boson, a selection based the reconstructed transverse W boson mass $m_{\mathrm{T}}^{\mathrm{W}}$ is made. The transverse W boson mass is defined as:

$$m_{\mathrm{T}} = \sqrt{\left(p_{\mathrm{T},\ell} + p_{\mathrm{T},\nu}\right)^2 - \left(p_{x,\ell} + p_{x,\nu}\right)^2 - \left(p_{y,\ell} + p_{y,\nu}\right)^2}, \tag{5.16}$$

where the transverse momentum components of the neutrino are approximated by the components of the missing transverse energy vector, $\vec{p}_{\mathrm{T}}^{\,miss}$.

5.7 Analysis strategy

The discrimination between the three signals $ST_{\mathrm{b,q}}$, $ST_{\mathrm{q,b}}$, and $ST_{\mathrm{b,b}}$ is based on three characteristics. First, for $ST_{\mathrm{b,q}}$ events, only a single b quark is present in the final state stemming from gluon splitting, thus resulting in a low-energy b-tagged jet, while the jet coming from the top quark decay is usually not b tagged. For $ST_{\mathrm{q,b}}$ events, a single b-tagged jet is produced in the top quark decay, and additional jets from gluon splitting are usually not b tagged. Both $ST_{\mathrm{q,b}}$ and $ST_{\mathrm{b,q}}$ processes therefore differ from $ST_{\mathrm{b,b}}$ by having a single b quark in the final state, as opposed to two for the latter process. However, this feature can only be exploited when the jet from gluon splitting is energetic enough to be reconstructed. Second, further discrimination is achieved by exploiting the features of the reconstructed top quark candidates. The kinematic and angular properties of the decay products exhibit significant differences depending on whether the correct jet is chosen, or if the jet that originated from the quark produced in the gluon splitting is used. For $ST_{\mathrm{b,q}}$ events, the top quark reconstructed with the correct jet assignment usually does not use the b-tagged jet in the event, while for $ST_{\mathrm{b,b}}$ and $ST_{\mathrm{q,b}}$, the top quark candidate is reconstructed by using the b-tagged jet in the majority of cases. It is therefore possible to differentiate between the $ST_{\mathrm{b,b}}$ and $ST_{\mathrm{b,q}}$ processes by comparing the features of top quark candidates reconstructed with or without b-tagged jets. Finally, different PDFs are involved in $ST_{\mathrm{b,b}}$ and $ST_{\mathrm{q,b}}$ processes, the latter drawing contributions from valence d quarks as well. Therefore, the kinematic properties of final-state particles may differ from the other channels. The

second characteristic, related to the correctness of the top quark reconstruction hypothesis, proves to be the strongest amongst the three mentioned criteria. While the $ST_{\mathrm{b,q}}$ and the $ST_{\mathrm{b,b}}$ processes can be differentiated by using this characteristic, the $ST_{\mathrm{q,b}}$ and the $ST_{\mathrm{b,b}}$ productions cannot, because their final-state signatures exhibit the same features. Events are divided into mutually exclusive "categories" according to the number of selected high-p_{T} jets and b-tagged high-p_{T} jets. In the following, categories are labelled as "njmt", referring to events with exactly n high-p_{T} jets, m of which are tagged as b jets. The 2-jets–1-tag category is populated by events that depend on V_{tb} in both production and decay, where the single reconstructed b jet comes in the majority of cases (85%) from top quark decays, and for the remaining cases from the second b jet from gluon splitting. This means that the jet from the second b quark fails either the jet p_{T} requirement or the b tag requirement, or both. Events coming from a process for which V_{td} or V_{ts} are involved, either in production or in decay, populate this category as well, with either the b-tagged jet coming from top quark decay or the secondary b quark from gluon splitting.

For t-channel signal events from all four processes in Fig. 5.1, the most distinctive features that allow the discrimination against backgrounds in the 2-jets–1-tag category rely on the fact that the second jet stems from the recoiling quark. For this reason the non-b-tagged jet is not used for the top quark reconstruction. This category is the one where the highest discrimination power for $ST_{\mathrm{b,b}}$ against backgrounds is achieved by making use of the features of the top quark decay products, such as the reconstructed top quark mass and $m_{\mathrm{T}}^{\mathrm{W}}$, and of the recoiling jet. However, the discrimination power with respect to other t-channel mechanisms is poor since jets from gluon splitting are typically not energetic enough to pass the p_{T} threshold, making it impossible to reconstruct two different top quark candidates.

The 3-jets–1-tag category is also populated by all t-channel processes of interest, but it differs from 2-jets–1-tag in the fact that it accommodates events in which the jet from gluon splitting has a higher p_{T} on average. For both the 2-jets–1-tag and 3-jets–1-tag categories, when the top quark decays through tWb,s vertices, the jet coming from the top quark usually does not pass the b tagging requirement since it stems from the hadronisation of a light quark. In all other cases, this jet passes the b tagging requirement, given the efficiency of the tagging algorithm.

The 3-jets–1-tag category is enriched in t-channel events by requiring $|\eta_{\mathrm{j}'}| > 2.5$, where $\eta_{\mathrm{j}'}$ is the pseudorapidity of the most forward jet. The two jets other than the most forward one are used to reconstruct the two top quark candidates. If the event is from the $ST_{\mathrm{b,q}}$ process, the b-tagged jet in the 3-jets–1-tag category will stem from gluon splitting, and the additional jet will have a higher chance of being the one coming from the top quark decay to an s or d quark. Variables of interest in this case are constructed by making use of the b jet and the least forward jet of

the remaining two, referred to as the extra jet. Such variables include the invariant mass of the lepton plus jet system (either the b jet or the extra jet), and several top quark kinematic variables constructed using a combination of the extra jet, the lepton, and p_{T}^{miss}.

Lastly, the 3-jets–2-tag category in mainly populated by events with the reconstructed b tagged jets in the final state. In this category, only $ST_{\mathrm{b,b}}$ processes are present but the most abundant contribution comes from $\mathrm{t\bar{t}}$ process and it is mainly used as a control region for this background.

The variables used for this analysis are the following:

- $|\eta_{\mathrm{j}'}|$: the absolute value of the pseudorapidity of the light jet recoiling from the top quark;
- $m_{\mathrm{T}}^{\mathrm{W}}$: the reconstructed W boson transverse mass defined as in the Sec. 5.6.2;
- m_{tX}: the reconstructed top quark mass as defined in Sec. 5.6, where X is the b jet and the extra jet for the n-jets–1-tag and it is the first and the second b jet in the 3-jets–2-tags;
- $m_{\ell\mathrm{j}}$: the lepton + the extra jet reconstructed mass;
- $m_{\ell\mathrm{j}'}$: the lepton + the light jet reconstructed mass;
- $m_{\ell\mathrm{b}}$: the lepton + the b jet reconstructed mass;
- $\not{E}_{\mathrm{T}}$: the amount of the missing energy in each event in the transverse plane $\eta - \phi$;
- CMVAv2 extra jet: is the value of the CMVAv2 b-tagging algorithm for the extra jet;
- $\cos\theta^{*}_{hel}$: the cosine in the top rest frame of the angle between the lepton 3-momenta in the W boson rest frame and the W boson 3-momenta;
- $\cos\theta^{*}_{pol}$: the cosine of the angle between the lepton and W boson in the top rest frame;
- $|\Delta\eta_{b-b}|$: is the absolute value of the difference between the pseudorapidity of the two b jets in the 3-jets–2-tags.

5.7.1 Data driven QCD extraction

The production of multijets through QCD processes has a very large cross section with respect to the one of the other processes relevant for this analysis. On the other hand, only a small fraction of these events mimics the lepton+jets final state of the applied event selection and the selection efficiency for QCD multijet events is therefore tiny. The combination of the aforementioned large cross section and the very small selection efficiency would require the generation of extremely large MC samples for this process in order to produce a sufficient number of events to allow to make a prediction in the signal region that would not be dominated by uncertainties on the MC statistics. Even in such scenario, one would not be guaranteed an accurate modelling because of the higher order corrections to QCD that might affect such corner of the phase space An alternative way of modelling QCD is to define sideband regions in data that are enriched in QCD events and take the distributions of the relevant kinematic variables directly from data.

The sideband region in the muon channel is defined by inverting the isolation criterion for the lepton ($I^{\ell}_{\text{rel}} > 0.2$). Using samples of simulated events from all relevant signal and background processes, the QCD-purity of the anti-isolated sideband region has been estimated to be 93.5%, for muon, and 92.3%, for electron in the 2-jets–1-tag region. The small contributions from non-QCD-processes are subtracted from the data to obtain the pure QCD templates.

The contribution to the sample of selected events from QCD processes is obtained from a fit to the distribution of the transverse W boson mass in the muon and in the electron channels, using the QCD templates derived from sideband regions. An extended maximum-likelihood fit with two parameters is performed to the m_{T}^{W} distribution:

$$F(m_{\text{T}}^{\text{W}}) = N_{QCD} \cdot Q(m_{\text{T}}^{\text{W}}) + N_{Non-QCD} \cdot B(m_{\text{T}}^{\text{W}}), \tag{5.17}$$

where $Q(m_{\text{T}}^{\text{W}})$ stands for the QCD template taken from the sideband region in data, $B(m_{\text{T}}^{\text{W}})$ is the non-QCD template obtained by summing up the simulated contributions from all other processes with prompt muons in the isolated region according to their predicted cross section. The fit parameter N_{QCD} denotes the number of QCD events and $N_{Non-QCD}$ represents the total number of non-QCD events. The N_{QCD} and $N_{Non-QCD}$ parameters are allowed to float during the fit to the m_{T}^{W} distribution. The entire range of the m_{T}^{W} distribution is fitted. This fit is performed separately for the 2-jets–1-tag and 3-jets–1-tag regions in the muon channel and in the electron channel. The fitted distributions for all relevant regions can be found in Fig. 5.5 for both the muon and electron channels.

The QCD contribution to the 3-jets–2-tags region is negligible and no dedicated fit is performed. For the 3-jets–1-tag region an extra scale factor is needed in order to have a better QCD yield estimation in the signal region ($m_{\text{T}}^{\text{W}} > 50$ GeV and

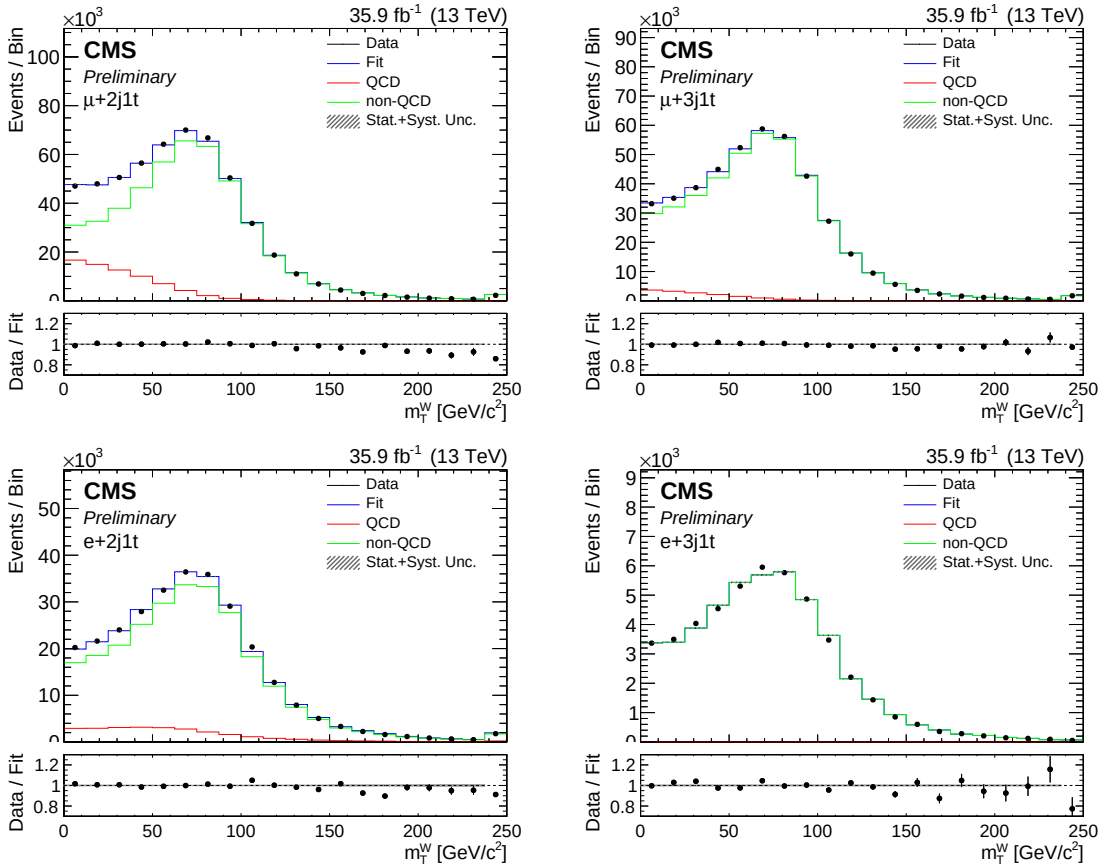

Figure 5.5: Results of the fit to the transverse mass of the W-boson in the 2-jets–1-tag and in the 3-jets–1-tag for the muon, on the top, and electron, on the bottom, channels.

$\eta_{j'} > 2.5$), and this is derived from the sideband as:

$$SF = \frac{N_{Data_{SB}}^{\eta_{j'}>2.5}}{N_{Data_{SB}}}. \tag{5.18}$$

The resulting QCD multijet contributions to the various regions are summarised in Tables 5.5.

5.7.2 QCD rejection in 2j1t and in 3j1t

After the QCD prediction is extracted from the data, in order to deplete the QCD events in the 2-jets–1-tag and 3-jets–1-tag, a $m_{\mathrm{T}}^{\mathrm{W}} > 50$ GeV cut is then applied. This variable is one of the most discriminant between QCD and other

Table 5.5: Number of QCD events extracted from the sideband region for both muon and electron channels in the 2-jets–1-tag and 3-jets–1-tag regions.

Channel	Process	2j1t		3j1t	
		Full $m_{\mathrm{T}}^{\mathrm{W}}$	$m_{\mathrm{T}}^{\mathrm{W}} > 50$	Full $m_{\mathrm{T}}^{\mathrm{W}}$	$m_{\mathrm{T}}^{\mathrm{W}} > 50 \& \eta_{\mathrm{j}'} > 2.5$
μ	QCD	69664 ± 284	15286 ± 89	15378 ± 259	431 ± 7
	non-QCD	468021 ± 302	317665 ± 1010	417035 ± 270	59951 ± 326
e	QCD	25838 ± 423	12005 ± 64	20 ± 1	2 ± 1
	non-QCD	259751 ± 438	182087 ± 812	47138 ± 65	32698 ± 250

processes, as shown in Fig. 5.6 and the requirement $m_{\mathrm{T}}^{\mathrm{W}} > 50$ GeV has an efficiency of $\sim 70\%$ for non QCD processes and only $\sim 20\%$ and $\sim 10\%$ QCD events survive in the 2-jets–1-tag and 3-jets–1-tag, respectively.

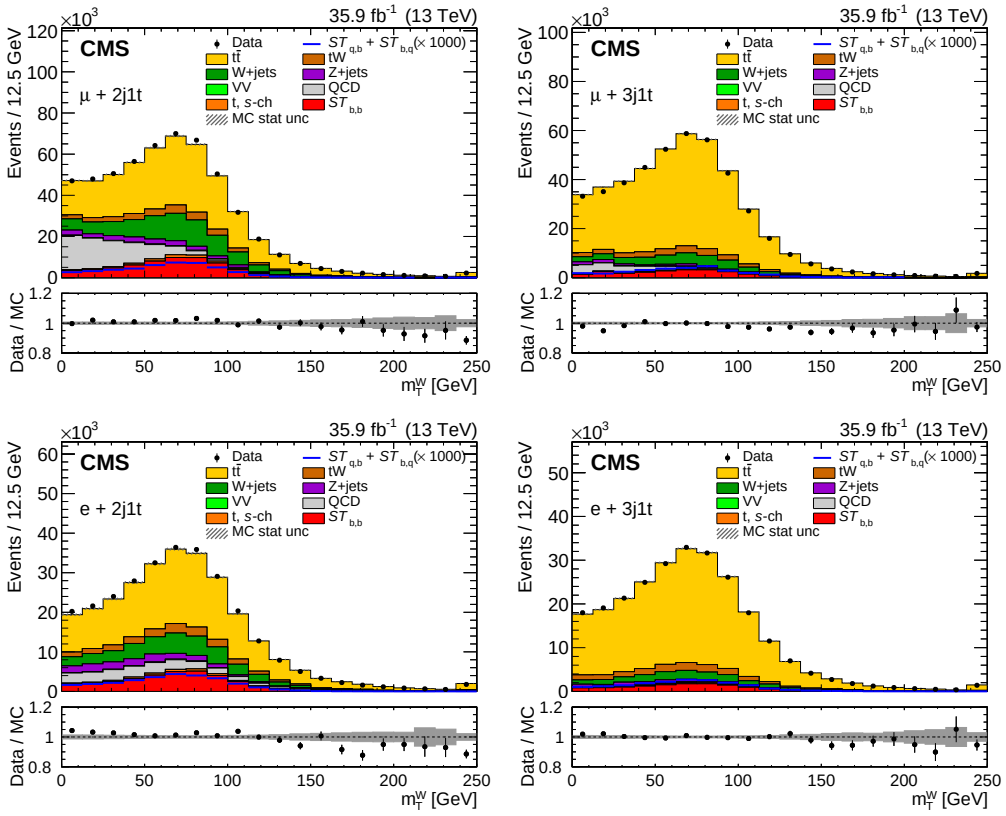

Figure 5.6: Transverse mass of the W boson in the 2-jets–1-tag and in the 3-jets–1-tag after the fit to the QCD data driven sample [153].

The region obtained after the $m_{\mathrm{T}}^{\mathrm{W}} > 50$ GeV cut is henceforth referred to as

QCD-depleted region. In the 3-jets–1-tag an extra scale factor taking into account the extrapolation to the $\eta_{j'} > 2.5$ region is added; this is extracted by the control region as the ratio between the yield of the data with and without the $\eta_{j'} > 2.5$ requirement applied.

5.7.3 Multivariate analysis

Since the signal yield is much smaller compared to the background yields, it is necessary to best exploit all kinematic variables described in Sec. 5.7 and the respective correlations to discriminate between the different signals amongst themselves and against other processes. For this reason, a multivariate analysis, MVA for short, is performed, by training some Boost Decision Trees (BDTs) using the TMVA tool [154] of ROOT [155]. In BDTs, the selection is done on a majority vote on the result of several decision trees, which are all derived from the same training sample by supplying different event weights during the training. Successive decision nodes are used to categorise the events as either signal or background. Each node uses only a single discriminating variable to decide if the event is signal-like ("goes right" conventionally down the tree structure) or background-like ("goes left"). This forms a tree like structure with "baskets" at the end (leave nodes), and an event is classified as either signal or background according to whether the basket where it ends up has been classified signal or background during the training. Training of a decision tree is the process to define the cut criteria for each node. The training starts with the root node. Here one takes the full training event sample and selects the variable and corresponding cut value that gives the best separation between signal and background at this stage. Using this cut criterion, the sample is then divided into two subsamples, a signal-like (right) and a background-like (left) sample. Two new nodes are then created for each of the two sub-samples and they are constructed using the same mechanism as described for the root node. The division is stopped once a certain node has reached either a minimum number of events, or a minimum or maximum signal purity. These leave nodes are then called signal or background if they contain more signal respective background events from the training sample. The idea behind the boosting is, that signal events from the training sample, that end up in a background node, or vice versa, background events in a signal note, are given a larger weight than events that are in the correct leave node. This results in a re-weighed training event sample, with which then a new decision tree can be developed. The boosting can be applied several times (typically 100-500 times) and one ends up with a set of decision trees (a "forest"). More information about the specific algorithm implemented in this tool can be found in Ref. [154].

5.7.4 Variables in 2j1t

The 2-jets–1-tag category is enriched in $ST_{\mathrm{b,b}}$ process and it is used as a control region for the estimation of this class of events. After the $m_{\mathrm{T}}^{\mathrm{W}} > 50$ GeV requirement, necessary to deplete the QCD events, the main source of background comes from $\mathrm{t\bar{t}}$ and $\mathrm{W}+\mathrm{jets}$ events that have the same topology in the final state. In order to discriminate against these two backgrounds a multivariate analysis has been performed.

Figure 5.7 shows pseudorapidity of the j' and the reconstructed mass with the lepton and b-jet four-momenta. These two variables turn out to be the most discriminating ones between the single-top $t-$channel and two most important backgrounds in this category: $\mathrm{t\bar{t}}$ and $\mathrm{W}+\mathrm{jets}$.

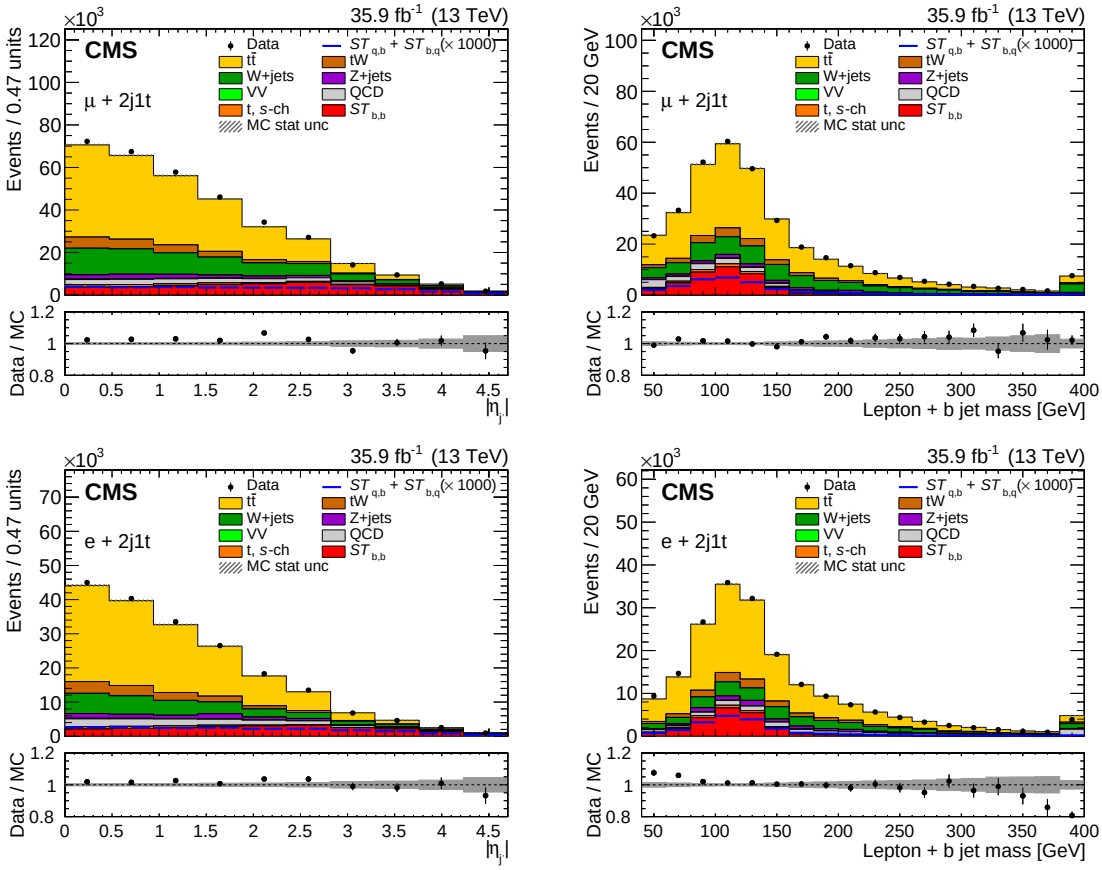

Figure 5.7: Distributions of the two most discriminating variables in the 2-jets–1-tag QCD-depleted region, which are used in the MVA analysis: on the top for the muon channel and on the bottom for the electron channel.

Six variables are used in the MVA: the $|\eta|$ of the non-b-tagged jet, the reconstructed top quark mass, the cosine of the angle between the W boson momentum in the top quark rest frame and the momentum of the lepton in the W boson rest frame, the cosine of the polarisation angle defined as the angle between the direction of the lepton and the light-quark momenta in the top quark rest frame, the invariant mass of the lepton and b-tagged jet system, and the invariant mass of the lepton and forward jet system.

The BDT is trained on exclusively dedicated samples that are not used in any other stage of the analysis. Due to limited amount of MC statistic for the W + jets sample in the electron channel, the training has been done only in the muon channel and the same discriminator is used for both the samples in the analysis.

Figure 5.8 shows the shapes of the variables used as input to the BDT trained in the 2-jets–1-tag category for both signal $ST_{\mathrm{b,b}}$ and $\mathrm{t\bar{t}}$ + W + jets backgrounds. Table 5.6 shows the results of the BDT discriminator in the QCD-depleted region

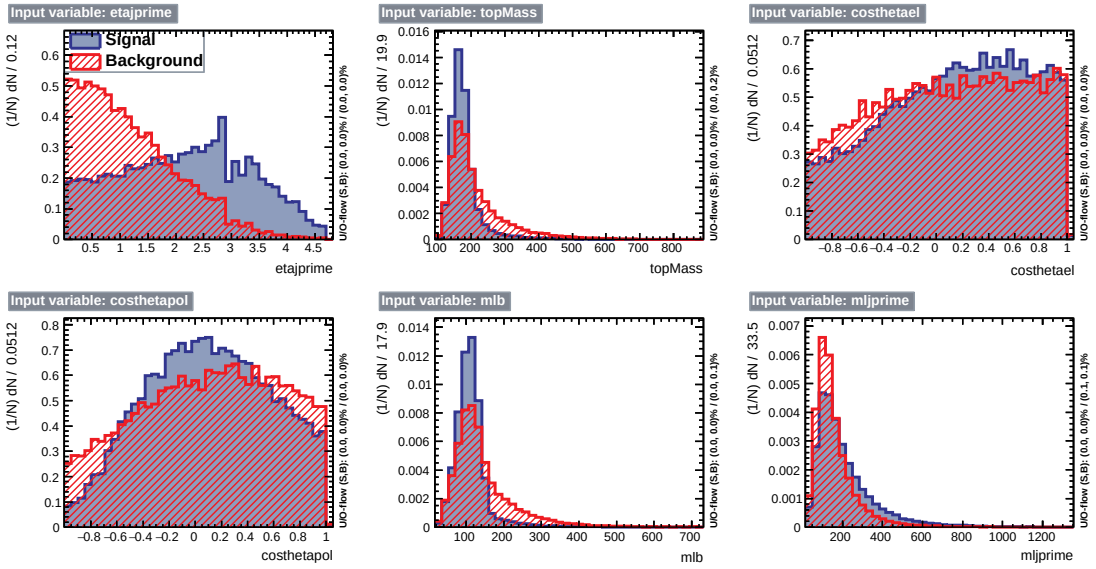

Figure 5.8: the plots show the shape of the variables used as input of the BDT training in the 2-jets–1-tag category.

in which single-top $t-$channel is considered as signal and $\mathrm{t\bar{t}}$ and W + jets are considered as background.

Figure 5.9 shows the overtraining test result and the Receiver Operating Characteristic (ROC) curve, whose area under the curve results to be 0.799, for the BDT obtained.

Table 5.6: Input variables for the BDTs trained for the single-top-quark $t-$channel versus $t\bar{t}$ and W + jets ranked according to their importance in the muon channel in the 2-jets–1-tag QCD-depleted region.

Rank	Variable	Rel. imp. [%]	Correlation to BDT	
			Signal	Background
1	$\|\eta\|$ light jet	21.40	+0.82	+0.53
2	lepton + b-jet mass	19.01	-0.29	-0.57
3	lepton + light jet mass	18.31	+0.37	+0.07
4	$\cos\theta^*_{pol}$	15.06	+0.05	+0.07
5	top-quark mass	15.02	-0.33	-0.54
6	$\cos\theta^*_{hel}$	11.20	+0.07	+0.07

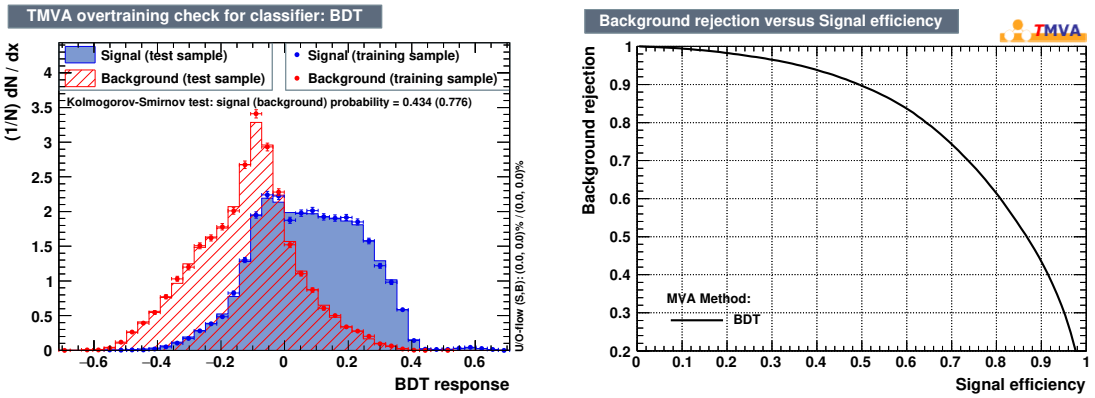

Figure 5.9: Classifier output distributions for the test (histograms) and training samples (dots) superimposed, on the left; Classifier background rejection vs signal efficiency, on the right.

Figure 5.10 shows the pre-fit distributions for the discriminator trained in the 2-jets–1-tag QCD-depleted region.

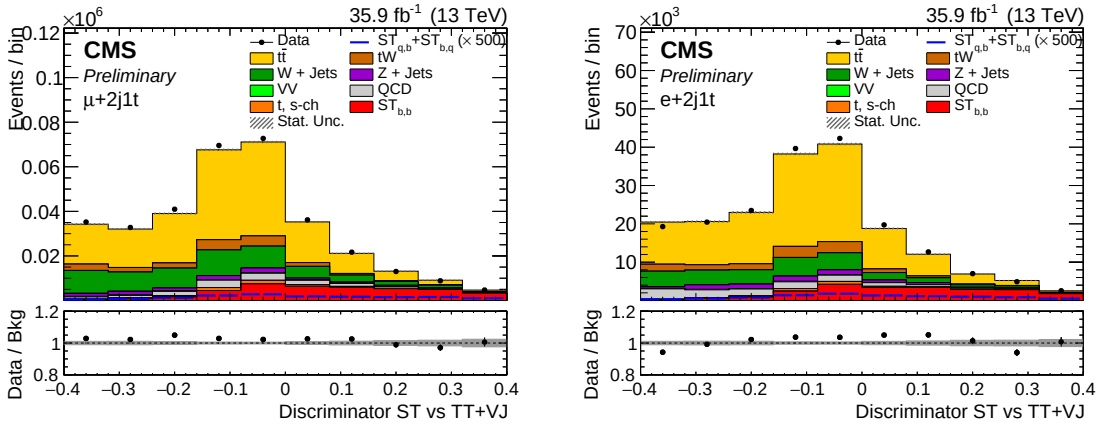

Figure 5.10: Distributions of the discriminator in the 2-jets–1-tag QCD-depleted region: on the left for the muon channel and on the right for the electron channel.

5.7.5 Variables in 3j1t

The 3-jets–1-tag category represents the signal region for the $ST_{\mathrm{b,q}}$ processes. After the $m_{\mathrm{T}}^{\mathrm{W}} > 50$ GeV cut is applied, the most discriminating variables are, for example, the pseudo-rapidity of the light jet, the W boson transverse mass and the response of the CMVAv2 tagger algorithm when applied to the extra jet selected.

Additional jets, low-p_{T} jets, are selected within the range $20 < p_{\mathrm{T}} < 40$ GeV and having $|\eta| < 2.4$. The leading extra jet is used to reconstruct a top-quark candidate. In case it is an event of the $ST_{\mathrm{b,q}}$ type, the b-jet of the 3-jets–1-tag will be stemming from gluon splitting, and the additional jet will have a high chance of being the one stemming from top-quark decay to s/d quarks.

Variables of interest in this sense are for example the mass between the lepton and either jet (the b-jet or the leading extra jet), the top-quark kinematic distributions built using the combination of the leading extra jet, MET and the lepton.

Then the QCD-depleted region is divided into two subcategories with a $\eta_{\mathrm{j}'}$ cut: a QCD-depleted-central region with a $\eta_{\mathrm{j}'} < 2.5$ cut and a QCD-depleted-forward region with $\eta_{\mathrm{j}'} > 2.5$ cut. The only region of interest is the forward one because it's enriched in signal events and so it's the only one used in the analysis.

Figure 5.11 shows the p_{T}^{miss} and the response of the CMVAv2 tagger algorithm when applied to the extra jet. These together with the $|\eta|$ of the most forward non-b-tagged jet, the mass of the top quark when it is reconstructed with the b-tagged jet (b-top quark), the cosine of the angle between the W boson momentum in the b-top quark rest frame and the momentum of the lepton in the W boson rest frame, the cosine of the polarisation angle defined as the angle between the direction of the lepton and the light-quark momenta in the b-top quark rest frame, $m_{\mathrm{T}}^{\mathrm{W}}$, the invariant mass of the lepton and b-tagged jet system, the invariant mass of the lepton and extra jet system, the invariant mass of the lepton and forward jet system, the number of low-p_{T} jets, the mass of the top quark when it is reconstructed with the non-b-tagged jet (non-b-top quark), the cosine of the angle between the W boson momentum in the non-b-top quark rest frame and the momentum of the lepton in the W boson rest frame, the cosine of the polarisation angle defined as the angle between the direction of the lepton and the light-quark momenta in the non-b-top quark rest frame, are used in the MVA in order to maximise the separation between signal and background.

Figure 5.12 shows the shape of the variables used as input to the BDT trained in the 3-jets–1-tag region. Table 5.7 shows the results of the BDT discriminator in the QCD-depleted-forward region in which $ST_{\mathrm{b,q}}$ is considered as signal and single-top $t-$channel, $\mathrm{t\bar{t}}$ and $\mathrm{W}+\mathrm{jets}$ are considered as background.

Figure 5.13 shows the overtraining test result and the ROC curve, which area is equal to 0.827, for the BDT obtained.

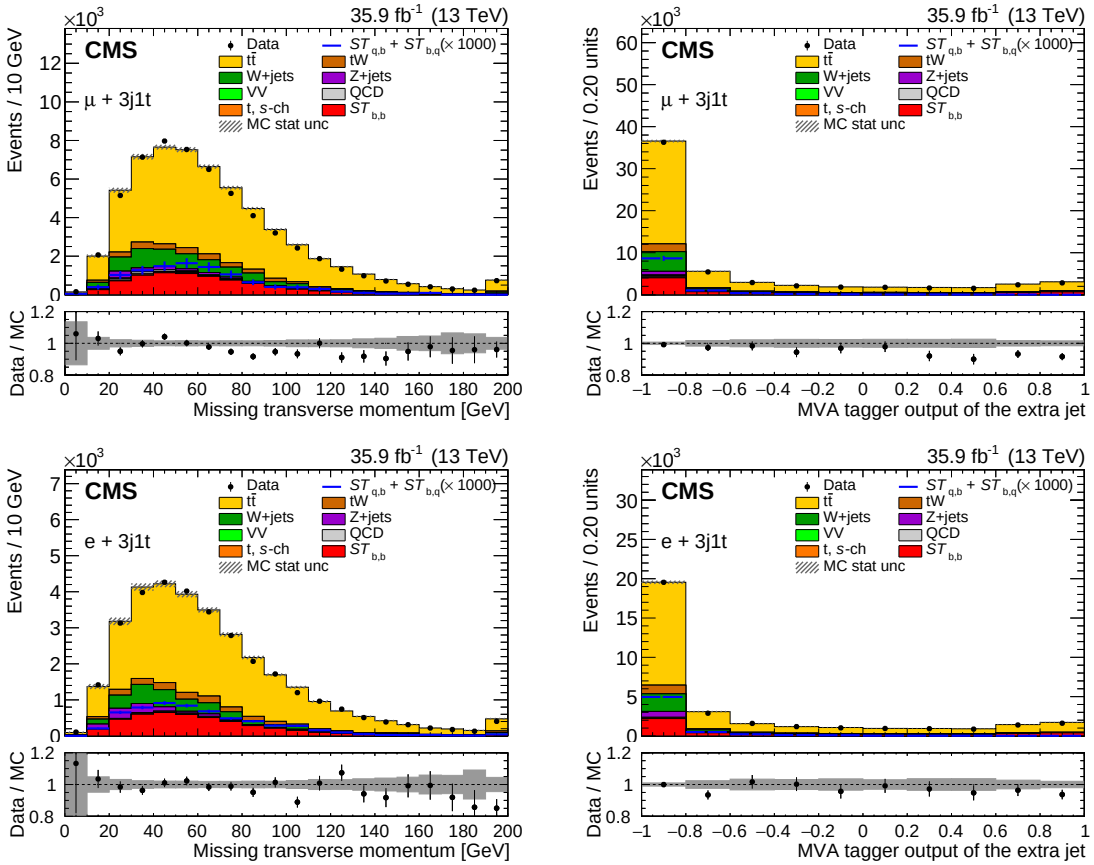

Figure 5.11: Distributions of the two most discriminating variables in the 3-jets–1-tag QCD-depleted-forward region, which are used in the MVA analysis: on the top for the muon channel and on the bottom for the electron channel.

Figure 5.14 shows the pre-fit distributions for the discriminator trained in the 3-jets–1-tag QCD-depleted-forward region.

Table 5.7: Input variables for the BDTs trained for the single-top-quark $t-$channel with $|V_{\mathrm{tq}}|^2$ vertex in decay versus standard single-top $t-$channel, $\mathrm{t\bar{t}}$ and $\mathrm{W}+\mathrm{jets}$ ranked according to their relative importance in the muon channel in the 3-jets–1-tag QCD-depleted-forward region.

Rank	Variable	Rel. imp. [%]	Correlation to BDT	
			Signal	Background
1	CMVA extra jet	9.2	-0.41	-0.61
2	W-boson transverse mass	8.6	-0.06	-0.15
3	$\not\!\!E_{\mathrm{T}}$	8.4	-0.15	-0.11
4	$\cos\theta^*_{hel}$	8.3	+0.17	+0.05
5	$\lvert\eta\rvert$ light jet	7.6	+0.33	+0.08
6	top-quark mass extra	7.1	-0.29	-0.18
7	no. extra jets	7.1	-0.39	-0.21
8	$\cos\theta^*_{pol}$	6.9	+0.16	+0.14
9	lepton + extra jet mass	6.9	-0.23	-0.19
10	$\cos\theta^*_{pol}$ extra	6.6	+0.09	+0.22
11	lepton + light jet mass	6.0	+0.15	-0.07
12	lepton + b-jet mass	6.0	+0.10	+0.07
13	$\cos\theta^*_{hel}$ extra	5.9	+0.01	-0.06
14	top-quark mas	5.4	+0.04	+0.07

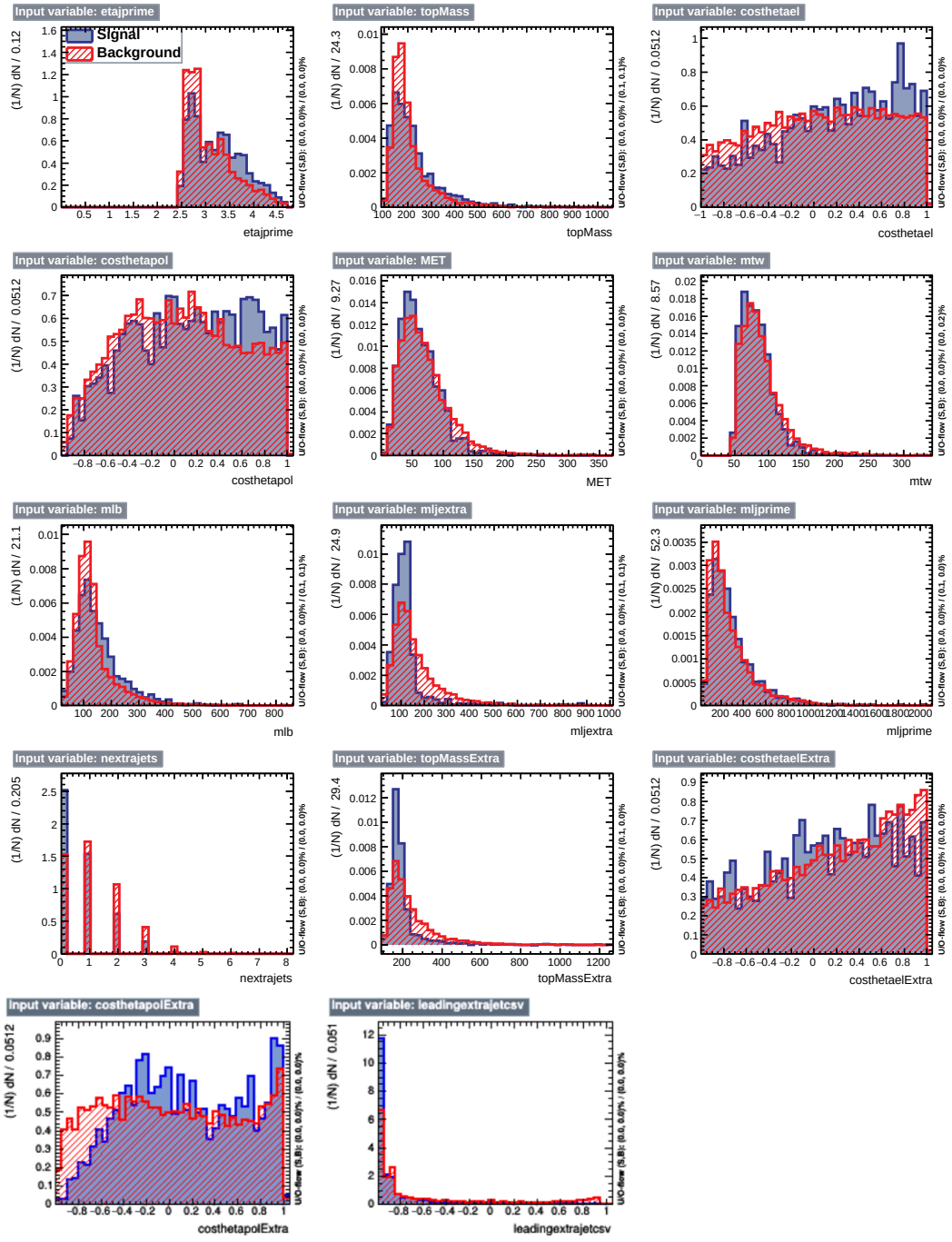

Figure 5.12: Shapes of the most discriminating variables used as input of the BDT training in the 3-jets–1-tag category, for signal, in blue, and for background, in red.

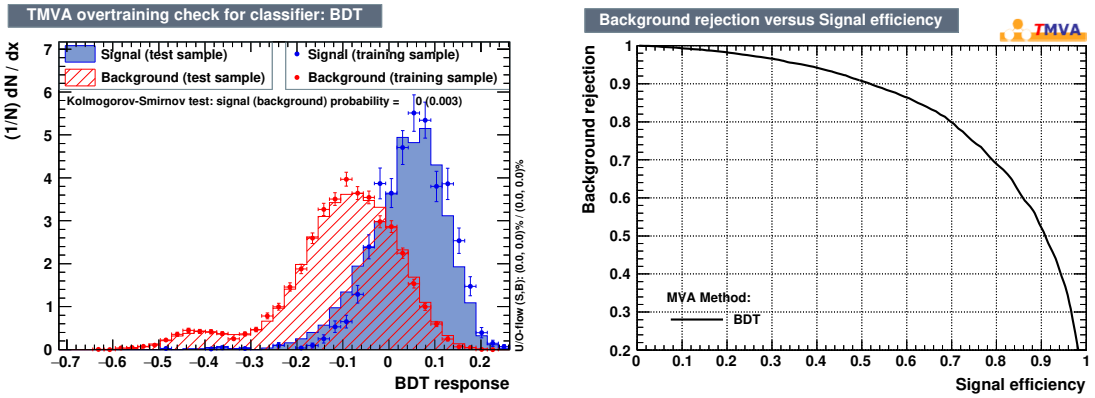

Figure 5.13: Classifier output distributions for the test (histograms) and training samples (dots) superimposed, on the left; Classifier background rejection vs signal efficiency, on the right, for the 3-jets–1-tag category.

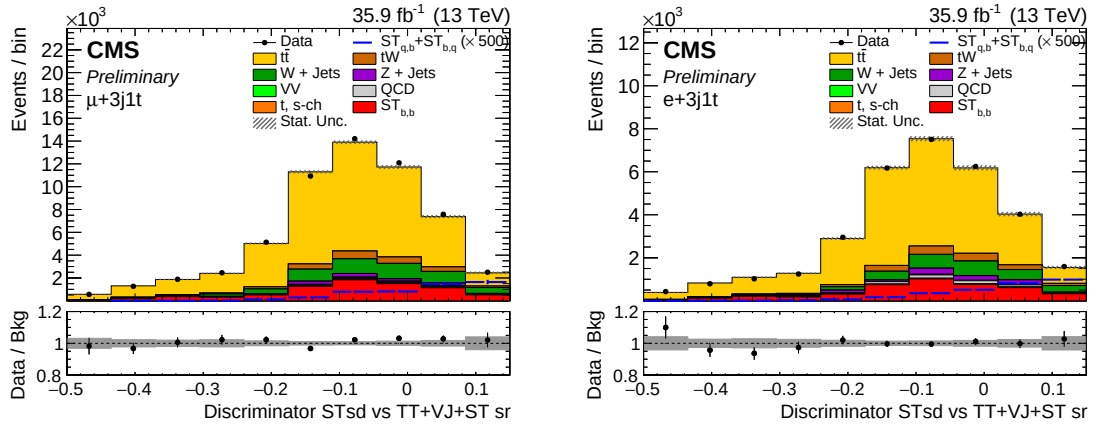

Figure 5.14: Distributions of the discriminator in the 3-jets–1-tag QCD-depleted region: on the left for the muon channel and on the right for the electron channel.

5.7.6 Variables in 3j2t

In the 3-jets–2-tags category, there are two b jets one stemming from the top-quark decay and one stemming from the gluon splitting. Both b jets are used to reconstruct a top-quark candidate and its correlated variables. In this case it is unnecessary to apply the $m_{\mathrm{T}}^{\mathrm{W}} > 50$ GeV cut since the amount of QCD events in this category is negligible. Also the cut on $\eta_{\mathrm{j}'}$ is irrelevant because this case is dominated by $\mathrm{t\bar{t}}$ sample. So only the study of single-top $t-$channel versus $\mathrm{t\bar{t}}$ is performed. In this category, variables of interest are the ones involving the kinematic variables of the light jet, like as the pseudorapidity of the light jet and the invariant mass of lepton and light jet system, reported in Fig. 5.15.

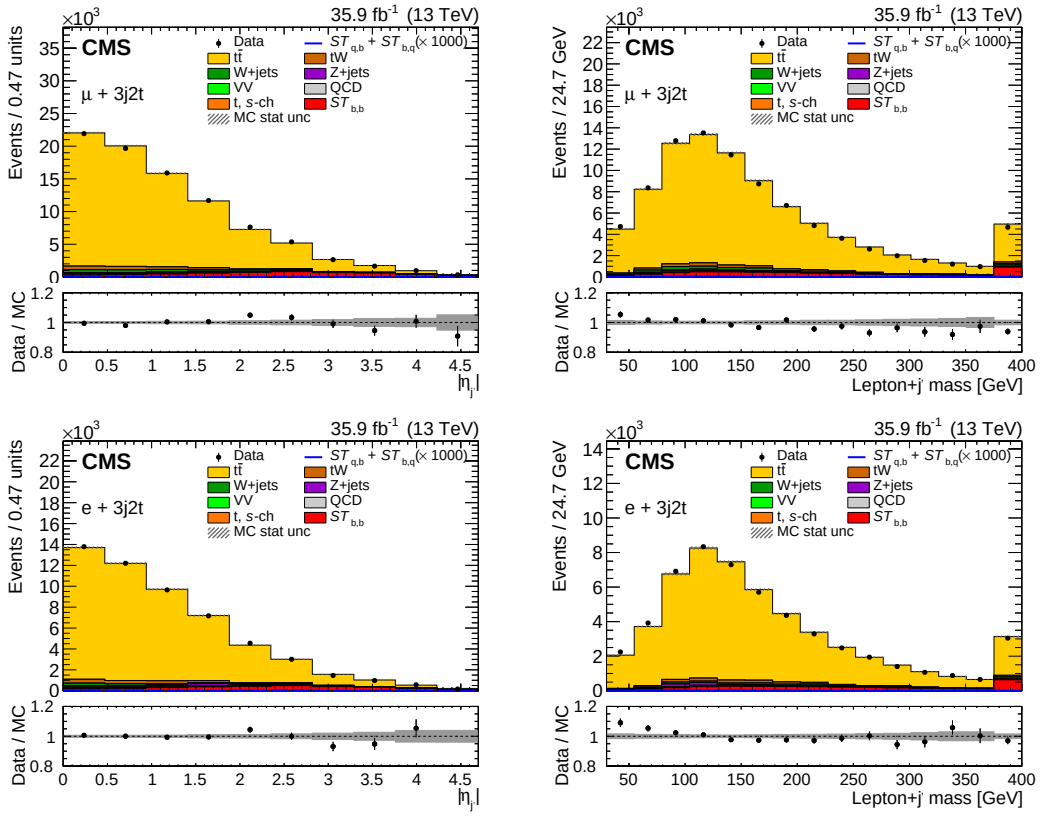

Figure 5.15: Distributions of the two most discriminating variables in the 3-jets–2-tags region, which are used in the MVA analysis: on the top for the muon channel and on the bottom for the electron channel.

These variables are used in the training of the MVA discriminator together with the mass of the top quark when it is reconstructed with the highest-p_{T} b-tagged jet (leading top quark), the cosine of the angle between the W boson momentum in

the leading top quark rest frame and the momentum of the lepton in the W boson rest frame, the cosine of the polarisation angle defined as the angle between the direction of the lepton and the light-quark momenta in the leading top quark rest frame, p_{T}^{miss}, $m_{\mathrm{T}}^{\mathrm{W}}$, the invariant mass of the lepton and the highest-p_{T} b-tagged jet system, the invariant mass of the lepton and lower-p_{T} b-tagged jet system, the number of low-p_{T} jets, the mass of the top quark when it is reconstructed with the lower-p_{T} b-tagged jet (non-leading top quark), the cosine of the angle between the W boson momentum in the non-leading top quark rest frame and the momentum of the lepton in the W boson rest frame, the cosine of the polarisation angle defined as the angle between the direction of the lepton and the light-quark momenta in the non-leading top quark rest frame, and the difference in η between the two b-tagged jets.

Figure 5.16 shows the shape of the variables used as input to the BDT trained in the 3-jets–2-tags region. Table 5.8 shows the results of the MVA in which single-top $t-$channel is considered as signal and $\mathrm{t\bar{t}}$ is considered as background.

Table 5.8: Input variables for the BDTs trained for the single-top-quark $t-$channel versus $\mathrm{t\bar{t}}$ ranked according to their importance in the muon channel.

Rank	Variable	Rel. imp. [%]	Correlation to BDT	
			Signal	Background
1	$\lvert\eta\rvert$ light jet	12.0	+0.77	+0.66
3	lepton + light jet mass	9.3	+0.38	+0.26
2	W-boson transverse mass	9.2	-0.06	+0.26
4	no. extra jets	9.1	-0.47	-0.43
5	$\cos\theta^{*}_{pol}$ second	7.0	+0.20	+0.14
6	$\lvert\Delta\eta_{b-b}\rvert$	6.9	+0.02	-0.02
7	$\cos\theta^{*}_{hel}$ leading	6.7	+0.11	+0.06
8	top-quark mass leading	6.6	-0.04	+0.01
9	lepton + second b-jet mass	6.6	-0.00	-0.13
10	lepton + leading b-jet mass	6.4	+0.01	-0.00
11	top-quark mass second	5.2	-0.03	-0.06
12	$\cos\theta^{*}_{pol}$ leading	5.2	+0.11	+0.11
13	$\cos\theta^{*}_{hel}$ second	5.0	-0.07	+0.03
14	$\not{E}_{\mathrm{T}}$	4.9	-0.036	-0.10

Figure 5.17 shows the overtaining test result and the ROC curve, with an area under the curve of 0.863, for the BDT obtained.

Figure 5.18 shows the pre-fit distributions for the discriminator trained in the 3-jets–2-tags category.

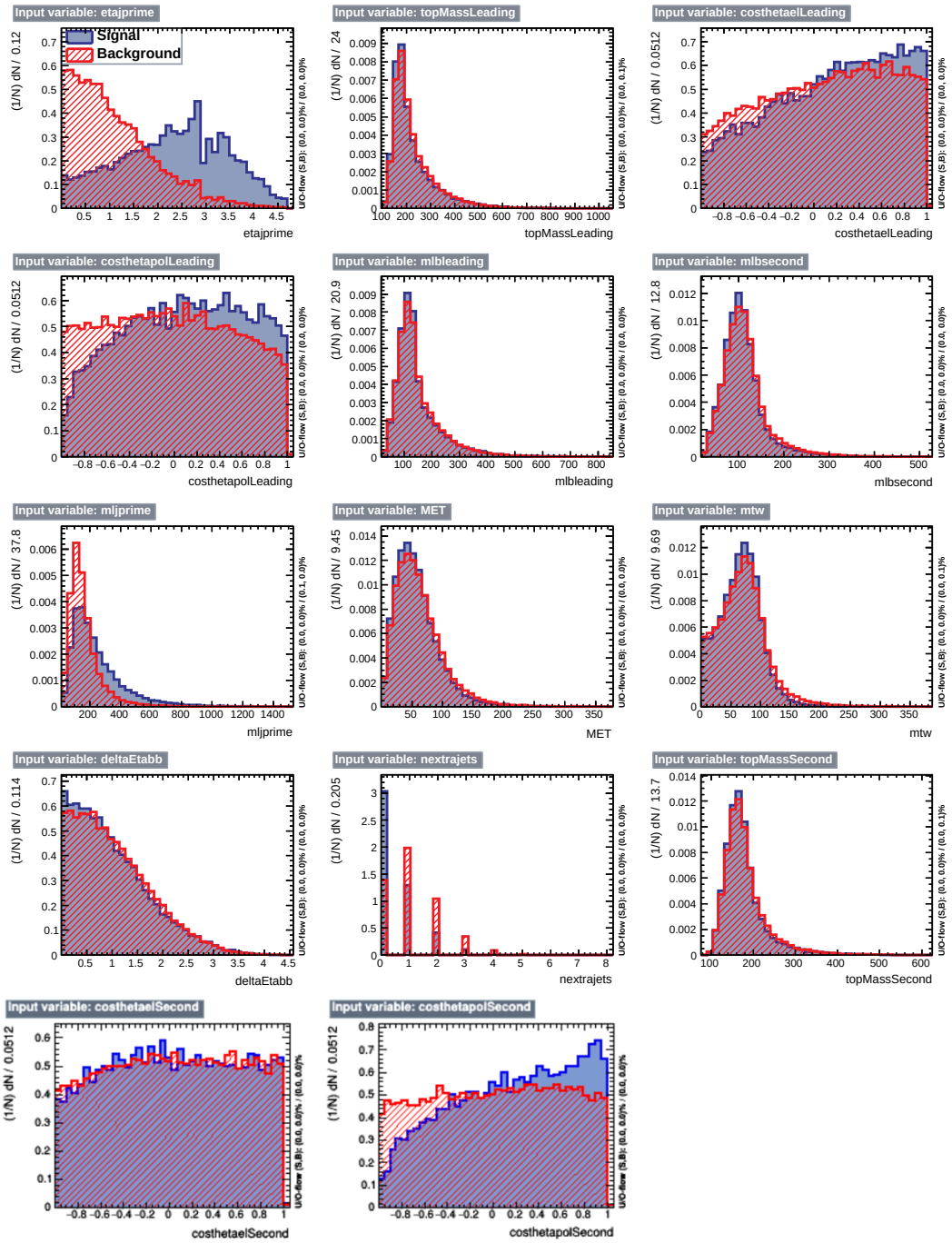

Figure 5.16: Shapes of the variables used as input of the BDT training in the 3-jets–2-tags category, for signal, in blue, and background, in red.

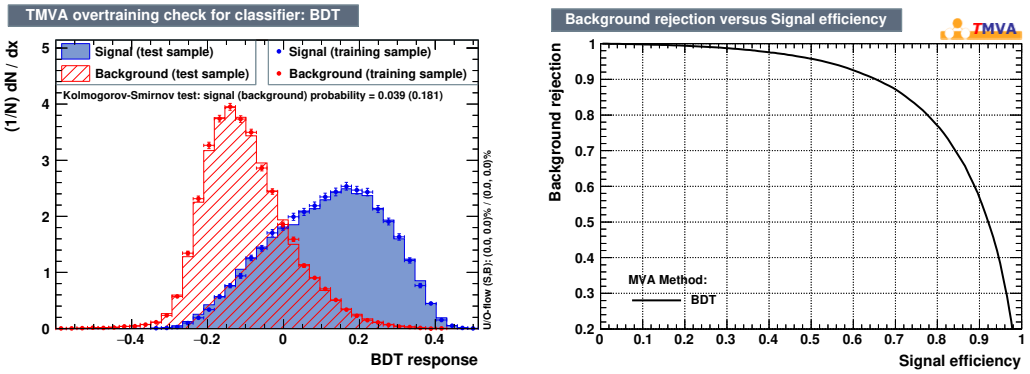

Figure 5.17: Classifier output distributions for the test (histograms) and training samples (dots) superimposed, on the left; Classifier background rejection vs signal efficiency, on the right.

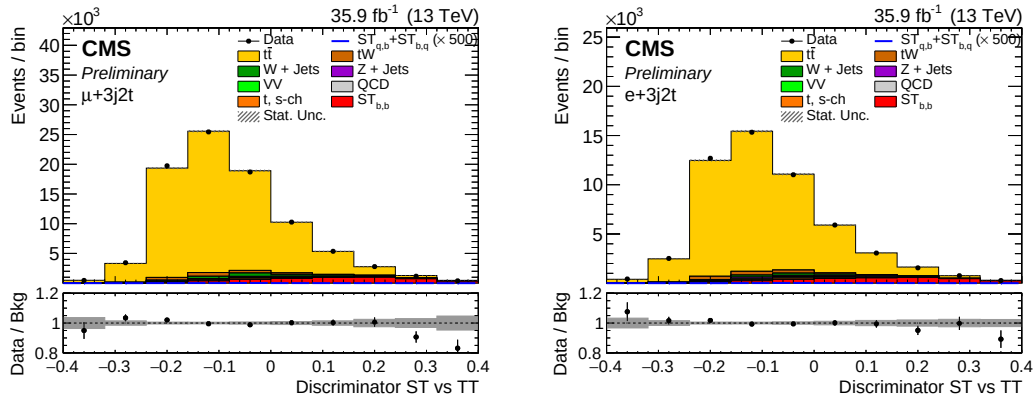

Figure 5.18: Distributions of the discriminators in the 3-jets–2-tags category: on the left for the muon channel and on the right for the electron channel.

5.8 Systematic uncertainties

Several sources of systematic uncertainties are considered in the analysis, divided in two groups depending on the treatment: uncertainties labelled as "profiled" are treated as nuisance parameters and profiled in the fit procedure described in Section 5.9, while those labelled as "nonprofiled" are estimated as the difference between the results of the fit procedure in different systematic scenarios. These latter uncertainties include the sources related to the modelling of the signal process, which cannot be constrained from the measurement since they apply to the full phase space and not only to the region in which the measurement is performed. Also included are the jet energy scale and resolution uncertainties, which play a major role in events featuring hadronic activity in the high-pseudorapidity region of the detector. They are also intertwined with the uncertainties in the modelling of the hadronisation and cause a larger uncertainty in the signal acceptance, which was not the case for previous measurements [34, 35]. For these reasons, a more conservative approach is preferred and these uncertainties are not profiled in the fit.

The impact of nonprofiled uncertainties is determined by repeating the analysis using varied templates according to the systematic uncertainty sources under study in the fit, instead of the nominal templates. The uncertainty due to a certain source is then taken as half the difference between the results for up and down variations of the effect.

In the following, the different uncertainty sources that are considered in the analysis are briefly described. For the sake of simplicity and better readability, they are grouped into profiled and nonprofiled uncertainties.

Profiled uncertainties

- *Limited size of simulated event samples*: The statistical uncertainty due to the limited size of the simulated event samples is evaluated for each bin with the Barlow–Beeston "light" method [156, 157].

- *Lepton trigger and reconstruction*: Single-muon and single-electron trigger and reconstruction efficiencies are estimated with a "tag-and-probe" method [158] from Drell–Yan events with the dilepton invariant mass in the Z boson peak.

- *Pileup*: The uncertainty in the average expected number of pileup interactions is propagated as a source of systematic uncertainty by varying the total p-p inelastic cross section by ±4.6% [159].

- $\mathrm{t\bar{t}}$ *modelling*: The following uncertainty sources cover potential mismodelling

of the $t\bar{t}$ process. Their effect is considered on both the acceptance and the cross section.

  - $t\bar{t}$ *renormalisation and factorisation scale uncertainties (μ_R/μ_F)*: The uncertainties caused by variations in the renormalisation and factorisation scales are considered by reweighting the BDT response distributions with different combinations of doubled/halved renormalisation and factorisation scales with respect to the nominal value of 172.5 GeV.
  - *Matching of matrix element and parton shower (ME-PS matching)*: The parameter that controls the matching between the matrix element level calculation and the parton shower, and that regulates the high-p_T radiation in the simulation is varied within its uncertainties.
  - *Initial- and final-state radiation:* The impact of variations in the initial-state and final-state radiation is studied by comparing the nominal sample with dedicated $t\bar{t}$ samples.
  - *Underlying event:* The effect of uncertainties in the modelling of the underlying event is studied by comparing the nominal sample with dedicated $t\bar{t}$ samples.

- *QCD multijet background process normalisation*: The QCD multijet background yield is assigned a 50% uncertainty, which is chosen conservatively to be much larger than the uncertainty from the m_T^W fit.

- W + jets *composition*: A separate uncertainty is dedicated to the fraction of W + jets events where the forward jet is generated by the parton showering.

- *Other backgrounds* μ_R/μ_F: In addition to $t\bar{t}$, the uncertainties due to variations in the renormalisation and factorisation scales are studied for the tW and W + jets processes by reweighting the distributions with weights corresponding to different combinations of halved or doubled factorisation and renormalisation scales. The effect is estimated for each process separately.

- *PDF for background processes*: The uncertainty due to the choice of PDF is estimated using reweighted histograms derived from all possible PDF sets of NNPDF 3.0 [160].

- *b tagging*: The uncertainties in the b tagging and mistagging efficiency measurements are split into different components and propagated to the efficiency of tagging b jets.

Nonprofiled uncertainties

- *Luminosity*: The integrated luminosity is known with a relative uncertainty of ±2.6% [161].
- *Jet energy scale (JES)*: All reconstructed jet four-momenta in simulated events are simultaneously varied according to the η- and p_{T}-dependent uncertainties in the JES. This variation in jet four-momenta is also propagated to p_{T}^{miss}.
- *Jet energy resolution (JER)*: A smearing is applied to account for the difference in the JER between simulation and data, and its uncertainty is estimated by increasing or decreasing the resolutions by their uncertainties.
- *Signal modelling*: The following uncertainty sources cover potential mismodelling of the single top quark t-channel signal processes. The effect of those uncertainties on the acceptance, and not on the cross section, is considered. In the fit procedure, the uncertainties are not considered as nuisance parameters in the fit but evaluated by repeating the full analysis using samples of simulated signal events that feature variations in the modelling parameters covering the systematic uncertainty sources under study.
  - *Signal $\mu_{\mathrm{R}}/\mu_{\mathrm{F}}$:* The uncertainties caused by variations in the renormalisation and factorisation scales are considered by reweighting the BDT response distributions according to weights corresponding to doubling/halving the nominal values of the scales [141, 142].
  - *Matching of matrix element and parton shower (ME-PS matching):* The parameter that controls the matching between the matrix element level calculation and the parton shower, and that regulates the high-p_{T} radiation in the simulation is varied within its uncertainties.
  - *Parton shower factorisation scale:* The renormalisation scales of the initial- and final-state parton shower are varied by factors of two and one half with respect to the nominal value of 172.5 GeV.
  - *PDF for signal process*: The uncertainty due to the choice of PDF is estimated using reweighted histograms derived from all PDF sets of NNPDF 3.0.

5.9 Fit procedure

The CKM matrix elements are extracted from the measured cross-section of the single-top $t-$channel process. For the extraction of single-top $t-$channel production cross-section, a simultaneous maximum likelihood fit to the multivariate

distributions in 2-jets–1-tag, 3-jets–1-tag and 3-jets–2-tags categories is performed. Higgs combination tool [162] is used to perform the statistical inference. The tool makes use of RooStats for the calculations. The further details on RooStats can be found in Ref. [163]. The fit procedure is divided in three steps:

- In the first step, a Maximum Likelihood fit to the $m_{\mathrm{T}}^{\mathrm{W}}$ distribution is performed for the QCD scale factor extraction. The scale factor is than used for the normalisation of QCD template.
- In the second step, the light quark distribution $\eta_{\mathrm{j}'}$ and $m_{\mathrm{T}}^{\mathrm{W}}$ are used to define different categories:
  - 2-jets–1-tag: in order to control the $\mathrm{t\bar{t}}$, $\mathrm{W}+\mathrm{jets}$ together with the $t-$channel a $m_{\mathrm{T}}^{\mathrm{W}} > 50$ GeV is required to deplete the QCD.
  - 3-jets–1-tag: in order to have a region enriched in $t-$channel V_{td}-V_{ts}, events where $\eta_{\mathrm{j}'} > 2.5$ and $m_{\mathrm{T}}^{\mathrm{W}} > 50$ GeV are required.
  - 3-jets–2-tags: no selection is performed in this region and used to control $\mathrm{t\bar{t}}$ background.
- In the last step, the Maximum Likelihood fit is performed simultaneously in the regions defined in step 2, while the QCD prior uncertainty and central value are taken from step 1. The presence of standard top-quark decay products, $|V_{\mathrm{tb}}|$, is now one of the major background to the $|V_{\mathrm{td}}|$ or $|V_{\mathrm{ts}}|$ extraction.

5.9.1 Fit variables

The $m_{\mathrm{T}}^{\mathrm{W}}$ variable is used for a first estimation of the QCD-Multijet background and the flat prior fitted is used as scale factor for the QCD template. In the QCD-depleted region a MVA analysis is performed, as described in Sec. 5.7, in order to obtain one MVA variables in the QCD-depleted region in the 2-jets–1-tag category and another MVA variable in the QCD-depleted-forward region in the 3-jets–1-tag category. The MVAs variables are obtained in the following way:

- the first is obtained considering the single-top $t-$channel as signal and the $\mathrm{t\bar{t}}$ and the $\mathrm{W}+\mathrm{jets}$ are considered as background in the QCD-depleted region in the 2-jets–1-tag category;
- the second is obtained considering the single-top $t-$channel decaying in s/d quarks as signal and the $\mathrm{t\bar{t}}$, standard single-top $t-$channel and $\mathrm{W}+\mathrm{jets}$ are considered as background in the QCD-depleted-forward region in the 3-jets–1-tag category;

- At the end, for the 3-jets–2-tags, the multivariate analysis consists in only one BDT variable obtained considering the single-top $t-$channel as signal and the $\mathrm{t\bar{t}}$ is considered as background without any cut.

The t-channel single top quark signals are parametrised with a flat prior representing the coupling strength, and all systematic uncertainties are treated as described in Section 5.8. The smaller background yields are allowed to vary in the fit, along with the respective scale uncertainties. The QCD multijet background is fitted with a flat prior nuisance, while $\mathrm{t\bar{t}}$ and $\mathrm{W}+\mathrm{jets}$ backgrounds are left floating within the respective systematic uncertainties. The t-channel $ST_{\mathrm{b,q}}$ and $\mathrm{t\bar{t}_{q,b}}$ processes do not distinguish between topologies depending on V_{td} or V_{ts} in the decay, while $ST_{\mathrm{q,b}}$ is sensitive to the different PDFs contributing to the processes. Figure 5.19 shows the distributions after the fit procedure has been applied for the muon (left) and the electron (right) channels.

The partial and total contributions of the profiled and nonprofiled uncertainties are given in Table 5.9.

5.10 Results

The contributions of each of the three CKM matrix elements to the different $ST_{\mathrm{b,b}}$, $ST_{\mathrm{b,q}}$, and $ST_{\mathrm{q,b}}$ cross sections, extracted from the fit procedure, are considered. In the SM, top quarks only decay to W bosons plus b, s, or d quarks, and their branching fractions are proportional to the magnitude squared of the respective matrix element, as given in Table 5.1. The fit results are given in terms of two signal strength parameters: the first, μ_b, refers to the $ST_{\mathrm{b,b}}$ process, and the second, μ_{sd}, to the sum of the $ST_{\mathrm{q,b}}$ and $ST_{\mathrm{b,q}}$ contributions.

By neglecting terms proportional to $|V_{\mathrm{td}}|^4$, $|V_{\mathrm{ts}}|^4$, the $ST_{\mathrm{q,b}}$ term can be written as proportional to $|V_{\mathrm{td}}|^2 + |V_{\mathrm{ts}}|^2$, with a contribution of order 5% that depends on $|V_{\mathrm{td}}|^2/|V_{\mathrm{ts}}|^2$. We consider variations on the latter contribution as negligible in the analysis. These assumptions can be justified because of the hierarchy observed in the first two rows of the CKM matrix. The signal strengths thus become:

$$\begin{aligned} \mu_b &= \frac{\sigma^{\mathrm{obs}}_{t\text{-ch,b}}\mathrm{BR(t \to Wb)}^{\mathrm{obs}}}{\sigma_{t\text{-ch,b}}\mathrm{BR(t \to Wb)}} \\ \mu_{sd} &= \frac{\sigma^{\mathrm{obs}}_{t\text{-ch,b}}\mathrm{BR(t \to Wsd)}^{\mathrm{obs}} + \sigma^{\mathrm{obs}}_{t\text{-ch,s,d}}\mathrm{BR(t \to Wb)}^{\mathrm{obs}}}{\sigma_{t\text{-ch,b}}\mathrm{BR(t \to Wsd)} + \sigma_{t\text{-ch,s,d}}\mathrm{BR(t \to Wb)}}, \end{aligned} \tag{5.19}$$

where $\mathrm{BR(t \to Wsd)}$ is the branching fraction for a top quark to decay to a W boson and either an s or d quark. Henceforth, the "obs" label will refer to the

Table 5.9: The sources and relative values in percent of the systematic uncertainty in the measurement of the $ST_{\mathrm{b,b}}$ cross section. The uncertainties are broken up into profiled and nonprofiled sources.

Treatment	Uncertainty	$\Delta\sigma_{ST_{\mathrm{b,b}}}/\sigma$ (%)
Profiled	Lepton trigger and reconstruction	0.50
	Limited size of simulated event samples	3.13
	$\mathrm{t\bar{t}}$ modelling	0.66
	Pileup	0.35
	QCD background normalisation	0.08
	W + jets composition	0.13
	Other backgrounds $\mu_{\mathrm{R}}/\mu_{\mathrm{F}}$	0.44
	PDF for background processes	0.42
	b tagging	0.73
	Total profiled	3.4
Nonprofiled	Integrated luminosity	2.5
	JER	2.8
	JES	8.0
	PDF for signal process	3.8
	Signal $\mu_{\mathrm{R}}/\mu_{\mathrm{F}}$	2.4
	ME-PS matching	3.7
	Parton shower scale	6.1
	Total nonprofiled	11.5
Total uncertainty		12.0

measured value of a quantity, and the absence of this label will mean the expected value. Equation (5.19) shows that the signal strengths are the ratios of the measured value of a quantity to the expected value.

One can write Eq. (5.19) more generally in terms of the top quark decay amplitudes or partial widths. The modulus of the matrix element from the partial width for each quark is factorised out. Thus, the top quark partial width to Wq can be written as $\Gamma_{\mathrm{q}} = \widetilde{\Gamma}_{\mathrm{q}}|V_{\mathrm{tq}}|^2$, where $\widetilde{\Gamma}_{\mathrm{q}}$ is the top quark partial width for $|V_{\mathrm{tq}}| = 1$. It is further assumed that $\widetilde{\Gamma}_{\mathrm{q}} = \widetilde{\Gamma}_{b}$, i.e. that any differences other than the CKM elements are negligible. Using this and the total width Γ_{t} of the top quark, we can

write Eq. (5.19) as:

$$\begin{aligned} \mu_b &= \frac{|V_{\mathrm{tb}}|^4_{\mathrm{obs}}\widetilde{\Gamma}^{\mathrm{obs}}_{\mathrm{q}}\Gamma_{\mathrm{t}}}{|V_{\mathrm{tb}}|^4\widetilde{\Gamma}_{\mathrm{q}}\Gamma^{\mathrm{obs}}_{\mathrm{t}}} \\ \mu_{sd} &= \frac{|V_{\mathrm{tb}}|^2_{\mathrm{obs}}\big(|V_{\mathrm{ts}}|^2_{\mathrm{obs}} + |V_{\mathrm{td}}|^2_{\mathrm{obs}}\big)\widetilde{\Gamma}^{\mathrm{obs}}_{\mathrm{q}}\Gamma_{\mathrm{t}}}{|V_{\mathrm{tb}}|^2\big(|V_{\mathrm{ts}}|^2 + |V_{\mathrm{td}}|^2\big)\widetilde{\Gamma}_{\mathrm{q}}\Gamma^{\mathrm{obs}}_{\mathrm{t}}}. \end{aligned} \tag{5.20}$$

The first fit extracts the signal strengths μ_b and μ_{sd}, whose values can be interpreted under different model assumptions. The signal strengths obtained are:

$$\begin{aligned} \mu_b &= 0.99 \pm 0.03\,(\mathrm{stat} + \mathrm{prof}) \pm 0.12\,(\mathrm{nonprof}) \\ \mu_{sd} &< 87 \text{ at } 95\% \text{ confidence level (CL)}, \end{aligned} \tag{5.21}$$

with a correlation factor of $\rho_{\mu_b,\mu_{sd}} = -0.25$. The first uncertainty on μ_b is the combination of the statistical and profiled systematic uncertainties, while the second is due to the nonprofiled systematic components. The upper limit on μ_{sd} takes into account both profiled and nonprofiled systematic uncertainties.

In the following, the signal extraction using the values of the CKM elements directly as parameters in the fit and applying constraints from the SM scenario and then two possible beyond-the-SM (BSM) extensions is described.

5.10.1 Measurement in the SM scenario

One can simplify Eq. (5.19) by assuming the SM unitarity constraint $|V_{\mathrm{tb}}|^2 + |V_{\mathrm{td}}|^2 + |V_{\mathrm{ts}}|^2 = 1$. The fit is repeated, taking $|V_{\mathrm{tb}}|$ as the single free parameter and replacing $|V_{\mathrm{td}}|^2 + |V_{\mathrm{ts}}|^2$ with $1 - |V_{\mathrm{tb}}|^2$. In this case, Eq. (5.19) becomes:

$$\begin{aligned} \mu_b &= \frac{|V_{\mathrm{tb}}|^4_{\mathrm{obs}}}{|V_{\mathrm{tb}}|^4} \\ \mu_{sd} &= \frac{|V_{\mathrm{tb}}|^2_{\mathrm{obs}}\big(1 - |V_{\mathrm{tb}}|^2_{\mathrm{obs}}\big)}{|V_{\mathrm{tb}}|^2\big(1 - |V_{\mathrm{tb}}|^2\big)}. \end{aligned} \tag{5.22}$$

The fit is only allowed to return values of $|V_{\mathrm{tb}}| \leq 1$, and the constraint $|V_{\mathrm{td}}|^2 + |V_{\mathrm{ts}}|^2 = 1 - |V_{\mathrm{tb}}|^2$ is imposed. Because of these constraints, Gaussian behaviour of the uncertainties cannot be assumed. Instead, pseudo-experiments are generated to evaluate the impact of nonprofiled uncertainties on the measurement, and the following confidence intervals are measured at 95% CL:

$$\begin{aligned} |V_{\mathrm{tb}}| &> 0.970 \\ |V_{\mathrm{td}}|^2 + |V_{\mathrm{ts}}|^2 &< 0.057. \end{aligned} \tag{5.23}$$

This measurement is comparable with the previous most precise estimate using $\mathrm{t\bar{t}}$ events from Ref. [47], and with the result of the combination of single top quark measurements in Ref. [43].

5.10.2 Measurements for two BSM scenarios

Any BSM contribution potentially enhancing $|V_{\mathrm{tb}}|^2$, $|V_{\mathrm{ts}}|^2$, or $|V_{\mathrm{td}}|^2$ can affect top quark production, decay, or both. Some BSM scenarios predict the presence of additional quark families. In this case, the CKM matrix is extended due to the mixing between the SM quarks and the new hypothesised ones. This would imply that the CKM matrix elements $|V_{\mathrm{tb}}|$, $|V_{\mathrm{ts}}|$, and $|V_{\mathrm{td}}|$ would not necessarily satisfy the unitarity constraint of $|V_{\mathrm{tb}}|^2 + |V_{\mathrm{ts}}|^2 + |V_{\mathrm{td}}|^2 = 1$. If these BSM quarks are heavier than the top quark, they would alter the CKM matrix elements without appearing as top quark decay products. They would thus not contribute directly to the top quark decay width Γ_{t}, but only indirectly because of the reduction in the absolute values of the corresponding SM CKM matrix elements.

For the first BSM scenario, it is assumed that the top quark decays through the same channels as in the SM case, and that the partial width of each decay only varies because of a modified CKM matrix element. In this case, by writing Γ_{t} and $\widetilde{\Gamma}_{\mathrm{q}}$ as a function of $|V_{\mathrm{tb}}|^2$ and $|V_{\mathrm{td}}|^2 + |V_{\mathrm{ts}}|^2$, Eq. (5.20) becomes:

$$\begin{aligned} \mu_{\mathrm{b}} &= \frac{|V_{\mathrm{tb}}|^4_{\mathrm{obs}}}{|V_{\mathrm{tb}}|^4\left(|V_{\mathrm{tb}}|^2_{\mathrm{obs}} + |V_{\mathrm{ts}}|^2_{\mathrm{obs}} + |V_{\mathrm{td}}|^2_{\mathrm{obs}}\right)} \\ \mu_{\mathrm{sd}} &= \frac{|V_{\mathrm{tb}}|^2_{\mathrm{obs}}\left(|V_{\mathrm{ts}}|^2_{\mathrm{obs}} + |V_{\mathrm{td}}|^2_{\mathrm{obs}}\right)}{\left(|V_{\mathrm{ts}}|^2 + |V_{\mathrm{td}}|^2\right)\left(|V_{\mathrm{tb}}|^2_{\mathrm{obs}} + |V_{\mathrm{ts}}|^2_{\mathrm{obs}} + |V_{\mathrm{td}}|^2_{\mathrm{obs}}\right)}. \end{aligned} \tag{5.24}$$

In this scenario, the measurement is performed leaving $|V_{\mathrm{tb}}|$ and $|V_{\mathrm{td}}|^2 + |V_{\mathrm{ts}}|^2$ as free parameters in the fit, resulting in:

$$\begin{aligned} |V_{\mathrm{tb}}| &= 0.988 \pm 0.027\,(\mathrm{stat} + \mathrm{prof}) \pm 0.043\,(\mathrm{nonprof}) \\ |V_{\mathrm{td}}|^2 + |V_{\mathrm{ts}}|^2 &= 0.06 \pm 0.05\,(\mathrm{stat} + \mathrm{prof})\,^{+0.04}_{-0.03}\,(\mathrm{nonprof}). \end{aligned} \tag{5.25}$$

In the second BSM scenario, the top quark partial width is unchanged, but the total width increases due to additional, undetected decays. In the fit, the partial widths for decays to known quarks are fixed, and the total width is a free parameter and allowed to vary. The effects on Γ_{t} due to variations in $|V_{\mathrm{tb}}|^2$, $|V_{\mathrm{td}}|^2$, and $|V_{\mathrm{ts}}|^2$ are neglected.

In this scenario, Eq. (5.20) is modified to:

$$\begin{aligned} \mu_{\mathrm{b}} &= \frac{|V_{\mathrm{tb}}|^4_{\mathrm{obs}}\Gamma_{\mathrm{t}}}{|V_{\mathrm{tb}}|^4\Gamma^{\mathrm{obs}}_{\mathrm{t}}} \\ \mu_{\mathrm{sd}} &= \frac{|V_{\mathrm{tb}}|^2_{\mathrm{obs}}\left(|V_{\mathrm{ts}}|^2_{\mathrm{obs}} + |V_{\mathrm{td}}|^2_{\mathrm{obs}}\right)\Gamma_{\mathrm{t}}}{|V_{\mathrm{tb}}|^2\left(|V_{\mathrm{ts}}|^2 + |V_{\mathrm{td}}|^2\right)\Gamma^{\mathrm{obs}}_{\mathrm{t}}}. \end{aligned} \tag{5.26}$$

Using $|V_{\mathrm{tb}}|^2$, $|V_{\mathrm{td}}|^2 + |V_{\mathrm{ts}}|^2$, and $R_\Gamma = \Gamma^{\mathrm{obs}}_{\mathrm{t}}/\Gamma_{\mathrm{t}}$ as the free parameters in the fit,

one obtains:

$$\begin{aligned} |V_{\mathrm{tb}}| &= 0.988 \pm 0.011\,(\mathrm{stat} + \mathrm{prof}) \pm 0.021\,(\mathrm{nonprof}) \\ |V_{\mathrm{td}}|^2 + |V_{\mathrm{ts}}|^2 &= 0.06 \pm 0.05\,(\mathrm{stat} + \mathrm{prof}) \pm 0.04\,(\mathrm{nonprof}) \\ R_{\Gamma} &= 0.99 \pm 0.42\,(\mathrm{stat} + \mathrm{prof}) \pm 0.03\,(\mathrm{nonprof}). \end{aligned} \tag{5.27}$$

The measured correlation factors between the three parameters are $\rho_{|V_{\mathrm{tb}}|,|V_{\mathrm{td}}|^2} = -0.19$, $\rho_{|V_{\mathrm{tb}}|,R_{\Gamma}} = -0.78$, and $\rho_{R_{\Gamma},|V_{\mathrm{td}}|^2} = -0.21$. This measurement is in good agreement with the other measurements from Refs. [43, 47, 164, 165], which however make use of the SM assumptions. The results for the second BSM scenario have a higher statistical precision than those for the first scenario because of the weaker dependence of the signal strength on $|V_{\mathrm{tb}}|$ for the first scenario.

Constraints on $|V_{\mathrm{td}}|$ and $|V_{\mathrm{ts}}|$ from precision low-energy measurements do not necessarily hold when BSM particles are present in the relevant Feynman diagram loops. Theoretical studies have shown that values of $|V_{\mathrm{ts}}|$ up to about 0.2 are possible in some BSM scenarios [166]. The measurements presented here establish a model-independent upper limit on $|V_{\mathrm{td}}|$ and $|V_{\mathrm{ts}}|$ by removing any assumed theoretical hypotheses. This will now allows new interpretations for possible mixing of SM and BSM processes.

Alternative approaches interpret the available single top quark measurements in terms of different scenarios for modifying the CKM matrix elements (see, for example, Ref. [167]), obtaining results that are comparable with the measurements obtained. Such approaches, however, do not allow changes in the decay vertex of the top quark, and do not consider possible similarities in the features of the $ST_{\mathrm{b,q}}$ signal and background processes.

The current analysis improves the precision on $|V_{\mathrm{tb}}|$ by 50% with respect to previous studies [34] by exploiting the tWb vertex in the top quark decay, and is more precise than the combined ATLAS and CMS measurement using data at $\sqrt{s} = 7$ and 8 TeV [43].

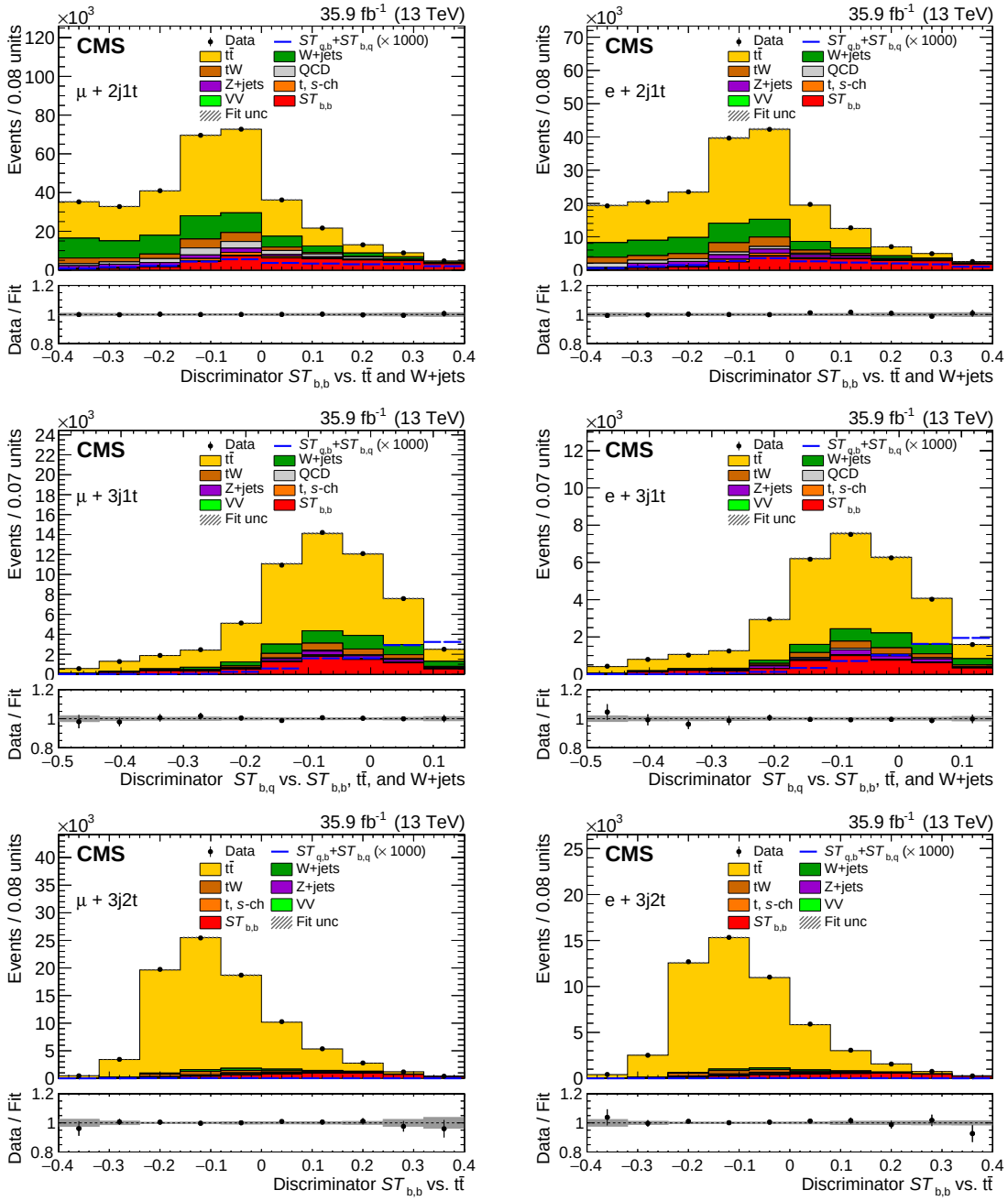

Figure 5.19: Distribution of the multivariate discriminators, comparing data to simulation normalised after the fit procedure, for the muon channel on the left and for the electron channel on the right, for 2-jets–1-tag (upper), 3-jets–1-tag (middle), and 3-jets–2-tag (lower). The vertical lines on the points and the hatched bands show the experimental and fit uncertainties, respectively. The expected distribution from the $ST_{\mathrm{q,b}} + ST_{\mathrm{b,q}}$ processes (multiplied by a factor of 1000) is shown by the solid blue line. The lower panels show the ratio of the data to the fit.

Chapter 6

Search for a new W′ boson coupling to tb

Despite the remarkable success the SM achieved in the description of Nature, it is not sufficient to explain the current picture of fundamental particle physics. Several other models arose providing an explanation of the open issues within the SM, and introduce new particles in the LHC energy range, as discussed in Sec. 2.1. Amongst such models, particularly interesting are the ones predicting the existence of new massive bosons, called Z′ and W′, with properties similar to the SM EW bosons. These bosons can be detected by the CMS experiment by performing a "bump hunt" search over a continuous background in case of narrow width resonance. Many studies of this type have already been performed at the LHC, but no significant excess has been found, cfr Sec. 2.4. The possibility remains of new physics not manifesting in a clear way as a peak in the invariant mass distribution, for example in case of wide width resonance. In this case, the technique of the bump hunting is not optimal, as the peak can be smeared becoming indistinguishable from a smooth deviation from the SM spectrum, as reported in Ref. [168]. In this case, the study of the couplings of these new particles with the SM ones, and the investigation of the spin-angular properties of the decay products can improve the sensitivity of the search. A particularly important role is played in this context by the top quark, that on one side has a strong coupling to the W′ and Z′ bosons, due to its large mass, on the other has a very distinct signature due to its decay chain that can be fully reconstructed in the detector This study focuses on the leptonic decay chains of hypothesised W′ boson, i.e. qq'→ W′ →tb→Wbb→ $\ell\nu$bb, where ℓ stands for e and μ including the leptonic decays of the τ lepton. The aim of this study is to investigate the properties of the final state and to obtain stringent exclusion limit of the existence of these new particle.

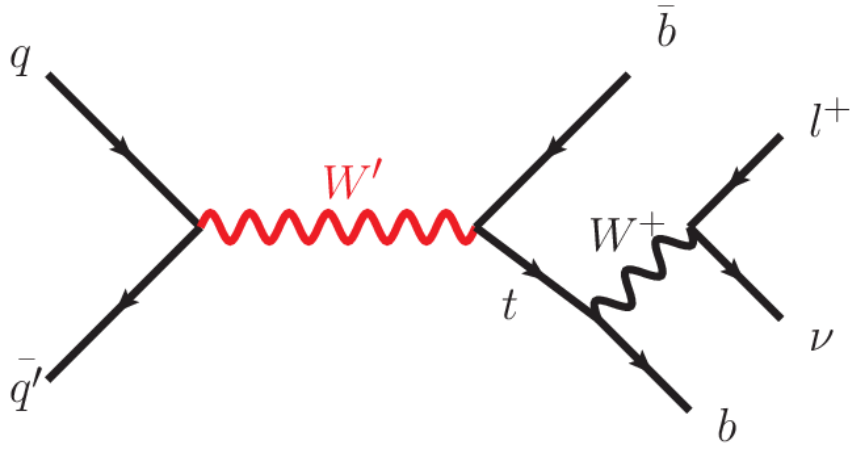

Figure 6.1: Leading Feynman diagram for the W′ production in the $s-$channel.

6.1 Process and final state

The advantage of an hadron collider in searches for new physics is that the momentum of the colliding partons is not fixed, so a wide range of masses for new particles is accessible and predictions from many models can be tested. At the LHC, the main production channel for a real (on-shell) W′ boson is the $s-$channel. This type of process allows to probe the mass of the hypothesised particle from its decay products. One of the most promising avenues for W′ searches is through its decays via third generation quarks, W′ →tb. The representative Feynman diagram at LO for the process under study is reported in Fig. 6.1. This channel has relatively small QCD multijet background comparing to to the channel W′ → ud, cs.

6.2 Analysis of CMS data

The analysis makes use of p-p collision data at $\sqrt{s} = 13$ TeV, corresponding to an integrated luminosity of 137.2 fb^{-1}, collected from 2016 to 2018 by the CMS experiment at the LHC. They are collected with triggers requiring either one muon or electron, or large amounts of hadronic activity HT in the final state. Table 6.1 shows the list of primary datasets employed in the analysis.

6.3 Physics objects and triggers

In order to define a sample enriched in signal events, a first set of selection requirements are designed to identify the final state objects that could come from

Dataset	Run	Integrated luminosity (fb^{-1})
SingleMuon(Electron/Photon)-JetHT	2016 B	5.8
SingleMuon(Electron/Photon)-JetHT	2016 C	2.6
SingleMuon(Electron/Photon)-JetHT	2016 D	4.2
SingleMuon(Electron/Photon)-JetHT	2016 E	4.0
SingleMuon(Electron/Photon)-JetHT	2016 F	3.1
SingleMuon(Electron/Photon)-JetHT	2016 G	7.5
SingleMuon(Electron/Photon)-JetHT	2016 H	8.6
SingleMuon(Electron/Photon)-JetHT	2017 B	4.8
SingleMuon(Electron/Photon)-JetHT	2017 C	9.6
SingleMuon(Electron/Photon)-JetHT	2017 D	4.3
SingleMuon(Electron/Photon)-JetHT	2017 E	9.3
SingleMuon(Electron/Photon)-JetHT	2017 F	13.5
SingleMuon(Electron/Photon)-JetHT	2018 A	14.0
SingleMuon(Electron/Photon)-JetHT	2018 B	7.1
SingleMuon(Electron/Photon)-JetHT	2018 C	6.9
SingleMuon(Electron/Photon)-JetHT	2018 D	31.9

Table 6.1: List of primary datasets of p-p collisions data produced at $\sqrt{s} = 13$ TeV and collected by CMS from 2016 to 2018 employed in the analysis. Collected data correspond to an integrated luminosity of 137.2 fb^{-1}.

a W′ boson candidate decay. Events are therefore retained if their final state presents exactly one lepton, muon or electron, at least 2 jets, and an amount of missing transverse energy, attributed to the escaping neutrino. Events are selected if a primary vertex is reconstructed and the noise filters are passed as reported in Sec. 4.1 and Sec. 4.6.

6.3.1 Trigger

Events are required to pass a combination of electron, photon, muon or hadronic triggers. According to this criterion, muons reconstructed by the offline trigger algorithm are selected if they pass a 50 GeV threshold in p_{T}, while electrons passing a higher threshold of 115 GeV are chosen. In order to recover lower p_{T} electrons, triggers including isolation criteria are also used. The hadronic triggers make use of the variable H_{T} defined as the transverse component of the total four-momentum of the reconstructed jets in the event. All the trigger paths used are reported in Table 6.2.

Purpose	Path	Year
High p_{T} electron	HLT_Ele115_CaloIdVT_GsfTrkIdT or HLT_Photon175	2016
	HLT_Ele115_CaloIdVT_GsfTrkIdT or HLT_Photon200	2017C to F, 2018
Low p_{T} electron	HLT_Ele27_WPTight_Gsf	2016
	HLT_Ele35_WPTight_Gsf	2017, 2018
Muon	HLT_Mu50 or HLT_TkMu50(from run 274954)	2016
	HLT_Mu50	2017B
	HLT_Mu50 or HLT_TkMu100 or HLT_OldMu100	2017C to F, 2018
HT	HLT_PFHT800 or HLT_PFHT900	2016B to F
	HLT_PFHT900	2016G
	HLT_PFHT780 or HLT_PFHT890	2017, 2018

Table 6.2: Complete list of trigger paths required for the analysis.

The trigger for high-p_{T} electrons needs to take into account the fact that, at large transverse moment, electrons can be reconstructed as photons by the algorithm used online at HLT level. Therefore, both electron and photon paths are used for the high-end of the specturm. In order to take into account differences between simulation and Data, trigger scale factors are derived ad hoc for this analysis, and the procedure is described in Sec. 6.5.1.

6.3.2 Electrons

Events with exactly one electron with $p_{\mathrm{T}} > 50$ GeV within a pseudorapidity acceptance $|\eta| < 2.2$ and passing the MVA NoIso WP90, as defined in Sec. 4.3, are selected. Furthermore, electrons in the barrel-endcap gap at $1.4442 < |\eta| < 1.566$

are excluded from the selection. In order to distinguish between prompt leptons from ones coming from secondary decay chains, usually included into a jet, one uses the isolation. But in this case, the electrons coming from the W′ decay chain, come from objects with a large boost, and they are often overlapped with a jet produced in the same decay chain, failing a standard isolation cut. A special isolation criterion, called "Mini isolation", is adopted, which allows to recover efficiency when leptons are produced in the decay chain of a boosted object. It is constructed by defining a cone whose radius varies with the p_{T} of the lepton as follows:

- 0.2 for lepton with $p_{\mathrm{T}} \leq 50$ GeV,
- 10 GeV/p_{T} for lepton with $50 < p_{\mathrm{T}} < 200$ GeV,
- 0.05 for lepton with $p_{\mathrm{T}} \geq 200$ GeV.

Isolation is then calculated for that lepton on that cone, reducing the probability of the overlap for more boosted topologies. For this analysis, electrons are required to have a mini isolation $I^{\mathrm{e}}_{\mathrm{mini}} < 0.1$, according to the studies reported in Appendix A.1.

6.3.3 Muons

Events with exactly one muon within the $|\eta| < 2.4$ region and reconstructed as tight muon by the PF algorithm as defined in Sec. 4.2 are considered. In order to be in the region with best trigger efficiency, they are required to have a $p_{\mathrm{T}} > 55$ GeV. Similarly as for the electrons, they must also have a mini isolation $I^{\mu}_{\mathrm{mini}} < 0.1$.

6.3.4 Veto on additional leptons

Events containing additional leptons besides either one muon or one electron as defined above, are removed from selection since they could increase contamination from dileptonic $\mathrm{t\bar{t}}$ background. Veto muons are defined as passing the loose identification criteria defined in Sec. 4.2 with $p_{\mathrm{T}} > 30$ GeV, and $I^{\mu}_{\mathrm{mini}} < 0.4$. In order to avoid overlap, they are also required not to pass the tight WP. Additional electrons pass the MVA NoIso WPLoose with $p_{\mathrm{T}} > 35$ GeV, $|\eta| < 2.2$, and $I^{\mathrm{e}}_{\mathrm{mini}} < 0.4$ are vetoed too. They are required to do not pass the MVA NoIso WP90 to avoid overlap.

6.3.5 Jets

Jets are reconstructed by the PF algorithm with the anti-k_{T} algorithm as described in Sec. 4.5. Two types of jets definitions are used in the analysis:

- jets clustered with a cone parameter of $R = 0.4$ (AK4 jets) are considered to search for b-jets coming from the W′ decay vertex, or from the jets from the top quark decay chain;
- jets clustered with a cone parameter of $R = 0.8$ (AK8 jets) are also used in the analysis, first to perform a loose preselection, and then in the final stages of the selection selection to veto hadronic top quarks coming from SM backgrounds.

Pileup contamination in AK4 jets is subtracted by making use of CHS algorithm, while the PUPPI one is used for AK8 jets.

Jets in both collections are required to pass a set of identification criteria corresponding to the "tight" working point. AK4 jets are considered for analysis with $|\eta| < 2.4$ and it is required that at least two of them have $p_{\mathrm{T}} > 100$ GeV. The presence of at least 2 AK8 jets is also required to reduce contamination from low-energy $\mathrm{t\bar{t}}$ and QCD events, while having a selection efficiency for W′ processes of 99.8%. This requirement comes from the fact that for signal, given the high boost of the decay products, the top decay products are reconstructed inside larger-radius jets and the b quark coming from W′ decay transports a large amount of energy and its shower has a larger area.

6.3.6 b tagging

In the signal final state, the two jets from W′ boson and top quark decay vertices come from the hadronisation of a b-quark.

AK4 jets within $|\eta| < 2.4$ are also considered for b-tagging, and the DeepCSV and DeepFlavor algorithms have both been studied. The study is reported in the appendix, Sec. A.1. The threshold that has been elected to define jets as b-jets corresponds to the medium working point of the DeepFlavor algorithm. The discriminant score, labelled as "DeepFlv", must be > 0.2770 for 2016, 2017, and 2018. This thresholds yields approximately a 1% mistag rate. In appendix Sec. A.1 more details are also given for the efficiency and mistag working points as a function of the jet transverse momentum.

In order to account for the different b-tagging efficiencies in data and MC, scale factors for b-jets, c-jets and light jets are employed to reweight MC events, with the same procedure already explained in Sec. 5.3.6.

6.3.7 Missing transverse energy

The PF-based $\vec{p}_{\mathrm{T}}^{\,miss}$ is the opposite of the vectorial sum of the transverse momenta of the identified PF particles, and it modulus is referred to as p_{T}^{miss}. It

Object	Requirements	Counts μ	Counts e
Tight muon	$p_{\mathrm{T}} > 55$ GeV $\quad \lvert\eta\rvert < 2.4 \quad I^{\mu}_{\mathrm{mini}} < 0.1$	1	0
Loose muon	$p_{\mathrm{T}} > 30$ GeV $\quad \lvert\eta\rvert < 2.4 \quad I^{\mu}_{\mathrm{mini}} < 0.4$	0	0
MVA WP80 NoIso electron	$E_{\mathrm{T}} > 35$ GeV $\quad \lvert\eta\rvert < 2.2 \quad I^{\mathrm{e}}_{\mathrm{mini}} < 0.1$	0	1
MVA WPLoose NoIso electron	$E_{\mathrm{T}} > 35$ GeV $\quad \lvert\eta\rvert < 2.2 \quad I^{\mathrm{e}}_{\mathrm{mini}} < 0.4$	0	0
p_{T}^{miss}	$p_{\mathrm{T}} > 50$ GeV		
Jet	$p_{\mathrm{T}} > 100$ GeV $\quad \lvert\eta\rvert < 2.4$	≥ 2	
b-jet	$p_{\mathrm{T}} > 100$ GeV $\quad \lvert\eta\rvert < 2.4 \quad$ DeepFlv ≥ 0.2770	≥ 0	

Table 6.3: Summary of all the physics objects defined, their corresponding selection requirements, and the number of candidate required for the muon and electron channels.

is assumed to be the momentum due to the neutrinos, escaping from the detectors without interacting. The signature of the signal processes is expected to have a significant amount of p_{T}^{miss}. A requirement of this variable can help reducing the contamination from QCD background processes, mainly $\mathrm{b\bar{b}}$ and $\mathrm{c\bar{c}}$, from which instead p_{T}^{miss} is expected to only to come from non-prompt neutrinos and resolution effects, yielding much lower values than the signal process. For this reason, it is requested $p_{\mathrm{T}}^{miss} > 120$ GeV.

All the physics objects and their selection requirements are summarised in Table 6.3.

6.4 Background description

The main sources of background that present a final state mimicking the one expected from the W′ decay are:

- $\mathrm{t\bar{t}}$: the production of a top quark-antiquark pair represents the main background source. Events where one top quark has a lepton in the decay chain and the other one decays to hadronic final states closely mimic the signal signature. The presence of two b-jets in the final state is a further challenge to discrimination of this background. Additional contamination comes from dileptonic decays where a lepton is not reconstructed or out of analysis acceptance.

- W + jets: processes where a W boson is produced is association with quarks, especially heavy flavour quarks, constitute the second main background together with $\mathrm{t\bar{t}}$. The W boson leptonic decay chain is the same as the one present in the signal processes and, if b-jets are reconstructed in the same

event, the final topology of the signal is matched in terms of physics objects content. An important feature is the absence of the top quark, that can be exploited to discriminate this type of background.

- QCD: strong interaction processes producing a quark-antiquark pair are also a background source. Nevertheless it is rare that these events have an high-p_{T} lepton in the final state and a significant amount of p_{T}^{miss}. The reconstructed invariant mass of the top quark is a powerful variable against this background.

- single top quark processes: both $t-$channel and tW associate productions have the same signature as the signal. The $s-$channel is instead the same process as signal but the interaction proceeds via a virtual W boson.

- Other minor backgrounds, like double vector boson production, are neglected since their production cross sections are much smaller than the processes listed above, and they could contribute to the final selection only in very rare final state topologies.

6.5 Simulated samples

Monte Carlo event generators are used to simulate signal and background samples. Single top quark and top quark pair production events are simulated as already described in Sec. 5.5. Simulated event samples with W boson in association with jets ($\mathrm{W}+\mathrm{jets}$) are generated using MadGraph5_MC@NLO 2.2.2. For these processes, events with up to two additional partons emitted in the hard scattering are simulated, and the FxFx merging scheme [150] is used to avoid double counting with parton emissions generated in the parton showering. Simulated QCD multijet events are generated at LO with PYTHIA 8.180 as a function of the HT activity of the event. For 2017 and 2018, the tune CP5 [169] is used for all the samples. The default parametrisation of the PDFs, the detector simulation and the pileup simulation are performed analogously as described in Sec. 5.5. Table 6.4 summarises the details of the simulations for the samples used in the analysis.

6.5.1 Data-MC corrections

Simulation is corrected to take into account several experimental effects which change year-by-year, due to the altered experimental conditions. For many of the corrections, scale factors are provided by the CMS Collaboration, and these are not described in detail. At this category belongs scale factors for muon and

Process	Matrix Element	Matching Method	Parton Shower	Tune	Cross Section × BR (pb)
pp→t$\bar{\text{b}}$	POWHEG-MadSpin	-	PYTHIA	CUETP8M1/CP5	136.02 (NLO)
pp→ $\bar{\text{t}}$b	POWHEG-MadSpin	-	PYTHIA	CUETP8M1/CP5	80.95 (NLO)
pp→tW	POWHEG	-	PYTHIA	CUETP8M1/CP5	35.6 (NLO)
pp→ $\bar{\text{t}}$W	POWHEG	-	PYTHIA	CUETP8M1/CP5	35.6 (NLO)
pp→tb→ $\ell\nu$bb (s-ch.)	MC@NLO	-	PYTHIA	CUETP8M1/CP5	10.32 (NLO)
pp→Wq→ $\ell\nu$j $70 < H_{\text{T}} < 100$	MC@NLO	FxFx	PYTHIA	CUETP8M1/CP5	1353.0 * 1.21
pp→Wq→ $\ell\nu$j $100 < H_{\text{T}} < 200$	MC@NLO	FxFx	PYTHIA	CUETP8M1/CP5	1345 * 1.21
pp→Wq→ $\ell\nu$j $200 < H_{\text{T}} < 400$	MC@NLO	FxFx	PYTHIA	CUETP8M1/CP5	359.7 * 1.21
pp→Wq→ $\ell\nu$j $400 < H_{\text{T}} < 600$	MC@NLO	FxFx	PYTHIA	CUETP8M1/CP5	48.91 * 1.21
pp→Wq→ $\ell\nu$j $600 < H_{\text{T}} < 800$	MC@NLO	FxFx	PYTHIA	CUETP8M1/CP5	12.05 * 1.21
pp→Wq→ $\ell\nu$j $800 < H_{\text{T}} < 1200$	MC@NLO	FxFx	PYTHIA	CUETP8M1/CP5	5.501 * 1.21
pp→Wq→ $\ell\nu$j $1200 < H_{\text{T}} < 2500$	MC@NLO	FxFx	PYTHIA	CUETP8M1/CP5	1.329 * 1.21
pp→Wq→ $\ell\nu$j $H_{\text{T}} > 2500$	MC@NLO	FxFx	PYTHIA	CUETP8M1/CP5	0.03216 * 1.21
pp→t$\bar{\text{t}}$	POWHEG	-	PYTHIA	CUETP8M2T4/CP5	831.8 (NLO)
pp→t$\bar{\text{t}}$ $700 < m_{\text{t}\bar{\text{t}}} < 1000$	POWHEG	-	PYTHIA	CUETP8M2T4/CP5	80.5 (NLO)
pp→t$\bar{\text{t}}$ $m_{\text{t}\bar{\text{t}}} > 1000$	POWHEG	-	PYTHIA	CUETP8M2T4/CP5	21.3 (NLO)
pp→q$\bar{\text{q}}$ $300 < H_{\text{T}} < 500$	MC@NLO	-	PYTHIA	CUETP8M2T4/CP5	347700 (NLO)
pp→q$\bar{\text{q}}$ $500 < H_{\text{T}} < 700$	MC@NLO	-	PYTHIA	CUETP8M2T4/CP5	32100 (NLO)
pp→q$\bar{\text{q}}$ $700 < H_{\text{T}} < 1000$	MC@NLO	-	PYTHIA	CUETP8M2T4/CP5	6831 (NLO)
pp→q$\bar{\text{q}}$ $1000 < H_{\text{T}} < 1500$	MC@NLO	-	PYTHIA	CUETP8M2T4/CP5	1207 (NLO)
pp→q$\bar{\text{q}}$ $1500 < H_{\text{T}} < 2000$	MC@NLO	-	PYTHIA	CUETP8M2T4/CP5	119.9 (NLO)
pp→q$\bar{\text{q}}$ $H_{\text{T}} > 2000$	MC@NLO	-	PYTHIA	CUETP8M2T4/CP5	25.24 (NLO)

Table 6.4: Simulated samples used for the three years in the analysis.

electron ID and isolation, pile-up reweighting, b-tagged or mis-tagged corrections, and JECs and JERs. Others corrections are specifically derived for this analysis and they are described in the following.

HEM15/16 issue in 2018

In 2018 Runs C and D, two sections of the Hadron Endcap have ceased functioning from run 319077 onward. In order to take this into account, events in these runs are vetoed when presenting one electron or one tight jet, as defined in Sec 6.3.2 and in Sec. 6.3.5 respectively, in the region $-3.2 < \eta < -1.3$ and $-1.57 < \phi < -0.87$. Simulated events with 2018 MC where an electron or jet falls in this region are weighted by the luminosity corresponding to the data period up to run 319077. This corresponds approximately to 35% of the total 2018 sample.

Figure 6.2 shows the effect of such correction on electron distributions.

Trigger efficiency measurement

The trigger efficiency has been measured by considering an orthogonal sample with respect to the one used for this analysis.

A selection requiring:

- 1 tight muon and 1 tight electron
- at least 2 jets with $p_{\text{T}} > 100$ GeV and $|\eta| < 2.4$

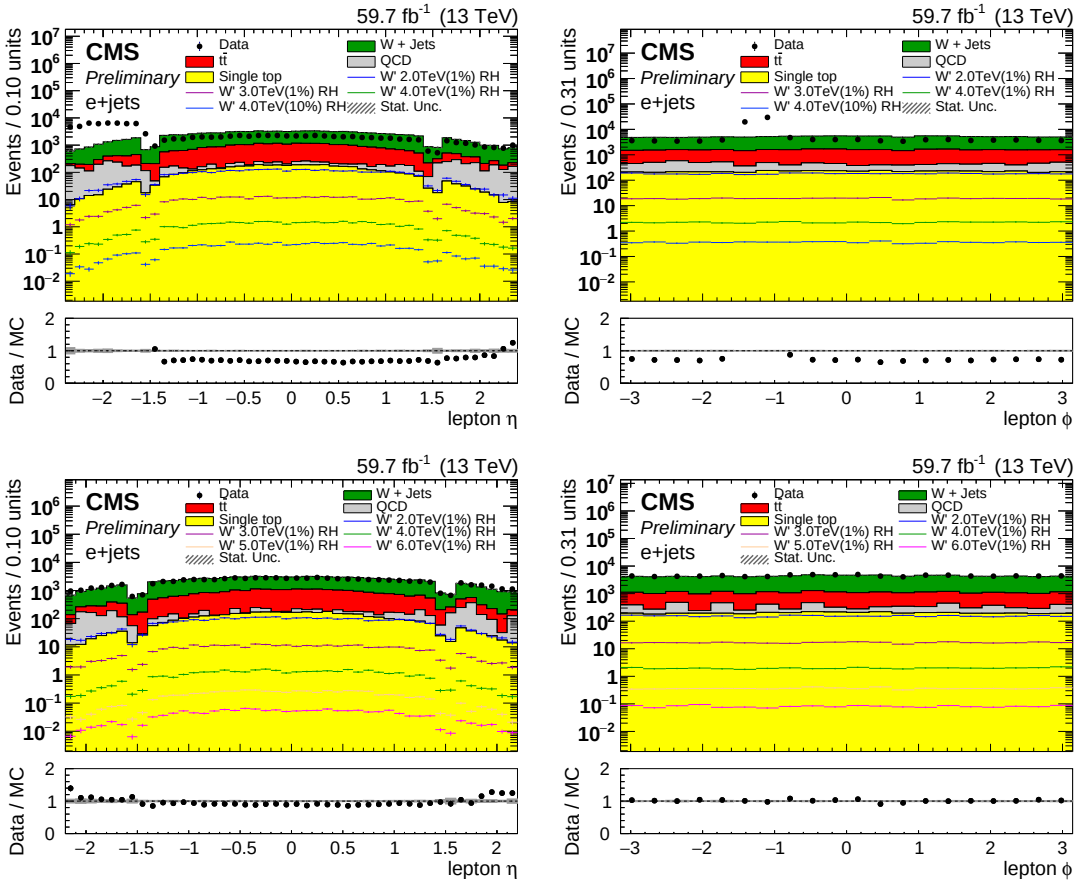

Figure 6.2: Distribution of electron η (left) and ϕ (right) before (top plots) and after (bottom plots) applying the correction described in Sec. 6.5.1.

This selection is applied to data samples described in Table 6.1, as well as on di-lepton $t\bar{t}$ samples. The efficiency is then derived as:

$$\epsilon = \frac{N_{pass}}{N_{total}}, \tag{6.1}$$

where for:

- Muon trigger efficiency: N_{total} is defined as the number of events in which the electron or photon triggers are fired and electron has $p_{\mathrm{T}} > 50$ GeV and N_{pass} is found by additionally requiring the muon or HT trigger are fired too;
- Electron trigger efficiency: N_{total} is defined as the number of events in which the muon trigger is fired and muon has $p_{\mathrm{T}} > 55$ GeV and N_{pass} is found by additionally requiring the electron or photon or HT trigger are fired too.

For this measurement, dedicated samples of di-leptonic $t\bar{t}$ MC are used while for Data the same samples used for the analysis have been considered. In order to have the most precise tuning of MC samples to reproduce the data, the trigger efficiency has been derived with p_{T}-$|\eta|$ dependence for muons and $|\eta|$-p_{T} for electrons. The different treatment for muons and electrons is done to be coherent with other corrections provided by CMS Collaboration. Figures 6.3, 6.4, and 6.5 show the trigger efficiency and scale factors for the three years.

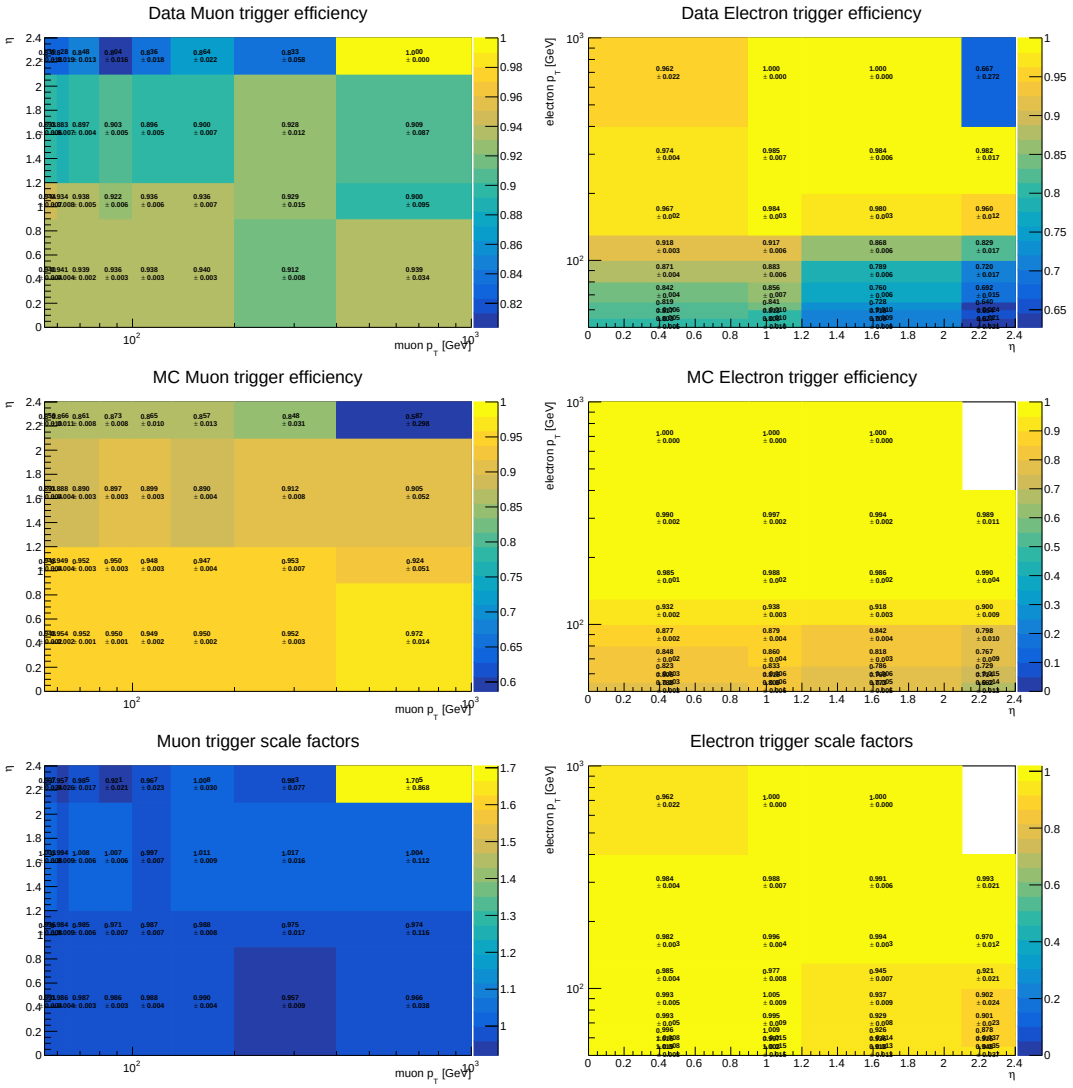

Figure 6.3: Trigger efficiency for data (top), $t\bar{t}$ (mid), and scale factor (bottom) in 2016 for muons (left), and electrons (right).

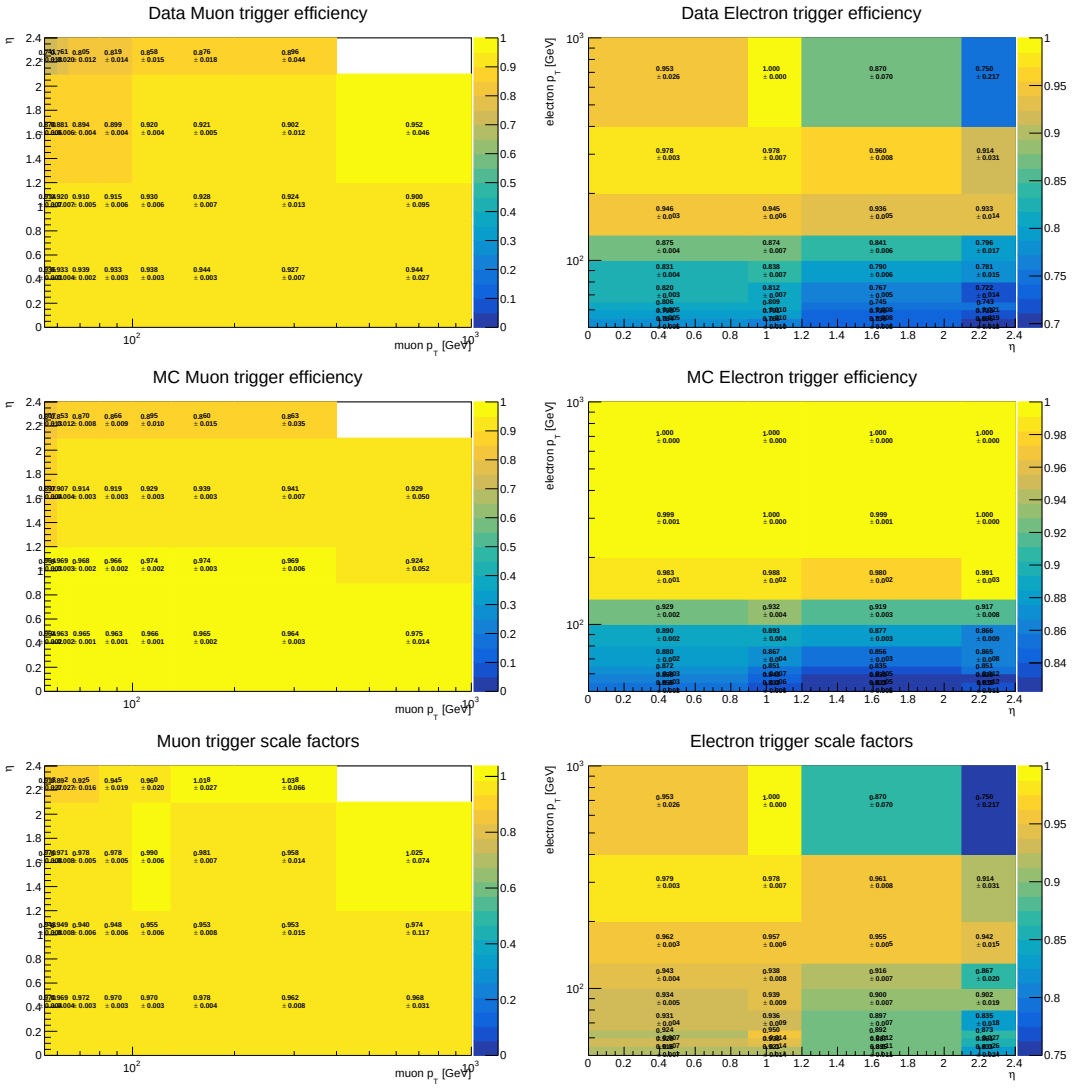

Figure 6.4: Trigger efficiency for data (top), $t\bar{t}$ (mid), and scale factor (bottom) in 2017 for muons (left), and electrons (right).

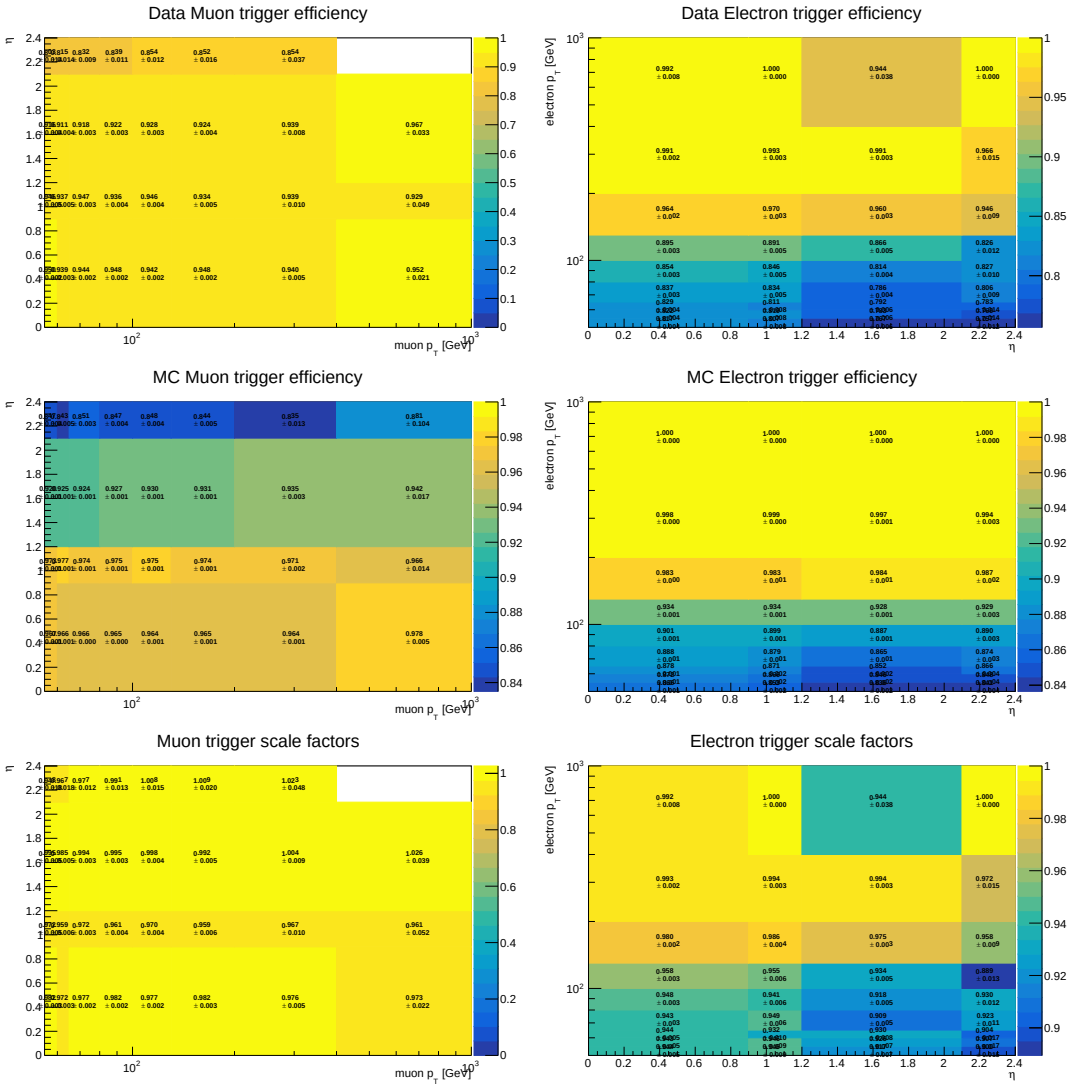

Figure 6.5: Trigger efficiency for data (top), $t\bar{t}$ (mid), and scale factor (bottom) in 2018 for muons (left), and electrons (right).

6.5.2 Physics selection

The physics selection aims at reducing backgrounds, in particular QCD multijet and low-H_T backgrounds, while retaining all relevant physics information for the signal. It is tailored on the features of the signal, in particular:

- the AK4 jet coming from the W′ boson decay is expected to be the most energetic (leading), since it carries about half of the energy of the W′ boson; so a leading AK4 jet $p_T > 300$ GeV requirement is applied.

- the AK4 jet coming from the top quark decay is expected to be the second in p_{T} (subleading): in this case the subleading AK4 jet is required to have $p_{\mathrm{T}} > 150$ GeV.

6.6 W′ reconstruction

After the physics selection on leptons, jet and p_{T}^{miss} is applied, these objects are used to reconstruct the W boson, the top quark and the W′ boson.

W boson reconstruction

The reconstruction of the W boson proceeds as described in Sec. 5.6.1.

In the case Eq. 5.14 returns two real solutions for $p_{z,\nu}$ (in 65% of all cases), the best W boson candidate is found by minimising the quantity:

$$\chi_{m_{\mathrm{W}}} = |m_{\mathrm{W}} - m_{\mathrm{W}i}|, \tag{6.2}$$

where $m_{\mathrm{W}i}$ is the mass of the reconstructed W boson with the $i-$th solution for $p_{z,\nu}$ and m_{W} the nominal mass of the W boson.

In case of imaginary solutions for $p_{z,\nu}$, the same strategy is followed as described in Sec. 5.6.1.

6.6.1 Top quark candidate reconstruction

After the reconstruction of both the unobserved neutrino and the W boson, the second step is the evaluation of the top quark four-momentum. It is crucial to choose the AK4 jet, referred to as $\mathrm{jet_{top}}$, which has to be coupled with the reconstructed W boson. By taking into account the features of a top quark decay, and the energy scale of the process it comes from, the three following criteria are deployed in parallel for the association:

- **chimass criterion**: as the W boson and the candidate jet are products of the top quark decay, one expects the invariant mass of the sum of the corresponding four-momenta to be as close as possible to the nominal value of the top quark mass, taken as 172.5 GeV. The $\mathrm{jet_{top}}$ can be chosen as the one minimising the quantity:

  $$\chi_{m_{\mathrm{t}}} = |m_{\mathrm{t}} - m_{\mathrm{t}i}| \tag{6.3}$$

  where $m_{\mathrm{t}i}$ is the mass of the reconstructed W boson with the $i-$th AK4 jet. Effects due to experimental and theoretical uncertainties on the top quark mass are expected to be of orders of magnitude smaller with respect to the experimental resolution of top quark mis-matching effects.

- **closest criterion**: the jet produced by the b quark is expected to be very close to the lepton produced in semileptonic top quark decay. Then the top quark four-momentum can be obtained by combining the reconstructed W boson and the closest jet, in ΔR, to the lepton.

- **subleading criterion**: considering the production and decay chain investigated in this study, the jets originate by either one of the two b quarks produced in the W′ decay final state. Given the energy scales of the hypothesised W′ decay chain, one expects the b-jets to be the two highest-p_{T} ones in the event. In particular, the leading AK4 jet in p_{T} is expected to be produced by the b quark coming from W′ boson, the second (i.e. subleading) one by the b quark coming from top quark decay. As a consequence, the subleading AK4 jet in p_T is chosen to properly reconstruct the top quark quark.

If the same AK4 jet satisfies at least two criteria, it is chosen to reconstruct the top quark four momentum. Instead if three different AK4 jets are selected by the criteria, the one pointed by the chimass criterion is selected as $\mathrm{jet_{top}}$. Figure 6.6 shows the top quark reconstructed mass for all years.

In order to reconstruct the W′ candidate in the event, another AK4 jet is needed, referred to as $\mathrm{jet_{W'}}$. This AK4 jet is chosen as the one with the highest-p_{T} in the jet collection after the choice of the $\mathrm{jet_{top}}$. The jet collection, in which the $\mathrm{jet_{top}}$ and $\mathrm{jet_{W'}}$ are selected, is composed of only AK4 b-jets, if in the event there are at least two AK4 b-jets. In the opposite case, the jet collection is composed of all the AK4 jets in the event, regardless their b-tagging values. This choice is motivated by the final state of the signal process, in which both jets should be b-jets. So, if a signal event has at least two AK4 jets passing the b-tagging requirements, and one of them is not selected to be the $\mathrm{jet_{top}}$, this is much more likely to happen because it fails the selection criteria rather than the b-tagging algorithm.

6.6.2 Event classification

The events are divided in categories depending on whether the AK4 jets that are tagged as b, are also tagged as $\mathrm{jet_{top}}$, or $\mathrm{jet_{W'}}$. The categories are:

- SR2B: at least two b jets are reconstructed in the event and both the $\mathrm{jet_{top}}$ and $\mathrm{jet_{W'}}$ are b tagged jets; this is the main signal region.

- SRT: only 1 jet is reconstructed as a b jet and it is the $\mathrm{jet_{top}}$.

- SRW: the $\mathrm{jet_{W'}}$ is a b jet and it is the only b jet in the events.

- CR0B: no b jet is reconstructed in the event; this category has a small contamination from signal and it is mainly used as a validation region for the analysis strategy.

The categories are also reported in Tab. 6.5 for reference.

number of bjets	jet_{top} is b-jet	$\text{jet}_{\text{W}'}$ is b-jet	type of region
		Control regions	
0	no	no	Control region (CR0B)
1	no	no	1-bjet control region (CR1B)
		Secondary signal regions	
1	yes	no	top jet SR (SRT)
1	no	yes	W′ jet SR (SRW)
		Main signal region	
≥ 2	yes	yes	Signal region (SR2B)

Table 6.5: Event categories defined in term of the total number of reconstructed b-jets and of the b-jettiness of the AK4 jets used for the reconstruction of the top quark and W′ boson candidates.

Signal events can end up in the secondary control region CR1B if both jet_{top} and $\text{jet}_{\text{W}'}$ are not reconstructed as coming from a b, and one extra jet in the events, identified as a b jet, was not selected neither as a jet_{top} or a $\text{jet}_{\text{W}'}$, however this is a relatively rare occurrence. Since in this region the composition of the backgrounds is different from the the one in three signal regions and it is very poor in signal, it is not further used in the analysis.

6.7 Analysis strategy

After the event reconstruction and categorisation are performed, a requirement on the mass of the reconstructed top quark is applied in order to improve the rejection of background contamination. In particular, the requirement $m_{\text{t}} > 120$ GeV, significantly reduces the QCD background, while a requirement $m_{\text{t}} < 220$ GeV helps in $\text{W} + \text{jets}$ events rejection. This allows to also remove top quark candidates from $\text{t}\bar{\text{t}}$ semileptonic events where either the b jet association failed, or rare dileptonic events that happened to pass the lepton veto. To further reduce the $\text{t}\bar{\text{t}}$ semileptonic events where the reconstruction succeeded, a requirement on the soft drop mass of the AK8 jets associated to the $\text{jet}_{\text{W}'}$, $m_{SD,AK8}$, is also applied. The soft drop declustering technique consists in removing the soft wide-angle radiation

from a jet [170]. The association between the AK4 and AK8 jets is performed by requiring the ΔR between these two jets to be less than 0.4. If such variable, i.e. the mass of the matched AK8 jet, has a soft-drop mass is greater than 60 GeV, the event is discarded. This is motivated by noting that the soft drop mass of an AK8 jet coming from an hadronic top quark decay is expected to be centred around the top quark mass. By requiring low values of the soft drop mass of the AK8 jet associated to the decay of the W′ boson, the signal purity can be improved. This requirement is synchronised with the analysis described in Ref. [97].

Figures 6.7, 6.8, 6.9, and 6.10 show the W′ mass for the CR0B, the two secondary signal regions and the 2 b jets signal region, respectively, after the W + jets veto and the $\mathrm{t\bar{t}}$ veto are applied.

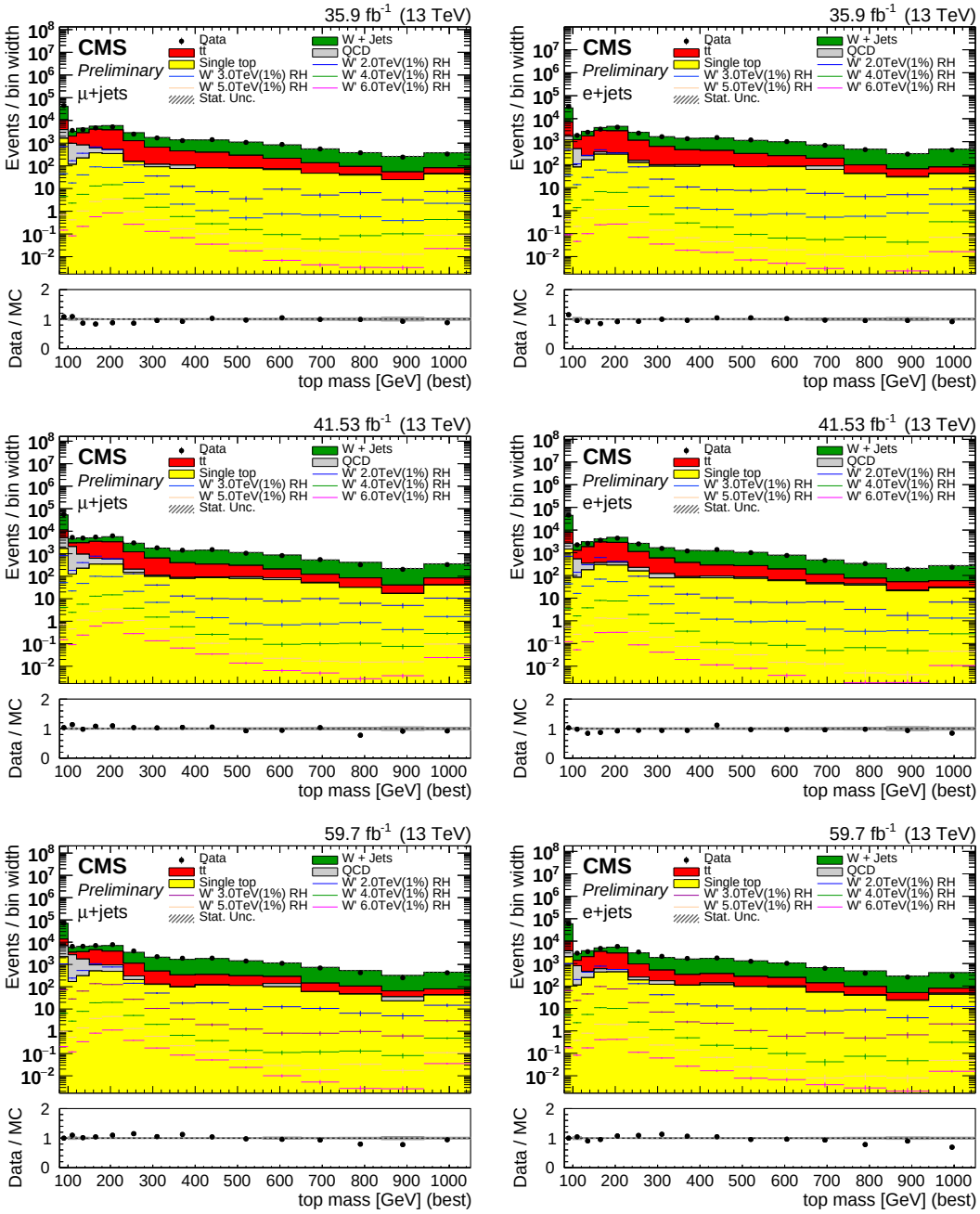

Figure 6.6: Top quark reconstructed mass for muons (left) and electrons (right) in 2016 (top), 2017 (mid), and 2018 (bottom).

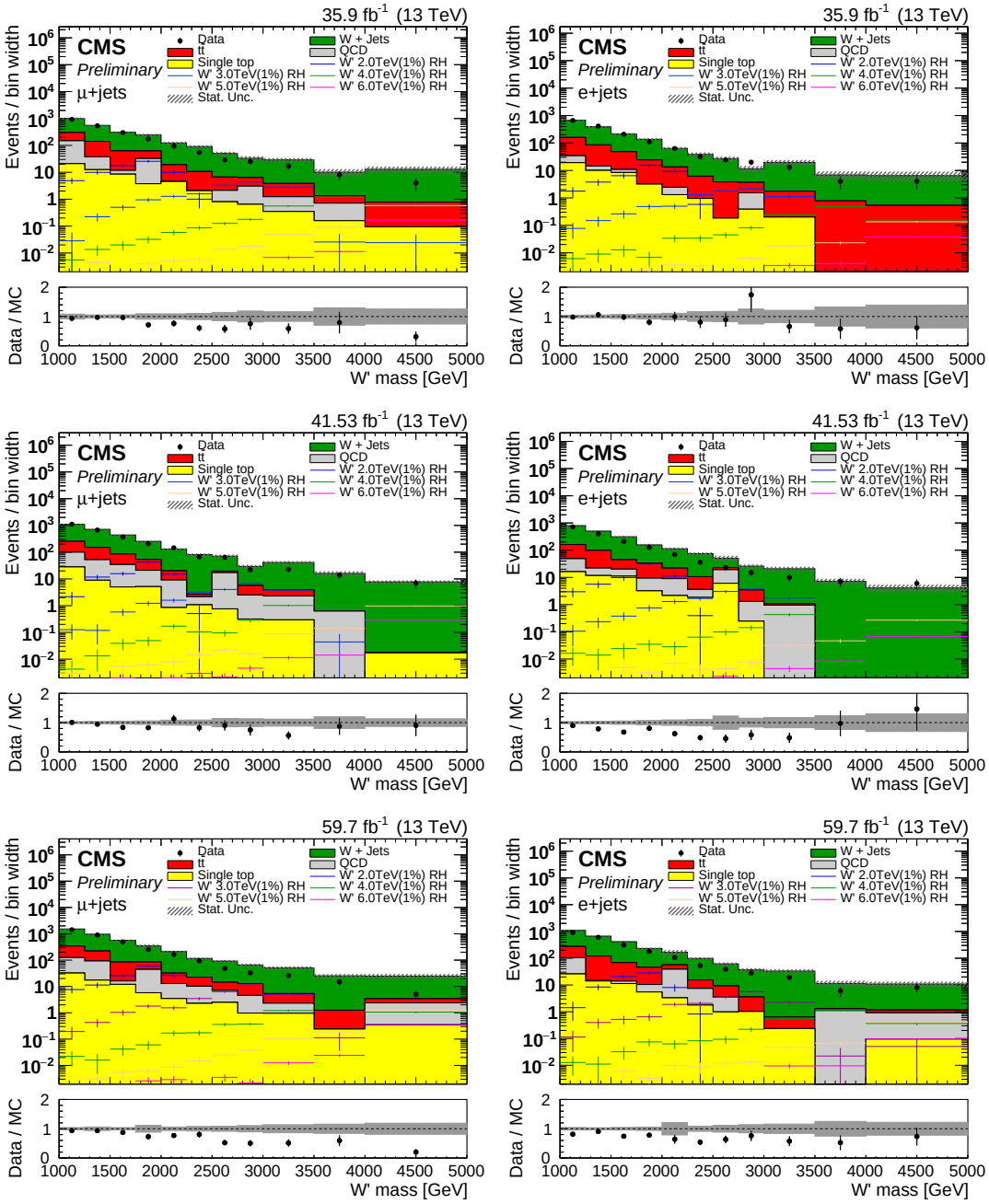

Figure 6.7: W′ reconstructed mass for muon (left) and electron (right) channel in the CR0B region in 2016 (top), 2017 (mid), and 2018 (bottom).

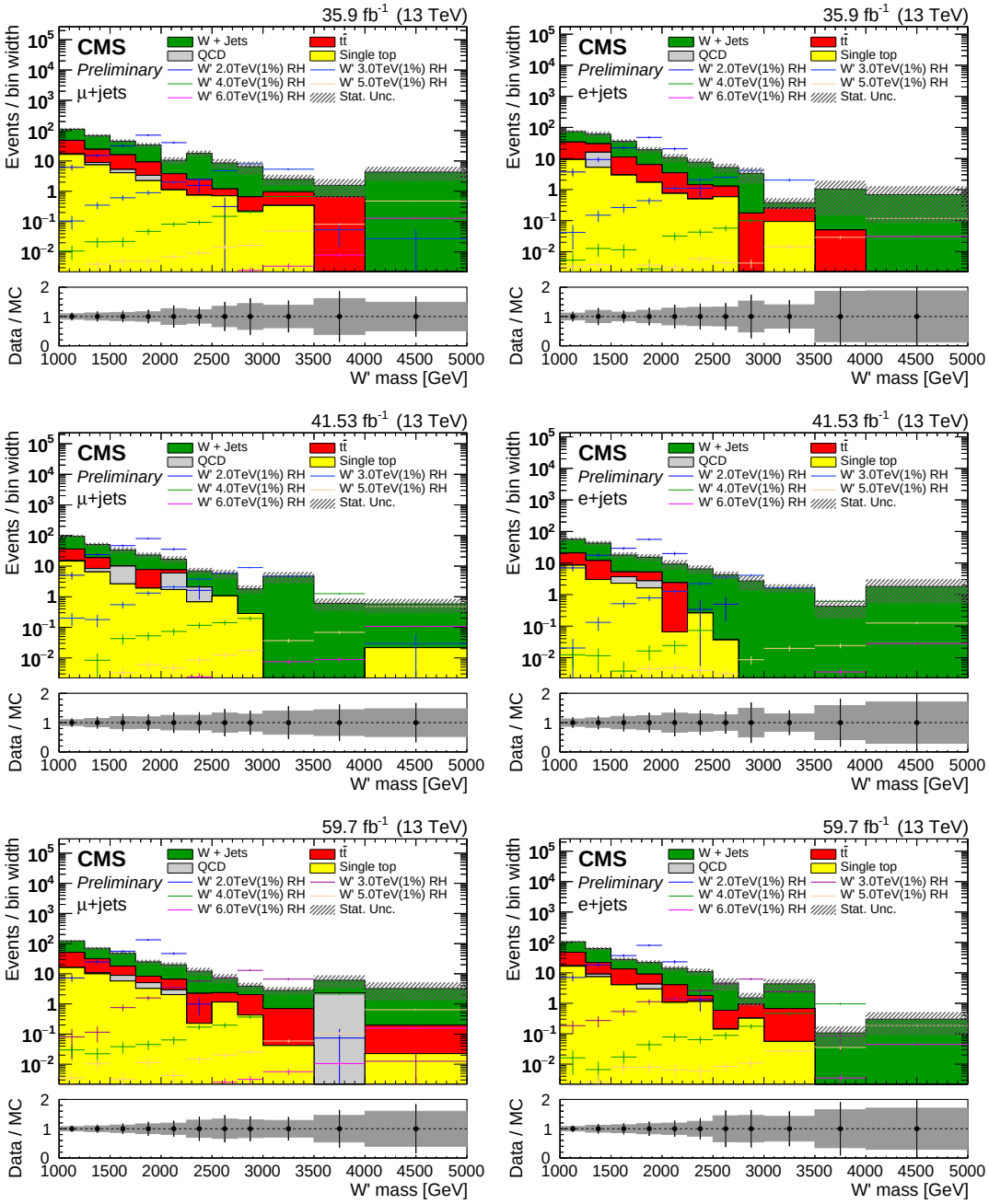

Figure 6.8: W′ reconstructed mass for muon (left) and electron (right) channel in the SRW region in 2016 (top), 2017 (mid), and 2018 (bottom).

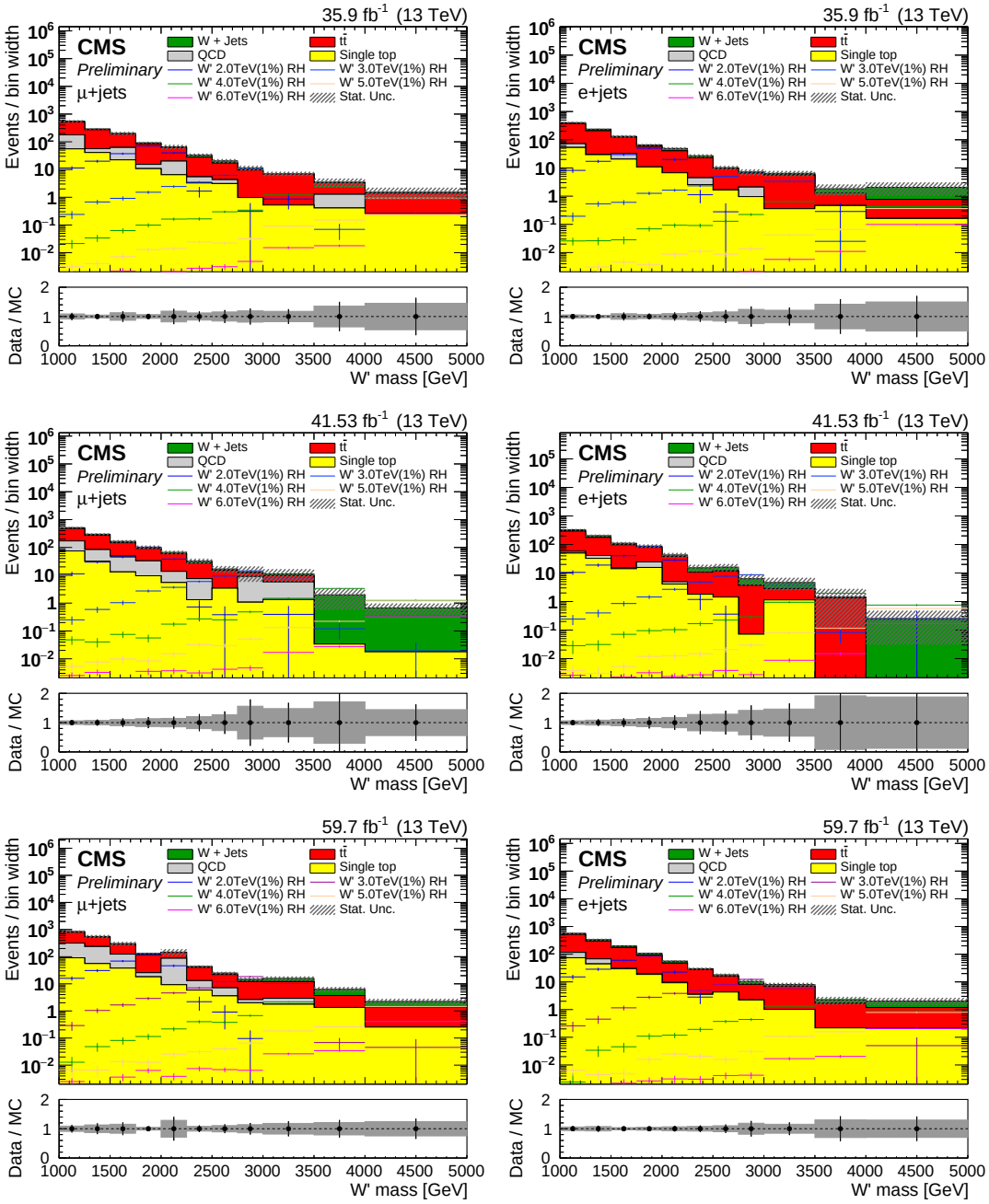

Figure 6.9: W′ reconstructed mass for muon (left) and electron (right) channel in the SRT region in 2016 (top), 2017 (mid), and 2018 (bottom).

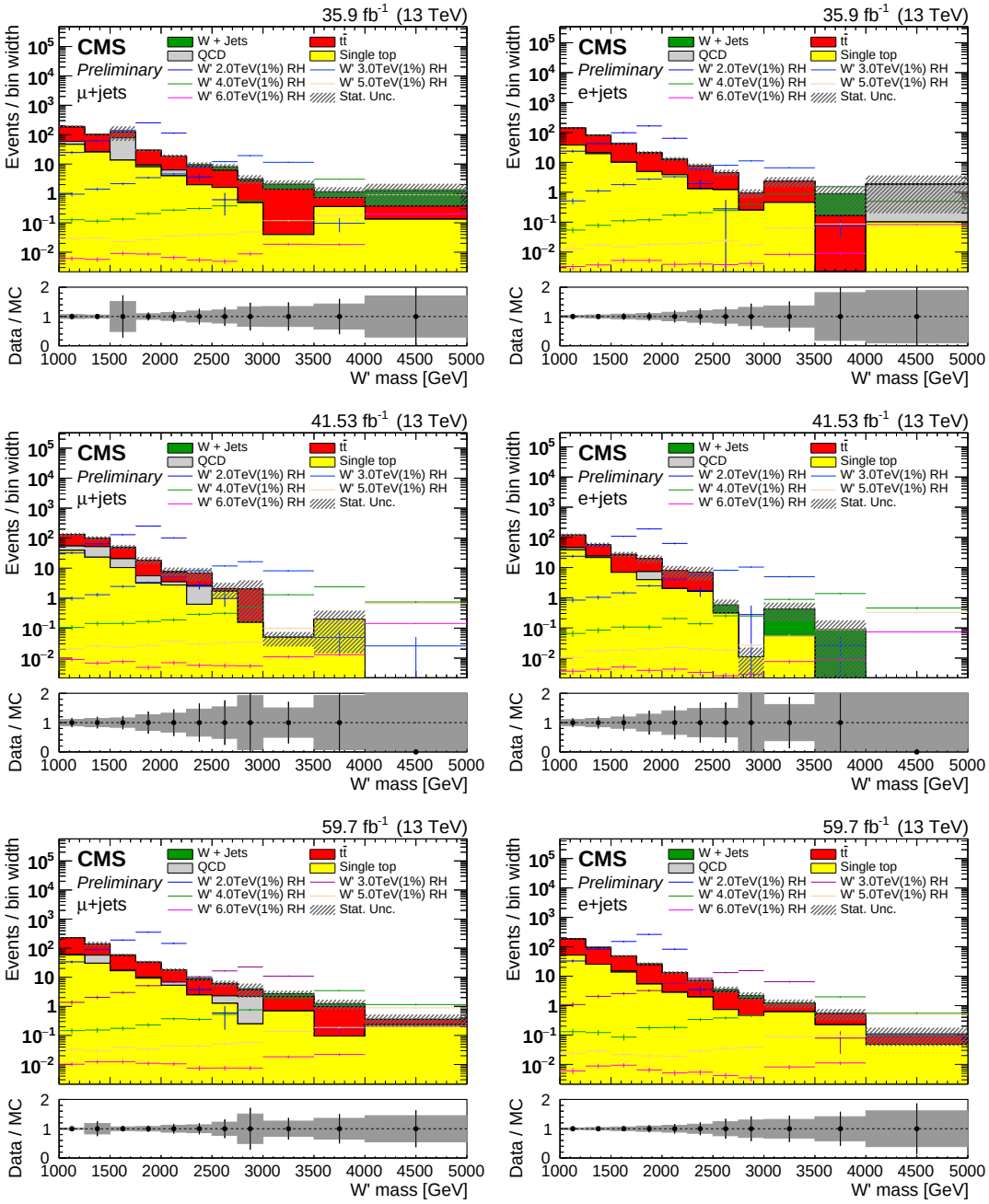

Figure 6.10: W′ reconstructed mass for muon (left) and electron (right) channel in the SR2B region in 2016 (top), 2017 (mid), and 2018 (bottom).

6.7.1 Background estimation

The most important backgrounds in the SR0B are $t\bar{t}$, W + jets, and single-top quarks processes. For the signal regions, the $t\bar{t}$ background is more abundant in the categories SRT and SR2B, while the W + jets is more abundant in the SRW one. Since in the SRW category there is a jet reconstructed as a b-jet, the W + jets background in this category is predominantly composed by a W boson in association with c or b quarks. For this reason, this contribution cannot be extracted from the CR0B category where the dominant contribution comes from W + light flavor jets. In order to infer backgrounds directly from data, additional control regions can be defined by inverting the requirements: $m_{\mathrm{t}} < 220$ GeV and/or $m_{SD,AK8} < 60$ GeV.

Control regions obtained with $m_{SD,AK8} > 60$ GeV turn out to have limited statistic for W + jets background and for this reason they are not considered in the background estimation. Instead the region with $m_{SD,AK8} < 60$ GeV and $m_{\mathrm{t}} > 220$ GeV, from now on referred to as region I, is more reliable for both W + jets, $t\bar{t}$ and single top quarks (ST) and it has been used for the background studies. The procedure followed for the background estimation consists in comparing the shapes of both W + jets, $t\bar{t}$ and ST together in the signal regions and their respective region with the m_{t} cut inverted. The ratio obtained by dividing the shapes in these regions has been fitted in order to extract a transfer function (TF) that allows to predict the shapes in the signal regions from the data from regions I. The procedure can be summed up in formulae as following:

$$\mathrm{SR2B}^{\mathrm{BKG}} = \mathrm{TF\_SR2B}(\mathrm{SR2B\_I}^{\mathrm{Data}} - \mathrm{SR2B\_I}^{\mathrm{QCD}}), \tag{6.4}$$

where:

$$\mathrm{TF\_SR2B} = \frac{\mathrm{SR2B}^{\mathrm{BKG}}}{\mathrm{SR2B\_I}^{\mathrm{BKG}}}. \tag{6.5}$$

The complete picture of the background estimation procedure is reported in Table 6.6.

Process	Region for limit extraction	Backgrounds shape provenance
W + jets +$t\bar{t}$ + ST	SR2B	SR2B_I
W + jets +$t\bar{t}$ + ST	SRW	SRW_I
W + jets +$t\bar{t}$ + ST	SRT	SRT_I
W + jets +$t\bar{t}$ + ST	CR0B	CR0B_I

Table 6.6: The table reports the background processes extracted from data, the region in which they are used and the one from which they are derived.

Figure 6.11 shows the ratio of the distributions between each category and its corresponding region I with 2016 MC, the analytic form for the function fitted and the fit results. The fit function is $N \cdot exp(a+bx+cx^2)$ for $t\bar{t}$ dominated regions and $N_1 \cdot exp(a+bx+cx^2)+N_2 \cdot exp(c+dx)$ for W + jets dominated regions. Muons and electrons show similar behaviour, in the SR2B the slope of the second exponential is significantly smaller due to the different $t\bar{t}$ and W + jets composition.

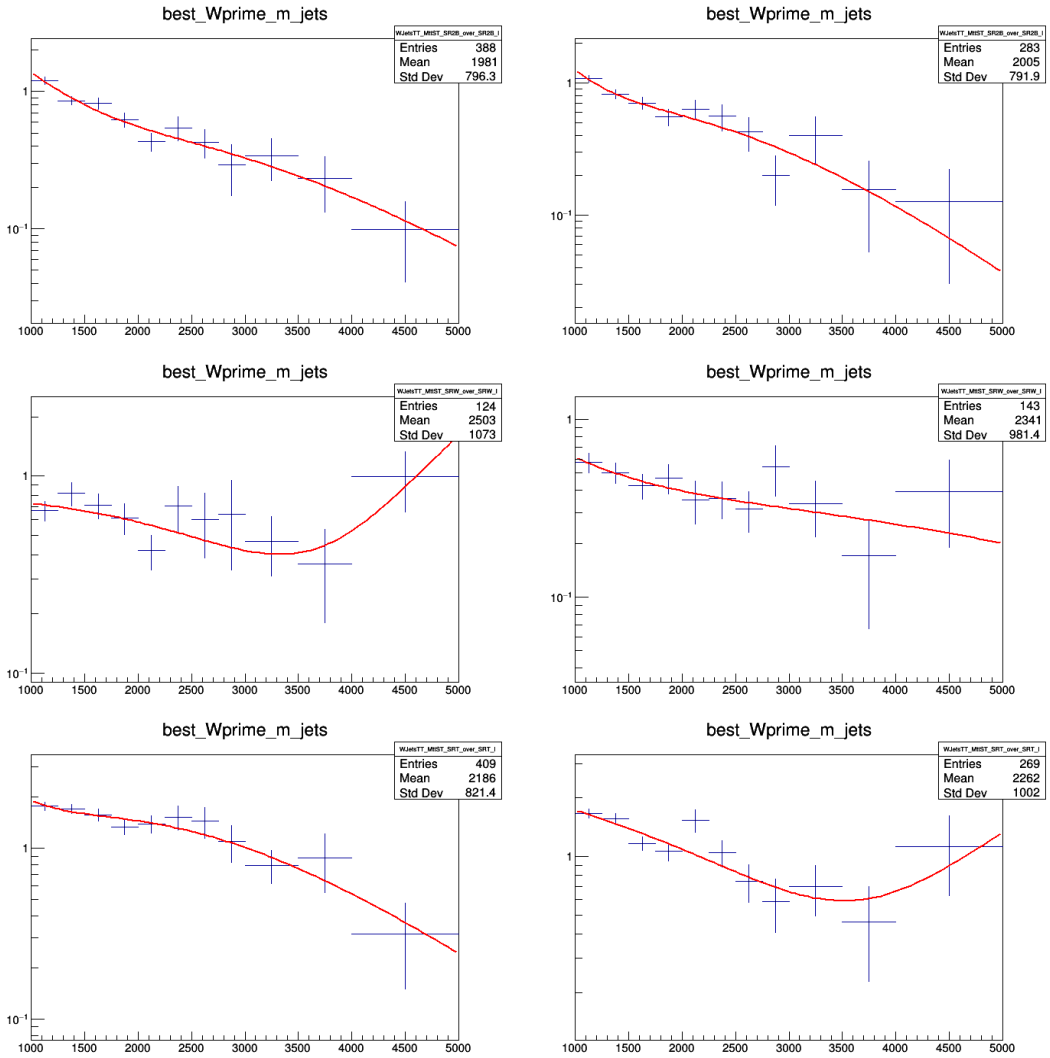

Figure 6.11: Ratio of the distributions between each category and its corresponding region I, the analytic form for the function fitted and the fit results for muon (left) and electron(right) for SR2B(top), SRW(middle), and SRT(bottom).

The data shape is fitted with a Landau function, and the number of events in each bin is evaluated from the function integral. The residual QCD multi-jets contribution is predicted from simulation. Statistical uncertainties on this fit are propagated to the corresponding SR. This method is preferred over simply subtracting the distribution bin-by-bin as it allows for smooth variations in the tail distribution, and reduces the bias in the fit.

Figure 6.12 shows the fit to the Landau function in the different regions for muon or electrons.

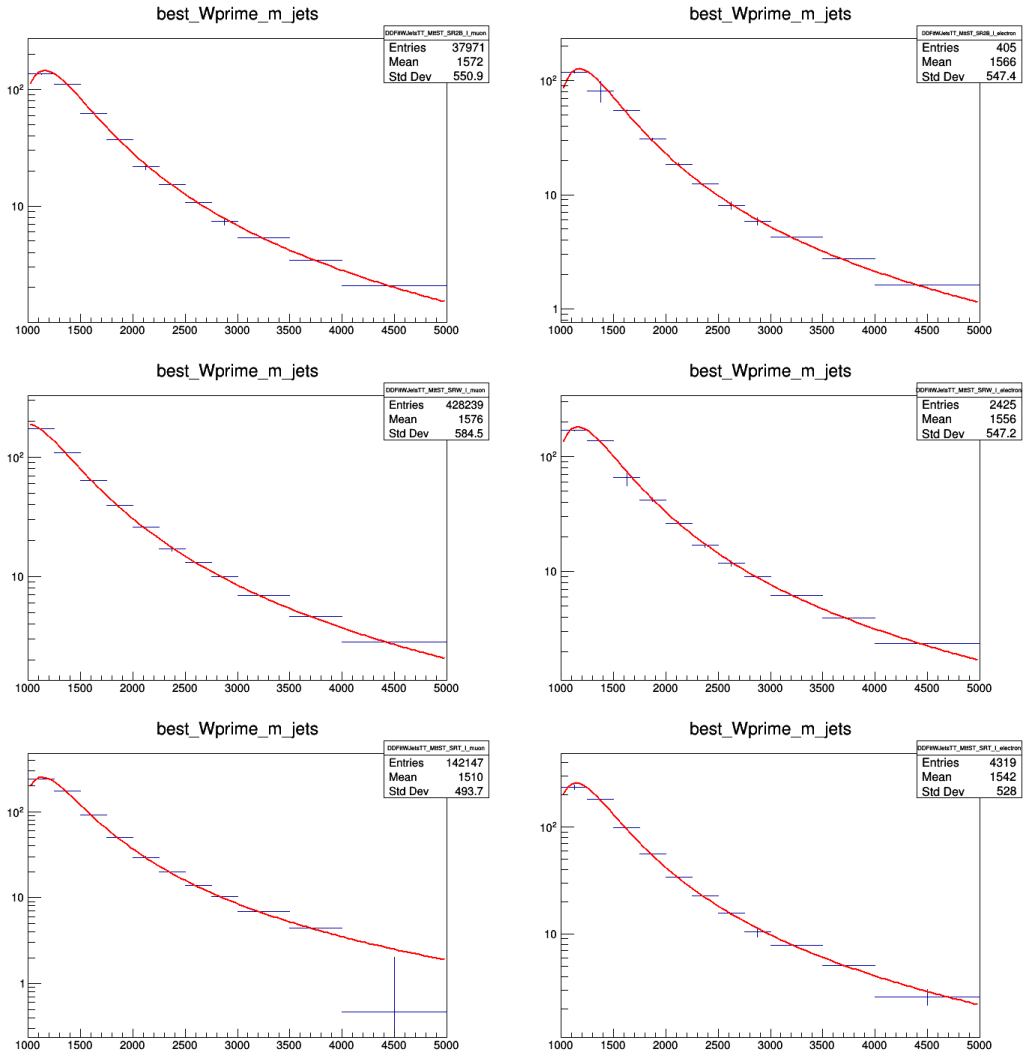

Figure 6.12: Fit to data fit in the the region I, for SR2B (first row), SRW (second row) SRT (third row), and CR0B (fourth row) for muons (left), and electrons (right).

Figure 6.13 shows the prediction compared to MC simulation for the signal regions and for the CR0B, where a closure test with data is also shown. In general, good agreement is found across the regions, with the only exception of the SRW for electrons, where an under-fluctuation can be observed in the MC over the prediction for a few bins. Also, data in CR0B seem to be mildly softer than MC, and this is reflected in the background estimate from CR0B_I as well.

Additionally, a nuisance on the functional dependence from the $W + \text{jets}$, $t\bar{t}$ and ST composition is added, as reported in Sec. 6.8.5.

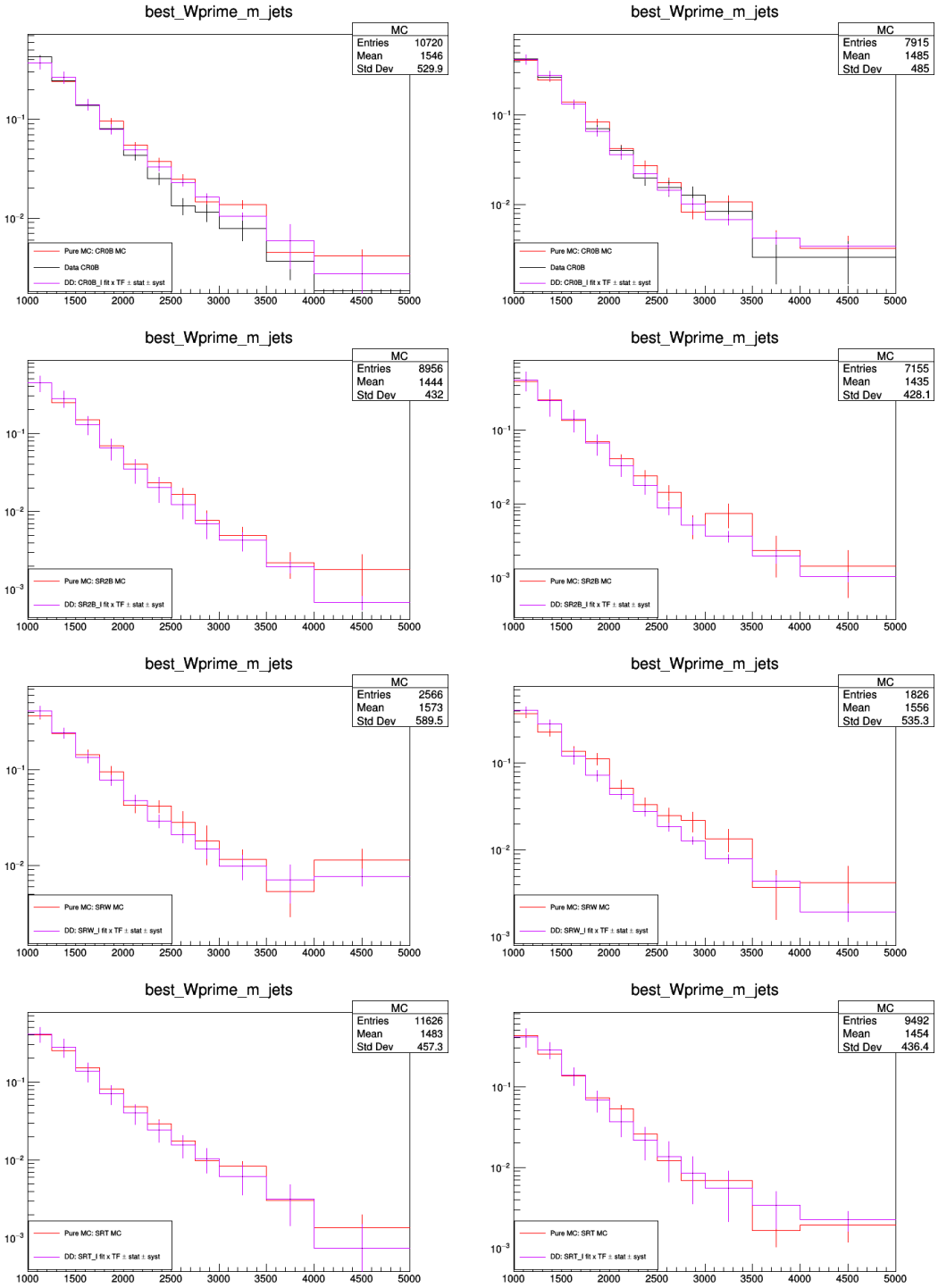

Figure 6.13: Closure tests for the transfer functions, in the three SR comparing MC in the SR vs MC driven prediction (red) and data based prediction (violet). For the former, stat. uncertainties are considered, for the latter, stat+syst from background composition are considered, see also description Sec.6.8. In the CR0B also data are compared (in black).

6.8 Systematic uncertainties

All systematic uncertainties are included as nuisance parameters in the extraction procedure, and considered as affecting both the shape and the yield of the reconstructed W′ distribution, unless otherwise stated in the description. The description of the systematic uncertainties relative to JECs and JER, Pileup modelling, and scale and PDF variations in the MC simulations is the same as already reported in Sec. 5.8 and will not be repeated in the following.

6.8.1 Prefiring

In 2016 and 2017 a portion of Trigger Primitives in the ECAL was associated with the wrong bunch crossing. Because of trigger rules vetoing subsequent events, this could cause a physics event to self-veto in case a trigger in the interested region was fired. The probability (or efficiency) to pre-fire has been measured per photon or jet, allowing then to calculate a per-event probability, by combinatorics of all the available photons and jets in each event. Events have been corrected for this effect with a per-event weight, and the uncertainties of the measured per-jet, per-photon efficiencies have been propagated throughout this chain.

6.8.2 Luminosity

According to the CMS Collaboration measurements, an uncertainty of 2.5%, 2.3%, and 2.5% on the 2016, 2017, and 2018 integrated luminosities are used, respectively [161, 171, 172]. This uncertainty is treated as rate only, and treated as uncorrelated across years.

6.8.3 b-tagging and mis-tag efficiency scale factors

Data-to-MC scale factors are applied to MC samples to reproduce the b-tagging and mis-tagging efficiencies as measured in data. The systematic effect is evaluated by varying the nominal scale factors of $\pm 1\sigma$ (where σ is the scale factor uncertainty). For b-jets, the uncertainty on the b-tagging efficiency SF is estimated in different p_{T} bins. For c-jets, the uncertainty is considered as twice the error for b-jets. For light jets, the uncertainty is a flat value. The uncertainty of the b-tagging SF is assumed to be fully correlated for b and c-jets, while it is assumed to be uncorrelated with light jets.

6.8.4 Trigger scale factor

The trigger efficiency scale factors have been measured in an orthogonal sample with respect to the one used in this analysis. The procedure is described in detail in Section 6.5.1. The systematic uncertainty due to the trigger efficiency is obtained by shifting the nominal value of the trigger scale factors of $\pm 1\sigma$ (where σ is the scale factor uncertainty).

6.8.5 Background estimation uncertainty

To take into account the uncertainty on the background estimation, stat. uncertainties on the fits to the region I and TF are propagated to the final shape. Additionally, the background composition in the MC is varied to account for possible mismodelling. The variation is by a factor 0.5(Down) / 2.0 (Up) for W + jets, 0.75(Down) / 1.33 (Up) for $t\bar{t}$, 0.667(Down) / 1.5 (Up) for single top quarks.

6.8.6 Summary on systematic uncertainties

Table 6.7 summarises the systematic uncertainties treatment.

Source	Processes affected	Process Correlation	Year Correlation	Type
Luminosity	signal, QCD, DDbkg	All Corr.	Uncorrelated	yield
Pileup	signal, QCD	All Corr.	Correlated	yield, shape
b tagging	signal, QCD	All Corr.	Correlated	yield, shape
mis-tagging	signal, QCD	All Corr.	Correlated	yield, shape
Trigger efficiency	signal, QCD	All Corr.	Correlated	yield, shape
Prefiring	signal, QCD	All Corr.	Uncorrelated	yield, shape
Jet energy scale	signal, QCD	All Corr.	Correlated	yield, shape
Jet energy resolution	signal, QCD	All Corr.	Correlated	yield, shape
PDF	QCD	Uncorrelated	Correlated	yield, shape
μ_R, μ_F	QCD	Uncorrelated	Correlated	yield, shape
TF uncertainty	DDbkg	Uncorrelated	Uncorrelated	yield, shape
ST composition	DDbkg	Uncorrelated	Correlated	yield, shape
$t\bar{t}$ composition	DDbkg	Uncorrelated	Correlated	yield, shape
W + jets composition	DDbkg	Uncorrelated	Correlated	yield, shape

Table 6.7: Summary of the systematic uncertainties. The second column reports whether it's correlated or uncorrelated across processes. The third column reports whether a systematic uncertainty is considered fully correlated or not across the years of data taking. The fourth column indicates whether the uncertainty affects both the yield and the shape of the distributions or the yield only. All uncertainties affect both signal and backgrounds.

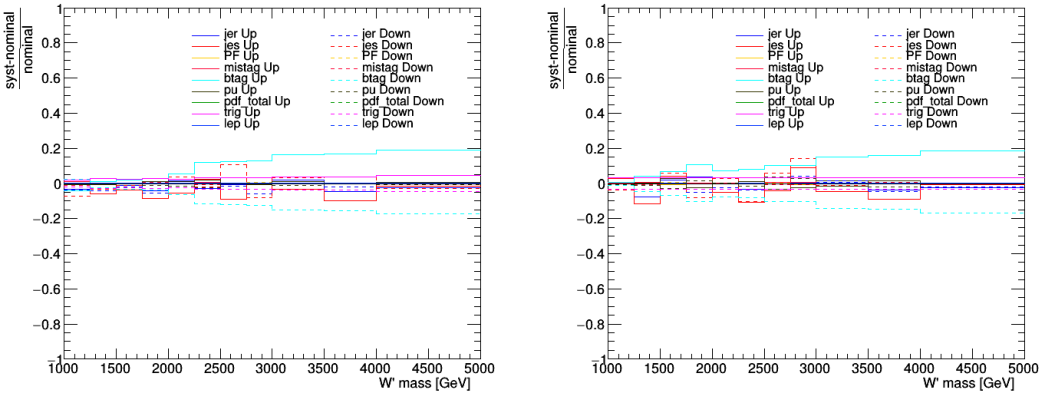

Figure 6.14: Example of the pre-fit magnitude of the systematic uncertainties affecting a signal sample (5 TeV) in the muon (left) and electron (right) for the year 2016.

Figure 6.14 shows an example of the magnitude of the different systematic uncertainties for the signal for muon and electron channel for 2016.

6.9 Fit procedure

After the requirements described in Sec. 6.7 have been applied, the W′ reconstructed mass shows a good discrimination power between signals and backgrounds, both in the signal and control regions. This variable has been used in the simultaneous maximum likelihood fit for the limit extraction. The fit configuration accommodates the three SRT, SRW and SR2B categories for both muon and electron channels. The fully floating parameter, r, represent the signal strength for the signal process taken into account for the different hypothesised masses. All systematic uncertainties described in Sec. 6.8 are treated as nuisance parameters.

6.9.1 Statistical tests

Several statistical tests are performed to ensure the procedure is robust. First of all, the impact of systematic uncertainties, treated as nuisance parameters, and the constraints on them originating from the fit are determined. The bias in case of signal absence, and in presence of a visible signal is also checked. Finally, a cross-check for the background extraction is performed with a fit in a control region to asses the whole procedure is reliable.

Impact plots

The impact of nuisances on the signal extraction is evaluated by performing the fit on an Asimov Dataset based on the a-posteriori expectation obtained in the background-only scenario. This means that all observables are set to the values obtained by fitting the background-only hypothesis. The impacts are evaluated by performing the full fit removing one by one the uncertainties, and evaluating the measured signal strength. The pull gives the constraint on that particular nuisance from data. Figure 6.15 shows an example of impact plot obtained from the fit for an hypothesised mass of the W′ boson equal to 4 TeV.

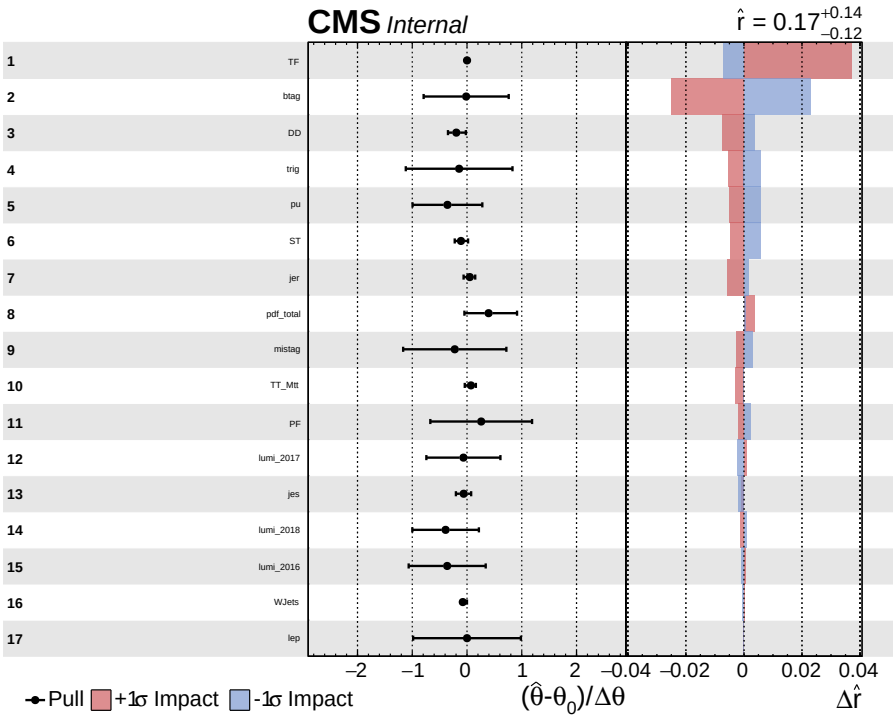

Figure 6.15: Impact plot showing the list of systematic uncertainties used in the fit, the pull with respect to their pre-fit value, and the impact of the final uncertainty.

Bias and signal injection

Pseudo-experiments have been generated either in the background-only hypothesis, and by injecting different quantities of signal. Figures 6.16 show the bias of the fit for a hypothesised for the W′ of 6 TeV assuming 0 signal strength, a signal strength of 1, 3, and 5, corresponding to value of significance equivalent to

8.5, 19, and 27 standard deviations from the background-only hypothesis, respectively. Figures 6.17 show the bias of the fit for a hypothesised for the W′ of 4

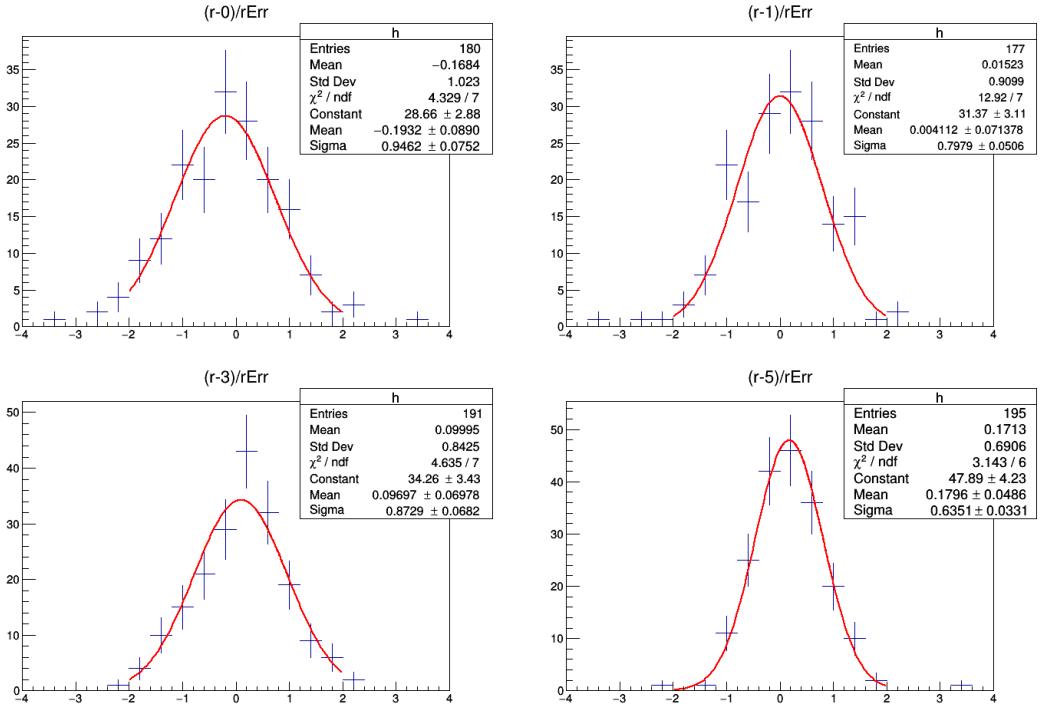

Figure 6.16: Results of the bias test performed for the signal sample at 2 TeV with 1% width in the background only hypothesis (up left), and different quantity of signal equal to 1 (up right), 3 (down left), and 5 (down right). The tests show no bias is present.

TeV assuming 0 signal strength, a signal strength of 1, 3, and 5, corresponding to value of significance equivalent to 8, 29, and 27 standard deviations from the background-only hypothesis, respectively. Figures 6.18 show the bias of the fit for a hypothesised for the W′ of 6 TeV assuming 0 signal strength, a signal strength of 5, 10, and 20, corresponding to value of significance equivalent to 6, 11, and 18 standard deviations from the background-only hypothesis, respectively.

6.10 Results

The results obtained for 2016 are shown in Fig. 6.19. For comparison the results obtained by the previous CMS analysis are also reported. Figure 6.20 shows the results for 2017 and 2018. Finally the data for the full Run-II are combined

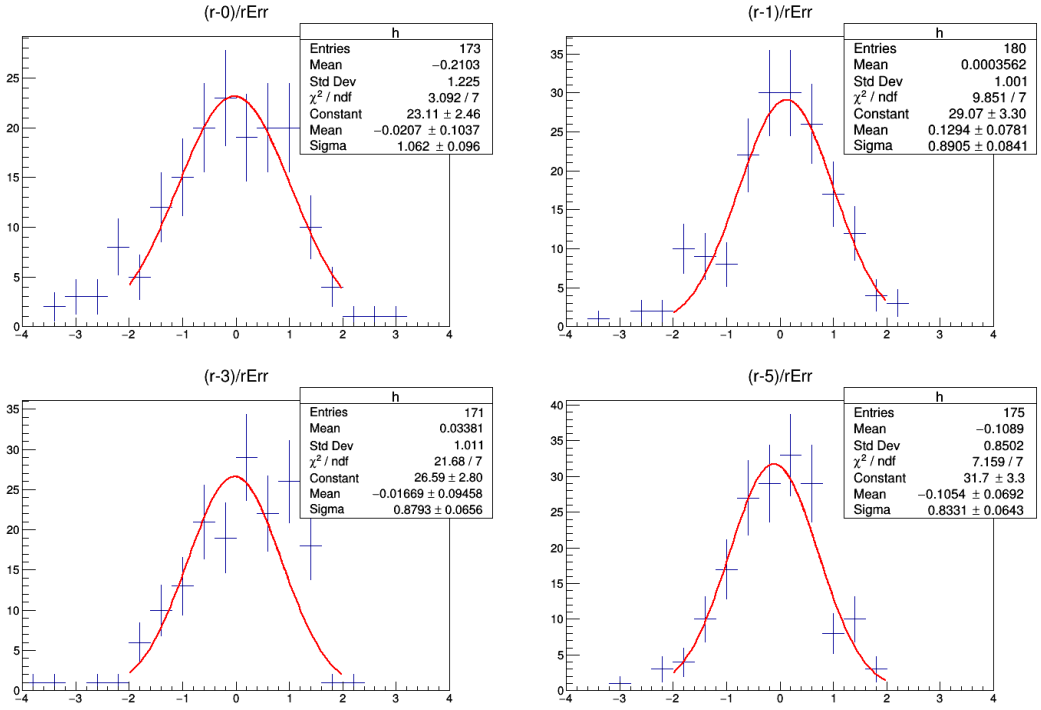

Figure 6.17: Results of the bias test performed for the signal sample at 4 TeV with 1% width in the background only hypothesis (up left), and different quantity of signal equal to 1 (up right), 3 (down left), and 5 (down right). The tests show no bias is present.

together and a fit is performed by using the entire statistics available at 13 TeV. The results for this case are are shown in Fig. 6.21.

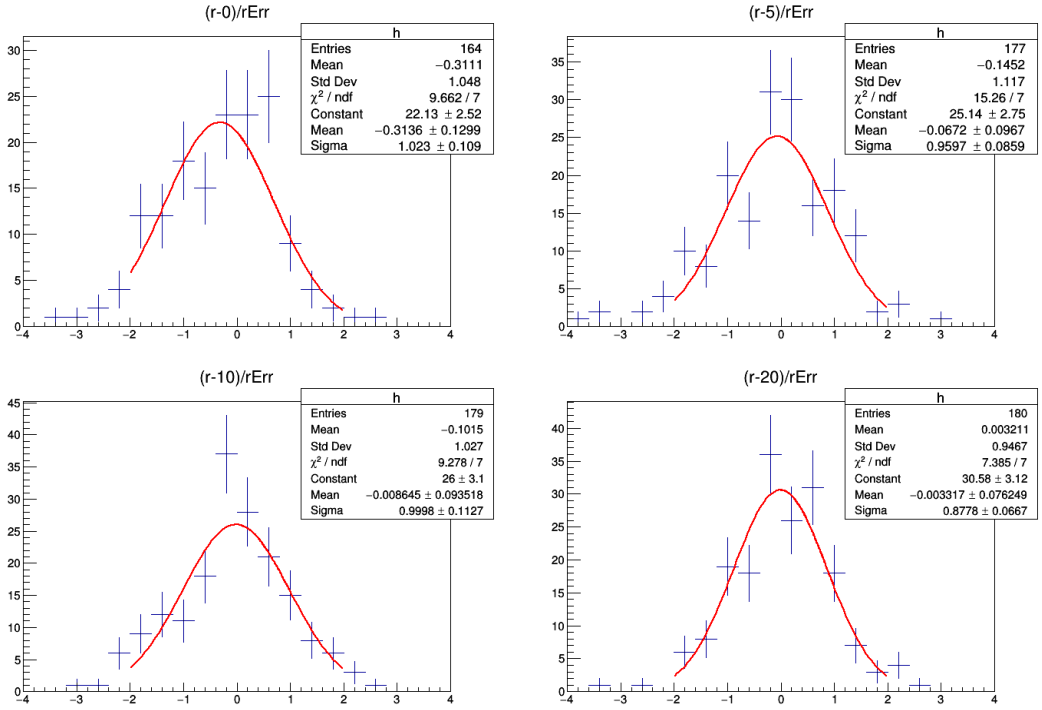

Figure 6.18: Results of the bias test performed for the signal sample at 6 TeV with 1% width in the background only hypothesis (up left), and different quantity of signal equal to 1 (up right), 3 (down left), and 5 (down right). The tests show no bias is present.

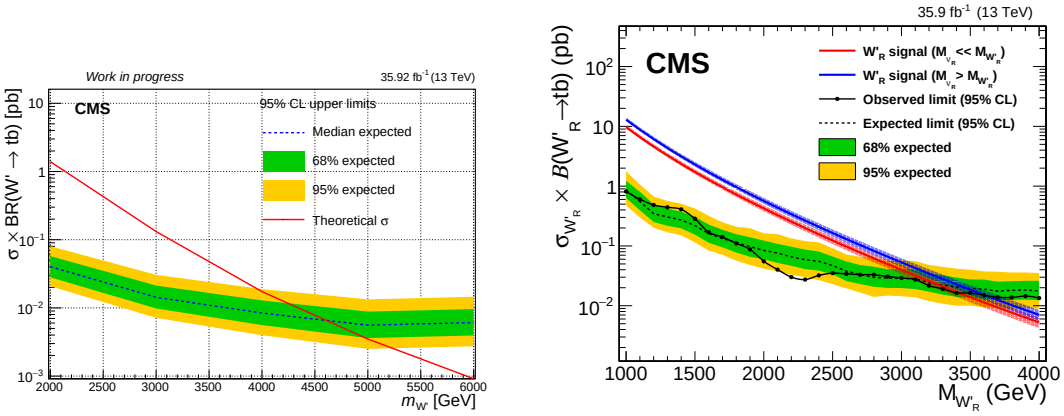

Figure 6.19: Results obtained by this analysis (left) compared to what has been obtained by the previous CMS analysis (right).

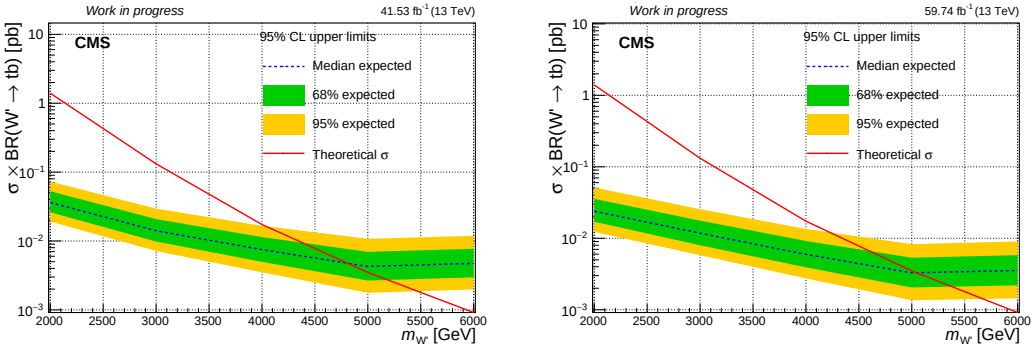

Figure 6.20: Results obtained by this analysis for the 2017 (left) and 2018 (right).

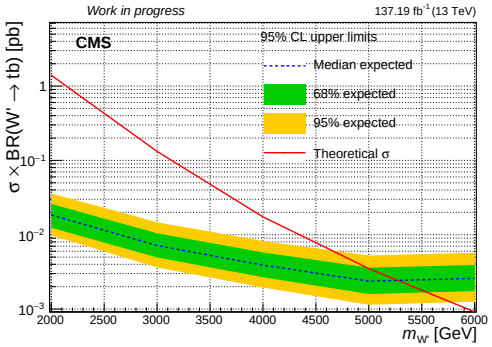

Figure 6.21: Results obtained by this analysis for the full Run-II dataset.

Conclusions

This thesis presented an investigation of the tWb electroweak vertex aimed at probing the prediction of the Standard Model (SM) and at searching for new physics contributions. The study was performed via a precision measurement of the tWq, with q being b, s, or d quark, electroweak vertexes entering the single top quark processes and via a direct search for new vector boson, predicted by many theories beyond the SM, that could alter the tWb vertex. The former measurement makes use of single top quark $t-$channel events in proton-proton collision data with a centre-of-mass energy of 13 TeV, collected with the CMS experiment at the LHC. The subset of data analysed corresponds to an integrated luminosity of 35.9 fb^{-1}. The dominant electroweak production mechanism for single top quarks is the $t-$channel and it features a tWq vertex, both in production and in decay. For this reason its cross section and branching fractions are sensitive to the strength of the electroweak coupling, making it a suitable channel for direct measurements of the magnitude of Cabibbo-Kobayashi-Maskawa (CKM) matrix elements $|V_{\text{tb}}|^2$, $|V_{\text{ts}}|^2$, and $|V_{\text{td}}|^2$. A precise determination of the magnitude of these parameters of the SM allows to search for hints of potential contributions from new physics beyond the SM. The analysis strategy makes use of leptonic decay channels of the top quarks, where a muon or electron is produced in association with a quark and a neutrino. A selection is performed by requiring one isolated lepton, muon or electron, and two or three jets, one or two of which must pass the b-tagging requirement, that is identified as coming from a b-quark. The events are distinguished into three different categories according to the number of jets and b tagged jets. The signal is composed of single top $t-$channel produced via or decaying to s/d quarks. A data driven based estimation technique is applied to obtain the QCD-multijet contribution directly from data. In each of these categories a multivariate analysis is performed in order to fully exploit the most important kinematic variables. The yields of the signal processes have been extracted through a simultaneous fit to data in different selected event categories, and the values of the CKM matrix elements have been inferred from the signal strengths, which are the ratios of the measured top quark t-channel cross sections times branching ratios to the expected values. The signal strengths obtained from the fit are $\mu_{\text{b}} = 0.99 \pm 0.12$,

where the uncertainty includes both the statistical and systematic components, and $\mu_{\mathrm{sd}} < 87$ at 95% confidence level (CL).

Under the SM assumption of CKM unitarity, the values are found to be:

$$|V_{\mathrm{tb}}| > 0.970$$
$$|V_{\mathrm{td}}|^2 + |V_{\mathrm{ts}}|^2 < 0.057,$$

where both limits are at 95% CL.

Two beyond the SM scenarios were directly probed, by means of different assumptions on the parameters. In the first one, the presence of additional quark families that are heavier than the top quark is assumed. The unitarity constraint for the three CKM matrix elements no longer holds, but the top quark decays through the same channels as in the SM. By assuming the partial width of each top quark decay only varies because of a modified CKM matrix element, the fit gives:

$$|V_{\mathrm{tb}}| = 0.988 \pm 0.051$$
$$|V_{\mathrm{td}}|^2 + |V_{\mathrm{ts}}|^2 = 0.06 \pm 0.06,$$

where the uncertainties include both the statistical and systematic components.

In the second scenario, the top quark width is left unconstrained under the assumption that the contributions to the total width from the mixing of the three families are negligible. The corresponding measured values are:

$$|V_{\mathrm{tb}}| = 0.988 \pm 0.024,$$
$$|V_{\mathrm{td}}|^2 + |V_{\mathrm{ts}}|^2 = 0.06 \pm 0.06,$$
$$\frac{\Gamma_{\mathrm{t}}^{\mathrm{obs}}}{\Gamma_{\mathrm{t}}} = 0.99 \pm 0.42,$$

where again, both the statistical and systematic uncertainties are included. The differences among the uncertainties in the presented scenarios are driven by the difference in the functional dependence of the observed event yields from the CKM matrix elements. This results in smaller uncertainties in $|V_{\mathrm{tb}}|$ for the case where a fourth–power dependence is considered with respect to the second–power dependence case.

All results are consistent with each other, and show no deviation with respect to extrapolations of low-energy measurements. These results are the first direct, model-independent measurements of the CKM matrix elements that involve the top quark, and provide the best determination of these fundamental SM parameters via single top quark measurements.

The second method of investigation aims at probing the tWb vertex via a direct search for new physics contribution due to the presence of a W′ boson. It is performed with proton-proton collisions with a centre-of-mass energy $\sqrt{s} = 13$

TeV collected by the CMS experiment at the LHC from and corresponding to 137,2 fb^{-1}. The process investigated is pp$\rightarrow$ W$'$ $\rightarrow$ tb, with the top quark decaying in a W boson and a b quark, where only leptonic W boson decay are considered. The selection requires the presence of exactly one lepton, a significant amount of transverse missing momentum and at least two jets. Requirements are applied to these objects to reject low-energy background and, in particular, QCD multijet events. The top quark is reconstructed starting from the final state objects by means of kinematic criteria aiming at the correct jet assignment. The events are categorised depending on whether the jets that are tagged as b, are also used in the reconstruction of the top quark or the W$'$ boson. After the categories are defined, additional requirements are applied on the top quark mass and on the mass of the wide cone jet including the jet used in the W$'$ reconstruction. These requirements are also inverted to obtained control regions from which the main backgrounds are extracted and by means of dedicated transfer functions used in the signal regions. Finally, a fit is performed for various hypothesised masses of the W$'$ boson and limits are set at 95% CL. The analysis is expected to exclude value of the W$'$ mass up to 5.2 TeV. In conclusion, in this work a new kind of measurement in the electroweak sector of top quark physics is pioneered, allowing to probe top quark couplings via charged current interaction, and the way for a set of model-independent searches for new particles is paved, fully exploiting the LHC potential in the search for new physics.

Appendix A

Optimisation studies for W' boson search

A.1 Lepton isolation studies

Due to the high number of interaction per bunch crossing and the high boost of the final state particles, the leptons can be mis-identified as jet or viceversa. To avoid this from happening, the reconstructed track of the lepton is required to be isolated in a fixed size cone around the lepton. The relative isolation for muons is defined as in Eq. 4.2 and the size of the cone varies from 0.4 to 0.05. Mini isolation allows to recover efficiency when leptons are produced in the decay chain of a boosted object. In such cases, it is likely that, when the boost is large, the lepton overlaps with a jet produced in the same decay chain, failing a standard isolation cut. Mini isolation is constructed by defining a cone whose radius varies with the p_{T} 0.2 and 0.05. Isolation is then calculated for that lepton on that cone, reducing the probability of the overlap for more boosted topologies. From of this study, reported in Table A.1, one can see that there is no gain from requiring MiniIso < 0.2 with respect to MiniIso < 0.1 and that $p_{\mathrm{T}} > 100\,\mathrm{GeV}$ seems to be a good choice for both muons and electrons.

b-tagging algorithm performance studies

The jet is tagged if the discriminator value is above some threshold value, often referred to as the cut value, and the efficiency is defined as the number of jets which have a discriminator value that is above that cut divided by the total number of jets (of the same flavor). In other words, the integral of the histogram from a certain discriminator cut up to infinity divided by the total number of jets. Various algorithms for b tagging developed by the CMS experiment can identify b jets with a typical efficiency between 40% and 70% while keeping the rate of

Table A.1: The table shows the efficiency for different sets of cut for (p_{T}, MiniIso).

Sample	MC	Muon							
		MiniIso < 0.1				MiniIso < 0.2			
		$p_{\mathrm{T}} > 50$	$p_{\mathrm{T}} > 75$	$p_{\mathrm{T}} > 100$	$p_{\mathrm{T}} > 125$	$p_{\mathrm{T}} > 50$	$p_{\mathrm{T}} > 75$	$p_{\mathrm{T}} > 100$	$p_{\mathrm{T}} > 125$
W′ 4 TeV	match	84.63 %	79.84 %	75.26 %	71.03 %	85.98 %	81.00 %	76.31 %	71.95 %
	no match	0.49 %	0.46 %	0.44 %	0.42 %	0.81 %	0.76 %	0.72 %	0.67 %
$t\bar{t}$	match	54.79 %	38.76 %	27.47 %	19.65	55.37 %	39.03 %	27.63 %	19.72 %
	no match	0.16 %	0.11 %	0.08 %	0.05	0.36 %	0.23 %	0.14 %	0.09 %
QCD	match	15.86 %	13.22 %	8.81 %	7.05%	17.62 %	14.10 %	9.69 %	7.93 %
	no match	0.11 %	0.10 %	0.09 %	0.09%	0.23 %	0.21 %	0.20 %	0.19 %
		Electron							
		MiniIso < 0.1				MiniIso < 0.2			
		$p_{\mathrm{T}} > 50$	$p_{\mathrm{T}} > 75$	$p_{\mathrm{T}} > 100$	$p_{\mathrm{T}} > 125$	$p_{\mathrm{T}} > 50$	$p_{\mathrm{T}} > 75$	$p_{\mathrm{T}} > 100$	$p_{\mathrm{T}} > 125$
W′ 4 TeV	match	85.40 %	79.63 %	74.01 %	68.84 %	85.77 %	79.87 %	74.18 %	68.97 %
	no match	3.50 %	3.21 %	2.95 %	2.69 %	4.37 %	3.98 %	3.60 %	3.25 %
$t\bar{t}$	match	56.92 %	40.16 %	28.22 %	20.04	57.29 %	40.29 %	28.28 %	20.07 %
	no match	1.83 %	1.34 %	0.96 %	0.69 %	2.57 %	1.84 %	1.28 %	0.88 %
QCD	match	40.26 %	36.36 %	35.06 %	28.57 %	41.56 %	36.36 %	35.06 %	28.57 %
	no match	2.36 %	2.10 %	1.82 %	1.61%	2.72 %	2.44 %	2.13 %	1.89 %

mis-identified light-flavor jets between 0.1% and 10%.

Tagger name	WP	WP Discr cut	Mistagging rate
DeepCSV	loose	0.1241	$\sim 10\%$
	medium	0.4184	$\sim 1\%$
	tight	0.7527	$\sim 0.1\%$
DeepJet (DeepFlavour)	loose	0.0494	$\sim 10\%$
	medium	0.2770	$\sim 1\%$
	tight	0.7264	$\sim 0.1\%$

Table A.2: The table reports the three working points with their relative discriminator values and mis-tagging rates for both the algorithms: DeepCSV and DeepFlavour.

Dedicated studies have been performed in order to investigate the efficiency of the different algorithms available and of the different working points, as reported in Table A.2. The b-tagging efficiency is defined by requiring the tagger discriminator + the MC truth (b-jet) while the mis-tagging rate is defined by requiring the tagger discriminator + MC truth (not b-jet). Figure A.1 reports the efficiencies of the b-tagging DeepCSV algorithm and its mistagging rate for signal, on the left, and the $t\bar{t}$ background.

As it can be seen from Fig. A.1 the performances are similar for both signal and background while the mis-tagging rate is a bit lower for signal with respect to

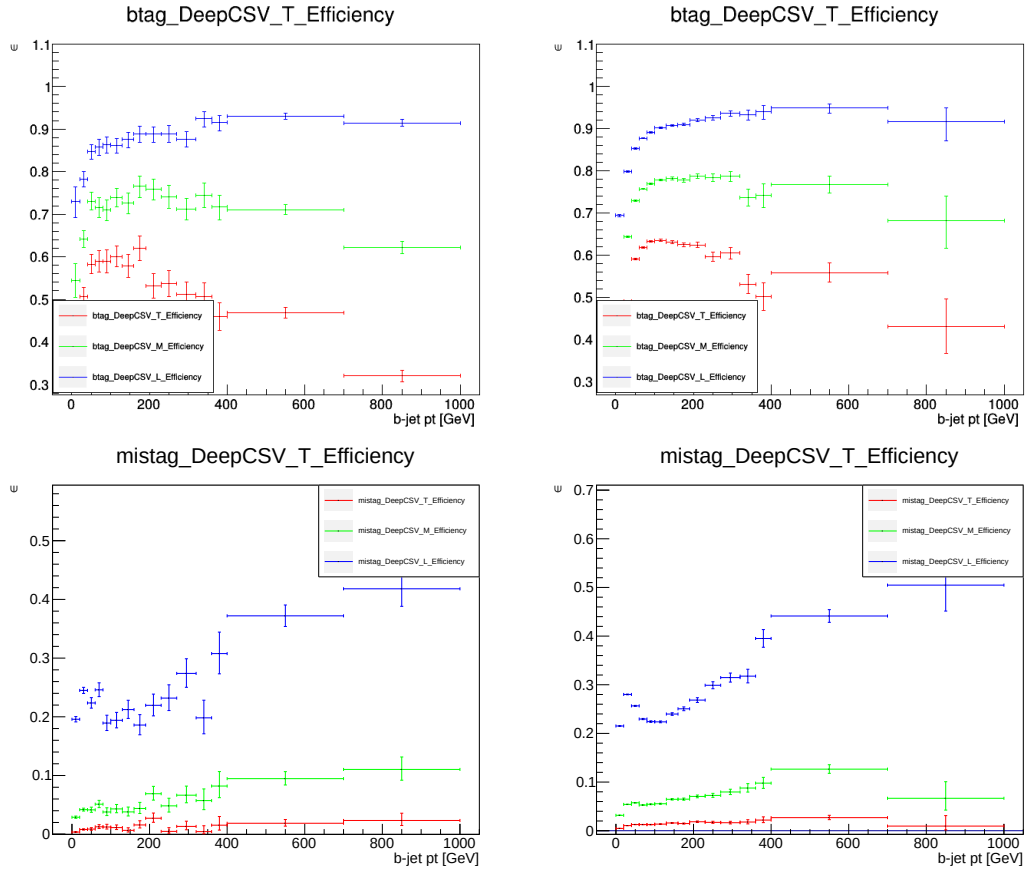

Figure A.1: The upper plots show the b-tag efficiency for signal (on the left) and $t\bar{t}$ background (on the right): the performances are similar for both of them. The lower plots show the mis-tagging rate for signal (on the left) and $t\bar{t}$ background (on the right).

the $t\bar{t}$ background. Additionally the loose WP (blue lines in the plots) has a huge mis-tagging rate for higher b-jet p_T.

Figure A.2 reports the efficiencies of the b-tagging DeepCSV algorithm and its mistagging rate for signal, on the left, and the $t\bar{t}$ background. The performances of the DeepFlavour algorithm are similar for both signal and $t\bar{t}$ background. The mis-tagging rate is also similar between signal and background but the loose working point exhibits a very strange behaviour at low b-jet p_T. The tagging efficiency is very similar between DeepCSV and DeepFlavour while the mis-tagging efficiency is better for the DeepFlavour tagger than the DeepCSV tagger. The medium working point of the DeepJet tagger is good for both efficiency and mis-tag rate and it will be used in the following of the analysis.

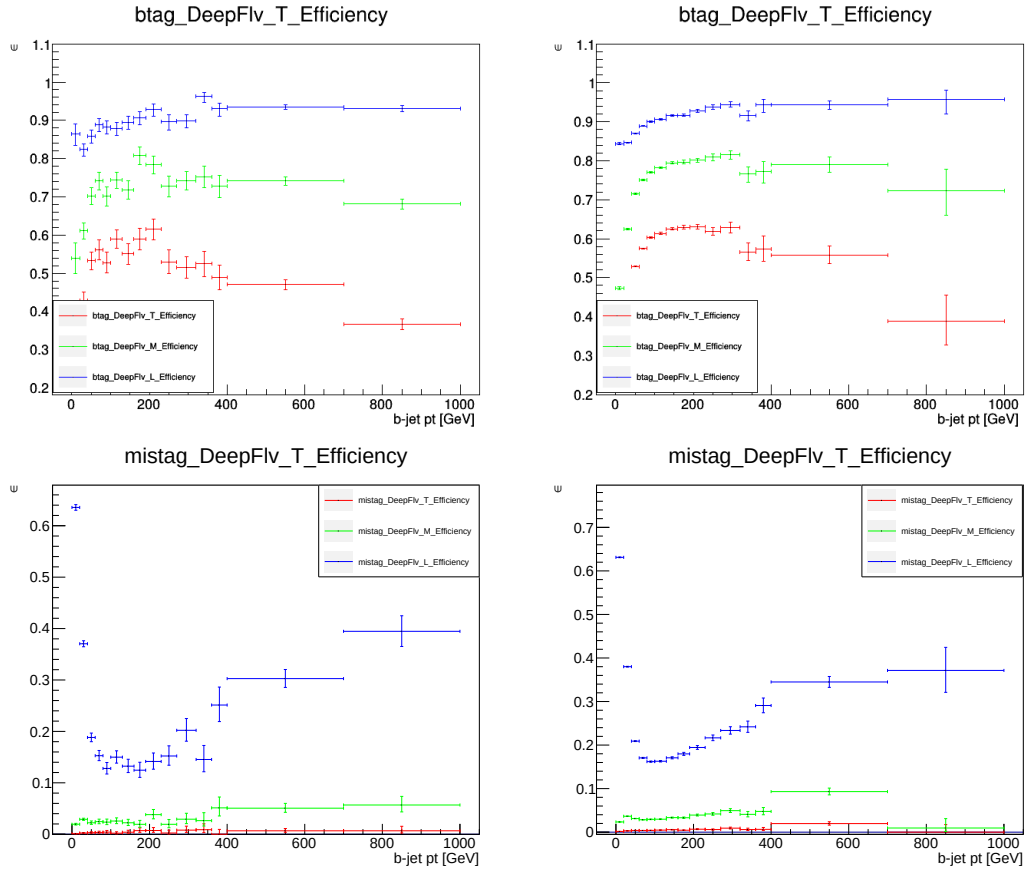

Figure A.2: The upper plots show the b-tag efficiency for signal (on the left) and $t\bar{t}$ background (on the right). The lower plots show the mis-tagging rate for signal (on the left) and $t\bar{t}$ background (on the right).

A.2 Kinematic plots

Figures A.3, A.4, A.5, A.6 show the p_T of the lepton, the leading jet, the subleading jet, and the missing transverse energy at selection level.

A.3 Data driven method checks

In fig. A.7 cross checks are shown here of the background extracted with different methods. MC in the regions SRX (with X=W,T,2B)and CR0B is compared with the full MC extrapolation, obtained by multiplying the MC in the region SRX_I, CR0B_I by the TF obtained by MC. This should yield a good closure, as it's an intrinsic mc-to-mc comparison.

Two predictions using data in SRX_I and CR0B_I are also shown, one obtained by taking the data template, the other by fitting it to a landau function. The main difference in the two is that in one case bin-by-bin stat. uncertainties are necessary, in the other uncertainties come from the fit procedure.

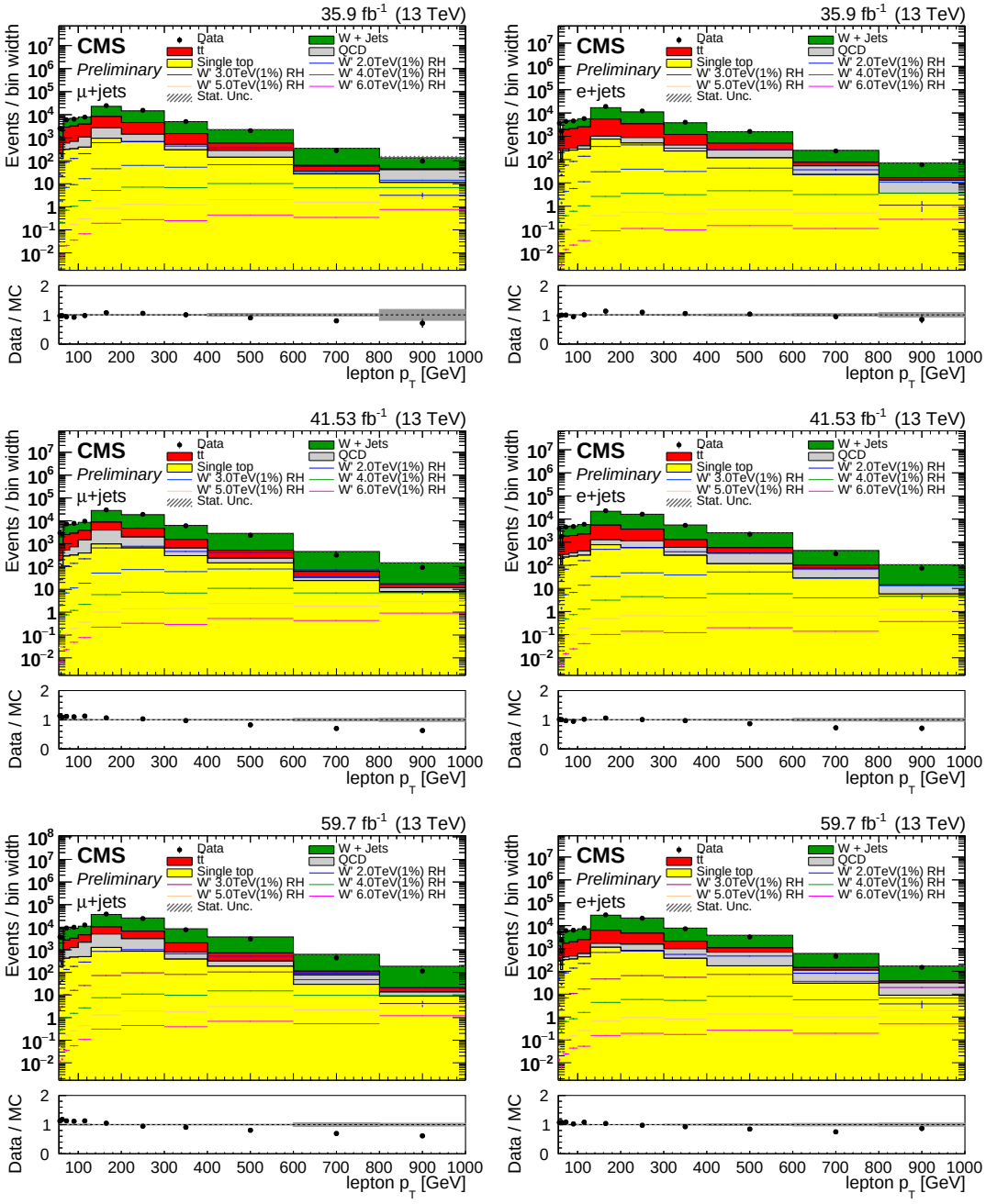

Figure A.3: Lepton p_{T} for muons (left) and electrons (right) in 2016 (top), 2017 (mid), and 2018 (bottom).

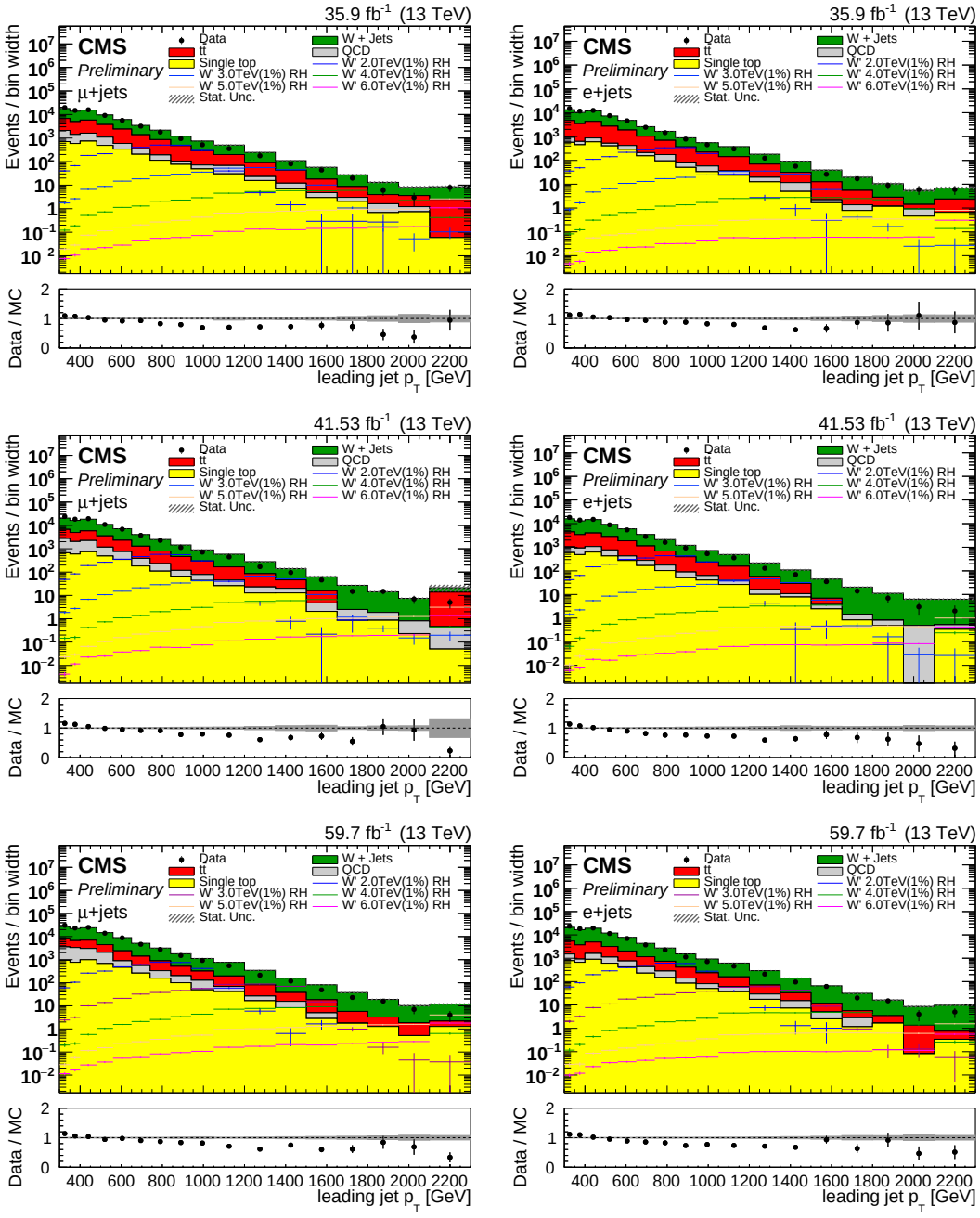

Figure A.4: Leading jet p_{T} for muons (left) and electrons (right) in 2016 (top), 2017 (mid), and 2018 (bottom).

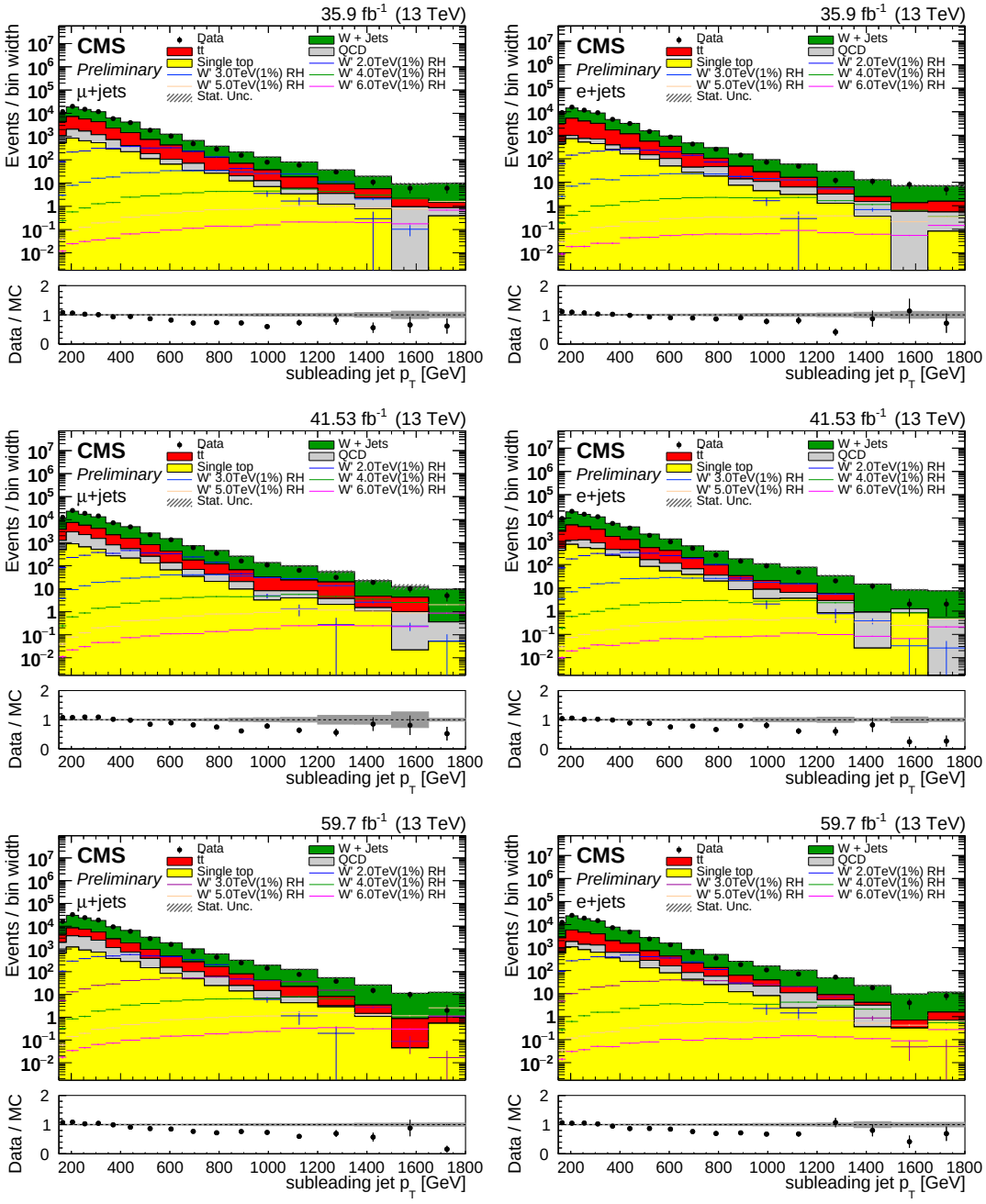

Figure A.5: Subleading jet p_{T} for muons (left) and electrons (right) in 2016 (top), 2017 (mid), and 2018 (bottom).

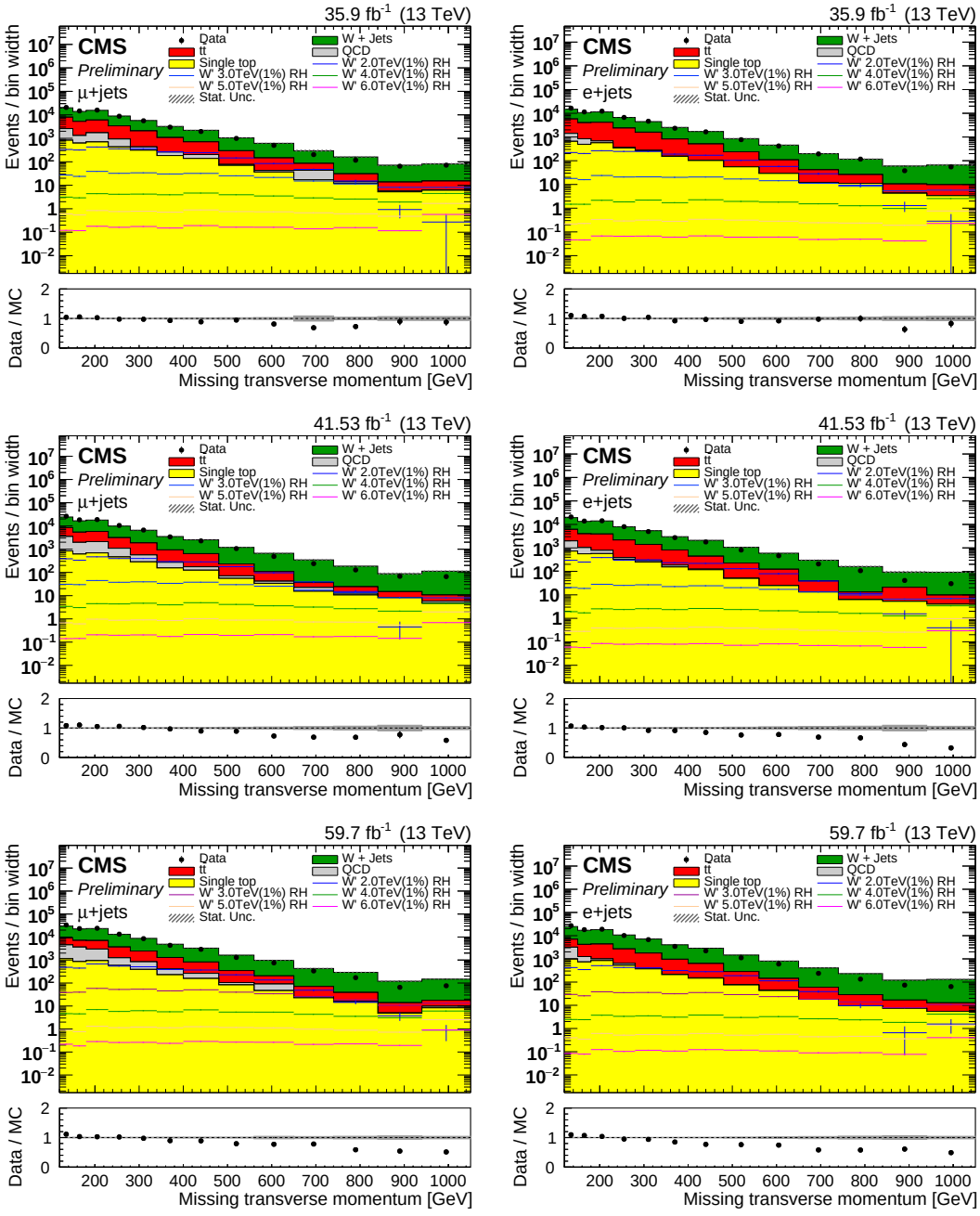

Figure A.6: MET for muons (left) and electrons (right) in 2016 (top), 2017 (mid), and 2018 (bottom).

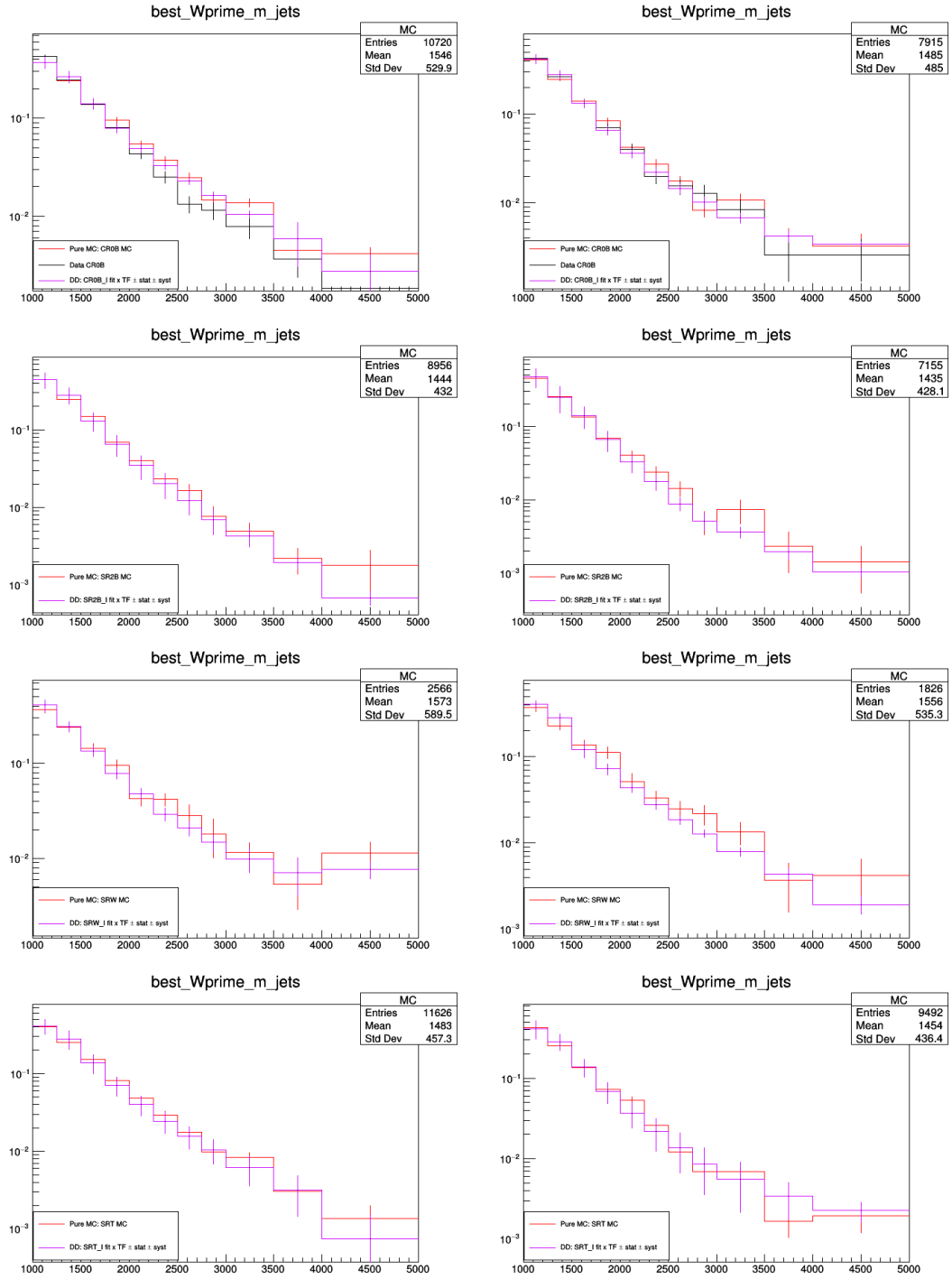

Figure A.7: Closure tests for the transfer functions, in the three SR comparing MC in the SR vs MC driven prediction (red), MC×TF closure check, and data based prediction with the subtraction (green) and fit (violet) methods. In the CR0B also data are compared (in black).

Acknowledgements

This thesis reports part of my activities carried on in my three years of Ph.D. program at the Naples University. I am satisfied to write these last lines since it means that I almost succeeded in obtaining my Ph.D. in Physics. From my point of view the whole experience can be summed up by the following picture:

Jokes aside, I am very proud of myself for reaching this goal, even if great part of the credits goes to Orso. Trying to simply limit his role as a supervisor would be reductive and unfair. His kindness and availability are only exceeded by his competences. He was always present during the entire Ph.D. period and his help was not only limited to physics problems. My best thanks goes to him. I cannot forget in these pages to thank my parents and my sisters, without their support I would never have succeeded in it. This work is dedicated to them. Another important person I would like to thank is Biagio, who is trying to initiate me at the obscure art of the hardware and detector's physics with his knowledge and experience, without sacrificing moments of fun. The time spent at the university would not have been the same without the company of my dearest colleagues and friends. With them I lived special moments also outside the working time and university and I am really thankful to have them in my life. Among them I would like to give a special thank to Marcello who shared with me courses, exams, schools and conferences. I had also the precious opportunity to stay for an entire year at

CERN thanks to INFN. There I met wonderful people that made this experience even more amazing. With them I shared very pleasant moments and they also made the COVID pandemic less regrettable than it was. A special mention goes to Dario who always opened his house for our Cinefellow program and for so many Fondue evenings. I also would like to thank my roommates Nicolò, Alessandro, Mario, Andrea and Marco that with their enthusiasm made it pleasant to live together. Lastly, but not for importance, I would like to give a special thank to Federica. She was fundamental to me with her support and her niceness and I am very happy to have had her by my side.

Bibliography

[1] S. L. Glashow. "Partial Symmetries of Weak Interactions". In: *Nucl. Phys.* 22 (1961), pp. 579–588. DOI: 10.1016/0029-5582(61)90469-2.

[2] Steven Weinberg. "A Model of Leptons". In: *Phys. Rev. Lett.* 19 (1967), pp. 1264–1266. DOI: 10.1103/PhysRevLett.19.1264.

[3] Abdus Salam. "Weak and Electromagnetic Interactions". In: *Conf. Proc. C* 680519 (1968), pp. 367–377. DOI: 10.1142/9789812795915_0034.

[4] F. Englert and R. Brout. "Broken Symmetry and the Mass of Gauge Vector Mesons". In: *Phys. Rev. Lett.* 13 (1964). Ed. by J. C. Taylor, pp. 321–323. DOI: 10.1103/PhysRevLett.13.321.

[5] Peter W. Higgs. "Broken symmetries, massless particles and gauge fields". In: *Phys. Lett.* 12 (1964), pp. 132–133. DOI: 10.1016/0031-9163(64)91136-9.

[6] G. S. Guralnik, C. R. Hagen, and T. W. B. Kibble. "Global Conservation Laws and Massless Particles". In: *Phys. Rev. Lett.* 13 (1964). Ed. by J. C. Taylor, pp. 585–587. DOI: 10.1103/PhysRevLett.13.585.

[7] G. Zweig. "An SU(3) model for strong interaction symmetry and its breaking. Version 1". In: (Jan. 1964).

[8] M. Y. Han and Yoichiro Nambu. "Three Triplet Model with Double SU(3) Symmetry". In: *Phys. Rev.* 139 (1965). Ed. by T. Eguchi, B1006–B1010. DOI: 10.1103/PhysRev.139.B1006.

[9] O. W. Greenberg. "Spin and Unitary Spin Independence in a Paraquark Model of Baryons and Mesons". In: *Phys. Rev. Lett.* 13 (1964), pp. 598–602. DOI: 10.1103/PhysRevLett.13.598.

[10] H. David Politzer. "Reliable Perturbative Results for Strong Interactions?" In: *Phys. Rev. Lett.* 30 (1973). Ed. by J. C. Taylor, pp. 1346–1349. DOI: 10.1103/PhysRevLett.30.1346.

[11] David J. Gross and Frank Wilczek. "Ultraviolet Behavior of Nonabelian Gauge Theories". In: *Phys. Rev. Lett.* 30 (1973). Ed. by J. C. Taylor, pp. 1343–1346. DOI: 10.1103/PhysRevLett.30.1343.

[12] G. Arnison et al. "Experimental Observation of Isolated Large Transverse Energy Electrons with Associated Missing Energy at $\sqrt{s} = 540$ GeV". In: *Phys. Lett. B* 122 (1983), pp. 103–116. DOI: 10.1016/0370-2693(83)91177-2.

[13] M. Banner et al. "Observation of Single Isolated Electrons of High Transverse Momentum in Events with Missing Transverse Energy at the CERN anti-p p Collider". In: *Phys. Lett. B* 122 (1983), pp. 476–485. DOI: 10.1016/0370-2693(83)91605-2.

[14] P. Bagnaia et al. "Evidence for $Z^0 \to e^+e^-$ at the CERN $\bar{p}p$ Collider". In: *Phys. Lett. B* 129 (1983), pp. 130–140. DOI: 10.1016/0370-2693(83)90744-X.

[15] F. Abe et al. "Evidence for top quark production in $\bar{p}p$ collisions at $\sqrt{s} = 1.8$ TeV". In: *Phys. Rev. Lett.* 73 (1994), pp. 225–231. DOI: 10.1103/PhysRevLett.73.225. arXiv: hep-ex/9405005.

[16] Georges Aad et al. "Observation of a new particle in the search for the Standard Model Higgs boson with the ATLAS detector at the LHC". In: *Phys. Lett. B* 716 (2012), pp. 1–29. DOI: 10.1016/j.physletb.2012.08.020. arXiv: 1207.7214 [hep-ex].

[17] Serguei Chatrchyan et al. "Observation of a New Boson at a Mass of 125 GeV with the CMS Experiment at the LHC". In: *Phys. Lett. B* 716 (2012), pp. 30–61. DOI: 10.1016/j.physletb.2012.08.021. arXiv: 1207.7235 [hep-ex].

[18] P. A. Zyla et al. "Review of Particle Physics". In: *PTEP* 2020.8 (2020), p. 083C01. DOI: 10.1093/ptep/ptaa104.

[19] E. Fermi. "An attempt of a theory of beta radiation. 1." In: *Z. Phys.* 88 (1934), pp. 161–177. DOI: 10.1007/BF01351864.

[20] C. Jarlskog. "Commutator of the Quark Mass Matrices in the Standard Electroweak Model and a Measure of Maximal CP Violation". In: *Phys. Rev. Lett.* 55 (1985), p. 1039. DOI: 10.1103/PhysRevLett.55.1039.

[21] Joachim Brod, Martin Gorbahn, and Emmanuel Stamou. "Standard-Model Prediction of ϵ_K with Manifest Quark-Mixing Unitarity". In: *Phys. Rev. Lett.* 125.17 (2020), p. 171803. DOI: 10.1103/PhysRevLett.125.171803. arXiv: 1911.06822 [hep-ph].

[22] W. J. Marciano and A. Sirlin. "On the Renormalization of the Charm Quartet Model". In: *Nucl. Phys. B* 93 (1975), pp. 303–323. DOI: 10.1016/0550-3213(75)90574-X.

[23] K. S. Babu. "Renormalization Group Analysis of the Kobayashi-Maskawa Matrix". In: *Z. Phys. C* 35 (1987), p. 69. DOI: 10.1007/BF01561056.

[24] J. Charles et al. "CP violation and the CKM matrix: Assessing the impact of the asymmetric B factories". In: *Eur. Phys. J. C* 41.1 (2005), pp. 1–131. DOI: 10.1140/epjc/s2005-02169-1. arXiv: hep-ph/0406184.

[25] Anders Andreassen, William Frost, and Matthew D. Schwartz. "Scale invariant instantons and the complete lifetime of the Standard Model". In: *Phys. Rev. D* 97.5 (2018), p. 056006. DOI: 10.1103/PhysRevD.97.056006. arXiv: 1707.08124 [hep-ph].

[26] Serguei Chatrchyan et al. "Measurement of the t-channel single top quark production cross section in pp collisions at $\sqrt{s} = 7$ TeV". In: *Phys. Rev. Lett.* 107 (2011), p. 091802. DOI: 10.1103/PhysRevLett.107.091802. arXiv: 1106.3052 [hep-ex].

[27] Serguei Chatrchyan et al. "Measurement of the Single-Top-Quark t-Channel Cross Section in pp Collisions at $\sqrt{s} = 7$ TeV". In: *JHEP* 12 (2012), p. 035. DOI: 10.1007/JHEP12(2012)035. arXiv: 1209.4533 [hep-ex].

[28] Georges Aad et al. "Measurement of the t-channel single top-quark production cross section in pp collisions at $\sqrt{s} = 7$ TeV with the ATLAS detector". In: *Phys. Lett. B* 717 (2012), pp. 330–350. DOI: 10.1016/j.physletb.2012.09.031. arXiv: 1205.3130 [hep-ex].

[29] Georges Aad et al. "Comprehensive measurements of t-channel single top-quark production cross sections at $\sqrt{s} = 7$ TeV with the ATLAS detector". In: *Phys. Rev. D* 90.11 (2014), p. 112006. DOI: 10.1103/PhysRevD.90.112006. arXiv: 1406.7844 [hep-ex].

[30] Vardan Khachatryan et al. "Measurement of the t-channel single-top-quark production cross section and of the $| V_{tb} |$ CKM matrix element in pp collisions at $\sqrt{s}$= 8 TeV". In: *JHEP* 06 (2014), p. 090. DOI: 10.1007/JHEP06(2014)090. arXiv: 1403.7366 [hep-ex].

[31] Morad Aaboud et al. "Measurement of the inclusive cross-sections of single top-quark and top-antiquark t-channel production in pp collisions at $\sqrt{s}$ = 13 TeV with the ATLAS detector". In: *JHEP* 04 (2017), p. 086. DOI: 10.1007/JHEP04(2017)086. arXiv: 1609.03920 [hep-ex].

[32] Albert M Sirunyan et al. "Cross section measurement of t-channel single top quark production in pp collisions at $\sqrt{s} = 13$ TeV". In: *Phys. Lett. B* 772 (2017), pp. 752–776. DOI: 10.1016/j.physletb.2017.07.047. arXiv: 1610.00678 [hep-ex].

[33] Morad Aaboud et al. "Fiducial, total and differential cross-section measurements of t-channel single top-quark production in pp collisions at 8 TeV using data collected by the ATLAS detector". In: *Eur. Phys. J. C* 77.8 (2017), p. 531. DOI: 10.1140/epjc/s10052-017-5061-9. arXiv: 1702.02859 [hep-ex].

[34] Albert M Sirunyan et al. "Measurement of the single top quark and antiquark production cross sections in the t channel and their ratio in proton-proton collisions at $\sqrt{s} = 13$ TeV". In: *Phys. Lett. B* 800 (2020), p. 135042. DOI: 10.1016/j.physletb.2019.135042. arXiv: 1812.10514 [hep-ex].

[35] Albert M Sirunyan et al. "Measurement of differential cross sections and charge ratios for t-channel single top quark production in proton–proton collisions at $\sqrt{s} = 13\,\text{TeV}$". In: *Eur. Phys. J. C* 80.5 (2020), p. 370. DOI: 10.1140/epjc/s10052-020-7858-1. arXiv: 1907.08330 [hep-ex].

[36] Guido Altarelli and G. Parisi. "Asymptotic Freedom in Parton Language". In: *Nucl. Phys. B* 126 (1977), pp. 298–318. DOI: 10.1016/0550-3213(77)90384-4.

[37] Yuri L. Dokshitzer. "Calculation of the structure functions for deep inelastic scattering and e+ e- annihilation by perturbation theory in quantum chromodynamics." In: *Sov. Phys. JETP* 46 (1977), pp. 641–653.

[38] V. N. Gribov and L. N. Lipatov. "Deep inelastic e p scattering in perturbation theory". In: *Sov. J. Nucl. Phys.* 15 (1972), pp. 438–450.

[39] Richard D. Ball et al. "Parton distributions from high-precision collider data". In: *Eur. Phys. J. C* 77.10 (2017), p. 663. DOI: 10.1140/epjc/s10052-017-5199-5. arXiv: 1706.00428 [hep-ph].

[40] Albert M Sirunyan et al. "Observation of Single Top Quark Production in Association with a Z Boson in Proton-Proton Collisions at $\sqrt{s}$ =13 TeV". In: *Phys. Rev. Lett.* 122.13 (2019), p. 132003. DOI: 10.1103/PhysRevLett.122.132003. arXiv: 1812.05900 [hep-ex].

[41] Albert M Sirunyan et al. "Evidence for the associated production of a single top quark and a photon in proton-proton collisions at $\sqrt{s} = 13$ TeV". In: *Phys. Rev. Lett.* 121.22 (2018), p. 221802. DOI: 10.1103/PhysRevLett.121.221802. arXiv: 1808.02913 [hep-ex].

[42] Jafari, A. and others. *CMS Top Quark Physics Summary Figures*. Twiki. 2020. URL: https://twiki.cern.ch/twiki/bin/view/CMSPublic/PhysicsResultsTOPSummaryFigures.

[43] Morad Aaboud et al. "Combinations of single-top-quark production cross-section measurements and $|f_{LV}V_{tb}|$ determinations at $\sqrt{s} = 7$ and 8 TeV with the ATLAS and CMS experiments". In: *JHEP* 05 (2019), p. 088. DOI: 10.1007/JHEP05(2019)088. arXiv: 1902.07158 [hep-ex].

[44] V. M. Abazov et al. "Precision measurement of the ratio $B(t \to Wb)/B(t \to Wq)$ and extraction of V_{tb}". In: *Phys. Rev. Lett.* 107 (2011), p. 121802. DOI: 10.1103/PhysRevLett.107.121802. arXiv: 1106.5436 [hep-ex].

[45] T. Aaltonen et al. "Measurement of $R = \mathcal{B}(t \to Wb)/\mathcal{B}(t \to Wq)$ in Top–quark–pair decays using Llepton+jets events and the full CDF Run II data set". In: *Phys. Rev. D* 87.11 (2013), p. 111101. DOI: 10.1103/PhysRevD.87.111101. arXiv: 1303.6142 [hep-ex].

[46] Timo Antero Aaltonen et al. "Measurement of $B(t \to Wb)/B(t \to Wq)$ in top-quark-pair decays using dilepton events and the full CDF run II data set". In: *Phys. Rev. Lett.* 112.22 (2014), p. 221801. DOI: 10.1103/PhysRevLett.112.221801. arXiv: 1404.3392 [hep-ex].

[47] Vardan Khachatryan et al. "Measurement of the ratio $\mathcal{B}(t \to Wb)/\mathcal{B}(t \to Wq)$ in pp collisions at $\sqrt{s} = 8$ TeV". In: *Phys. Lett. B* 736 (2014), pp. 33–57. DOI: 10.1016/j.physletb.2014.06.076. arXiv: 1404.2292 [hep-ex].

[48] Matthew Baumgart and Brock Tweedie. "A New Twist on Top Quark Spin Correlations". In: *JHEP* 03 (2013), p. 117. DOI: 10.1007/JHEP03(2013)117. arXiv: 1212.4888 [hep-ph].

[49] Albert M Sirunyan et al. "Measurement of the top quark polarization and $t\bar{t}$ spin correlations using dilepton final states in proton-proton collisions at $\sqrt{s} = 13$ TeV". In: *Phys. Rev. D* 100.7 (2019), p. 072002. DOI: 10.1103/PhysRevD.100.072002. arXiv: 1907.03729 [hep-ex].

[50] Ennio Salvioni, Giovanni Villadoro, and Fabio Zwirner. "Minimal Z' models: Present bounds and early LHC reach". In: *JHEP* 11 (2009), p. 068. DOI: 10.1088/1126-6708/2009/11/068. arXiv: 0909.1320 [hep-ph].

[51] Ennio Salvioni et al. "Non-universal minimal Z' models: present bounds and early LHC reach". In: *JHEP* 03 (2010), p. 010. DOI: 10.1007/JHEP03(2010)010. arXiv: 0911.1450 [hep-ph].

[52] Christophe Grojean, Ennio Salvioni, and Riccardo Torre. "A weakly constrained W' at the early LHC". In: *JHEP* 07 (2011), p. 002. DOI: 10.1007/JHEP07(2011)002. arXiv: 1103.2761 [hep-ph].

[53] J. de Blas, J. M. Lizana, and M. Perez-Victoria. "Combining searches of Z' and W' bosons". In: *JHEP* 01 (2013), p. 166. DOI: 10.1007/JHEP01(2013)166. arXiv: 1211.2229 [hep-ph].

[54] T. Appelquist, A. Chodos, and P. G. O. Freund, eds. *Modern Kaluza-Klein theories*. 1987.

[55] Th. Kaluza. "Zum Unitätsproblem der Physik". In: *Int. J. Mod. Phys. D* 27.14 (2018), p. 1870001. DOI: 10.1142/S0218271818700017. arXiv: 1803.08616 [physics.hist-ph].

[56] O. Klein. "The Atomicity of Electricity as a Quantum Theory Law". In: *Nature* 118 (1926), p. 516. DOI: 10.1038/118516a0.

[57] Oskar Klein. "Quantum Theory and Five-Dimensional Theory of Relativity. (In German and English)". In: *Z. Phys.* 37 (1926). Ed. by J. C. Taylor, pp. 895–906. DOI: 10.1007/BF01397481.

[58] Nima Arkani-Hamed, Savas Dimopoulos, and G. R. Dvali. "The Hierarchy problem and new dimensions at a millimeter". In: *Phys. Lett. B* 429 (1998), pp. 263–272. DOI: 10.1016/S0370-2693(98)00466-3. arXiv: hep-ph/9803315.

[59] H. Davoudiasl, J. L. Hewett, and T. G. Rizzo. "Bulk gauge fields in the Randall-Sundrum model". In: *Phys. Lett. B* 473 (2000), pp. 43–49. DOI: 10.1016/S0370-2693(99)01430-6. arXiv: hep-ph/9911262.

[60] Alex Pomarol. "Gauge bosons in a five-dimensional theory with localized gravity". In: *Phys. Lett. B* 486 (2000), pp. 153–157. DOI: 10.1016/S0370-2693(00)00737-1. arXiv: hep-ph/9911294.

[61] Sanghyeon Chang et al. "Bulk standard model in the Randall-Sundrum background". In: *Phys. Rev. D* 62 (2000), p. 084025. DOI: 10.1103/PhysRevD.62.084025. arXiv: hep-ph/9912498.

[62] Tony Gherghetta and Alex Pomarol. "Bulk fields and supersymmetry in a slice of AdS". In: *Nucl. Phys. B* 586 (2000), pp. 141–162. DOI: 10.1016/S0550-3213(00)00392-8. arXiv: hep-ph/0003129.

[63] Nima Arkani-Hamed, Massimo Porrati, and Lisa Randall. "Holography and phenomenology". In: *JHEP* 08 (2001), p. 017. DOI: 10.1088/1126-6708/2001/08/017. arXiv: hep-th/0012148.

[64] David B. Kaplan. "Flavor at SSC energies: A New mechanism for dynamically generated fermion masses". In: *Nucl. Phys. B* 365 (1991), pp. 259–278. DOI: 10.1016/S0550-3213(05)80021-5.

[65] Nima Arkani-Hamed, Andrew G. Cohen, and Howard Georgi. "Electroweak symmetry breaking from dimensional deconstruction". In: *Phys. Lett. B* 513 (2001), pp. 232–240. DOI: 10.1016/S0370-2693(01)00741-9. arXiv: hep-ph/0105239.

[66] N. Arkani-Hamed et al. "The Littlest Higgs". In: *JHEP* 07 (2002), p. 034. DOI: 10.1088/1126-6708/2002/07/034. arXiv: hep-ph/0206021.

[67] T. D. Lee and Chen-Ning Yang. "Question of Parity Conservation in Weak Interactions". In: *Phys. Rev.* 104 (1956), pp. 254–258. DOI: 10.1103/PhysRev.104.254.

[68] Alessio Maiezza et al. "Left-Right Symmetry at LHC". In: *Phys. Rev. D* 82 (2010), p. 055022. DOI: 10.1103/PhysRevD.82.055022. arXiv: 1005.5160 [hep-ph].

[69] W. Grimus. "Introduction to left-right symmetric models". In: *4th Hellenic School on Elementary Particle Physics*. Mar. 1993, pp. 619–632.

[70] F. Pisano and V. Pleitez. "An SU(3) x U(1) model for electroweak interactions". In: *Phys. Rev. D* 46 (1992), pp. 410–417. DOI: 10.1103/PhysRevD.46.410. arXiv: hep-ph/9206242.

[71] P. H. Frampton. "Chiral dilepton model and the flavor question". In: *Phys. Rev. Lett.* 69 (1992), pp. 2889–2891. DOI: 10.1103/PhysRevLett.69.2889.

[72] Andrzej J. Buras et al. "The Anatomy of Quark Flavour Observables in 331 Models in the Flavour Precision Era". In: *JHEP* 02 (2013), p. 023. DOI: 10.1007/JHEP02(2013)023. arXiv: 1211.1237 [hep-ph].

[73] David J. Muller and Satyanarayan Nandi. "Top flavor: A Separate SU(2) for the third family". In: *Phys. Lett. B* 383 (1996), pp. 345–350. DOI: 10.1016/0370-2693(96)00745-9. arXiv: hep-ph/9602390.

[74] Yoichiro Nambu and G. Jona-Lasinio. "Dynamical model of elementary particles based on an analogy with superconductivity I." In: *Phys. Rev.* 122 (1961). Ed. by T. Eguchi, pp. 345–358. DOI: 10.1103/PhysRev.122.345.

[75] Yoichiro Nambu and G. Jona-Lasinio. "Dynamical model of elementary particles based on an analogy with superconductivity II." In: *Phys. Rev.* 124 (1961). Ed. by T. Eguchi, pp. 246–254. DOI: 10.1103/PhysRev.124.246.

[76] Roberta Calabrese et al. "The TopFlavor scheme in the context of W' searches at LHC". In: (Apr. 2021). arXiv: 2104.06720 [hep-ph].

[77] E. Boos et al. "Interference between W' and W in single-top quark production processes". In: *Phys. Lett. B* 655 (2007), pp. 245–250. DOI: 10.1016/j.physletb.2007.03.064. arXiv: hep-ph/0610080.

[78] J. Alwall et al. "The automated computation of tree-level and next-to-leading order differential cross sections, and their matching to parton shower simulations". In: *JHEP* 07 (2014), p. 079. DOI: 10.1007/JHEP07(2014)079. arXiv: 1405.0301 [hep-ph].

[79] Zack Sullivan. "Fully Differential W' Production and Decay at Next-to-Leading Order in QCD". In: *Phys. Rev. D* 66 (2002), p. 075011. DOI: 10.1103/PhysRevD.66.075011. arXiv: hep-ph/0207290.

[80] Daniel Duffty and Zack Sullivan. "Model independent reach for W-prime bosons at the LHC". In: *Phys. Rev. D* 86 (2012), p. 075018. DOI: 10.1103/PhysRevD.86.075018. arXiv: 1208.4858 [hep-ph].

[81] Pierre Artoisenet et al. "Automatic spin-entangled decays of heavy resonances in Monte Carlo simulations". In: *JHEP* 03 (2013), p. 015. DOI: 10.1007/JHEP03(2013)015. arXiv: 1212.3460 [hep-ph].

[82] Albert M Sirunyan et al. "Search for heavy resonances decaying to a top quark and a bottom quark in the lepton+jets final state in proton–proton collisions at 13 TeV". In: *Phys. Lett. B* 777 (2018), pp. 39–63. DOI: 10.1016/j.physletb.2017.12.006. arXiv: 1708.08539 [hep-ex].

[83] Georges Aad et al. "Search for a heavy charged boson in events with a charged lepton and missing transverse momentum from pp collisions at $\sqrt{s} = 13$ TeV with the ATLAS detector". In: *Phys. Rev. D* 100.5 (2019), p. 052013. DOI: 10.1103/PhysRevD.100.052013. arXiv: 1906.05609 [hep-ex].

[84] Albert M Sirunyan et al. "Search for high-mass resonances in final states with a lepton and missing transverse momentum at $\sqrt{s} = 13$ TeV". In: *JHEP* 06 (2018), p. 128. DOI: 10.1007/JHEP06(2018)128. arXiv: 1803.11133 [hep-ex].

[85] Morad Aaboud et al. "Search for High-Mass Resonances Decaying to $\tau\nu$ in pp Collisions at $\sqrt{s}$=13 TeV with the ATLAS Detector". In: *Phys. Rev. Lett.* 120.16 (2018), p. 161802. DOI: 10.1103/PhysRevLett.120.161802. arXiv: 1801.06992 [hep-ex].

[86] Albert M Sirunyan et al. "Search for a W' boson decaying to a τ lepton and a neutrino in proton-proton collisions at $\sqrt{s} = 13$ TeV". In: *Phys. Lett. B* 792 (2019), pp. 107–131. DOI: 10.1016/j.physletb.2019.01.069. arXiv: 1807.11421 [hep-ex].

[87] Georges Aad et al. "Search for dijet resonances in events with an isolated charged lepton using $\sqrt{s} = 13$ TeV proton-proton collision data collected by the ATLAS detector". In: *JHEP* 06 (2020), p. 151. DOI: 10.1007/JHEP06(2020)151. arXiv: 2002.11325 [hep-ex].

[88] Morad Aaboud et al. "Search for new phenomena in dijet events using 37 fb^{-1} of pp collision data collected at $\sqrt{s}$ =13 TeV with the ATLAS detector". In: *Phys. Rev. D* 96.5 (2017), p. 052004. DOI: 10.1103/PhysRevD.96.052004. arXiv: 1703.09127 [hep-ex].

[89] Albert M Sirunyan et al. "Search for high mass dijet resonances with a new background prediction method in proton-proton collisions at $\sqrt{s} = 13$ TeV". In: *JHEP* 05 (2020), p. 033. DOI: 10.1007/JHEP05(2020)033. arXiv: 1911.03947 [hep-ex].

[90] Morad Aaboud et al. "Search for heavy resonances decaying to a W or Z boson and a Higgs boson in the $q\bar{q}^{(\prime)}b\bar{b}$ final state in pp collisions at $\sqrt{s} = 13$ TeV with the ATLAS detector". In: *Phys. Lett. B* 774 (2017), pp. 494–515. DOI: 10.1016/j.physletb.2017.09.066. arXiv: 1707.06958 [hep-ex].

[91] Morad Aaboud et al. "Search for heavy resonances decaying into a W or Z boson and a Higgs boson in final states with leptons and b-jets in 36 fb^{-1} of $\sqrt{s} = 13$ TeV pp collisions with the ATLAS detector". In: *JHEP* 03 (2018). [Erratum: JHEP 11, 051 (2018)], p. 174. DOI: 10.1007/JHEP03(2018)174. arXiv: 1712.06518 [hep-ex].

[92] Albert M. Sirunyan et al. "Search for heavy resonances decaying into a vector boson and a Higgs boson in final states with charged leptons, neutrinos and b quarks at $\sqrt{s} = 13$ TeV". In: *JHEP* 11 (2018), p. 172. DOI: 10.1007/JHEP11(2018)172. arXiv: 1807.02826 [hep-ex].

[93] Albert M Sirunyan et al. "Search for heavy resonances that decay into a vector boson and a Higgs boson in hadronic final states at $\sqrt{s} = 13$ TeV". In: *Eur. Phys. J. C* 77.9 (2017), p. 636. DOI: 10.1140/epjc/s10052-017-5192-z. arXiv: 1707.01303 [hep-ex].

[94] Duccio Pappadopulo et al. "Heavy Vector Triplets: Bridging Theory and Data". In: *JHEP* 09 (2014), p. 060. DOI: 10.1007/JHEP09(2014)060. arXiv: 1402.4431 [hep-ph].

[95] Morad Aaboud et al. "Search for vector-boson resonances decaying to a top quark and bottom quark in the lepton plus jets final state in pp collisions at $\sqrt{s} = 13$ TeV with the ATLAS detector". In: *Phys. Lett. B* 788 (2019), pp. 347–370. DOI: 10.1016/j.physletb.2018.11.032. arXiv: 1807.10473 [hep-ex].

[96] Morad Aaboud et al. "Search for $W' \to tb$ decays in the hadronic final state using pp collisions at $\sqrt{s} = 13$ TeV with the ATLAS detector". In: *Phys. Lett. B* 781 (2018), pp. 327–348. DOI: 10.1016/j.physletb.2018.03.036. arXiv: 1801.07893 [hep-ex].

[97] Albert M Sirunyan et al. "Search for W' bosons decaying to a top and a bottom quark at $\sqrt{s}$ =13 TeV in the hadronic final state". In: (Apr. 2021). arXiv: 2104.04831 [hep-ex].

[98] R. Sekhar Chivukula et al. "A Three Site Higgsless Model". In: *Phys. Rev. D* 74 (2006), p. 075011. DOI: 10.1103/PhysRevD.74.075011. arXiv: hep-ph/0607124.

[99] Yue Zhang et al. "Right-handed quark mixings in minimal left-right symmetric model with general CP violation". In: *Phys. Rev. D* 76 (2007), p. 091301. DOI: 10.1103/PhysRevD.76.091301. arXiv: 0704.1662 [hep-ph].

[100] Paul Langacker and S. Uma Sankar. "Bounds on the Mass of W(R) and the W(L)-W(R) Mixing Angle xi in General SU(2)-L x SU(2)-R x U(1) Models". In: *Phys. Rev. D* 40 (1989), pp. 1569–1585. DOI: 10.1103/PhysRevD.40.1569.

[101] J. F. Bueno et al. "Precise measurement of parity violation in polarized muon decay". In: *Phys. Rev. D* 84 (2011), p. 032005. DOI: 10.1103/PhysRevD.84.032005. arXiv: 1104.3632 [hep-ex].

[102] Gary Prezeau, M. Ramsey-Musolf, and Petr Vogel. "Neutrinoless double beta decay and effective field theory". In: *Phys. Rev. D* 68 (2003), p. 034016. DOI: 10.1103/PhysRevD.68.034016. arXiv: hep-ph/0303205.

[103] "LHC Machine". In: *JINST* 3 (2008). Ed. by Lyndon Evans and Philip Bryant, S08001. DOI: 10.1088/1748-0221/3/08/S08001.

[104] K. Aamodt et al. "The ALICE experiment at the CERN LHC". In: *JINST* 3 (2008), S08002. DOI: 10.1088/1748-0221/3/08/S08002.

[105] G. Aad et al. "The ATLAS Experiment at the CERN Large Hadron Collider". In: *JINST* 3 (2008), S08003. DOI: 10.1088/1748-0221/3/08/S08003.

[106] S. Chatrchyan et al. "The CMS Experiment at the CERN LHC". In: *JINST* 3 (2008), S08004. DOI: 10.1088/1748-0221/3/08/S08004.

[107] A. Augusto Alves Jr. et al. "The LHCb Detector at the LHC". In: *JINST* 3 (2008), S08005. DOI: 10.1088/1748-0221/3/08/S08005.

[108] V Karimaki et al. *The CMS tracker system project: Technical Design Report*. Technical design report. CMS. Geneva: CERN, 1997. URL: http://cds.cern.ch/record/368412.

[109] *The CMS tracker: addendum to the Technical Design Report*. Technical design report. CMS. Geneva: CERN, 2000. URL: http://cds.cern.ch/record/490194.

[110] *The CMS electromagnetic calorimeter project: Technical Design Report*. Technical design report. CMS. Geneva: CERN, 1997. URL: http://cds.cern.ch/record/349375.

[111] *The CMS hadron calorimeter project: Technical Design Report*. Technical design report. CMS. Geneva: CERN, 1997. URL: http://cds.cern.ch/record/357153.

[112] *The CMS magnet project: Technical Design Report*. Technical design report. CMS. Geneva: CERN, 1997. URL: http://cds.cern.ch/record/331056.

[113] A Tapper and Darin Acosta. *CMS Technical Design Report for the Level-1 Trigger Upgrade*. Tech. rep. CERN-LHCC-2013-011. CMS-TDR-12. June 2013. URL: http://cds.cern.ch/record/1556311.

[114] Sergio Cittolin, Attila Rácz, and Paris Sphicas. *CMS The TriDAS Project: Technical Design Report, Volume 2: Data Acquisition and High-Level Trigger. CMS trigger and data-acquisition project*. Technical design report. CMS. Geneva: CERN, 2002. URL: http://cds.cern.ch/record/578006.

[115] A Colaleo et al. *CMS Technical Design Report for the Muon Endcap GEM Upgrade*. Tech. rep. CERN-LHCC-2015-012. CMS-TDR-013. June 2015. URL: http://cds.cern.ch/record/2021453.

[116] F. Sauli. "GEM: A new concept for electron amplification in gas detectors". In: *Nucl. Instrum. Meth. A* 386 (1997), pp. 531–534. DOI: 10.1016/S0168-9002(96)01172-2.

[117] M. Abbas et al. "Performance of prototype GE1 / 1 chambers for the CMS muon spectrometer upgrade". In: *Nucl. Instrum. Meth. A* 972 (2020), p. 164104. DOI: 10.1016/j.nima.2020.164104. arXiv: 1903.02186 [physics.ins-det].

[118] Heinz Raether. *Electron avalanches and breakdown in gases*. Washington: Butterworths, 1964, p. 191.

[119] S. Bachmann et al. "Discharge mechanisms and their prevention in the gas electron multiplier (GEM)". In: *Nucl. Instrum. Meth. A* 479 (2002), pp. 294–308. DOI: 10.1016/S0168-9002(01)00931-7.

[120] M. Abbas et al. "Detector Control System for the GE1/1 slice test". In: *JINST* 15.05 (2020), P05023. DOI: 10.1088/1748-0221/15/05/P05023.

[121] D. Abbaneo et al. "Layout and Assembly Technique of the GEM Chambers for the Upgrade of the CMS First Muon Endcap Station". In: *Nucl. Instrum. Meth. A* 918 (2019), pp. 67–75. DOI: 10.1016/j.nima.2018.11.061. arXiv: 1812.00411 [physics.ins-det].

[122] Kamon, T. and others. *GEM DPG Public Page*. Twiki. 2020. URL: https://twiki.cern.ch/twiki/bin/view/CMSPublic/GEMDPGPublic.

[123] Paolo Azzurri. "Track Reconstruction Performance in CMS". In: *Nucl. Phys. B Proc. Suppl.* 197 (2009). Ed. by Pietro Govoni et al., pp. 275–278. DOI: 10.1016/j.nuclphysbps.2009.10.084. arXiv: 0812.5036 [physics.ins-det].

[124] A. M. Sirunyan et al. "Particle-flow reconstruction and global event description with the CMS detector". In: *JINST* 12.10 (2017), P10003. DOI: 10.1088/1748-0221/12/10/P10003. arXiv: 1706.04965 [physics.ins-det].

[125] Serguei Chatrchyan et al. "Description and performance of track and primary-vertex reconstruction with the CMS tracker". In: *JINST* 9.10 (2014), P10009. DOI: 10.1088/1748-0221/9/10/P10009. arXiv: 1405.6569 [physics.ins-det].

[126] W. Adam et al. "Reconstruction of electrons with the Gaussian sum filter in the CMS tracker at LHC". In: *eConf* C0303241 (2003), TULT009. DOI: 10.1088/0954-3899/31/9/N01. arXiv: physics/0306087.

[127] Gavin P. Salam. "Towards Jetography". In: *Eur. Phys. J. C* 67 (2010), pp. 637–686. DOI: 10.1140/epjc/s10052-010-1314-6. arXiv: 0906.1833 [hep-ph].

[128] Matteo Cacciari, Gavin P. Salam, and Gregory Soyez. "The anti-k_t jet clustering algorithm". In: *JHEP* 04 (2008), p. 063. DOI: 10.1088/1126-6708/2008/04/063. arXiv: 0802.1189 [hep-ph].

[129] Matteo Cacciari, Gavin P. Salam, and Gregory Soyez. "FastJet User Manual". In: *Eur. Phys. J. C* 72 (2012), p. 1896. DOI: 10.1140/epjc/s10052-012-1896-2. arXiv: 1111.6097 [hep-ph].

[130] *Pileup Removal Algorithms*. Tech. rep. CMS-PAS-JME-14-001. Geneva: CERN, 2014. URL: http://cds.cern.ch/record/1751454.

[131] Daniele Bertolini et al. "Pileup Per Particle Identification". In: *JHEP* 10 (2014), p. 059. DOI: 10.1007/JHEP10(2014)059. arXiv: 1407.6013 [hep-ph].

[132] Vardan Khachatryan et al. "Jet energy scale and resolution in the CMS experiment in pp collisions at 8 TeV". In: *JINST* 12.02 (2017), P02014. DOI: 10.1088/1748-0221/12/02/P02014. arXiv: 1607.03663 [hep-ex].

[133] "Performance of missing energy reconstruction in 13 TeV pp collision data using the CMS detector". In: (Aug. 2016).

[134] *Identification of b quark jets at the CMS Experiment in the LHC Run 2*. Tech. rep. CMS-PAS-BTV-15-001. Geneva: CERN, 2016. URL: http://cds.cern.ch/record/2138504.

[135] A. M. Sirunyan et al. "Identification of heavy-flavour jets with the CMS detector in pp collisions at 13 TeV". In: *JINST* 13.05 (2018), P05011. DOI: 10.1088/1748-0221/13/05/P05011. arXiv: 1712.07158 [physics.ins-det].

[136] Emil Bols et al. "Jet Flavour Classification Using DeepJet". In: *JINST* 15.12 (2020), P12012. DOI: 10.1088/1748-0221/15/12/P12012. arXiv: 2008.10519 [hep-ex].

[137] Makoto Kobayashi and Toshihide Maskawa. "CP Violation in the Renormalizable Theory of Weak Interaction". In: *Prog. Theor. Phys.* 49 (1973), pp. 652–657. DOI: 10.1143/PTP.49.652.

[138] Paolo Nason. "A New method for combining NLO QCD with shower Monte Carlo algorithms". In: *JHEP* 11 (2004), p. 040. DOI: 10.1088/1126-6708/2004/11/040. arXiv: hep-ph/0409146.

[139] Stefano Frixione, Paolo Nason, and Carlo Oleari. "Matching NLO QCD computations with Parton Shower simulations: the POWHEG method". In: *JHEP* 11 (2007), p. 070. DOI: 10.1088/1126-6708/2007/11/070. arXiv: 0709.2092 [hep-ph].

[140] Simone Alioli et al. "A general framework for implementing NLO calculations in shower Monte Carlo programs: the POWHEG BOX". In: *JHEP* 06 (2010), p. 043. DOI: 10.1007/JHEP06(2010)043. arXiv: 1002.2581 [hep-ph].

[141] Rikkert Frederix, Emanuele Re, and Paolo Torrielli. "Single-top t-channel hadroproduction in the four-flavour scheme with POWHEG and aMC@NLO". In: *JHEP* 09 (2012), p. 130. DOI: 10.1007/JHEP09(2012)130. arXiv: 1207.5391 [hep-ph].

[142] Simone Alioli et al. "NLO single-top production matched with shower in POWHEG: s- and t-channel contributions". In: *JHEP* 09 (2009). [Erratum: JHEP 02, 011 (2010)], p. 111. DOI: 10.1088/1126-6708/2009/09/111. arXiv: 0907.4076 [hep-ph].

[143] Stefano Frixione, Paolo Nason, and Giovanni Ridolfi. "A Positive-weight next-to-leading-order Monte Carlo for heavy flavour hadroproduction". In: *JHEP* 09 (2007), p. 126. DOI: 10.1088/1126-6708/2007/09/126. arXiv: 0707.3088 [hep-ph].

[144] Tom Melia et al. "W^+W^-, WZ and ZZ production in the POWHEG BOX". In: *JHEP* 11 (2011), p. 078. DOI: 10.1007/JHEP11(2011)078. arXiv: 1107.5051 [hep-ph].

[145] Paolo Nason and Giulia Zanderighi. "W^+W^- , WZ and ZZ production in the POWHEG-BOX-V2". In: *Eur. Phys. J. C* 74.1 (2014), p. 2702. DOI: 10.1140/epjc/s10052-013-2702-5. arXiv: 1311.1365 [hep-ph].

[146] Emanuele Re. "Single-top Wt-channel production matched with parton showers using the POWHEG method". In: *Eur. Phys. J. C* 71 (2011), p. 1547. DOI: 10.1140/epjc/s10052-011-1547-z. arXiv: 1009.2450 [hep-ph].

[147] Torbjorn Sjostrand, Stephen Mrenna, and Peter Z. Skands. "A Brief Introduction to PYTHIA 8.1". In: *Comput. Phys. Commun.* 178 (2008), pp. 852–867. DOI: 10.1016/j.cpc.2008.01.036. arXiv: 0710.3820 [hep-ph].

[148] Vardan Khachatryan et al. "Event generator tunes obtained from underlying event and multiparton scattering measurements". In: *Eur. Phys. J. C* 76.3 (2016), p. 155. DOI: 10.1140/epjc/s10052-016-3988-x. arXiv: 1512.00815 [hep-ex].

[149] *Investigations of the impact of the parton shower tuning in Pythia 8 in the modelling of* $\mathrm{t\bar{t}}$ *at* $\sqrt{s} = 8$ *and 13 TeV*. Tech. rep. CMS-PAS-TOP-16-021. Geneva: CERN, 2016. URL: http://cds.cern.ch/record/2235192.

[150] Rikkert Frederix and Stefano Frixione. "Merging meets matching in MC@NLO". In: *JHEP* 12 (2012), p. 061. DOI: 10.1007/JHEP12(2012)061. arXiv: 1209.6215 [hep-ph].

[151] Richard D. Ball et al. "Reweighting and Unweighting of Parton Distributions and the LHC W lepton asymmetry data". In: *Nucl. Phys. B* 855 (2012), pp. 608–638. DOI: 10.1016/j.nuclphysb.2011.10.018. arXiv: 1108.1758 [hep-ph].

[152] S. Agostinelli et al. "GEANT4–a simulation toolkit". In: *Nucl. Instrum. Meth. A* 506 (2003), pp. 250–303. DOI: 10.1016/S0168-9002(03)01368-8.

[153] Albert M Sirunyan et al. "Measurement of CKM matrix elements in single top quark t-channel production in proton-proton collisions at $\sqrt{s} = 13$ TeV". In: *Phys. Lett. B* 808 (2020), p. 135609. DOI: 10.1016/j.physletb.2020.135609. arXiv: 2004.12181 [hep-ex].

[154] Andreas Hocker et al. "TMVA - Toolkit for Multivariate Data Analysis". In: (Mar. 2007). arXiv: physics/0703039.

[155] I. Antcheva et al. "ROOT: A C++ framework for petabyte data storage, statistical analysis and visualization". In: *Comput. Phys. Commun.* 180 (2009), pp. 2499–2512. DOI: 10.1016/j.cpc.2009.08.005. arXiv: 1508.07749 [physics.data-an].

[156] Roger J. Barlow and Christine Beeston. "Fitting using finite Monte Carlo samples". In: *Comput. Phys. Commun.* 77 (1993), pp. 219–228. DOI: 10.1016/0010-4655(93)90005-W.

[157] J. S. Conway. "Incorporating Nuisance Parameters in Likelihoods for Multisource Spectra". In: *PHYSTAT 2011*. 2011, pp. 115–120. DOI: 10.5170/CERN-2011-006.115. arXiv: 1103.0354 [physics.data-an].

[158] Vardan Khachatryan et al. "Measurements of Inclusive W and Z Cross Sections in pp Collisions at $\sqrt{s} = 7$ TeV". In: *JHEP* 01 (2011), p. 080. DOI: 10.1007/JHEP01(2011)080. arXiv: 1012.2466 [hep-ex].

[159] Albert M Sirunyan et al. "Measurement of the inelastic proton-proton cross section at $\sqrt{s} = 13$ TeV". In: *JHEP* 07 (2018), p. 161. DOI: 10.1007/JHEP07(2018)161. arXiv: 1802.02613 [hep-ex].

[160] Jon Butterworth et al. "PDF4LHC recommendations for LHC Run II". In: *J. Phys. G* 43 (2016), p. 023001. DOI: 10.1088/0954-3899/43/2/023001. arXiv: 1510.03865 [hep-ph].

[161] *CMS Luminosity Measurements for the 2016 Data Taking Period*. Tech. rep. CMS-PAS-LUM-17-001. Geneva: CERN, 2017. URL: http://cds.cern.ch/record/2257069.

[162] Petrucciani, G. and others. *Documentation of the RooStats-based statistics tools for Higgs PAG*. Twiki. 2012. URL: https://twiki.cern.ch/twiki/bin/view/CMS/SWGuideHiggsAnalysisCombinedLimit.

[163] Lorenzo Moneta et al. "The RooStats Project". In: *PoS* ACAT2010 (2010). Ed. by T. Speer et al., p. 057. DOI: 10.22323/1.093.0057. arXiv: 1009.1003 [physics.data-an].

[164] Victor Mukhamedovich Abazov et al. "An Improved determination of the width of the top quark". In: *Phys. Rev. D* 85 (2012), p. 091104. DOI: 10.1103/PhysRevD.85.091104. arXiv: 1201.4156 [hep-ex].

[165] Morad Aaboud et al. "Direct top-quark decay width measurement in the $t\bar{t}$ lepton+jets channel at $\sqrt{s}$=8 TeV with the ATLAS experiment". In: *Eur. Phys. J. C* 78.2 (2018), p. 129. DOI: 10.1140/epjc/s10052-018-5595-5. arXiv: 1709.04207 [hep-ex].

[166] Johan Alwall et al. "Is $V_{\mathrm{tb}} \simeq 1$?" In: *Eur. Phys. J. C* 49 (2007), pp. 791–801. DOI: 10.1140/epjc/s10052-006-0137-y. arXiv: hep-ph/0607115.

[167] Wenxing Fang et al. "Model-independent constraints on the CKM matrix elements $|V_{tb}|$, $|V_{ts}|$ and $|V_{td}|$". In: *JHEP* 03 (2019), p. 022. DOI: 10.1007/JHEP03(2019)022. arXiv: 1807.07319 [hep-ph].

[168] Albert M Sirunyan et al. "Search for resonant $\mathrm{t\bar{t}}$ production in proton-proton collisions at $\sqrt{s} = 13$ TeV". In: *JHEP* 04 (2019), p. 031. DOI: 10.1007/JHEP04(2019)031. arXiv: 1810.05905 [hep-ex].

[169] Albert M Sirunyan et al. "Extraction and validation of a new set of CMS PYTHIA8 tunes from underlying-event measurements". In: *Eur. Phys. J. C* 80.1 (2020), p. 4. DOI: 10.1140/epjc/s10052-019-7499-4. arXiv: 1903.12179 [hep-ex].

[170] Andrew J. Larkoski et al. "Soft Drop". In: *JHEP* 05 (2014), p. 146. DOI: 10.1007/JHEP05(2014)146. arXiv: 1402.2657 [hep-ph].

[171] *CMS luminosity measurement for the 2017 data-taking period at* $\sqrt{s}$ = 13 TeV. Tech. rep. CMS-PAS-LUM-17-004. Geneva: CERN, 2018. URL: http://cds.cern.ch/record/2621960.

[172] *CMS luminosity measurement for the 2018 data-taking period at* $\sqrt{s}$ = 13 TeV. Tech. rep. CMS-PAS-LUM-18-002. Geneva: CERN, 2019. URL: http://cds.cern.ch/record/2676164.